



Instituto de Física de Cantabria
Departamento de Física Moderna
Universidad de Cantabria

Optimal treatment of foreground and systematics to exploit present and future CMB data

***Tratamiento óptimo de contaminantes y sistemáticos para la explotación
presente y futura de datos del Fondo Cósmico de Microondas***

Memoria presentada para optar al título de Doctor en Ciencias Físicas
por la Universidad de Cantabria

por

Elena de la Hoz López-Collado

Bajo la supervisión de Patricio Vielva Martínez y Enrique Martínez González

Patricio Vielva Martínez, Doctor en Ciencias Físicas e Investigador Científico del Consejo Superior de Investigaciones Científicas

y

Enrique Martínez González, Doctor en Ciencias Físicas y Profesor de Investigación del Consejo Superior de Investigaciones Científicas

CERTIFICAN que la presente memoria

Tratamiento óptimo de contaminantes y sistemáticos para
la explotación presente y futura de datos
del Fondo Cósmico de Microondas

ha sido realizada, bajo su dirección, por Elena de la Hoz López-Collado, y constituye su Tesis para optar al grado de Doctor por la Universidad de Cantabria. Asimismo, emiten su conformidad para que la presente Memoria sea depositada y se celebre, ulteriormente, la correspondiente Lectura y Defensa.

En Santander, a 14 de noviembre de 2022,

Fdo.: Dr. Patricio Vielva Martínez

Fdo.: Dr. Enrique Martínez González

*A Kiko, mi
apoyo incondicional*

Agradecimientos

El trabajo de esta tesis se ha extendido durante varios años con sus correspondientes altibajos. Spoiler, la pandemia hizo mucho daño. Sin embargo, hay mucha gente que ha estado ahí durante todo el proceso y sin la cual este documento no existiría. Por eso creo que es necesario dedicarles una sección.

Primero de todo, me gustaría agradecer a Patri. Nunca podría haber soñado con un director mejor, tanto calidad profesional como personal. No puedo expresar con palabras toda la gratitud que siento, muchísimas gracias por todo.

También quiero agradecer a todo el grupo de cosmología del IFCA, porque el doctorado no hubiera sido así de bueno sin vosotros. Me gustaría hacer especial mención a mis compañeros de despacho: Patricia, a la que voy a echar mucho de menos ahora que nos tenemos que separar; Chemi que ha sido uno de mis mayores apoyos desde que llego, Guille con el que no puedes parar de reírte y a Alberto con el que compartí muy buenos momentos. Tampoco, me puedo olvidar del resto de la gente del IFCA, en especial a la piña del comedor, me habéis dado la vida.

Esta tesis tampoco habría sido posible sin la ayuda de los investigadores que me acogieron durante mis estancias: a Eiichiro Komatsu del Max-Planck für Astrophysik y a Radek Stompor del Centre Pierre Binétruy, muchas gracias.

A mi segunda casa, ProBox y su gente, que se sienten como familia. Sin vosotros no sé donde hubiera acabado mi salud mental. A mis amigos que siempre están pasa lo que pase Carmen, Joseki, Cris, Raquel, Unai, tenéis un sitio especial en mi corazón.

Por último y obviamente no menos importante, a mis padres, mis hermanas Isa y Car, y Kiko. Vosotros sois el mayor pilar de mi vida. Os quiero.

*"The journey of a thousand miles begins
with one step."*

Lao Tzu

One of the most awaited milestones in cosmology is the detection of primordial gravitational waves, as they constitute compelling evidence of an inflationary phase. In principle, they can be measured through the imprint left on the B-mode signal of the Cosmic Microwave Background. However, this detection entails many experimental and data analysis challenges since it is relatively faint compared to other B-mode sources, e.g., astrophysical foregrounds, lensed E- to B-modes, and systematic errors. This thesis is one of many efforts in the field of data analysis to detect this signal in an unbiased manner.

This work is a compilation thesis that includes several studies performed in the context of component separation applied to Cosmic Microwave Background polarization data. It presents three different applications of component separation. i.e., the study and optimization of experimental designs (P. I), the mitigation of systematic errors (P. II & P. III), and the characterization of astrophysical foregrounds (P. IV). It contains the following publications:

- P. I: **de la Hoz, E.**, Vielva, P., Barreiro, R. B., & Martínez-González, E. (2020). On the detection of CMB B-modes from the ground at low frequency. *Journal of Cosmology and Astroparticle Physics*, 2020(06), 006.
- P. II: **de la Hoz, E.**, Diego-Palazuelos, P., Martínez-González, E., Vielva, P., Barreiro, R. B., & Bilbao-Ahedo, J. D. (2022). Determination of polarization angles in CMB experiments and application to CMB component separation analyses. *Journal of Cosmology and Astroparticle Physics*, 2022(03), 032.
- P. III: Krachmalnicoff, N., Matsumura, T., **de la Hoz, E.**, Basak, S., Gruppuso, A., Minami, Y., Baccigalupi, C., Komatsu, E., Martínez-González, E., Vielva, P. & LiteBIRD collaboration. (2022). In-flight polarization angle calibration for LiteBIRD: blind challenge

and cosmological implications. *Journal of Cosmology and Astroparticle Physics*, 2022(01), 039.

- P. IV: **de la Hoz, E.**, Barreiro, R. B., Vielva, P., Martínez-González, E., Rubiño-Martín, J. A., Casaponsa, B., Guidi, F., Ashdown, M., Génova-Santos, R. T. & QUIJOTE collaboration (2022). QUIJOTE scientific results - VIII. Diffuse polarized foregrounds from component separation with QUIJOTE-MFI. *Monthly Notices of the Royal Astronomical Society*. In press.

"El camino de mil millas empieza con un paso."

Lao Tzu

Uno de los hitos más esperados en cosmología es la detección de las ondas gravitacionales primordiales, ya que constituirían una prueba irrefutable de la existencia de un periodo inflacionario. En principio, pueden medirse a través de la huella marcada en la señal del modo B del Fondo Cósmico de Microondas. Sin embargo, esta detección conlleva muchos retos desde el punto de vista experimental y de análisis de datos, ya que es relativamente débil en comparación con otras fuentes de modos B, como los contaminantes astrofísicos, los modos lensados de E a B, y los errores sistemáticos. Esta tesis es uno de los muchos esfuerzos en el campo del análisis de datos dedicados a la detección de esta señal de forma insesgada.

Este trabajo es una tesis por compendio de artículos que incluye varios estudios realizados en el contexto de la separación de componentes aplicada a los datos de polarización del Fondo Cósmico de Microondas. Presenta tres aplicaciones diferentes de la separación de componentes en este campo, en particular, el estudio y optimización de los diseños experimentales (P. I), la mitigación de los errores sistemáticos (P. II & P. III), y la caracterización de contaminantes astrofísicos (P. IV). Contiene las siguientes publicaciones:

- P. I: **de la Hoz, E.**, Vielva, P., Barreiro, R. B., & Martínez-González, E. (2020). On the detection of CMB B-modes from the ground at low frequency. *Journal of Cosmology and Astroparticle Physics*, 2020(06), 006.
- P. II: **de la Hoz, E.**, Diego-Palazuelos, P., Martínez-González, E., Vielva, P., Barreiro, R. B., & Bilbao-Ahedo, J. D. (2022). Determination of polarization angles in CMB experiments and application to CMB component separation analyses. *Journal of Cosmology and Astroparticle Physics*, 2022(03), 032.

- P. III: Krachmalnicoff, N., Matsumura, T., **de la Hoz, E.**, Basak, S., Gruppuso, A., Minami, Y., Baccigalupi, C., Komatsu, E., Martínez-González, E., Vielva, P. & LiteBIRD collaboration. (2022). In-flight polarization angle calibration for LiteBIRD: blind challenge and cosmological implications. *Journal of Cosmology and Astroparticle Physics*, 2022(01), 039.
- P. IV: **de la Hoz, E.**, Barreiro, R. B., Vielva, P., Martínez-González, E., Rubiño-Martín, J. A., Casaponsa, B., Guidi, F., Ashdown, M., Génova-Santos, R. T. & QUIJOTE collaboration (2022). QUIJOTE scientific results - VIII. Diffuse polarized foregrounds from component separation with QUIJOTE-MFI. *Monthly Notices of the Royal Astronomical Society*. In press.

I	Introduction	1
1	The Universe we live in	3
1.1	The Concordance Model: Λ CDM	6
1.1.1	Λ CDM components	6
1.1.2	Model parameters	9
1.2	Observational Probes	11
1.2.1	Big Bang Nucleosynthesis	11
1.2.2	Cosmic Microwave Background	13
1.2.3	Large Scale Structure	15
1.2.4	Standard Objects	16
1.3	Open Questions	18
2	Cosmic Microwave Background	21
2.1	CMB Temperature	22
2.1.1	Angular power spectrum	22
2.1.2	Cosmological interpretation	24
2.2	CMB Polarization	26
2.2.1	Angular power spectra	26
2.2.2	CMB Polarization Science	28
2.3	Primordial B-modes Detection Challenges	29
2.3.1	Astrophysical Foregrounds	29
2.3.2	Lensed E- to B-Modes	35
2.3.3	Systematic Effects	38
2.4	Component Separation	41
2.4.1	Non-parametric methodologies	42
2.4.2	Parametric methods	49

II	Thesis contributions	53
3	Included publications	55
3.1	B-SeCRET	56
3.2	Published applications	57
3.2.1	Experimental Design	57
3.2.2	Systematics control	57
3.2.3	Foreground characterization	58
3.3	P. I: On the detection of CMB B-modes from ground at low frequency	61
3.4	P. II: Determination of polarization angles in CMB experiments and applica- tion to CMB component separation analyses	92
3.5	P. III: In-flight polarization angle calibration for LiteBIRD: blind challenge and cosmological implications	122
3.6	P. IV: QUIJOTE scientific results –VIII. Diffuse polarized foregrounds from component separation with QUIJOTE-MFI	161
4	Conclusions	183
5	Conclusiones	187

List of Figures

(1.1) Nuclei Abundances	12
(1.2) CMB spectrum.	14
(1.3) Matter power spectrum	15
(1.4) Hubble diagram for the Pantheon sample	17
(2.1) CMB angular power spectra	24
(2.2) Sketch of Thomson Scattering	27
(2.3) Inflation constraints	28
(2.4) Astrophysical coponents' SED	30
(2.5) Synchrotron's spectral index spectrum	33
(2.6) Faraday rotation angle	34
(2.7) Lensing power spectrum	37

Part I

Introduction

The Universe we live in

"It is far better to grasp the universe as it really is than to persist in delusion, however satisfying and reassuring."

Carl Sagan

The main topic of this thesis is parametric component separation techniques and their applications to Cosmic Microwave Background science. However, it is interesting to take a step back and review how far we have come in our quest to understand the Universe before addressing it. This chapter introduces the *concordance model* of cosmology, the Λ CDM model, and the observational probes that have contributed most to our understanding of the Universe. The chapter concludes with the open questions that remain unanswered in this fascinating field.

"How is the world that surrounds us?", "How does it originated?", "Does it have an origin?"... Humanity has questioned and theorized about the world we live in for longer than anyone can remember. However, it was not until Einstein published the General Theory of Relativity that testable theories of the Universe were developed. Einstein's revolutionary idea was that gravity was not a force but an acceleration caused by the wrapping of spacetime (Einstein, 1916). The theory can be encapsulated in Einstein's equations which provide a mathematical relationship between spacetime's geometry and the constituents that populate spacetime. These equations are summarized in the following celebrated equation¹:

$$G_{\mu\nu} + \Lambda g_{\mu\nu} = 8\pi G T_{\mu\nu} , \quad (1.1)$$

¹The equation is given in natural units, i.e., $c = \hbar = 1$.

where $G_{\mu\nu}$ and $g_{\mu\nu}$ are the Einstein and the metric tensor, which encloses the spacetime properties, $T_{\mu\nu}$ is the stress-energy tensor that depends on the properties of the constituents, G is Newton's constant, and Λ is a cosmological constant.

After the birth of General Relativity, remarkable progress was made in our understanding of the Universe:

⇒ **Size of the Universe:** In 1920, this issue was addressed in the renowned *Great Debate*. The astronomers Harlow Shapley and Heber Curtis discussed the nature of spiral nebulae and the size of the Universe. The former supported that the Universe was mainly the Milky Way, and these nebulae were relatively small objects located on the outskirts of the "Universe". On the other hand, the latter believed they were large independent objects far from our Galaxy, implying that the Universe was larger. This controversy ended when Edwin Hubble, measuring the distance using Cepheid variable stars², showed that Andromeda and other nebulae lie outside the Milky Way (Hubble, 1926).

⇒ **Expansion of the Universe:** Between the 1920s and 1930s, several authors derived the solutions of Einstein's equations for an isotropic homogeneous expanding universe. From the Friedmann-Lemaître-Robertson-Walker (FLRW) metric given as

$$ds^2 = -dt^2 + a(t)^2 \left[\frac{dr^2}{1 - kr^2} + r^2(d\theta^2 + \sin^2\theta d\phi^2) \right], \quad (1.2)$$

where k is proportional to the space curvature, and $a(t)$ is the scale factor that relates the comoving distance with the physical distance, i.e., $a(t)$ accounts for the expansion of the Universe, one can obtain the solutions for this type universe³. The solutions, also known as the Friedmann and acceleration equations, are

$$\left(\frac{\dot{a}}{a} \right)^2 = \frac{8\pi G}{3} \rho - \frac{k}{a^2} + \frac{\Lambda}{3}, \quad (1.3)$$

$$\frac{\ddot{a}}{a} = -\frac{4\pi G}{3} (\rho + 3P) + \frac{\Lambda}{3}, \quad (1.4)$$

where ρ and P are the density and pressure of the universe's constituents. These equations combined with the continuity equation

$$\dot{\rho} + 3H(\rho + p) = 0 \quad (1.5)$$

are used to determine the dynamics of the universe⁴.

From the solution for an expanding universe, Georges Lemaître, in 1927, predicted

²Henrietta Leavitt's discovery of the period-luminosity Cepheid's relationship in 1912 played a crucial role in the galaxies' distance measurements (Leavitt & Pickering, 1912).

³Here, I follow the standard convention in cosmology and assign a positive sign to the spatial coordinates.

⁴The dynamics are explained with two equations, the third equation is redundant.

the distance-redshift relation, i.e., the distant galaxies must be moving away from us (Lemaître, 1927). For an object with no comoving⁵ motion, the distance-velocity relationship is

$$v = \frac{d}{dt}(ax) = \frac{da}{dt}x = \frac{1}{a} \frac{da}{dt}d \simeq H_0 d, \quad (1.6)$$

where x and d are the physical and comoving distance, and H_0 is the Hubble constant at the present time, which measures how fast the distant galaxies are receding from us. In 1929, Hubble using his measurements of the velocities and Vesto Slipher's spiral nebulae's redshifts, demonstrated this fact (Hubble, 1929). The latter constitutes the first evidence of the expansion of the Universe.

- ⇒ **Evidence of non-baryonic matter:** In 1933, Fritz Zwicky found a discrepancy between the estimated mass of the Coma cluster using the virial theorem and the expected from electromagnetic measurements (Zwicky, 1933). Using the observed rotational velocities of the galaxies, he calculated the gravitational mass of the cluster, finding that it was at least 400 times greater than the one calculated based on their luminosity. Thus, there needed to be a form of nonluminous matter, which Zwicky named *dunkle materie*, i.e., dark matter. Decades later, in the 1970s, Vera Rubin and Kent Ford measured the rotation curves of spiral galaxies at large radii (Rubin & Ford, 1970). Contrary to the expectation of finding a decreasing behavior with increasing radius as $r^{-1/2}$, the curves flatten. The existence of an additional non-visible matter that extends beyond the galactic disk resolves this inconsistency.
- ⇒ **Big-Bang theory:** During the 1950s, there were two popular theories of the evolution of the Universe. A steady-state model developed primarily by Fred Hoyle and the Big Bang theory based on Lemaître's work. George Gamow and his colleagues Ralph Alpher and Robert Herman delved into the theoretical development of the Big Bang model. The former introduced the origin of chemical elements, now termed Big Bang Nucleosynthesis (BBN) (Alpher et al., 1948), while the other predicted the existence of isotropic, near-blackbody background radiation, the Cosmic Microwave Background (CMB) (Gamow, 1956; Alpher & Herman, 1948). The discovery of the CMB in 1964 by Arno Penzias and Robert Wilson consolidated the Big Bang theory (Dicke et al., 1965).
- ⇒ **Inflation:** During the 1970s, several problems intrinsic to the Big Bang theory were pointed-out, e.g., the Horizon, Flatness, and the absence of magnetic monopoles problems. An exponential expansion of the Universe during its beginning solves the issues raised (Vazquez et al., 2018). This theory coined as *inflation* was first developed by Alan Guth (Guth & Tye, 1980) and Katsuhiko Sato (Sato, 1981) independently. However, this theory was problematic because the model did not reheat properly, i.e., it

⁵A comoving coordinate system is a reference frame that expands accordingly with the universe's expansion. Thus, while the physical distance between two comoving objects increases as the space expands, their comoving distance remains constant.

did not generate any radiation. Andrei Linde, and Andreas Albrecht & Paul Steinhardt independently found a solution (Linde, 1982; Albrecht & Steinhardt, 1982). In their model, inflation occurs due to a scalar field rolling down a potential energy hill instead of tunneling out of a false vacuum state like in the previous model.

⇒ **Accelerated expansion:** At the end of the twentieth century, studies of Supernova Type Ia (SN Ia) found that the Universe was expanding in an accelerated fashion (Riess et al., 1998; Perlmutter et al., 1999). As a result, a cosmological constant Λ was revived to describe a form of dark energy responsible for the accelerated expansion of the Universe⁶.

Despite these developments, Modern Cosmology did not become a precision science until the last few decades. The latter results from the substantial increase of observational data from telescopes operating across the entire electromagnetic spectrum.

The rest of the chapter is devoted to reviewing the state-of-the-art in Cosmology. Section 1.1 summarizes the cosmological concordance model (Λ CDM). Then, Section 1.2 describes the most important observational probes from which we derive cosmological information. Finally, Section 1.3 outlines the field's most important open questions.

1.1 The Concordance Model: Λ CDM

The Λ CDM (Lambda Cold Dark Matter) model, also known as the *concordance* or standard model of cosmology, is the simplest model that reasonably explains the observations. This model makes the following assumptions: i) we live in a Euclidean universe ($k = 0$) composed of ii) a cosmological constant Λ which accounts for the accelerated expansion of the Universe, iii) cold dark matter, i.e., non-relativistic dark matter particles that only interact through the gravitational effects with iv) Standard Model particles (baryonic matter), and finally v) the existence of primordial, adiabatic, Gaussian quantum perturbations which constitute the seed of the structure we observe today. This section reviews the Λ CDM pillars (Section 1.1.1), focusing on the initial perturbations seeded by inflation, and the model parameters Section 1.1.2.

1.1.1 Λ CDM components

Dark energy (Λ). It is the dominant component in the present Universe, accounting for 68% of its total energy density. A positive cosmological constant with a fixed equation of state value $w \simeq -1$ was reintroduced to explain the accelerated expansion of the Universe from supernovae observations⁷. There are extensions of Λ CDM in which the equation of

⁶Einstein first proposed a cosmological constant to counteract the effect of gravity and achieve a static universe. After Hubble's confirmation that the Universe was expanding, this cosmological constant was abandoned until this discovery.

⁷Some models do not require dark energy to explain the accelerated expansion of the Universe. These models usually fall in the category of modified gravity models (Joyce et al., 2016).

state evolve with time (Chevallier & Polarski, 2001) but current observations favor the cosmological constant (Planck Collaboration et al., 2020a).

Cold Dark Matter (CDM). Around 27% of the Universe's content, today is formed of a non-visible matter not included in the Standard Model of particle physics. Unlike baryonic, dark matter does not interact with photons and has only been detected through gravitational effects. The nature of this matter is still unknown, with many proposed candidates, e.g., WIMPs, axions, primordial black holes, etc. (Arbey & Mahmoudi, 2021). The term *cold* dark matter refers to models of non-relativistic dark matter particles. If the particles were *hot*, there would be a significantly different structure than what we observe today (Viel et al., 2013).

Standard Model particles. The remaining 5% of the Universe content is composed of known matter, i.e., the one described by the Standard Model of particle physics (SM). The SM describes the known fundamental particles in nature and their interaction. Although it is a well-established theory, it cannot explain measurements such as neutrino oscillations (Fukuda et al., 1998; Ahmad et al., 2002). A new field known as astroparticle physics has recently emerged to study elementary particles and their relationships to astrophysics and cosmology. One of its main motivations is the typical energy scales targeted with measurements of the early Universe, which are not achievable from particle colliders.

Primordial perturbations. The inflation process described in the previous section introduces a natural way of generating the initial scalar perturbations responsible for the structure observed today. Although there are many models to explain the inflation mechanism (Martin et al., 2014), the most popular is the *single field slow-roll* model mainly due to its simplicity. A scalar field ϕ evolves slowly over an almost flat part of its self-interaction potential $V(\phi)$ (exponential expansion) until it falls into a minimum where it oscillates and gives rise to the particles in a process called *reheating* (TsujiKawa, 2003).

The inflaton field ϕ can be split up into two components

$$\phi(t, \mathbf{x}) = \phi_0(t) + \delta\phi(t, \mathbf{x}), \quad (1.7)$$

where $\phi_0(t)$ is the homogenous background field, and $\delta\phi(t, \mathbf{x})$ the quantum perturbations of the field. Assuming the FLRW metric (eq. 1.2) and restricting to the case of a homogeneous field, the energy density and the pressure density of the field ϕ are

$$\rho_\phi = \frac{1}{2}\dot{\phi}^2 + V(\phi), \quad (1.8)$$

$$p_\phi = \frac{1}{2}\dot{\phi}^2 - V(\phi). \quad (1.9)$$

The equation of state is then

$$w_\phi \equiv \frac{\rho_\phi}{p_\phi} = \frac{\frac{1}{2}\dot{\phi}^2 + V(\phi)}{\frac{1}{2}\dot{\phi}^2 - V(\phi)}, \quad (1.10)$$

which shows that a scalar field can lead to negative pressure ($w_\phi < 0$) and accelerated expansion ($w_\phi < -1/3$) if the potential energy dominates over the kinetic energy. The evolution of the background field is described in reviews such as Baumann (2009).

We are interested in the quantum fluctuations generated during inflation $\delta\phi(x, t)$. These fluctuations were driven to scales much larger than the Hubble horizon⁸ during this period of exponential expansion. There, they froze and turned into metric perturbations. These metric perturbations were of two types: scalar and tensor perturbations. The scalar perturbations constituted the initial “seeds” of the structure observed today, while the tensor perturbations generated primordial gravitational waves.

Let $\Phi(k)$ be the vacuum operator at the wavenumber scale k . The expectation value of the vacuum fluctuations is zero, unlike their non-zero variance. Assuming statistical homogeneity, the power spectrum of the fluctuations $P_\phi(k)$ is given by

$$\langle \Phi(\mathbf{k})\Phi^*(\mathbf{k}') \rangle = P_\phi(k) (2\pi)^3 \delta_D^{(3)}(\mathbf{k} - \mathbf{k}'). \quad (1.11)$$

where $\langle \dots \rangle$ represents the ensemble average of the fluctuations. If the perturbations are Gaussian⁹, then the power spectrum contains all the statistical information. The power spectrum of the scalar fluctuations generally is parametrized as follows

$$\mathcal{P}_\mathcal{R} = 2\pi^2 \mathcal{A}_s k^{-3} \left(\frac{k}{k_*} \right)^{n_s-1}, \quad (1.12)$$

and the tensor fluctuations power spectrum is parametrized as

$$\mathcal{P}_T = 2\pi^2 \mathcal{A}_T k^{-3} \left(\frac{k}{k_*} \right)^{n_T}, \quad (1.13)$$

where \mathcal{A}_s (\mathcal{A}_T) is the amplitude of the scalar (tensor) perturbations at the pivot scale k_* and

$$n_s - 1 = \frac{d \ln \mathcal{P}_\mathcal{R}(k)}{d \ln k}, \quad (1.14)$$

$$n_T = \frac{d \ln \mathcal{P}_T(k)}{d \ln k}, \quad (1.15)$$

are the scalar and tensor tilts, respectively. Instead of \mathcal{A}_T , the power of the tensor perturba-

⁸The Hubble horizon defines the boundary between the particles that can be observed from a given point in spacetime and those that are inaccessible at a given time.

⁹For single-field slow-roll inflation, the amount of non-Gaussianity is small.

Table 1.1: Λ CDM parameters. Best fit parameters obtained using the combination of data from *Planck* CMB temperature and polarization power spectra (including lensing reconstruction) and BAO data (Planck Collaboration et al., 2020a).

ω_b	ω_c	$100\theta_{MC}$	τ	$\ln(10^{10}A_s)$	n_s
0.02242	0.11933	1.04101	0.0561	3.047	0.9665

tions is often studied using

$$r \equiv \frac{\mathcal{A}_T}{\mathcal{A}_s}, \quad (1.16)$$

known as the *tensor-to-scalar* ratio. In the case of slow-roll models, these parameters are not independent, $r = -8n_T$. As a result, any slow-roll inflationary model requires only three independent parameters: \mathcal{A}_s , n_s , and r .

Observations (Planck Collaboration et al., 2016c) have shown that the initial scalar perturbations are, as predicted

- ⇒ Gaussian, i.e., the information is contained in the first two order moments,
- ⇒ adiabatic, i.e., the perturbations can be expressed as a time shift in the background scalar field (Gordon, 2001)

$$\delta\phi = \dot{\phi}_0(t)\delta t(t, \mathbf{x}), \quad (1.17)$$

- ⇒ and nearly scale-invariant, i.e., there are no privileged scales in the primordial density field.

Nowadays, the focus is on detecting the signal generated by tensor perturbations since it would be solid evidence of an inflationary phase. The tensor perturbations create primordial gravitational waves (PGWs) from quantum fluctuations of the metric. The detection of PGWs with interferometers such as LIGO or LISA is not guaranteed. Only a few inflation models beyond the standard single-field slow-roll model predict that the PGWs will be detectable with these experiments (Campeti et al., 2021; Komatsu, 2022). However, they leave an imprint in the polarization pattern of CMB, which may be detectable with future and planned experiments. The following chapter Chapter 2 presents the expectations regarding this detection with future CMB experiments.

1.1.2 Model parameters

The standard Λ CDM condenses the knowledge of the Universe in a set of six independent parameters¹⁰. Given a set of parameters, one can derive the rest of the model parameters. The set of independent parameters is not unique, i.e., several parameter combinations can explain the whole model. Observations of the CMB, the brightness/redshift relation for

¹⁰Sometimes r is an additional parameter of the model.

supernovae, and large-scale galaxy clustering have placed tight constraints on the model parameters. Tab. 1.1 shows the current best fit model parameters using *Planck* and Baryonic Acoustic Oscillations (BAO) data (Planck Collaboration et al., 2020a). Here, I review the model parameters categorized by the information they contain.

Initial perturbations

These parameters contain information on primordial perturbations. The subset of parameters commonly include $\{A_s, n_s\}$, (eq. 1.12). This set describes the power spectrum of the primordial scalar fluctuations responsible for the seeds whose evolution leads to the formation of structures. The tensor-to-scalar ratio r can be included to describe the power spectrum of tensor fluctuations.

Geometry, composition, and evolution of the Universe

This category incorporates the parameters that describe the geometrical properties of the Universe, its evolution, and its composition, which are interrelated. An example of geometrical parameters is the angular diameter distance to the sound horizon at the last scattering surface¹¹ θ_{MC} . Parameters that describe the Universe's evolution are the current expansion rate (H_0), which is redundant with θ_{MC} , or the age of the Universe.

The evolution of the Universe also depends on the relative density of its constituents, i.e., baryons (b), CDM (c), dark energy (Λ), radiation (r), and curvature (k). The components' content usually is expressed in terms of

$$\Omega_X \equiv \rho_X / \rho_{\text{crit}}, \quad (1.18)$$

which is the density of component X relative to the critical density, $\rho_{\text{crit}} = 3H^2 / (8\pi G)$, i.e., the Universe density for which the spatial geometry is flat.

Not all parameters listed here are independent or constrained by observations. Due to the Universe's expansion, Ω_r is approximately 0. Moreover, since current constraints are compatible with a flat Universe, Ω_k is assumed null. The total energy content adds up to unity, hence Ω_Λ can be calculated from Ω_c and Ω_b . Sometimes the former parameters are exchanged by the baryon $\omega_b = \Omega_{0b} h^2$ and cold dark matter $\omega_c = \Omega_{0c} h^2$ energy densities, where $h = H_0 / 100 \text{ km s}^{-1} \text{ Mpc}^{-1}$ is the dimensionless Hubble constant. Thus, possible subsets are for example: $\{\Omega_b, \Omega_c, H_0\}$, $\{\omega_b, \omega_c, H_0\}$, or $\{\omega_b, \omega_c, \theta_{MC}\}$.

Astrophysical parameters

They are associated with astrophysical processes such as radiation transfer, ionization, and recombination. Important parameters are the ones that establish the beginning of Reionization. During Reionization, hydrogen is ionized again due to the formation of stars and

¹¹The last scattering surface is the spherical surface around the observer such that the radius of the shell is the distance each photon has traveled since recombination. These concepts are introduced in Section 1.2.2.

galaxies. The reionization optical depth (τ) characterizes the start of this period

$$\tau = \sigma_T \int_0^{z_{\text{rei}}} dz n_e(z), \quad (1.19)$$

where σ_T is the Thomson scattering rate, $n_e(z)$ is electron density as a function of the redshift, and z_{rei} is the redshift at the start of reionization.

1.2 Observational Probes

This section reviews the observational probes that test our cosmological models. These probes are the light element abundances (Section 1.2.1), the CMB spectrum and its temperature and polarization anisotropies (Section 1.2.2), large scale-structure (LSS) probes (Section 1.2.3), and *standardizable* objects (Section 1.2.4).

1.2.1 Big Bang Nucleosynthesis

Big Bang Nucleosynthesis (BBN) refers to the time of the Universe when the temperature dropped sufficiently for light elements to form. The physical processes of this epoch can be explained using well-established nuclear physics. Mild changes in the conditions at the time of BBN can cause detectable deviations in primordial abundances. Thus, precision observations of light element abundances constitute a probe of both cosmological models and particle physics scenarios.

BBN starts when the Universe's energy drops below typical nuclear binding energies. By the time of BBN, the Universe had already experienced an inflationary epoch and an asymmetric baryogenesis mechanism, which resulted in a small surplus of baryons. The latter condition is necessary, as otherwise there would have not been sufficient baryons to make up for the amount observed today (Pospelov & Pradler, 2010). The cosmic plasma was composed of neutrons, protons, electrons, photons, and neutrinos, tightly coupled and in local thermal equilibrium. High-energy photons prevented the formation of atoms and bound nuclei. As the Universe expanded, the temperature decreased, and the scattering rate of the processes that kept all these constituents coupled started to become less efficient:

1. When the temperature fell below a few MeV, the neutrinos decoupled from the rest of the plasma.¹²
2. Around $T \sim 0.8 \text{ MeV}$, the process by which protons transformed into neutrons became unlikely. The ratio of neutrons to protons settled then around 1/6, but it kept decreasing due to neutron via β decay.

¹²Like photons from the CMB, there are primordial neutrinos that bathe the Universe, CνB (cosmic neutrino background). However, since neutrinos are not very energetic and barely interact with SM particles, their detection is more challenging than for CMB photons.

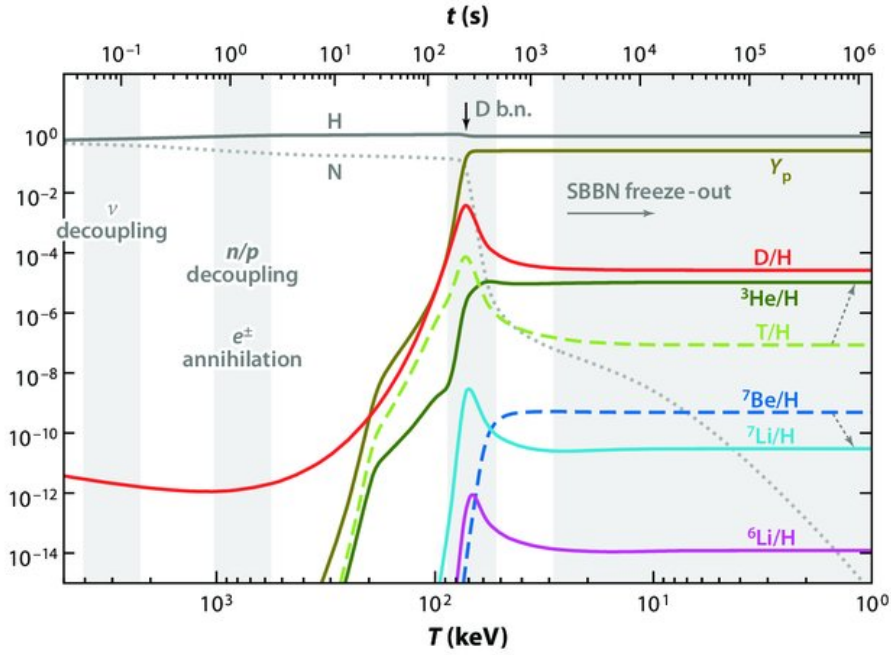


FIGURE 1.1: Nuclei abundances. Light elements' relative abundances as a function of the Universe's temperature/time. SBBN stands for standard BBN. The dashed line shows the abundance of unstable elements that decay into other stable elements. Figure from (Pospelov & Pradler, 2010).

3. The formation of deuterium (D) was not favored due to a large number of photons with energies close to the D binding energy ~ 2.2 MeV. When the density of those energetic photons decreased enough, the abundance of D increased and triggered other nuclear reactions.
4. Stable helium nuclei (${}^4\text{He} \equiv Y_p$) started to form at that time. ${}^4\text{He}$ became the most abundant nuclei as it neither decays nor combines easily to form heavier nuclei. Moreover, ${}^4\text{He}$ is favored over D since the binding energy of helium is larger.
5. At the end of BBN, the main nuclear reactions dropped out of equilibrium, and the abundance of light elements froze out.

Fig. 1.1 shows the evolution of light elements abundances. Heavier elements (with atomic number $A \gtrsim 8$) were formed much later in stars' synthesis process and cosmic rays. These predicted abundances depend on the density of protons and neutrons during BBN, i.e., on baryon density Ω_b , since most baryons were in the form of protons and neutrons at that time. The comparison of predicted abundances with observations provides a test of physics laws in the early Universe and constrains the baryon density.

The most reliable measurement of light element abundances is that of deuterium, obtained by measuring an absorption feature in the spectrum of distant quasars at high redshifts (Burles & Tytler, 1998). Most measurements of the abundances are consistent with other probes, such as CMB anisotropies. The observations show that baryonic matter accounts for at most 5% of the critical density, i.e., another hint of the existence of dark matter

(Aver et al., 2015; Cooke et al., 2018).

It is worth mentioning that there are tensions between the observational measurements of ${}^7\text{Li}$ abundance and other probes. The problem is known as the “Cosmic Lithium Problem”. This abundance is obtained from the absorption lines of the ${}^7\text{Li}$ in the atmosphere of metal-poor stars. These measurements show that the ${}^7\text{Li}$ concentration is independent of temperature and metallicity, an effect known as the “Spite Plateau”. This result significantly disagrees with the concordance model value, based on the CMB anisotropies Bertulani (2019); Bertulani et al. (2022).

1.2.2 Cosmic Microwave Background

The temperature decreased as the Universe expanded. Around redshift $z \sim 1100$, it dropped enough that the energetics favored the formation of neutral species, like hydrogen. Before, any hydrogen produced was quickly ionized by energetic photons. Around that moment, the photons decoupled from the cosmic plasma and have free streamed until today. This process is called *recombination*.

The interactions of electrons and photons before recombination ensured the thermal equilibrium of the photons. Since this thermal equilibrium was maintained after decoupling, the CMB is now an isotropic radiation that bathes all the observable Universe with a nearly black-body distribution. Due to the Universe’s expansion, the radiation became less energetic, lowering the temperature to ~ 2.7 K today.

In 1964, A. Penzias and B. Wilson discovered a background noise of unknown origin while calibrating a microwave antenna designed to study the reflection of radio waves from Echo balloon satellites (Penzias & Wilson, 1965). They detected a homogeneous and uniform signal compatible with a background noise of ~ 3.5 K, later identified as the predicted CMB radiation Dicke et al. (1965).

The COBE (COsmic Background Explorer) NASA satellite measured the microwave sky from space between 1989 and 1993 to study the spectral dependence of this signal. COBE’s experiment FIRAS confirmed the black-body spectrum of the CMB (Mather et al., 1994), Fig. 1.2, which constituted compelling evidence for the Big Bang theory¹³.

In addition to measuring the black-body spectrum, COBE’s experiment DIRBE detected anisotropies in the CMB¹⁴ of 1 part in 10^5 . These anisotropies, predicted by inflation, contain information about the initial scalar perturbations. One can compare these anisotropies with those predicted by the study of the evolution of the initial perturbations. Since the initial perturbations are compatible with Gaussianity, the statistics of these anisotropies are studied using the second-order moment, commonly in Fourier space using the *angular power spectrum*. The angular power spectrum is related to the initial perturbations as

¹³Although the black-body spectrum was measured with high precision, FIRAS did not have enough sensitivity to detect spectral distortions. These distortions contain complementary information about the Universe and are yet to be measured (Kogut et al., 2016).

¹⁴After removing the dipole pattern generated by the Doppler effect.

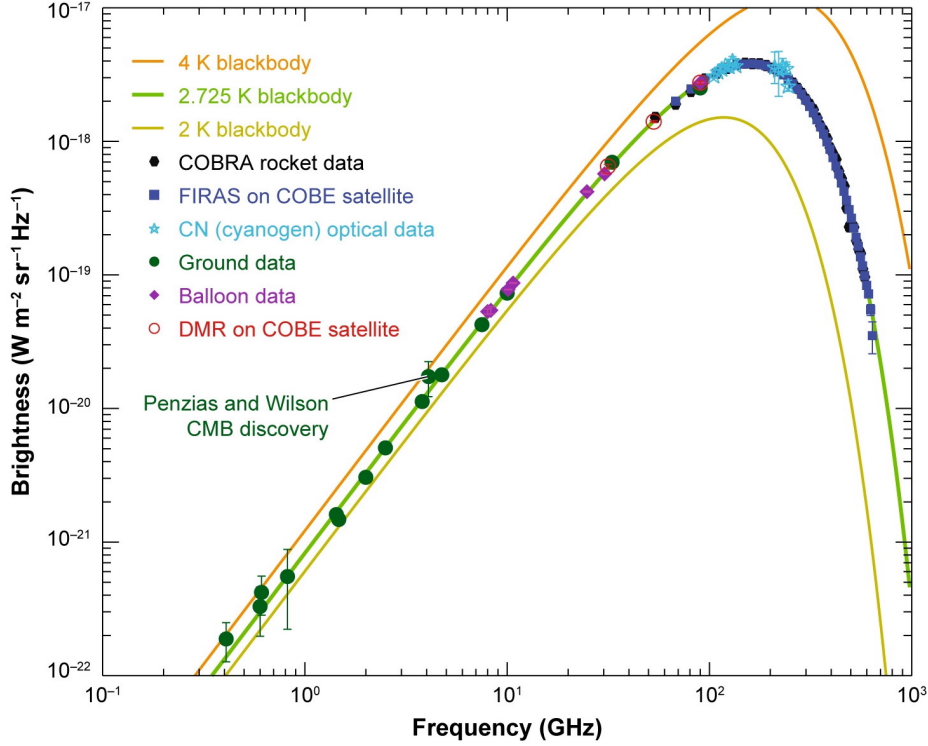


FIGURE 1.2: CMB spectrum. Expected black-body curves for different temperatures along with CMB measurements. Figure from Samtleben et al. (2007).

follows¹⁵

$$C(\ell) = \frac{2}{\pi} \int_0^\infty dk k^2 P_{\mathcal{R}}(k) |\mathcal{T}_\ell|^2, \quad (1.20)$$

where $P_{\mathcal{R}}(k)$ is given in eq. 1.12, and \mathcal{T}_ℓ is the transfer function that contains the evolution of photons. Therefore, CMB anisotropies contain information about the early Universe ($P_{\mathcal{R}}$) and the history of the Universe (\mathcal{T}_ℓ). Derivations of the transfer function can be found in cosmology books such as Baumann (2022); Dodelson & Schmidt (2020), and can be calculated using Boltzmann solvers such as CAMB (Code for Anisotropies in the Microwave Background) (Lewis et al., 2000) and CLASS (Cosmic Linear Anisotropy Solving System) (Blas et al., 2011).

These anisotropies have been measured by WMAP (Wilkinson Microwave Anisotropy Probe) (Hinshaw et al., 2013), and more accurately by *Planck* (Planck Collaboration et al., 2020a). Those observations have provided some of the most stringent constraints to the Λ CDM model. Chapter 2 reviews the cosmological information contained in the CMB anisotropies.

¹⁵The average ensemble value of the anisotropies is zero.

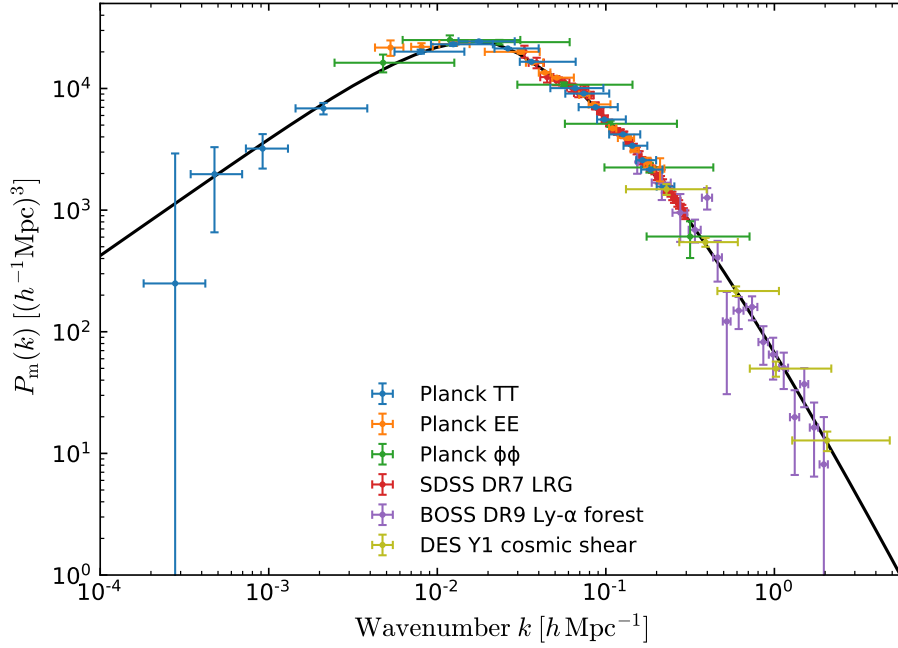


FIGURE 1.3: Matter power spectrum. Linear-theory matter power spectrum (at $z = 0$) inferred from different cosmological probes. The black solid line shows the theoretical prediction. Figure from (Planck Collaboration et al., 2020a).

1.2.3 Large Scale Structure

LSS refers to the distribution of galaxies and matter on scales larger than individual galaxies. Observations of the galaxies' distribution show that the Universe at scales $\lesssim 100$ Mpc is not homogeneous (Shen et al., 2003; Colless, 1999). The matter is mainly distributed along filaments, clusters and walls, between which lie cosmic voids.

The structure we observe today is the evolution of the initial perturbations on matter density. In the late universe, the perturbations remain small on large scales and can be studied using linear theory similar to the study of CMB anisotropies. However, the matter perturbations on small scales (less than ~ 10 Mpc) have become large and are no longer explainable with linear physics¹⁶. In the linear regime (large scales), the matter power spectrum is

$$P_m(k, a) = \frac{8\pi^2}{25} \frac{k^4}{\Omega_m^2 H_0^4} P_{\mathcal{R}}(k) T^2(k) D_+(a), \quad (1.21)$$

where $T(k)$ is the transfer function, which describes the evolution of perturbations, and $D_+(a)$ is the growth factor that accounts for the scale-independent growth at late times.

These theoretical predictions can be compared to observations of galaxies distributions. The observed matter density inhomogeneities field in the Universe at a given point in space-

¹⁶Models that take into account non-linearities are used to extract the cosmological information from the small scales (Bernardeau et al., 2002).

time is

$$\delta_g(\mathbf{n}) = \frac{\rho_g(\mathbf{n}) - \bar{\rho}_g}{\bar{\rho}_g}, \quad (1.22)$$

where $\rho_g(\mathbf{n})$ is the galaxy density field at position \mathbf{n} , and $\bar{\rho}_g$ is the average galaxy density. From its Fourier transform

$$\delta_m(\mathbf{k}) = \int d^3n \delta(\mathbf{n}) e^{-i\mathbf{k}\cdot\mathbf{n}}, \quad (1.23)$$

one can calculate the matter power spectrum as

$$\langle \delta_m(\mathbf{k}) \delta_m(\mathbf{k}') \rangle = (2\pi)^3 P_m(k) \delta_{\mathbf{k},\mathbf{k}'}. \quad (1.24)$$

Fig. 1.3 shows the current observational constraints on the matter power spectrum (Planck Collaboration et al., 2020a).

Other cosmological probes that benefit from galaxy surveys data and provide a complementary check of the model but are not covered here include weak gravitational lensing (Refregier, 2003), BAO measurements described in Section 1.2.4, and redshifts space distortions (Percival et al., 2011).

1.2.4 Standard Objects

Standard objects are astrophysical observations that have a particular property fixed, e.g., the light curve of SN Ia, the length of BAO, etc. (Heavens et al., 2014). They can be used as probes of the Universe's geometry and growth of fluctuations. Below, I present a brief overview of some popular standard objects used for cosmological inference.

SN Ia events occur in binary systems where at least one of the stars is a white dwarf. The unique spectral fingerprint of this brilliant explosion makes SN Ia excellent *standard candles*, i.e., their absolute magnitude depends on other observables. Mainly, the characteristic time required for the luminosity to decay after the peak.

SN Ia can populate the Hubble diagram and be used to perform cosmological inference. The relationship between the luminosity distance as a function of redshift is given by

$$d_L = (1+z) c \int_0^z \frac{dz'}{H(z')}, \quad (1.25)$$

where the cosmological model dependence appears through the definition of $H(z)$. The luminosity distance is related to the distance modulus μ as follows

$$\mu(z) = 5 \log(d_L/10\text{pc}), \quad (1.26)$$

and the distance modulus of a supernova is

$$\mu(z) = m_{\text{obs}} - M + \alpha x_1 + \beta C + \Delta_M + \Delta_B \quad (1.27)$$

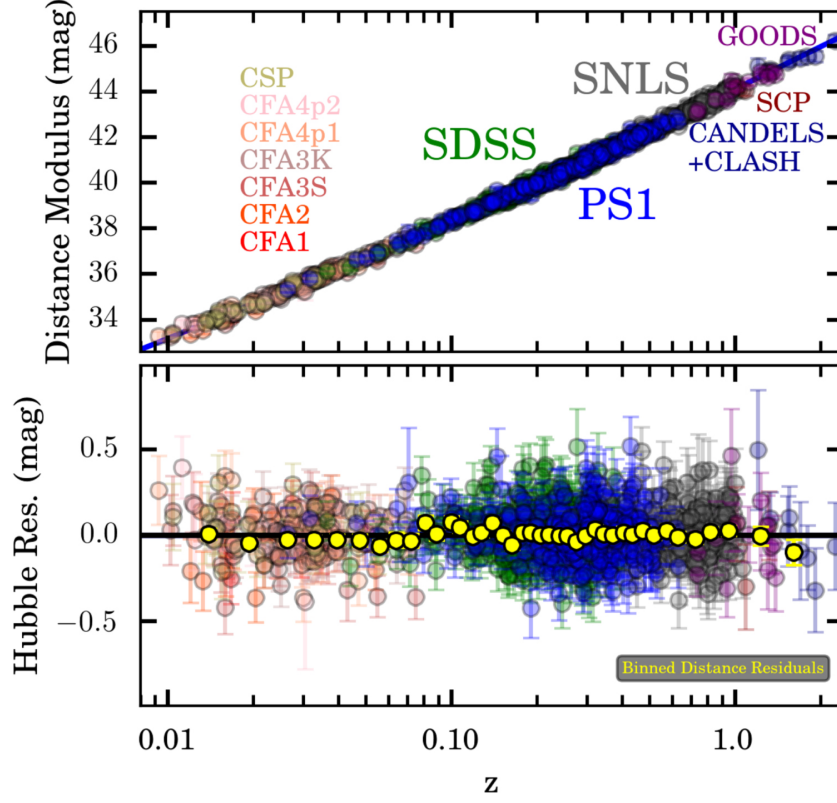


FIGURE 1.4: Hubble diagram for the Pantheon sample. Top: distance modulus eq. 1.26 as a function of redshift. Bottom: residuals to the best-fit cosmology. Figure from Scolnic et al. (2018).

where m is the observed apparent magnitude, and M is the absolute magnitude. The coefficients α and β model the relation between luminosity with the stretch and color, respectively. Δ_M and Δ_B are distance corrections based on the host galaxy mass and predicted biases from simulations, respectively. Fig. 1.4 shows the distance modulus versus redshift relationship using the Pantheon sample (Scolnic et al., 2018). Apart from obtaining a measurement of the Hubble constant, they can place constraints on the cosmological parameters. For example, assuming a flat Λ CDM Universe, the expansion rate¹⁷ is given by

$$H(z) = H_0 \left(\Omega_m (1+z)^3 + \Omega_\Lambda \right)^{1/2}. \quad (1.28)$$

SN Ia measurements can help break degeneracies with other probes and explore extensions of Λ CDM.

Another example of standard candles are radio quasars, which are used to obtain the Hubble parameter (Qi et al., 2021; Liu et al., 2022). However, the validity of their standardized relationship is not confirmed.

A well-known standard ruler for length scales in cosmology is the BAO. Acoustic oscillations were generated by competing effects in the photon-baryon plasma before recombination. The Universe's primordial fluctuations created slightly over (under) dense regions

¹⁷Note that at large redshift the linear relation assumed in eq. 1.6 does not hold.

yielding potential wells (hills). Gravity attracts the photon-baryon fluid to the potential wells, but radiation pressure resists it, causing acoustic oscillations. After recombination, radiation was able to free-stream, and gravity started to dominate, causing LSS to form and imprint around the bubbles of matter created by acoustic waves. The length of these bubbles is set by the maximum distance the acoustic waves could travel in the primordial plasma before recombination. This length provides a measurement of the angular diameter distance to a given redshift and the distance interval associated with a given redshift interval. Thus, BAO measurements are an independent way to test the expansion and evolution of the Universe, as well as constrain parameters such as Ω_Λ (Eisenstein et al., 2005).

Finally, gravitational waves are promising standard sirens for detecting the Hubble parameter (Abbott et al., 2021). The current detection $H_0 = 68.7^{+17.0}_{-7.8}$ has large error bars, but they are expected to shrink as more events are detected. An accurate detection of H_0 from gravitational waves is very valuable since their measurement is completely independent of CMB and SN Ia measurements and could help elucidate the origin of the tension between early and late time measurements (Perivolaropoulos & Skara, 2022).

1.3 Open Questions

Despite its undeniable success, several tensions between observations and Λ CDM have emerged as the accuracy of cosmological observations improved. Some examples are

- ⇒ The Hubble tension, i.e., the significant ($> 4\sigma$) difference between the locally measured Hubble constant H_0 , and the value obtained from the CMB observations (Aloni et al., 2022).
- ⇒ The growth tension, i.e., the discrepancy between weak lensing and CMB measurements of S_8 (Perivolaropoulos & Skara, 2022).
- ⇒ CMB anomalies, including the lack of power on large angular scales, the Cold Spot anomaly, quadrupole-octopole alignment, hemispherical power asymmetry, lensing anomaly, preference for odd parity correlations, (Planck Collaboration et al., 2020c).
- ⇒ The Cosmic Lithium Problem described in Section 1.2.1 (Bertulani et al., 2022).

The reader is referred to Perivolaropoulos & Skara (2022) for a review on the Λ CDM challenges. Apart from these tensions, there are several questions that the model is not able to answer

- ⇒ What is dark matter?
- ⇒ What is dark energy?
- ⇒ Did inflation happen? If so, which mechanism generated inflation?

These questions are commonly included among the scientific priorities in the Science Programmes Plans of funding agencies. Some examples are ESA's ongoing *Cosmic Vision* program¹⁸, and its successor *Voyage 2050*¹⁹, or the current *Astronomy and Astrophysics Decadal Survey* developed by the National Research Council of the National Academy of Sciences in the United States (National Academies of Sciences et al., 2021). In conclusion, Cosmology is a very active and fascinating field that tries to provide answers to fundamental and philosophical questions.

After this general review of the field, I describe in more detail the main focus of my research, i.e., component separation (CS) techniques and their application to CMB science (Chapter 2). In particular, I worked on the characterization and removal of astrophysical foregrounds and systematic effects to extract the CMB polarization signal. Chapter 3 presents an overview of those works along with the thesis publications. Finally, Chapter 4 and Chapter 5 summarize the conclusions from the published studies I conducted during my Ph.D. in English and Spanish, respectively.

¹⁸<https://sci.esa.int/web/cosmic-vision/-/38658-cosmic-vision-2015-2025-the-universe>

¹⁹<https://www.cosmos.esa.int/web/voyage-2050>

Cosmic Microwave Background

"El CMB es como el cerdo, se aprovechan hasta los andares."

Patricio Vielva

After measuring the CMB temperature anisotropies to the cosmic variance limit, the CMB community's focus has shifted to polarization anisotropies. The latter can shed light on inflation, especially if primordial B-modes generated by tensor perturbations are detected. Future and planned CMB experiments aim at reaching sensitivities on the order of $\sigma_r \sim 10^{-3}$, which entails many experimental and data analysis challenges. This chapter reviews CMB science and the challenges associated with the search for primordial B-mode detection. Moreover, I review the latest developments in CS algorithms to surpass these limitations.

The CMB is a uniform relic radiation from the Universe's infancy whose discovery constituted solid evidence against the steady-state Universe model in favor of the Big Bang origin of the Universe. The CMB is a fundamental tool to study the Universe due to the information encoded in its anisotropies. Current observations have measured the temperature anisotropies to the maximum precision attainable. Observations agree remarkably well with the predictions of Λ CDM and have placed tight constraints on its parameters.

The focus is now set on the characterization of polarization anisotropies. The latter contains complementary information to that from temperature and can help break model parameter degeneracies. In addition, CMB polarization is a unique probe to test the inflationary paradigm. Since primordial B-modes can only be generated by tensor perturbations, their detection would be a smoking gun for inflation. Moreover, a detection would help differentiate among the plethora of inflationary models. On the other hand, the detection of

this signal is extremely challenging since it is very faint compared to other B-mode sources. Thus, efficient CS algorithms are mandatory to be able to extract this primordial signal.

This chapter reviews the status of CMB science and primordial B-modes search. Section 2.1 describes the CMB temperature anisotropies and their cosmological information. Analogously, Section 2.2 reviews the polarization case and the current upper bounds on the tensor-to-scalar ratio from polarized CMB observations. Section 2.3 outlines the experimental and data analysis challenges that the detection of this faint signal presents. Finally, Section 2.4 reviews the different CS algorithms proposed in the literature to address the challenges presented in the previous section.

2.1 CMB Temperature

As mentioned in Section 1.1.1, if primordial fluctuations are nearly Gaussian, the second-order moment contains almost all the CMB information, i.e., the two-point correlation function in the real space or the angular power spectrum in Fourier space¹. Section 2.1.1 outlines the relationship between the observed temperature fluctuations and the power spectrum. Then, Section 2.1.2 summarizes the information extracted from the CMB temperature fluctuations.

2.1.1 Angular power spectrum

The observed fluctuations around the CMB mean temperature are

$$\Theta(\eta, \mathbf{x}, \theta, \phi) = \frac{T(\eta, \mathbf{x}, \theta, \phi) - T(\eta)}{T(\eta)}, \quad (2.1)$$

where (η, \mathbf{x}) define the observing position in spacetime, (θ, ϕ) a direction on the unit sphere, and $T(\eta)$ is the average CMB temperature at conformal time

$$\eta = \int_0^t \frac{dt'}{a(t')} = \int_z^\infty \frac{dz'}{H(z')}, \quad (2.2)$$

i.e., the time it would take a photon to travel from redshift z to the furthest observable distance in a comoving frame. The temperature anisotropies are a scalar field defined on the sphere, hence they can be expanded as a superposition of spherical harmonics

$$\Theta(\eta, \mathbf{x}, \theta, \phi) = \sum_{\ell=1}^{\infty} \sum_{m=-\ell}^{\ell} a_{\ell m}(\eta, \mathbf{x}) Y_{\ell m}(\theta, \phi), \quad (2.3)$$

¹Higher order moments such as the bispectrum or trispectrum test deviations from Gaussianity (Planck Collaboration et al., 2016d, 2020d).

where the spherical functions are

$$Y_{\ell m}(\theta, \phi) = \sqrt{\frac{2\ell+1}{4\pi}} \sqrt{\frac{(\ell-m)!}{(\ell+m)!}} P_{\ell}^m(\cos \theta) e^{im\phi}, \quad (2.4)$$

and P_{ℓ}^m are the Legendre polynomials of order m . The multipole ℓ describes the angular size, while the order $m \in [-\ell, \ell]$ describes the angular orientations of a fluctuation mode. In this decomposition, the $\ell = 1$ term measures the amplitude of the dipolar pattern, whose major contribution comes from the Doppler shift due to the motion of the Solar system relative to the CMB. The contribution of this kinetic dipole is on the order of 10^{-3} K and is usually removed for CMB analyses. The set of spherical harmonic functions satisfies orthonormality in the sphere

$$\int_{\Omega} d\Omega Y_{\ell m}(\theta, \phi) Y_{\ell' m'}^*(\theta, \phi) = \delta_{\ell\ell'} \delta_{mm'}, \quad (2.5)$$

where Ω is the sphere's solid angle.

We are limited to measuring at our location in space-time (η_0, \mathbf{x}_0) , i.e., here and now. Throughout the rest of the text, $(\eta, \mathbf{x}) = (\eta_0, \mathbf{x}_0)$, and I omit their dependence. The spherical harmonic coefficients are then given by

$$a_{\ell m} = \int_{\Omega} d\Omega \Theta(\theta, \phi) Y_{\ell m}^*(\theta, \phi). \quad (2.6)$$

We cannot predict the actual value of the $a_{\ell m}$ coefficients since we only have information on the distribution from which primordial fluctuations were generated (eq. 1.12). However, we can compare them with the estimated distribution from which these $a_{\ell m}$ were drawn, i.e., a Gaussian distribution with zero mean $\langle a_{\ell m} \rangle = 0$, and variance

$$\langle a_{\ell m} a_{\ell' m'} \rangle = \delta_{\ell\ell'} \delta_{mm'} C_{\ell}. \quad (2.7)$$

As stated above, we can only measure $a_{\ell m}(\eta_0, \mathbf{x}_0)$, hence we cannot estimate C_{ℓ} as in eq. 2.7. The maximum likelihood estimator of C_{ℓ} from the observed sky is given as

$$\hat{C}_{\ell} = \frac{1}{2\ell+1} \sum_{m=-\ell}^{\ell} |a_{\ell m}|^2. \quad (2.8)$$

As a result, there is a fundamental uncertainty in our estimation of C_{ℓ} known as the cosmic variance. Given that the $a_{\ell m}$ coefficients are drawn from the same distribution, each $a_{\ell m}$ has the same variance for a given ℓ . The cosmic variance is

$$\sigma^2(C_{\ell}) = \frac{2}{2\ell+1} C_{\ell}^2. \quad (2.9)$$

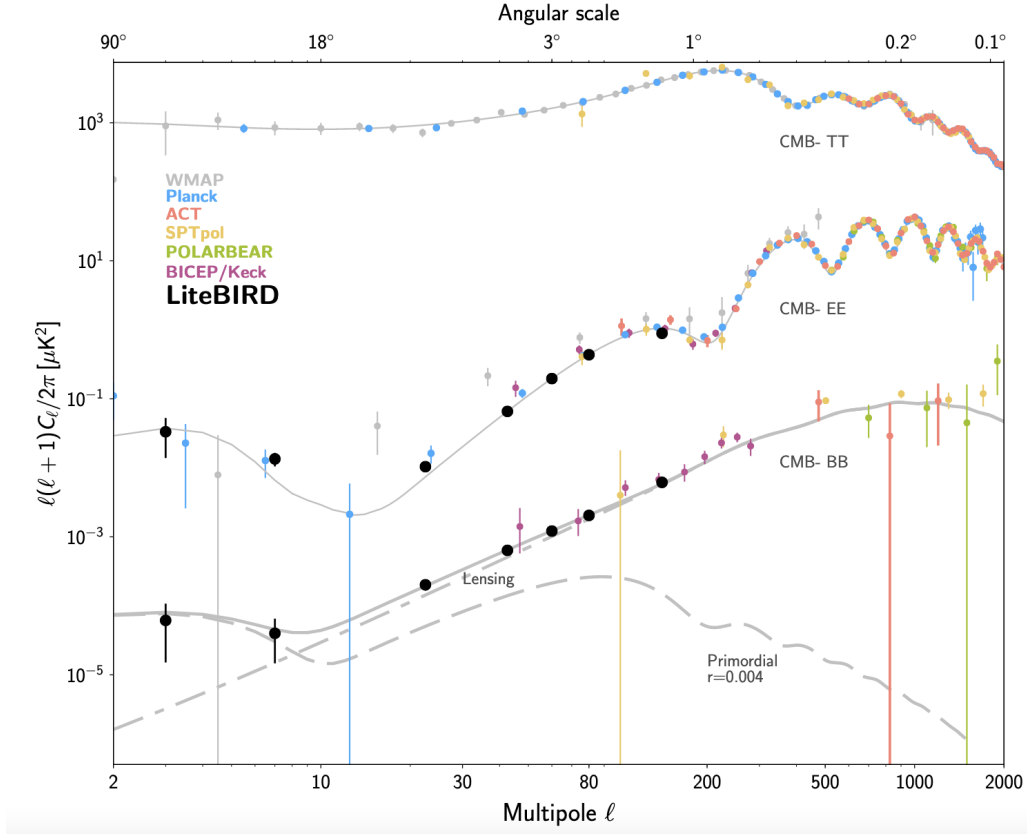


FIGURE 2.1: CMB angular power spectra. CMB TT, EE, and BB power spectra observations (colored points) and the expected polarization sensitivity of LiteBIRD (black points) over the theoretical prediction from the best-fit ΛCDM model and $r = 0.004$. Figure from (LiteBIRD Collaboration et al., 2022).

Fig. 2.1 shows the observations of temperature angular power spectrum (CMB - TT) over the best-fit ΛCDM model. The power spectrum is given in terms of

$$\mathcal{D}_\ell = \frac{\ell(\ell+1)}{2} C_\ell, \quad (2.10)$$

for visualization purposes.

2.1.2 Cosmological interpretation

CMB temperature anisotropies have placed some of the most stringent constraints on ΛCDM parameters. However, they cannot independently estimate all parameters since there are partial degeneracies, i.e., the effect of changing one parameter can be obtained by varying other parameters. This section summarizes the relationship between the cosmological information and the CMB temperature angular power spectrum. For a comprehensive review, the reader is referred to Hu & Dodelson (2002); Scott & Smoot (2006).

Eq. 1.20 shows that the power spectrum contains information on both the primordial fluctuations and the physical processes that the CMB photons underwent. Therefore, the

different scale regimes are associated with different physical processes. The scales can be split into two categories, i.e., the scales within the horizon at the time of recombination ($\ell \gtrsim 100$) and those that were not ($\ell \lesssim 100$), hence unaffected by the physical processes experienced by photons at recombination. Furthermore, there are two types of CMB anisotropies: *primary anisotropies* generated at the time of decoupling, and *secondary anisotropies* generated during the photons' trip toward us. Let's review first the effects of primary anisotropies:

- ⇒ At scales $\ell \gtrsim 100$, we observe two main effects, the acoustic oscillations described in Section 1.2.4 ($100 \lesssim \ell \lesssim 1000$) and diffusion damping ($\ell \gtrsim 1000$). The acoustic oscillations' peaks correspond to the specific modes that reached their maximum amplitude at the time of decoupling. The peaks' shapes can constrain several Λ CDM parameters. For example, the position of the first peak gives information about the curvature of the Universe and current limits show that our Universe is compatible with being flat. This parameter is degenerate with Ω_Λ as modifications of the latter produce similar results.

Diffusion damping occurs when the distance traveled by photons during recombination is comparable to the physical scales of the fluctuations. Since the formation of neutral species is not instantaneous, photons continue to scatter with electrons and execute a random walk. This random walk mixes the hot and cold photons at these scales, and the anisotropies average out.

- ⇒ The $\ell \lesssim 100$ scales are larger than the sound horizon at the time of decoupling and do not exhibit the typical acoustic oscillations pattern. At these scales, the main contribution comes from the Sachs-Wolfe effect. This effect results in CMB photons being redshifted due to them losing energy when climbing out of gravitational wells at the last scattering surface.

In addition, the low multiples show the scales that have only recently re-entered the horizon and provide a direct measurement of the initial conditions. Therefore, they can constrain parameters related to initial perturbations, such as A_s and n_s .

The primary anisotropies are affected by several physical effects that happen between the last scattering surface and the observer. These secondary anisotropies lead to deviations from the anisotropies generated at recombination at different scale regimes. Well-known processes that generate secondary anisotropies are the Sunyaev-Zeldovich effect (Sunyaev & Zeldovich, 1970), the Integrated Sachs-Wolfe effect (Sachs & Wolfe, 1967), the Rees-Sciama effect (Rees & Sciama, 1968), the Rayleigh Scattering by neutral species (Yu et al., 2001), gravitational lensing, see Section 2.3.2, reionization (Sugiyama et al., 1993), and the Ostriker-Vishniac effect (Ostriker & Vishniac, 1986).

2.2 CMB Polarization

Before recombination, CMB photons were coupled to electrons via Thomson scattering. This type of scattering induces polarization due to the quadrupolar moment of the temperature field and its angular dependence (Zaldarriaga & Seljak, 1997; Seljak & Zaldarriaga, 1997), which is given by

$$\frac{d\sigma}{d\Omega} = \frac{3\sigma_T}{8\pi} |\mathbf{n} \cdot \mathbf{n}'|^2, \quad (2.11)$$

where \mathbf{n} (\mathbf{n}') is the polarization direction of the incident (scattered) radiation. Let's consider an unpolarized monochromatic ray coming from the $-x$ direction. The electric field components are

$$E_i = a_i(t) \cos(\omega_0 t - \theta_i(t)), \quad i \in \{y, z\}. \quad (2.12)$$

Let the ray be scattered by an electron at the origin and deflected in the $+y$ direction. The electric field of the scattered ray can be decomposed into x and z components. Then, the incident ray E_y does not contribute to the scattered light radiation since it is orthogonal to x and z . On the other hand, the incident E_z is fully transmitted since the dot product in eq. 2.11 is unity. Thus, Thomson scattering produces linearly polarized light. If the radiation field is isotropic, the net result of all scattered light rays will be unpolarized. The contributions from orthogonal polarization states, coming from orthogonal incident directions, cancel out. However, the CMB intensity field had a quadrupolar pattern. In this case, the hotter (colder) radiation incident from the $-x$ ($-z$) direction generates higher (lower) intensity along the z (x) axis for the outgoing wave, producing linearly polarized light (Hu & White, 1997), see Fig. 2.2.

2.2.1 Angular power spectra

The CMB radiation can be described in terms of the Stokes parameters I, Q, and U since V is null as there is no circular polarization. Unlike intensity, the Q and U Stokes parameters are not scalar fields and depend on the reference frame. Under a reference frame rotation of an angle ϕ around the direction of observation Q and U transform as

$$\begin{pmatrix} \tilde{Q} \\ \tilde{U} \end{pmatrix} = \begin{pmatrix} \cos(2\phi) & -\sin(2\phi) \\ \sin(2\phi) & \cos(2\phi) \end{pmatrix} \begin{pmatrix} Q \\ U \end{pmatrix}. \quad (2.13)$$

Q and U can be represented as a complex spin ± 2 quantity, $Q \pm iU$. The latter can be expanded in the base of spin-weighted spherical harmonics

$$(Q \pm iU)(\mathbf{n}) = \sum_{\ell=2}^{\infty} \sum_{m=-\ell}^{\ell} a_{\ell m}^{\pm 2} Y_{\ell m}(\mathbf{n}). \quad (2.14)$$

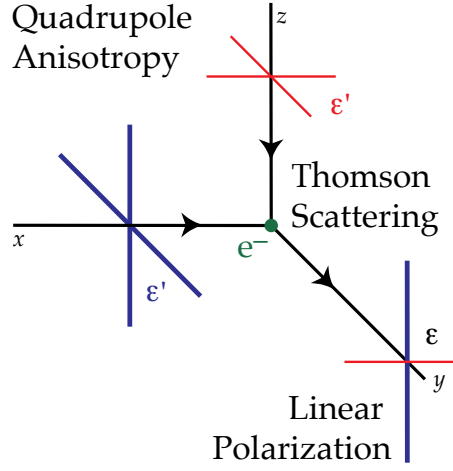


FIGURE 2.2: Sketch of Thomson Scattering. Sketch of Thomson scattering inducing linear polarization in a radiation field with quadrupolar moment. Figure from (Hu & White, 1997).

These harmonic coefficients can be combined as follows

$$a_{\ell m}^E = \frac{1}{2} \left(a_{\ell m}^{+2} + a_{\ell m}^{-2} \right), \quad (2.15)$$

$$a_{\ell m}^B = \frac{-i}{2} \left(a_{\ell m}^{+2} - a_{\ell m}^{-2} \right), \quad (2.16)$$

to obtain spherical harmonic coefficients of scalar fields. They are the so-called E (gradient) and B (rotational) fields. Analogous to T, E-modes are sourced by scalar and tensor perturbations, while B-modes are only sourced by tensor perturbations. Therefore, the B-mode power spectrum constitutes a unique probe to search for primordial tensor perturbations.

From the cross-correlation of the T, E, and B-modes, one obtains a set of six angular power spectra

$$C_\ell^{XY} = \left\langle a_{\ell m}^X a_{\ell m}^{Y*} \right\rangle, \quad (2.17)$$

where $X, Y \in \{T, E, B\}$. Analogously to eq. 2.8,

$$\hat{C}_\ell^{XY} = \frac{1}{2\ell + 1} \sum_{m=-\ell}^{\ell} a_{\ell m}^X a_{\ell m}^{Y*}, \quad (2.18)$$

is a maximum likelihood estimator of the ensemble-averaged C_ℓ^{XY} . Current observations of these power spectra are summarized in Fig. 2.1. If parity is conserved, C_ℓ^{TB} and C_ℓ^{EB} must be zero since T and E are invariant under parity flip, while B changes sign.

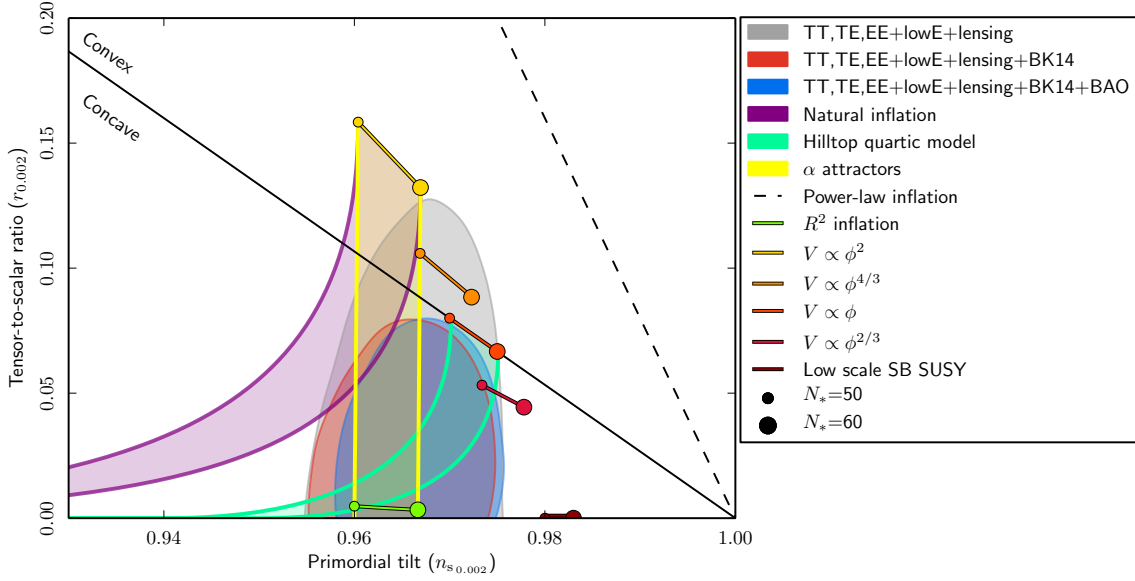


FIGURE 2.3: Inflation constraints. Limits on the tensor-to-scalar ratio as a function of n_s in the Λ CDM model at 95% CL, from Planck alone (grey), including BICEP2/Keck data 2014 (red) and BAO (blue). Lines show the predictions of several models of inflations as a function of the number of e-folds N_* . Figure from (Planck Collaboration et al., 2020a).

2.2.2 CMB Polarization Science

The CMB scientific community aims to improve polarization measurements enough to detect primordial B-modes. The search for PGWs is being tackled both from the ground, with experiments such as the Simons Observatory (SO) (Ade et al., 2019), BICEP/Keck array (Ade et al., 2022), CMB-S4 (Abazajian et al., 2019), and from space, e.g., with LiteBIRD (Lite (Light) satellite for the studies of B-mode polarization and Inflation from cosmic background Radiation Detection) (LiteBIRD Collaboration et al., 2022), and PICO (Probe of Inflation and Cosmic Origins) (Hanany et al., 2019). Their main goal is to detect or at least constrain r with a sensitivity $\lesssim 10^{-3}$.

Currently, the best upper bound on the tensor-to-scalar ratio is $r < 0.032$ at 95% CL, set by the combination of Planck, BICEP2/KeckArray and baryon acoustic-oscillation data (Tristram et al., 2022). Even though there is no theoretical lower bound for this quantity, in a non-detection case, these experiments will rule out a handful of inflation model families. Fig. 2.3 shows the constraints on inflationary models from *Planck*.

Apart from its weakness, this primordial signal is obscured by other B-mode sources, e.g., by astrophysical foregrounds, lensed E- to B-modes, and systematics effects. Contamination from those sources might prevent the detection of primordial B-modes. Section 2.3 reviews these contaminants and their impact on the search for PGWs.

In addition to the primordial B-modes search, CMB polarization has a wealth of cosmological information (Komatsu, 2022). Some examples are the following

⇒ **Reionization optical depth.** After reionization, CMB photons can be scattered again

by electrons along their line of sight, which results in slight changes in the angular power spectrum. Since the density of electrons along their path depends on τ (eq. 1.19), CMB anisotropies can provide constraints on this parameter. The main reionization signature in the E-mode power spectrum is a bump around $\ell \sim 10$ called *reionization bump*, Fig. 2.1.

- ⇒ **Cosmic birefringence.** Most of the Universe is composed of dark matter and dark energy, whose origin is still unknown. A possible explanation of either dark matter or dark energy is a parity-violating pseudo-scalar field (Gubitosi & Paci, 2013; Marsh, 2016). That field would couple with the Standard Model particles via a Chern-Simons interaction. This type of interaction introduces a shift between the phase velocities of the right- and left-handed helicity. As a result, the Universe behaves as a birefringent material, i.e., it rotates the plane of linear polarization as the CMB photons advance along their path.

There have been a possible detection of non-zero birefringent angle using the C_ℓ^{EB} data from *Planck* (Diego-Palazuelos et al., 2022a,b), and C_ℓ^{EB} and C_ℓ^{TB} data from *Planck* and WMAP (Eskilt & Komatsu, 2022). However, the measurement might be affected by the contamination of EB from dust. Future CMB polarization measurements will help resolve the origin of this birefringent angle.

- ⇒ Tests of the **fluke hypothesis** of temperature anomalies. The polarization information can test whether the anomalies observed in the temperature data are statistical anomalies or new physics beyond ΛCDM . Examples of these anomalies are the hemispherical asymmetry, the low variance at large scale, or the CMB Cold Spot (Planck Collaboration et al., 2020c).

Other scientific outcomes from CMB polarization are reviewed in (Ade et al., 2019; Abazajian et al., 2019; Hanany et al., 2019; LiteBIRD Collaboration et al., 2022).

2.3 Primordial B-modes Detection Challenges

The relative weakness of primordial B-modes makes its detection a tremendous experimental challenge, requiring high-sensitivity experiments as well as an exquisite control of systematics. In this section, I review the different contaminants that might prevent us from measuring this elusive signal, i.e., astrophysical foregrounds (Section 2.3.1), lensed E- to B-modes (Section 2.3.2), and systematic effects (Section 2.3.3).

2.3.1 Astrophysical Foregrounds

The microwave sky is not populated only by the relic CMB radiation, other astrophysical processes are emitting in this frequency range. Those emissions, in the context of CMB sci-

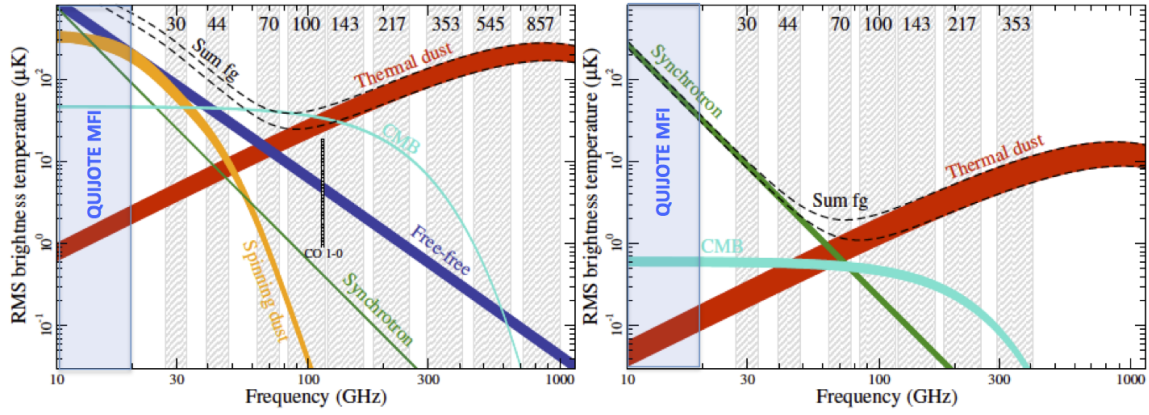


FIGURE 2.4: Astrophysical components' SED. Temperature (left) and polarization (right) SEDs of the main components of the microwave sky. Figure from <http://www.radioforegrounds.eu/>.

ence, constitute a source of error and are known as Galactic and extragalactic foregrounds². Foregrounds must be removed or marginalized over to retrieve unbiased estimates of the CMB and its anisotropies. The different CS algorithms used to extract the CMB from the microwave signal are covered in Section 2.4.

There are differences between the intensity and polarized microwave sky. Temperature measurements show at least four independent diffuse foregrounds, namely synchrotron, free-free, anomalous microwave emission (AME), and thermal dust radiation, but only two have been detected in polarization, synchrotron, and thermal dust. Fig. 2.4 shows the components' spectral energy distribution (SED) in temperature and polarization.

The rest of the section covers the physics behind the thermal dust and synchrotron emission. Then, I outline the status of the AME polarization and the contamination by polarized sources. The section finishes with a brief description of the unpolarized foregrounds.

Thermal dust

Thermal dust radiation refers to the far-infrared light emitted by dust grains after being heated by UV and optical photons from the interstellar medium (Draine, 2011). This radiation has a polarized component due to the alignment of aspherical grains with the magnetic field. The dust grains emit most efficiently along their long axis, which tends to align parallel to the magnetic field.

The study and characterization of this component are crucial for removing the B-modes sourced by dust and detecting primordial B-mode. An improper signal subtraction could lead to a false claim of primordial gravitational waves detection as in BICEP2 Collaboration et al. (2014), where the detected B-mode signal came from thermal dust radiation (BICEP2/Keck Collaboration et al., 2015). Apart from the detection of PGWs, other studies require accurate knowledge of thermal dust radiation. For example, a non-zero dust C_{ℓ}^{EB}

²The foreground name refers to the fact that these sources are emitting between us and the last scattering surface.

can bias the measurements of cosmic birefringence (Clark et al., 2021; Diego-Palazuelos et al., 2022b; Eskilt & Komatsu, 2022; Diego-Palazuelos et al., 2022a).

Assuming that the far-infrared opacity of dust grains is well-modeled by a power law, the thermal dust spectral energy distribution (SED) can be expressed as a modified black-body (mbb)

$$D(\nu, \mathbf{n}) = A_d(\mathbf{n}) \nu^{\beta_d} B(\nu, T_d), \quad (2.19)$$

where β_d is the opacity spectral index, T_d is the dust grains temperature, and $B(\nu, T)$ is the Planck function. This model correctly fits the data from current CMB experiments, i.e., *Planck* and BICEP/Keck. In their CS analysis with intensity data (Planck Collaboration et al., 2016a), *Planck* explored alternative parametrizations such as the two-component modified black-body (2mbb) model from Finkbeiner et al. (1999). However, they concluded that there was no strong preference between the mbb and the 2mbb models. They could fit the data with just three parameters, i.e., $\{A_d, \beta_d, T_d\}$, $\{A_d^1, A_d^2, T_d^1\}$, or $\{A_d^1, A_d^2, \beta_d^1\}$. Analyses including higher frequency data, i.e., *Planck* and DIRBE data, (Meisner & Finkbeiner, 2015) show that the 2mbb provides a better fit than the mbb. In the case of polarization, *Planck* did not have sufficient signal-to-noise ratio (S/N) to constrain the spectral parameters (β_d, T_d).

Recent studies suggest that the dust component might be more complicated than expected. For example:

- ⇒ There is theoretical ground that suggests that there might be differences between intensity and polarization SEDs. For example, if the thermal dust emission comes from two grain populations (e.g., silicate and carbonaceous grains) with different polarization properties (Hensley & Bull, 2018). Moreover, there have been some hints of differences between polarization and intensity SEDs coming from analyses using *Planck* data (Ritacco et al., 2022).
- ⇒ Several effects can lead to *frequency decorrelation*, i.e., when the observed polarized emission at one frequency is an imperfect predictor of the polarized emission at another frequency. Some of those effects are
 - Temperature and composition of interstellar dust grains are known to vary in the interstellar medium, resulting in the spatial variability of the dust SED. The average of different SEDs by the instrumental beam integration can yield frequency decorrelations (Chluba et al., 2017).
 - If there are multiple dust clouds with different dust SEDs along the line of sight, or if the magnetic fields in these clouds are misaligned, then the polarization angle of the dust emission becomes decorrelated across frequencies. Several works have studied this effect and concluded that it biases both the dust parameters and the CMB (Tassis & Pavlidou, 2015; Sponseller & Kogut, 2022; McBride et al., 2022). Moreover, Pelgrims et al. (2021); Ritacco et al. (2022) found hints of possible frequency decorrelation.

Studies such as Remazeilles et al. (2016); Hensley & Bull (2018) simulated different microwave skies using complex thermal dust models and tried to recover the CMB assuming the dust is well-modeled by an mbb model. The results showed that incorrect modeling leads to large biases on r . Moreover, some models were problematic since they showed an acceptable goodness-of-fit while introducing biases. High-frequency information can solve the problem of incorrect goodness-of-fit estimations since the differences between model predictions are more significant at those frequencies. Future missions such as LiteBIRD, SO, and CMB-S4 will give more insight into thermal dust due to their sensitivity increase and wide frequency span.

Synchrotron

Diffuse synchrotron radiation is generated by relativistic cosmic ray (CR) electrons interacting with the Galactic magnetic field. Electrons and positrons spiral around the field lines, emitting radiation as they travel in a circular path. This radiation may be highly polarized perpendicular to the field lines (Rybicki & Lightman, 1979), and is one of the most dominant Galactic components at low frequencies (see Fig. 2.4). Its SED depends on the magnetic field strength and cosmic ray energy. Assuming that the cosmic ray distribution is well described as a power law $N(E) \propto E^p$, the synchrotron spectrum is also modeled as a power law

$$S(\mathbf{n}) = A_s(\mathbf{n}) \left(\frac{\nu}{\nu_s} \right)^{\beta_s}, \quad (2.20)$$

where A_s is the synchrotron's intensity measured at ν_s in the \mathbf{n} direction, and β_s is the spectral index. β_s is expected to have some spatial variability and to vary with frequency due to aging, synchrotron self-absorption, multiple components along the line of sight, etc. (Siah & Wiita, 1990; Chevalier, 1998). Therefore a model with a curvature parameter might be better suited:

$$S(\mathbf{n}) = A_s(\mathbf{n}) \left(\frac{\nu}{\nu_s} \right)^{\beta_s + c_s \log \frac{\nu}{\nu_{cs}}}, \quad (2.21)$$

This curvature parameter is equivalent to the first-order moment of the power law expansion presented in Chluba et al. (2017).

The characterization of the synchrotron parameters from intensity observations is very challenging due to the large model degeneracies with other low-frequency foregrounds such as *bremsstrahlung* emission or AME (Planck Collaboration et al., 2016e). Most observations show that the synchrotron spectrum steepens from $\beta_s \simeq -2.5$ at 22 MHz to $\beta_s \simeq -3.0$ above 23 GHz, de Oliveira-Costa et al. (2008); Guzmán et al. (2011), which are in rough agreement with CR model predictions. These CR models have been used in CMB CS analysis, e.g., in *Planck's* CS analysis with intensity data (Planck Collaboration, 2016). Fig. 2.5 shows the spectral dependence of β_s as a function of the latitude obtained using the GALPROP model (Orlando & Strong, 2013) applied in that analysis. The model clearly shows a flatter spectral index at frequencies below 3 GHz favoring the curvature model.

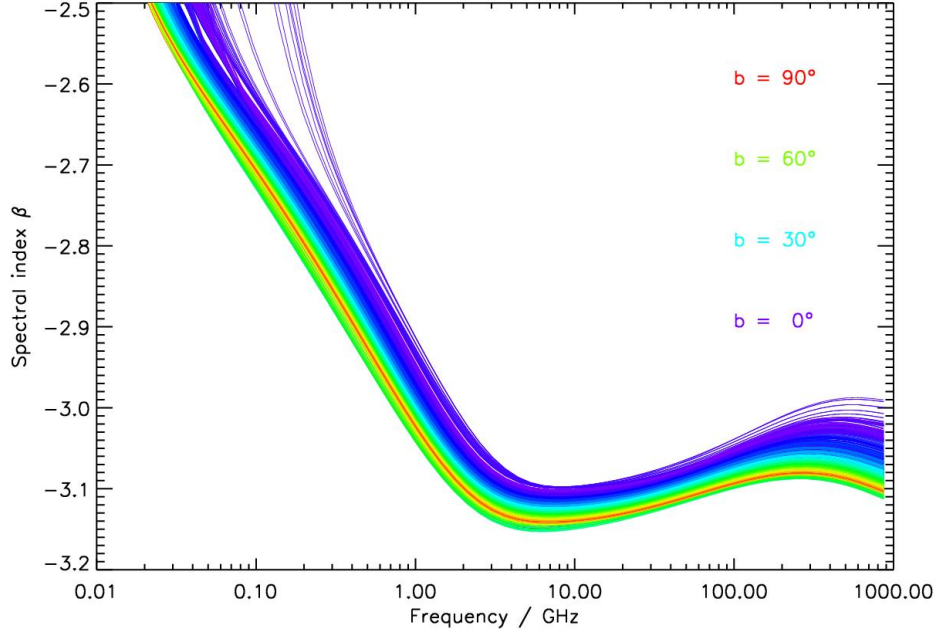


FIGURE 2.5: Synchrotron's spectral index spectrum. Predicted synchrotron's spectral index spectrum for different latitudes obtained using the model from (Orlando & Strong, 2013). Figure from (Planck Collaboration et al., 2016e).

Polarization measurements yield a cleaner characterization of the synchrotron's spectral index since it constitutes the dominant emission at frequencies below $\lesssim 70$ GHz. However, the current best polarization maps from the spatial missions WMAP and *Planck* have a low S/N ratio and cannot be used to calculate accurate spectral indices alone. Current foreground simulators codes such as PySM (Thorne et al., 2017) use the β_s template obtained by extrapolating, using a power law, the Haslam's 408 MHz intensity map to WMAP polarized K band (23 GHz) (Miville-Deschênes et al., 2008). To test the existence of the synchrotron's curvature, one needs measurements between 408 MHz and 23 GHz.

Our knowledge of the synchrotron has increased significantly from new data of ground-based experiments operating in the 2-20 GHz range. Those experiments are S-PASS at 2.3 GHz over the southern sky (Carretti et al., 2019), C-BASS at 5 GHz (Jones et al., 2018) and QUIJOTE-MFI at 11-19 GHz (Rubiño-Martín et al., 2022) measuring the northern sky. The results from C-BASS and S-PASS are the following

- ⇒ **S-PASS:** Krachmalnicoff et al. (2018) estimated the polarized synchrotron spectral index in harmonic space using S-PASS power spectra along with those from the lowest frequency bands of WMAP and *Planck*. They showed that the synchrotron emission is compatible with a power law with $\beta_s = -3.22 \pm 0.08$, but emphasized: “the need of more data at intermediate frequencies to better constrain this parameter”. Combining the S-PASS total polarized intensity maps with those coming from WMAP and *Planck* they obtained a map of the synchrotron spectral index β_s at an angular resolution of 2° on about 30% of the sky, and found significant spatial variations. Moreover, they studied the level of synchrotron contamination in CMB B-modes obtaining that

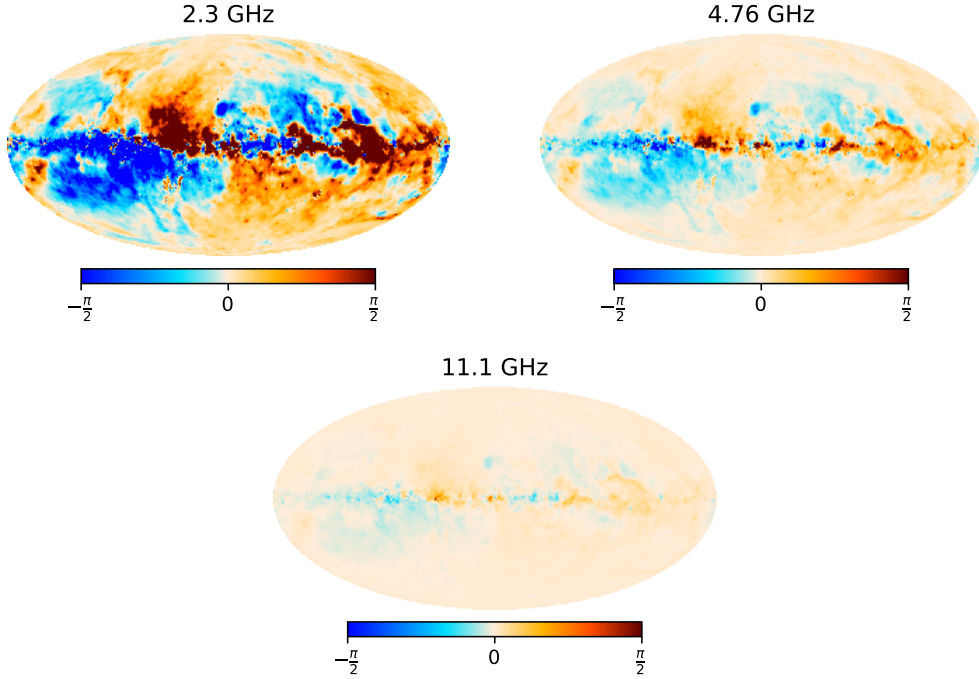


FIGURE 2.6: Faraday rotation angle. Predicted rotation Faraday Rotation angles at S-PASS, C-BASS, and MFI lowest frequency channel using the model from (Hutschenreuter et al., 2022).

the minimum contamination is at the level of an equivalent tensor-to-scalar ratio of $r_{\text{synch}} \simeq 10^{-3}$.

⇒ **C-BASS:** Using their intensity map instead of the Haslam map along with WMAP K-band, Harper et al. (2022) found marginal evidence for a steepening $\Delta\beta = -0.06 \pm 0.02$ of the Galactic synchrotron spectrum at high frequencies. Moreover, they obtained that the mean spectral index at those high-frequencies is $\langle\beta_s\rangle = -3.10 \pm 0.02$. Since the typical differences between the spectral indices at 22.8 GHz derived using the 408 MHz or 4.76 GHz map are small, they concluded that the power law model of the Galactic synchrotron to high frequencies remains a reasonable model.

The advantage of experiments such as S-PASS and C-BASS is that they measure at low frequencies, where the synchrotron has higher S/N. Furthermore, they are more likely to detect a curvature value in the synchrotron model, as shown in Fig. 2.5. However, frequencies below 10 GHz suffer from depolarization caused by Faraday Rotation effects. Fig. 2.6 shows the predicted rotated angle due to Faraday Rotation using the model from (Hutschenreuter et al., 2022). The QUIJOTE-MFI instrument can measure the low-frequency regime without being significantly affected by this effect except in regions close to the galactic plane. P.IV presents the analysis and characterization of the polarized synchrotron using the final data from the MFI instrument along with ancillary data from WMAP and *Planck*, see Section 3.

Anomalous Microwave Emission

The physical origin of AME and whether it is polarized is still an open debate (Dickinson et al., 2018). Several models have been proposed to explain this emission, including spinning dust particles (Draine & Lazarian, 1998; Ali-Haïmoud, 2013), magnetic dipole emission (Draine & Lazarian, 1999), and spinning nano-diamonds (Greaves et al., 2018). For most of these models, the predicted polarization fraction of the AME emission is less than 5%. From the data analysis point of view, no evidence of polarization has been found in compact region studies (the most stringent constraints on the polarization fraction, Π , have been provided by (Génova-Santos et al., 2017), $\Pi < 0.22\%$ at 41 GHz).

Polarized Extragalactic sources

The majority of extragalactic sources appear as point-like in CMB experiments whose resolution is relatively poor, above the arc min scales. Some point sources observed in temperature observations exhibit some degree of polarization, which is generally small, on the order of a few percent (Trombetti et al., 2018). Before performing CS analyses, contamination from point sources must be subtracted or masked. If polarized point sources are not accounted for, they can contaminate the CMB B-modes, biasing the tensor-to-scalar ratio $r \lesssim 0.05$ (Tucci & Toffolatti, 2012; Puglisi et al., 2018).

Unpolarized Foregrounds

There are other foreground components whose emissions are significant for intensity analyses. For example, at low frequencies, the Galactic emission from the bremsstrahlung radiation generated by electron-ion scattering in interstellar plasma (free-free). At high frequencies, in addition to thermal dust, there is an isotropic extragalactic emission known as cosmic infrared background (CIB), coming from different sources, e.g., dusty star-forming galaxies, quasars, intergalactic stars, inter-cluster dust in the Local group, etc. Other contributions include CO line emission and the Sunyaev-Zeldovich effect from clusters of galaxies (Sunyaev & Zeldovich, 1972). The problem is simplified in polarization because several of these emissions (free-free, CIB, SZ, etc.) are not expected to be polarized, at least significantly.

2.3.2 Lensed E- to B-Modes

CMB photons are subject to weak gravitational lensing by large-scale structures in their path from the last scattering to us. The effect of cosmic shear is to deflect the photons' direction of motion, i.e., it introduces a distortion of the hot and cold spots of the temperature field around massive structures. Moreover, weak lensing changes the polarization patterns yielding a mix of E-modes and B-modes. Since E-modes are significantly more intense than B-modes, this mixing acts as a source of B-mode noise. In this section, I review the CMB weak lensing mechanism and its effects on the power spectrum.

From the time of decoupling to us, CMB photons experience multiple small local deflections by the matter distribution. The observed deflection vector is the sum of all the deflections by lenses between ourselves and the last scattering surface. In the Born approximation, the total deflection angle is (Lewis & Challinor, 2006; Hanson et al., 2010)

$$\alpha(\mathbf{n}) = -2 \int_0^{\chi_*} d\chi \frac{f_K(\chi_* - \chi)}{f_K(\chi_*) f_K(\chi)} \nabla \Phi(\chi \mathbf{n}, \eta_0 - \chi), \quad (2.22)$$

where χ_* is the conformal distance to the last scattering surface, and η_0 is the conformal time today, the ∇ operator denotes the covariant derivative on the sphere, and $f_K(\chi)$ is the angular diameter distance³, and ϕ is the deflection field

$$\alpha(\mathbf{n}) = \nabla \phi(\mathbf{n}). \quad (2.23)$$

This approximation holds as long as the deflection angles are sufficiently small. The average deflection angle that CMB photons suffer is of the order of ~ 2 arcmin, which validates the approximation.

The lensing potential depends on the geometry of spacetime and is a cosmology probe complementary to the primary anisotropies of the CMB. Lensing generates small amounts of non-Gaussianity to the CMB, which introduces information into the higher-order CMB statistics. Some estimators exploit these high-order moments to extract the lensing potential power spectrum (Qu et al., 2022). Fig. 2.7 shows the latest CMB observational measurements of this power spectrum.

Let's study the effects of lensing in the power spectra in the flat space approximation. The conclusions drawn are the same for the full-sky Hu (2000). Weak lensing of the CMB modifies the primary anisotropy according to the deflection angle $\nabla \phi$. The lensed anisotropy field is

$$\tilde{\Theta}(\mathbf{n}) = \Theta(\mathbf{n}) + \nabla_i \phi(\mathbf{n}) \nabla^i \Theta(\mathbf{n}) + \frac{1}{2} \nabla_i \phi(\mathbf{n}) \nabla_j \phi(\mathbf{n}) \nabla^i \nabla^j \Theta(\mathbf{n}) + \dots, \quad (2.24)$$

where \mathbf{n} is a unitary vector representing a point on the unit sphere. The Fourier coefficients of the lensed field are

$$\tilde{\Theta}(\mathbf{l}) = \int d\mathbf{n} \Theta(\mathbf{n}) e^{-i\mathbf{l} \cdot \mathbf{n}} = \Theta(\mathbf{l}) - \int \frac{d^2 \mathbf{l}'}{(2\pi)^2} \Theta(\mathbf{l}') L(\mathbf{l}, \mathbf{l}'), \quad (2.25)$$

where

$$L(\mathbf{l}, \mathbf{l}') = \phi(\mathbf{l} - \mathbf{l}')(\mathbf{l} - \mathbf{l}') \cdot \mathbf{l}' + \frac{1}{2} \int \frac{d^2 \mathbf{l}''}{(2\pi)^2} \phi(\mathbf{l}'') \phi^*(\mathbf{l}'' + \mathbf{l}' - \mathbf{l})(\mathbf{l}'' \cdot \mathbf{l}')(\mathbf{l}'' + \mathbf{l}' - \mathbf{l}) \cdot \mathbf{l}'. \quad (2.26)$$

³The angular diameter distance is the function that relates comoving distances to subtended angles on the sky depending on the curvature of space.

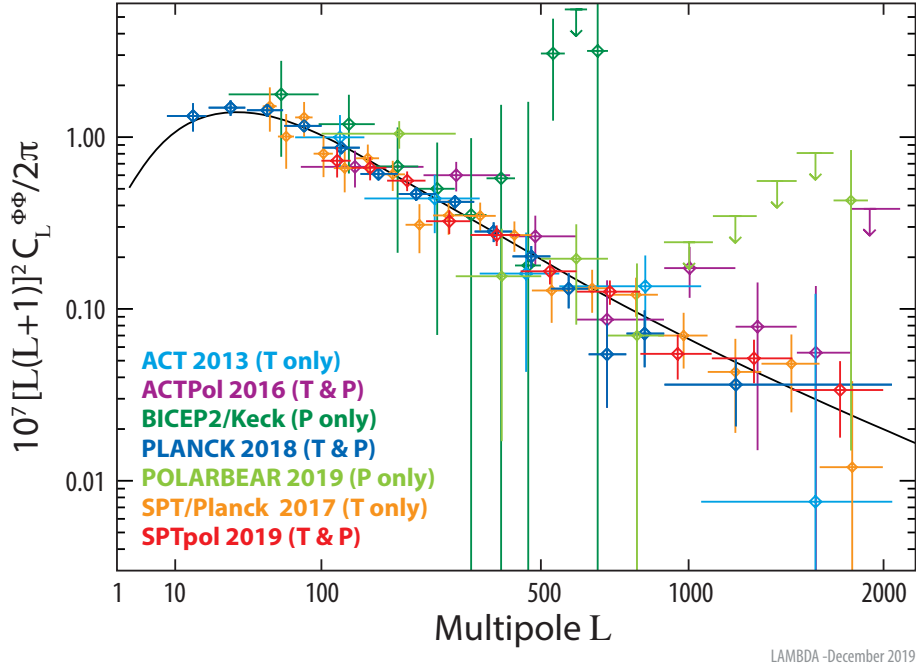


FIGURE 2.7: Lensing power spectrum. CMB measurements of the gravitational lensing power spectrum. The theoretical lensing power spectrum for the best-fit Λ CDM model is shown in black. Image Credit: NASA / LAMBDA Archive Team.

From these coefficients, one can obtain the lensed power spectrum

$$\tilde{C}_l^{TT} = \left(1 - l^2 R^\phi\right) C_l^{TT} + \int \frac{d^2 l'}{(2\pi)^2} \left(l' (1 - l')\right)^2 C_{|1-l'|}^{\phi\phi} C_{l'}^{TT}, \quad (2.27)$$

where

$$R^\phi = \frac{1}{2} \langle |\nabla \phi|^2 \rangle = \frac{1}{4\pi} \int \frac{d\ell}{\ell} \ell^4 C_\ell^{\phi\phi}. \quad (2.28)$$

The second term in eq. 2.27 represents a convolution of the unlensed temperature power spectrum with the lensing potential power spectrum. This can be seen as a convolution with a narrow window function (Hu, 2000), i.e., a convolution with the power spectrum shown in Fig. 2.7. Thus, the effect of the lensing is the blurring of the acoustic peaks. At small scales, where the unlensed CMB has little power due to diffusion damping, this convolution introduces some additional power from the $C_\ell^{\phi\phi}$.

Analogously, the Fourier coefficients of the lensed polarization spectra are

$$\pm \tilde{X}(l) = \pm X(l) - \int \frac{d^2 l'}{(2\pi)^2} \pm X(l') e^{\pm 2i(\psi_{l'} - \psi_l)} L(l, l'), \quad (2.29)$$

where $\pm \tilde{X}(l) = E(l) \pm iB(l)$, $(\psi_{l'} - \psi_l)$ is the rotation of the l' base in the direction of l . The

power spectra are then

$$\tilde{C}_l^{EE} = (1 - l^2 R^\phi) C_l^{EE} + \int \frac{d^2 \mathbf{l}'}{(2\pi)^2} \left(\mathbf{l}' (1 - \mathbf{l}') \right)^2 C_{|\mathbf{l} - \mathbf{l}'|}^{\phi\phi} \left[\xi_\ell^+ + \cos(4\psi_{\mathbf{l}'}) \xi_\ell^- \right], \quad (2.30)$$

$$\tilde{C}_l^{BB} = (1 - l^2 R^\phi) C_l^{BB} + \int \frac{d^2 \mathbf{l}'}{(2\pi)^2} \left(\mathbf{l}' (1 - \mathbf{l}') \right)^2 C_{|\mathbf{l} - \mathbf{l}'|}^{\phi\phi} \left[\xi_\ell^+ - \cos(4\psi_{\mathbf{l}'}) \xi_\ell^- \right], \quad (2.31)$$

$$\tilde{C}_l^{TE} = (1 - l^2 R^\phi) C_l^{TE} + \int \frac{d^2 \mathbf{l}'}{(2\pi)^2} \left(\mathbf{l}' (1 - \mathbf{l}') \right)^2 C_{|\mathbf{l} - \mathbf{l}'|}^{\phi\phi} C_{\mathbf{l}'}^{TE} \cos(2\psi_{\mathbf{l}'}), \quad (2.32)$$

where $\xi_\ell^\pm = (C_{\mathbf{l}'}^{EE} \pm C_{\mathbf{l}'}^{BB})$. Since the lensing due to tensor perturbations is small, we can assume $B(1) \simeq 0$. Under this assumption eq. 2.30 and eq. 2.31 become

$$\tilde{C}_l^{EE} = (1 - l^2 R^\phi) C_l^{EE} + \int \frac{d^2 \mathbf{l}'}{(2\pi)^2} \left(\mathbf{l}' (1 - \mathbf{l}') \right)^2 C_{|\mathbf{l} - \mathbf{l}'|}^{\phi\phi} C_{\mathbf{l}'}^{EE} \cos^2(2\psi_{\mathbf{l}'}), \quad (2.33)$$

$$\tilde{C}_l^{BB} = \int \frac{d^2 \mathbf{l}'}{(2\pi)^2} \left(\mathbf{l}' (1 - \mathbf{l}') \right)^2 C_{|\mathbf{l} - \mathbf{l}'|}^{\phi\phi} C_{\mathbf{l}'}^{EE} \sin^2(2\psi_{\mathbf{l}'}). \quad (2.34)$$

The effects of weak lensing on the E and TE power spectra are similar to that of temperature. The convolution with the lensing potential power spectrum blurs the features of the spectrum and adds power at small scales.

In the case of the B-mode power spectrum, lensing leaks power from E- to B-modes as eq. 2.34 shows. This contribution acts like white noise at multipoles $\ell \lesssim 1000$ (see Fig. 2.1), similar to an instrumental white-noise level of $\sim 5 \mu\text{K-arcmin}$. This B-mode source of error will challenge the detectability of r with future CMB experiments. To mitigate this contaminant, several *delensing* procedures have been proposed in the literature, see Diego-Palazuelos et al. (2020) for a complete comparison, and have been applied to data from current CMB experiments (Planck Collaboration et al., 2016b; Carron et al., 2017; BICEP/Keck Collaboration et al., 2021), and in forecasts of future CMB experiments (Diego-Palazuelos et al., 2020; Namikawa et al., 2022).

2.3.3 Systematic Effects

Planned and future CMB experiments will reach unprecedented levels of sensitivity in the quest for primordial B-modes. Therefore, excellent control of systematic effects is mandatory. Incomplete correction of instrumental or environmental effects due to inaccurate modeling or a lack of knowledge can lead to significant biases in the tensor-to-scalar ratio. Planned and future CMB experiments suffer from many systematic effects, which depend on the experimental design. The aim of this section is not to provide an exhaustive review of systematic effects, but to outline some of the most detrimental for CMB polarization measurements.

Polarization angle

A harmful systematic arises from a plausible non-zero detector polarization angle. This polarization angle leads to the mixing of the measured E- and B-modes, i.e.,

$$\begin{pmatrix} a_{\ell m}^{\text{E}_{\text{obs}}} \\ a_{\ell m}^{\text{B}_{\text{obs}}} \end{pmatrix} = \begin{pmatrix} \cos(2\alpha) & -\sin(2\alpha) \\ \sin(2\alpha) & \cos(2\alpha) \end{pmatrix} \begin{pmatrix} a_{\ell m}^{\text{E}} \\ a_{\ell m}^{\text{B}} \end{pmatrix}, \quad (2.35)$$

where $a_{\ell, m}^{\text{X}_{\text{obs}}}$ ($a_{\ell, m}^{\text{X}}$) is the observed (true) X-mode spherical harmonic coefficients ($X \in \{\text{E}, \text{B}\}$), and α is the miscalibrated polarization angle. Due to the power asymmetry between E- and B-modes, this power transfer can hinder the detection of the PGWs signal. Future experiments need polarization uncertainties to be on the arcminute level to meet their $\sigma_r \lesssim 10^{-3}$ sensitivity requirements (Vielva et al., 2022).

There are several procedures to calibrate the detector's polarization angles:

- ⇒ Artificial calibrators (Sayre et al., 2020; Chiang et al., 2010; Casas et al., 2021)
- ⇒ Natural astrophysical sources like Crab nebula (Polarbear Collaboration et al., 2020; Aumont et al., 2020).
- ⇒ Previous CMB measurements (Chiang et al., 2010).

However, these methodologies can only obtain an uncertainty on the order of $\sim 0.5 - 1^\circ$. This thesis includes two works (P.II and P.III) that can recover polarization angles from multi-frequency data. One methodology relies on nulling the EB cross-spectra (P.II and P.III), while the other calculates the polarization angles during CS (P.II). Both methods mitigate the systematic residuals enough to recover an unbiased tensor-to-scalar ratio.

Beam characterization

Imperfect beam characterization by uncertainties in beam measurements or beam modeling is a significant source of systematic errors. The beam pattern of a given experiment can be divided into the main lobe, where the system angular response is the largest, and sidelobes. Sidelobes are caused by non-ideal interactions in the system and can be further split into near and far sidelobes. Improper characterization of the different parts of the beam yields different systematic errors, e.g.,

- ⇒ **Far sidelobe pick-up.** The main source of residuals comes from far-side lobe pick-up. The Galactic B-mode signal is leaked to higher latitude signals. The mismatch between the excess signal at different bands leads to residuals in the CMB maps after CS (LiteBIRD Collaboration et al., 2022).
- ⇒ **Beam asymmetries.** An asymmetric beam can produce a signal amplitude proportional to the scanning angle. If not properly accounted for with, for example, the

half-wave plate (HWP) modulation and scanning strategy, this effect produces E- to B-modes leakage (Gallardo et al., 2018).

Half-wave plate systematic effects

Several polarization experiments will include an HWP in their design, e.g., SO-SATs (Salatino et al., 2018), and LiteBIRD (LiteBIRD Collaboration et al., 2022). Fast-rotating HWPs allow for the quasi-instantaneous estimation of the Stokes parameters I, Q, and U. Due to their birefringent nature, HWPs cause a phase shift in the linear polarization. Therefore, by rotating the HWP, the linearly polarized fraction of the incoming radiation can be modulated, and the Stokes parameters are separated using their associated modulation. Another benefit of rotating HWPs is that they mitigate a handful of potential systematics by modulating the linear polarization of the radiation⁴, e.g., $I \rightarrow P$ leakage due to asymmetric beams.

However, HWPs can introduce new systematic effects. HWPs are complex systems, and their transmissivity generally is modeled either using the Jones formalism

$$\mathbf{E}_{\text{out}} = \mathbf{J} \mathbf{E}_{\text{in}}, \quad (2.36)$$

or the Mueller matrix formalism

$$\mathbf{S}_{\text{out}} = \mathbf{M} \mathbf{S}_{\text{in}}, \quad (2.37)$$

where out and in refer to the output and input radiation, $\mathbf{E} = (E_x \ E_y)^T$ is the electric field vector, $\mathbf{S} = (I \ Q \ U \ V)^T$ is a vector whose elements are the Stokes parameters, and \mathbf{J} and \mathbf{M} are matrices that characterize the transmission of the incoming radiation. The effect of the HWPs depends on both the frequency and the incidence angle of the radiation, hence examples of systematic effects induced by HWPs are

- ⇨ **Instrumental polarization.** As a result of the HWP anisotropic transmission, a small fraction of the unpolarized incoming radiation with oblique incident angles is converted to polarization. This results in non-zero M_{QI} and M_{UI} elements in the Mueller matrix.
- ⇨ **Polarization efficiency.** An ideal HWP introduced a known phase shift for a given frequency ν_* . For frequencies different from ν_* , the HWP deviates from this ideal behavior. Thus, uncertainties on the HWP parameter can lead to errors in the polarization efficiency. The mismatch of polarization efficiencies among bands leads to B-mode residuals.

⁴There are other modulating techniques aside from rotating HWPs such as Boresight rotation (BICEP2 and Keck Array Collaborations et al., 2015).

Other systematic effects

There are a plethora of other systematic effects. Some worth mentioning are bandpass mismatch, gain systematic effects, pointing errors, ghosting effects, cross talk, atmosphere, ground-pick up, radio frequency interference, cosmic ray glitches, etc.

In conclusion, the weakness of the primordial signal imposes stringent constraints on the characterization of these effects. However, at the end of the day, the problem is not the known systematics, but the unexpected ones⁵ which will have to be addressed *a posteriori*.

2.4 Component Separation

As explained before, we need to isolate the CMB from the measured signal to extract the cosmological information. Since most component separation methods operate on multi-frequency signal maps⁶, let's describe the component separation problem at the map level. Ignoring for now any systematic effect, the i -th channel signal at the pixel p is

$$d_{i,p} = \int d\Omega \int d\nu B_i(\nu, \mathbf{n}) \left(\sum_{c \in N_c} g_i(\nu) f_{p,c}(\nu) s_{p,c} \right) + n_{i,p}, \quad (2.38)$$

where $B_i(\nu, \mathbf{n})$ is the instrument beam, $s_{p,c}$ and $f_{p,c}(\nu)$ are the amplitude and the scaling law of the component c , $g_i(\nu)$ is the i -th channel's spectral bandpass, N_c is the number of microwave components, and $n_{i,p}$ is instrumental noise. Assuming that the beam B is constant within the bandpass, eq. 2.38 simplifies to

$$d_{i,p} = B_i * \left(\sum_{c \in N_c} f_{p,c}^i(\nu) s_{p,c} \right) + n_{i,p}, \quad (2.39)$$

where $f_{p,c}^i(\nu) = \int d\nu g_i(\nu) f_{p,c}(\nu)$ is the weighted scaling law over the bandpass, and $*$ is the convolution operator. For multi-frequency data (N_ν number of channels), eq. 2.39 can be expressed in matrix form as

$$\mathbf{d}_p = B * \mathbf{A}_p \mathbf{s}_p + \mathbf{n}_p = \mathbf{A}_p \hat{\mathbf{s}}_p + \mathbf{n}_p \quad (2.40)$$

where \mathbf{d}_p , \mathbf{s}_p , $\hat{\mathbf{s}}_p$, and \mathbf{n}_p are the data, amplitude, beam-convolved amplitude, and noise vectors, and \mathbf{A}_p is the so-called mixing matrix ($N_\nu \times N_c$).

The simplest method to extract the CMB signal is by inverting the linear system in eq. 2.40, i.e., finding the matrix \mathbf{W} that returns the best s estimator $\tilde{\mathbf{s}} = \mathbf{W}\mathbf{d}$. Notable

⁵For example the rate of cosmic-ray impacts in *Planck* was significantly larger than expected (Catalano et al., 2014).

⁶There are component separation methods that work on time-ordered data (Galloway et al., 2022).

solutions⁷ are the Wiener filter solution

$$\mathbf{W} = \left[\mathbf{A}^\dagger \mathbf{N}^{-1} \mathbf{A} + \mathbf{C}_s^{-1} \right]^{-1} \mathbf{A}^\dagger \mathbf{N}^{-1}, \quad (2.41)$$

where \mathbf{N} and \mathbf{C}_s are the noise and signal covariance matrices, and the Generalized Least Squares solution (GLS)

$$\mathbf{W} = \left[\mathbf{A}^\dagger \mathbf{N}^{-1} \mathbf{A} \right]^{-1} \mathbf{A}^\dagger \mathbf{N}^{-1}, \quad (2.42)$$

which provides the minimum variance solution if the signal is stochastic in the former or deterministic in the latter (Tegmark & Efstathiou, 1996; Bouchet & Gispert, 1999). The Wiener solution does not satisfy the condition of minimum foreground residuals, i.e., the solution can be biased. The GLS returns an unbiased estimation, but the noise contribution can be large.

The problem of CS in the context of CMB has undergone massive development from these linear inversion solutions. CS methodologies can be classified into blind and non-blind methods, i.e., methods that do not rely on prior information of the foregrounds and those that do. However, this classification is not representative anymore since methodologies have started to mix to improve their performance. Here, I classify the CS techniques using an almost orthogonal base, i.e., parametric and non-parametric CS methods⁸. Both parametric and non-parametric methods have advantages and disadvantages, but consistency between them is required to claim a robust detection. Below, I review the non-parametric and parametric CS techniques in Section 2.4.1 and Section 2.4.2, respectively.

2.4.1 Non-parametric methodologies

Non-parametric methods do not require physical modeling of the sky components. This class is highly heterogeneous, covering methods that rely on very different assumptions. The methods can be subclassified as

- ⇒ Methods whose only restriction is that the sources be statistically independent. These methods are generally referred to as *blind* and contain Internal Linear Combination (ILC), Independent Component Analysis (ICA), and Generalized Morphological Component Analysis (GMCA).
- ⇒ The template fitting method, which subtracts the unwanted components using either internal or external templates of the contaminants.
- ⇒ Methods that rely on Machine Learning to separate the components, e.g., using Convolutional Neural Networks (CNN).

⁷For a comprehensive review on linear inversion solutions see (Delabrouille & Cardoso, 2007).

⁸I point out those methods that are at the boundary between these classes.

Internal Linear Combination

This method makes little assumptions regarding the signal. It only assumes that the component of interest x is uncorrelated with the rest, and that x 's SED is known. The ILC solution is a weighted linear combination of the frequency maps

$$\hat{s}_x = \sum_{\nu} \omega_{\nu} \mathbf{d}_{\nu}, \quad (2.43)$$

or spherical harmonics

$$\hat{a}_{\ell m}^x = \sum_{\nu} \omega_{\ell}^{\nu} a_{\ell m}^{\nu}. \quad (2.44)$$

The weights satisfy the following conditions.

1. The variance of \hat{s} (analogously of $\hat{a}_{\ell m}$) is minimum

$$\frac{\partial}{\partial \boldsymbol{\omega}} \left(\boldsymbol{\omega}^T \mathbf{C} \boldsymbol{\omega} \right) = 0, \quad (2.45)$$

$$\frac{\partial}{\partial \omega_{\ell}} \left(\omega_{\ell}^T \mathbf{C}_{\ell} \omega_{\ell} \right) = 0, \quad (2.46)$$

where $\mathbf{C} = \mathbf{d} \mathbf{d}^T$ and $C_{\ell}^{i,j} = \langle (a_{\ell m}^i)^{\dagger} a_{\ell m}^j \rangle$ are the corresponding covariance matrix in real and harmonic space. From now on, \mathbf{C} is used for both.

2. They are constrained by

$$\boldsymbol{\omega}^T \mathbf{a}_x = 1, \quad (2.47)$$

where \mathbf{a}_x is the component x 's SED⁹ to ensure that the x component is preserved, i.e.,

$$\hat{s} = \boldsymbol{\omega}^T \mathbf{d} = \boldsymbol{\omega}^T (\mathbf{A} \mathbf{s} + \mathbf{n}) = s_x + \sum_{\nu} \sum_{c \in F} \omega_{\nu} A_{\nu,c} s_c + \boldsymbol{\omega}^T \mathbf{n}, \quad (2.48)$$

where F is the set of foreground components.

The solution to the minimization problem is

$$\boldsymbol{\omega} = \left(\mathbf{a}_x^T \mathbf{C}^{-1} \mathbf{a}_x \right)^{-1} \mathbf{a}_x^T \mathbf{C}^{-1}. \quad (2.49)$$

This method has been applied successfully to CMB data (Tegmark et al., 2003; Bennett et al., 2003; Hinshaw et al., 2007). Advantages of the ILC method is that there are no assumptions made about the foregrounds SED. In addition, the algorithm maximizes the S/N of the x component. On the other hand, if the assumption of x being uncorrelated with the other components is not fulfilled, the recovered \hat{s}_x is no longer unbiased. The foregrounds are also assumed to have spatially invariant spectral behavior, which is not a realistic scenario.

⁹If the component is the CMB and the signal is in thermodynamic units, \mathbf{a}_x is a N_{ν} vector whose elements are equal to one.

Due to these drawbacks, multiple extensions of this methodology that improve performance have been developed. Below, I describe briefly some of the most popular:

⇒ Due to the uncertainty principle, pixel-space (harmonic-space) ILC methods are fully local in pixel (harmonic) space and non-local in harmonic (pixel) space. Non-local weights are not optimal for CS. To circumvent this issue, (Delabrouille et al., 2009) implemented an ILC solution in *needlets* domain, called NILC. *Needlets* are a wavelet decomposition of the sphere that satisfy the condition of being perfectly localized in the harmonic domain and potentially excellent localization in the pixel domain. Other ILC implementations using different wavelets are SILC, and its polarization analogous spin-SILC (Rogers et al., 2016a,b).

⇒ The ILC does not provide the minimal foreground variance solution. Since foreground residuals are difficult to propagate, it is interesting to find solutions that minimize this contribution. To minimize the foreground residuals, one can include orthogonal constraints, i.e.,

$$\omega^T \mathbf{b}_i = 0, \quad (2.50)$$

where \mathbf{b}_i is the SED vector of the modeled foreground $i \in 1, \dots, m$, and m is the number of modeled foreground components. Since it uses information regarding the components' SED, this model lies in the border between parametric and non-parametric methods. This solution yields reduced foreground residuals at the cost of larger noise residuals. Thus, there is a trade-off between the two sources of error. Another advantage of this extension is that it can recover both the CMB and the thermal Sunyaev–Zeldovich contribution, with vanishing contamination from the other.

Implementations of this extension are cILC (Remazeilles et al., 2011a), GNILC (Remazeilles et al., 2011b), and MILCA (Hurier et al., 2013). To account for possible incorrect modeling of the foreground SED, cMILC (Remazeilles et al., 2021) adds the null constraints of the SED moment expansion derived by (Chluba et al., 2017).

⇒ The natural extension to polarization data is to find the minimum variance of Q and U maps. However, Q and U are spinorial components that depend on the coordinate system, which generates problems. For example, subtracting a constant contribution from Q or U induces E- to B-mode leakage. Fernández-Cobos et al. (2016) proposed an extension called PILC, using the $Q \pm iU$ quantities instead. This method minimizes the variance of the polarization intensity, i.e., $P = |Q + iU|$, instead of Q and U independently.

Independent Component Analysis

ICA methods rely only on the assumption that the components are statistically independent. Given an estimator of this independence, the ICA methods try to find the matrix \mathbf{W} that

optimizes the independence of \hat{s} obtained as

$$\hat{s} = \mathbf{W}d. \quad (2.51)$$

The definition of an independence estimator is not unique. Therefore, there are several ICA methods in the literature whose main difference arises from this definition. Below, I provide a brief description of some popular ICA implementations.

⇒ The **fastICA** method proposed by (Hyvarinen, 1999) and implemented for CMB analysis in (Maino et al., 2002). This method relies on the following two assumptions:

1. The components are independent.
2. The signal has at most one Gaussian component.

The second assumption is fulfilled since the CMB signal is compatible with being Gaussian, and the foregrounds are non-Gaussian. The independence of the components is determined in terms of their non-Gaussianity. According to the central limit theorem, the linear mixture of the sources is more Gaussian than the components alone. Thus, **fastICA** finds the weights that maximize the non-Gaussianity of \hat{s} .

Non-Gaussianity can be quantified using different estimators, e.g., with moments whose order is higher than 2. In **fastICA**, the non-Gaussianity is calculated using the neg-entropy estimator, since it is more robust than other statistics in the presence of noise.

There have been several applications of this method. For example, applications to COBE (Maino et al., 2002) and WMAP (Maino et al., 2007; Bottino et al., 2010) data, simulated 21 cm maps (Wolz et al., 2015), and to detect CO line from *Planck* data using kurtosis as a measure of non-Gaussianity (Ichiki et al., 2014).

⇒ The spectral matching ICA (**SMICA**) method (Delabrouille et al., 2003; Patanchon et al., 2005; Cardoso et al., 2008) exploits the statistics in the harmonic space. The weights are

$$\mathbf{W}_\ell = \frac{\mathbf{A}^\dagger \mathbf{C}_\ell^{-1}}{\mathbf{A}^\dagger \mathbf{C}_\ell^{-1} \mathbf{A}} \quad (2.52)$$

where \mathbf{C}_ℓ is the $N_\nu \times N_\nu$ spectral covariance matrix. Given the linear mixture of eq. 2.40 the spectral covariance matrix can be expressed as

$$\mathbf{C}_\ell = \mathbf{A} \mathbf{C}_{s,\ell} \mathbf{A}^\dagger + \mathbf{N}_\ell. \quad (2.53)$$

The statistical independence between components yield

$$\mathbf{C}_{s,\ell} = \text{diag} (C_{1,\ell}, \dots, C_{N_c,\ell}) . \quad (2.54)$$

For CMB studies, the spectral covariance matrix is usually modeled as

$$\mathbf{C}_\ell(\theta) = \begin{bmatrix} \mathbf{a} & \mathbf{F} \end{bmatrix} \begin{bmatrix} C_\ell^{\text{cmb}} & 0 \\ 0 & \mathbf{P}_\ell \end{bmatrix} \begin{bmatrix} \mathbf{a} & \mathbf{F} \end{bmatrix}^\dagger + \mathbf{N}_\ell, \quad (2.55)$$

where \mathbf{a} is the CMB SED, \mathbf{F} is an $N_\nu \times (N_c - 1)$ matrix containing the foreground emissivities, and \mathbf{P}_ℓ is an $(N_c - 1) \times (N_c - 1)$ matrix containing the foreground cross spectra. SMICA finds the set of parameters $\theta = \{\mathbf{a}, \mathbf{F}, C_\ell^{\text{cmb}}, \mathbf{P}_\ell, \mathbf{N}_\ell\}$, that minimizes the difference between eq. 2.53 and the empirical spectral density matrices

$$\hat{\mathbf{C}} = \frac{1}{2\ell + 1} \sum_m \mathbf{d}_{\ell,m} \mathbf{d}_{\ell,m}^\dagger, \quad (2.56)$$

as follows

$$\hat{\theta} = \arg \min_{\theta} \sum_{\ell} (2\ell + 1) \left[\text{Tr} \left(\hat{\mathbf{C}} \mathbf{C}_\ell(\theta)^{-1} \right) + \log \det \mathbf{C}_\ell(\theta) \right]. \quad (2.57)$$

In general SMICA fixes \mathbf{a} and fits the foreground parameters, assuming that \mathbf{P}_ℓ is positive definite.

- ⇒ Other implementations of ICA methods are Vansyngel et al. (2016) that introduces Bayesian inference in the SMICA methodology, or PoLEMICA an extension of SMICA to polarization (Aumont & Macías-Pérez, 2007).

Generalized Morphological Component Analysis

GMCA is a blind source separation technique that aims to disentangle the components by exploiting sparsity in a given base Bobin et al. (2007). In the context of CMB studies, GMCA is performed in the wavelet space to take advantage of the sparsity of the foregrounds in this domain (Bobin et al., 2008). In the GMCA setting, each source s_j in the wavelet domain can be uniquely decomposed as

$$s_j = \alpha_j \boldsymbol{\Phi}, \quad (2.58)$$

where α_j are the expansion coefficients, and $\boldsymbol{\Phi}$ is the wavelet orthonormal basis. On this basis, the linear mixture can be expressed as

$$\mathbf{D} = \mathbf{A} \boldsymbol{\alpha} \boldsymbol{\Phi} + \mathbf{N}. \quad (2.59)$$

GMCA finds a solution of \mathbf{A} by maximizing the sparsity of the sources in the wavelet basis by optimizing

$$\min_{\boldsymbol{\alpha}, \mathbf{A}} \frac{1}{2} \left\| \mathbf{D} \boldsymbol{\Phi}^T - \mathbf{A} \boldsymbol{\alpha} \right\|_F^2 + \lambda \sum_{j=1}^{N_c} \left\| \alpha_j \right\|_p, \quad (2.60)$$

where $\|\mathbf{X}\|_F^2$ stands for the Frobenius norm, and $\|\alpha\|_p$ is the p norm. GMCA can be applied as a blind method to optimize the separation of the CMB or benefit from parametrizing \mathbf{A} to characterize the foreground components, as shown in (Leach et al., 2008).

There have been several extensions in the literature of this model. For example, the local-generalized morphological component analysis LGMCA generalizes the GMCA method by accounting for beams' variability across frequencies, as well as spatial variations of the components' SED (Bobin et al., 2013). The latter is achieved by incorporating locally variable mixing matrices and running multiple independent GMCA models on different partitions of a sky map. The HGMCA method (Wagner-Carena et al., 2020) extends LGMCA by enforcing global consistency among the GMCA models across several partitions of the map through the use of hierarchical priors.

Template Fitting

This component separation technique assumes that the foreground contribution can be described as a superposition of fixed spatial templates $\{t_j\}_{j=1,\dots,N_t}$. The CMB signal in the channel ν is then

$$\hat{s}_\nu = \mathbf{d}_\nu - \sum_{j=1}^{N_t} \beta_j \mathbf{t}_j, \quad (2.61)$$

where β_j is obtained by minimizing the variance of the cleaned map, i.e.,

$$\arg \min_{\beta} \hat{s}_\nu \mathbf{C}^{-1} \hat{s}_\nu, \quad (2.62)$$

where \mathbf{C} is the total covariance matrix of the template-corrected data, i.e., calculated as the sum of the CMB and instrumental noise contributions (both from the map to be cleaned and the templates). Since this is a linear combination, this methodology is applicable in pixel, spherical harmonics, or wavelet space. Some implementations of this technique are the following:

- ⇒ SEVEM (Fernández-Cobos et al., 2012) is a map domain implementation of the template cleaning approach to component separation. The foreground templates are calculated as the difference between a pair of similar frequency maps to remove the CMB signal. SEVEM generates multiple foreground-cleaned frequency channel maps, which are later combined into a unique CMB map using a weighting scheme. This methodology was applied in *Planck* analyses (Planck Collaboration et al., 2016a, 2020a,e).
- ⇒ The WI-FIT method (Hansen et al., 2006) applies this technique in the wavelet domain. Working in this domain is advantageous since it returns lower uncertainties on the foreground coefficients than a similar pixel-based approach. The method does not require external templates as it uses internal templates calculated as differences of frequency channels.

- ⇒ In the pixel domain, the method assumes that each component scaling law is spatially invariant, i.e., $d_j(\nu, p) = a_j(\nu)s_j(p)$. This assumption generally does not hold and can introduce biases in parameters such as the tensor-to-scalar ratio. In this direction, the Delta-MAP method (Ichiki et al., 2019) generalizes the internal template fitting technique to account for spatially varying spectral parameters to first order in perturbation, so it can now be considered a parametric method.

Convolutional Neural Networks

Deep learning (DL) has sparked a lot of interest in recent years, with applications in a wide range of fields, including cosmology. The recovery of CMB foreground-cleaned maps from microwave data is one of the many applications of DL in this field. Although there are some approaches to solving this problem with feed-forward neural networks (Baccigalupi et al., 2000; Nørgaard-Nielsen & Jørgensen, 2008), this task is commonly performed using a convolutional CNN (Ronneberger et al., 2015). CNNs are a DL model for processing data with a grid pattern, such as images, that is inspired by the organization of animal visual cortex. They are particularly effective for cleaning foregrounds from maps due to their large anisotropic nature. CNNs process structural information, identifying patterns and structures that help remove these sources.

CNNs are mathematical models based on multi-layer neural networks. They are composed of three types of layers: convolution, pooling, and fully connected layers. The first two layers, convolution and pooling, are used to identify and extract features. The fully connected layer is applied to map the extracted features into the final output. The specific function of each type of layer is the following

- ⇒ The convolutional layers filter the input images by convolving them with small filters (or kernels), whose values are weights to be learned. The filter is applied with a bias across the entire image, and a feature map is generated after applying a nonlinear activation function.
- ⇒ The pooling layers reduce the dimensions of feature maps by grouping map patches into a given value. Two popular pooling methods are average and max pooling.
- ⇒ The fully connected layers get the output from the previous layer as input and apply a linear transformation followed by an activation function.

The weights and biases of all layers are optimized through a backpropagation algorithm during training by minimizing the loss function.

In machine learning, CMB foreground cleaning is classified as an image-to-image problem. Therefore, the CNN implementations for this task usually apply a *U-Net* architecture (Ronneberger et al., 2015). It consists of a contracting path followed by an expansive path, giving the characteristic U-shape. The contracting path is typically a convolutional network that obtains the features of the image. The expansive path combines the features and

spatial information through a sequence of up-convolutions and concatenations to generate high-resolution features and eventually the final image.

There are several implementations of this algorithm in the literature

- ⇒ Petroff et al. (2020) implemented a CNN with these characteristics to extract the CMB from *Planck*'s intensity data. Their algorithm makes use of *DeepSphere* (Perraudin et al., 2019) combined with the HEALPix scheme (Górski et al., 2005) to extend traditional CNNs to the sphere, making it more suitable for this type of analysis.
- ⇒ Wang et al. (2022) showed that regular CNNs, i.e., using 2D rectangular patches, can extract the foreground cleaned CMB maps. They applied their methodology to simulations of *Planck* HFI intensity data, and CMB-S4 polarization data with good results.
- ⇒ Casas et al. (2022) demonstrated that these algorithms are robust against various levels of contamination from Galactic foregrounds and point sources.
- ⇒ Jeffrey et al. (2022) recovered the CMB signal using only a single frequency of simulated data for a BICEP-like sky patch. Their algorithm applies Moment Networks, i.e., a hierarchy of U-Net CNNs, to sample the posterior probability of the CMB signal pixel.

2.4.2 Parametric methods

Parametric methods use the components' SEDs to model the mixing matrix. Unlike non-parametric methods, they provide a physical characterization of both the CMB and the foregrounds. On the other hand, incorrect modeling of the sky can lead to severe bias in the recovered parameters and the derived cosmological parameters. The parametric methods are subdivided into the following classes

- ⇒ Correlated Component Analysis (CCA) techniques that rely on the data's second-order statistics to extract the spectral parameters.
- ⇒ Bayesian methods that benefit from the use of prior information to disentangle components.

Correlated Component Analysis

CCA (Bedini et al., 2005; Bonaldi et al., 2006) estimates the mixing matrix by exploiting the information on the second-order statistics of the data. Unlike ICA methods, in which each pair of components is assumed to be independent, CCA algorithm makes no assumptions about the independence or lack of correlations between those pairs. The method exploits the spatial structure of the individual component maps to estimate the parameters of each component's scaling model. The spatial structure of the maps is taken into account through

the covariance matrices at different shifts (τ, Φ)

$$\mathbf{C}_d(\tau, \Phi) = \left\langle [d(\theta, \phi) - \mu_d] [d(\theta + \tau, \phi + \Phi) - \mu_d]^T \right\rangle = \mathbf{A}(\theta) \mathbf{C}_s(\tau, \Phi) \mathbf{A}(\theta)^T + \mathbf{N}(\tau, \Phi), \quad (2.63)$$

where μ_d is the mean data vector, (θ, ϕ) are the pixel's coordinates in spherical units, and $\mathbf{C}_d(\tau, \Phi)$, $\mathbf{C}_s(\tau, \Phi)$ and $\mathbf{N}(\tau, \Phi)$ are the data, signal, and noise covariance matrices, respectively. \mathbf{C}_s and the spectral parameters θ of the mixing matrix are obtained by minimizing

$$\sum_{\tau, \Phi} \left\| \mathbf{A}(\theta) \mathbf{C}_s(\tau, \Phi) \mathbf{A}(\theta)^T - [\mathbf{C}_d(\tau, \Phi) - \mathbf{N}(\tau, \Phi)] \right\|, \quad (2.64)$$

for a sufficient large set of shift pairs (τ, Φ) . Once the mixing matrix is estimated the components can be reconstructed applying either a Wiener (eq. 2.41) or GLS filter (eq. 2.42). CCA can also be performed in the harmonic domain (Ricciardi et al., 2010). Examples of the application of this method are given in (Leach et al., 2008; Hervías-Caimapo et al., 2022).

Bayesian parametric methods

Bayesian parametric methods benefit from prior information to disentangle signal components. Given a parametric model of the signal components $m(\boldsymbol{\nu}, \theta)$, the methods try to maximize the following posterior distribution

$$\mathcal{P}(\theta|\mathbf{d}) \propto \mathcal{P}(\mathbf{d}|\theta) \mathcal{P}(\theta), \quad (2.65)$$

where $\mathcal{P}(\mathbf{d}|\theta)$ is commonly known as the likelihood and $\mathcal{P}(\theta)$ is prior information of the model parameters θ . Assuming Gaussian noise, the likelihood of the data is

$$\mathcal{P}(\mathbf{d}|\theta) = \frac{\exp\left(-\frac{1}{2} (\mathbf{d} - m(\boldsymbol{\nu}, \theta))^T \mathbf{N}^{-1} (\mathbf{d} - m(\boldsymbol{\nu}, \theta))\right)}{\sqrt{(2\pi)^{N_\nu} \det(\mathbf{N})}}. \quad (2.66)$$

These methods commonly apply sampling algorithms to find the set of θ that maximizes the posterior distribution. Examples of sampling methods are Metropolis–Hasting sampling, nested sampling, and affine-invariant ensemble Markov chain Monte Carlo (MCMC) (Allison & Dunkley, 2014).

Because of the high dimensionality of the parameter space, the total distribution rarely is sampled directly. Most methods rely on sampling conditional distributions to circumvent this issue. Let the target distribution \mathcal{P} be a function of $(\mathcal{A}, \mathcal{B}, \mathbf{d})$, one can generate a joint sample $(\mathcal{A}_i, \mathcal{B}_i)$ by sampling

$$\mathcal{A}_i \leftarrow \mathcal{P}(\mathcal{A}|\mathcal{B}_{i-1}, \mathbf{d}), \quad (2.67)$$

$$\mathcal{B}_i \leftarrow \mathcal{P}(\mathcal{B}|\mathcal{A}_i, \mathbf{d}), \quad (2.68)$$

where $\mathcal{P}(\mathcal{A}|\mathcal{B}_{i-1})$ ($\mathcal{P}(\mathcal{B}|\mathcal{A}_i)$) is the probability of \mathcal{A} (\mathcal{B}) given \mathcal{B}_{i-1} (\mathcal{A}_i) and d .

There are many implementations of this methodology in the literature, both in the real and harmonic space. Some examples are:

- ⇒ **Commander2** (Eriksen et al., 2008) is an implementation of this Bayesian parametric method that works in the map domain and was one of the component separation methods applied in the *Planck* analyses (Planck Collaboration et al., 2016a; Planck Collaboration, 2016; Planck Collaboration et al., 2020b,e). Recently they released a new version of the algorithm called **Commander3** (Galloway et al., 2022), which incorporates the time-ordered data processing and mapmaking in the pipeline. This self-contained approach improves the error propagation estimation compared to methods that split the analysis into several steps.
- ⇒ **xForecast** is a parametric pixel-based component separation method that accounts for the propagation of systematic and statistical foregrounds residuals into the cosmological likelihood (Stompor et al., 2009; Errard et al., 2011; Stompor et al., 2016).
- ⇒ **BFoRe** is a foreground removal tool at map level that fits the independent spectral parameters of the synchrotron and dust in different patches of the sky (Alonso et al., 2017).
- ⇒ Azzoni et al. (2022) introduced a hybrid implementation of this method, i.e., it operates at map and power spectrum levels. First, the foreground amplitudes are obtained at the map level, assuming homogeneous spectral properties. Then the foreground contribution is subtracted from the data, and the residual foreground contamination is modeled and subtracted at the power spectrum level.
- ⇒ A special case of Bayesian parametric methods is the so-called Maximum Entropy Method (**MEM**). Since foreground components are known to be highly non-Gaussian, the **MEM** technique proposes to find the parameters that maximize entropy. This is achieved by imposing an entropic prior (Hobson & Lasenby, 1998). Examples of the application of this technique are given in (Barreiro et al., 2004; Stolyarov et al., 2002). **fastMEM** (Stolyarov et al., 2005) extends the methodology to account for spatial variations of the spectral parameters by including additional components. These components are the following terms in the Taylor expansion of the SEDs' corresponding parameters.
- ⇒ Finally, P. I, included in this thesis, presents **B-SeCRET** a Bayesian parametric component separation that includes a self-consistent approach to obtain an estimate of the combined foreground and instrumental model residuals power spectrum.

Several extensions of the methodology incorporate the clustering of the spectral parameters to decrease the statistical uncertainty of the parameters. Some examples are Errard & Stompor (2019), where the regions are chosen as super-pixels at a lower **HEALPix** resolution.

In Grumitt et al. (2020), the regions are obtained using clustering algorithms such as the mean-shift clustering algorithm. Puglisi et al. (2022) presented a new methodology based on spectral clustering to define geometrical affine regions with similar spectral parameters.

After reviewing the main challenges that the search for primordial B-modes presents and the capabilities of CS methods, and in particular Bayesian parametric methods, we can now turn our attention to the main contributions of this thesis presented in the next chapter.

Part II

Thesis contributions

Included publications

*"I was taught that the way of progress was
neither swift nor easy."*

Marie Curie

This chapter summarizes the publications included in this Thesis. The studies were performed in the context of CS applied to CMB polarization data. The papers present three applications of CS. CS was applied first to study and optimize the constraining power of proposed experiments. Second, to mitigate systematic errors by including their effects in the modeling. Finally, to characterize and improve the modeling of astrophysical foregrounds.

This work is a compilation thesis. It contains the following publications:

- P. I: **de la Hoz, E.**, Vielva, P., Barreiro, R. B., & Martínez-González, E. (2020). On the detection of CMB B-modes from the ground at low frequency. *Journal of Cosmology and Astroparticle Physics*, 2020(06), 006.
- P. II: **de la Hoz, E.**, Diego-Palazuelos, P., Martínez-González, E., Vielva, P., Barreiro, R. B., & Bilbao-Ahedo, J. D. (2022). Determination of polarization angles in CMB experiments and application to CMB component separation analyses. *Journal of Cosmology and Astroparticle Physics*, 2022(03), 032.
- P. III: Krachmalnicoff, N., Matsumura, T., **de la Hoz, E.**, Basak, S., Gruppuso, A., Minami, Y., Baccigalupi, C., Komatsu, E., Martínez-González, E., Vielva, P. & LiteBIRD collaboration. (2022). In-flight polarization angle calibration for LiteBIRD: blind challenge and cosmological implications. *Journal of Cosmology and Astroparticle Physics*, 2022(01), 039.

P.IV: **de la Hoz, E.**, Barreiro, R. B., Vielva, P., Martínez-González, E., Rubiño-Martín, J. A., Casaponsa, B., Guidi, F., Ashdown, M., Génova-Santos, R. T. & QUIJOTE collaboration (2022). QUIJOTE scientific results - VIII. Diffuse polarized foregrounds from component separation with QUIJOTE-MFI. *Monthly Notices of the Royal Astronomical Society*. In press.

The overarching element of these publications is the application of CS methods to CMB-related problems. In this chapter, I describe the Bayesian parametric method that I developed called B-SeCRET, Section 3.1, and its applications included in this work, Section 3.2. The publications are appended at the end of this chapter.

3.1 B-SeCRET

The B-SeCRET (Bayesian-Separation of Components and Residuals Estimate Tool) methodology is a parametric pixel-based maximum-likelihood method, which relies on an Affine-Invariant Markov Chain Monte Carlo (MCMC) Ensemble sampler to draw samples from a posterior distribution (Foreman-Mackey et al., 2013).

B-SeCRET applies Bayesian inference to determine the best-fit model parameters given some prior information. In Bayesian statistics, the probability of the model parameters θ_p given the signal data \mathbf{d}_p at the pixel p is proportional to the probability of the \mathbf{d}_p given θ_p times the probability of θ_p , i.e.,

$$\mathcal{P}(\theta_p|\mathbf{d}_p) \propto \mathcal{P}(\mathbf{d}_p|\theta_p)\mathcal{P}(\theta_p). \quad (3.1)$$

$\mathcal{P}(\theta_p)$ is commonly known as the prior information, whereas $\mathcal{P}(\mathbf{d}_p|\theta_p)$ is usually referred to as the likelihood. Assuming Gaussian noise, the likelihood of the data can be expressed as

$$\mathcal{P}(\mathbf{d}_p|\theta_p) = \frac{\exp\left(-\frac{1}{2}(\mathbf{d}_p - \mathbf{S}_p)^T \mathbf{C}^{-1}(\mathbf{d}_p - \mathbf{S}_p)\right)}{\sqrt{(2\pi)^N \det(\mathbf{C})}}, \quad (3.2)$$

where \mathbf{C} is the noise covariance matrix, N is the number of elements in the \mathbf{d}_p array, and \mathbf{S}_p is the parametric model considered.

To draw samples from the posterior probability we use the PYTHON implementation `emcee` (Foreman-Mackey et al., 2013) of an affine-invariant ensemble sampler for MCMC (Goodman & Weare, 2010). In each pixel, the best-fit parameters and their uncertainties are obtained as the median and the standard deviation of their respective marginalized posterior probability.

B-SeCRET includes a self-consistent approach to obtain an estimate of the combined foreground and instrumental model residuals power spectrum. The use of a residual model prevents biases in derived parameters from the CMB caused by insufficient foreground removal. The procedure to obtain the residual model estimate is based on simulations derived

using the best-fits of model parameters.

3.2 Published applications

The papers are split into three categories, corresponding to the different applications of the CS method. The applications are the following: assessing the performance of proposed experiments, Section 3.2.1, mitigating systematic errors, Section 3.2.2, and, improving the characterization of astrophysical foregrounds, Section 3.2.3.

3.2.1 Experimental Design

Initiatives for new CMB experiments require extensive exploratory studies of all the instrumental characteristics parameter space to find the optimal configuration that meets their scientific objectives. Furthermore, funding agencies want proposals that are convincing and well-justified.

In P. I (de la Hoz et al., 2020) we assessed whether a ground-based experiment operating in the low-frequency regime (10-120 GHz) can reach a precision of $\sigma_r \lesssim 10^{-3}$. This study was conducted in the context of the ELFS (European Low-Frequency Survey) initiative. The ELFS project is a collaborative international effort to map low-frequency microwave emissions with unprecedented sensitivity, coverage, and angular resolution.

We found several arrangements that satisfied the objective of detecting PGWs with a precision of $\sigma_r \lesssim 10^{-3}$. Furthermore, we demonstrated that the proposed experiment helps constrain the low foreground parameters in planned missions such as LiteBIRD. As a result, this improves the recovery of the CMB signal and the detection of PGWs with this mission.

3.2.2 Systematics control

Future polarization CMB experiments will require unprecedented sensitivities to detect the imprint of PGWs in the CMB polarization, posing new challenges in the systematic instrumental effects control. As explained in Section 2.3.3, miscalibrated polarization angles are one of the most significant known sources of systematic error. In particular, this systematic can bias the estimated tensor-to-scalar ratio derived from LiteBIRD data, if the requirements are not reached (Vielva et al., 2022).

LiteBIRD is a planned satellite mission whose primary objective is the detection of PGWs through the footprint left on the polarized CMB B-modes (LiteBIRD Collaboration et al., 2022). It has been selected by the Japan Aerospace Exploration Agency (JAXA) as a Strategic L-class mission and its launch is planned for the late 2020s. Its design is optimized for CMB B-mode detection on large angular scales, and its principal scientific goal is reaching $\sigma_r \lesssim 10^{-3}$.

In P. II (de la Hoz et al., 2022a) we implemented two methodologies to estimate the zero-point instrumental polarization angles from multi-frequency data. The first one is based on

nulling the cross-angular power spectrum between E- and B-modes. The other recovers the polarization angles by including them in the CS analysis as model parameters. In the latter case, we apply the results from the previous methodology as prior information.

I applied the first method in the *blind challenge* conducted for P. III (Krachmalnicoff et al., 2022). This publication is a LiteBIRD collaboration paper where we presented LiteBIRD's in-flight calibration strategy. Furthermore, I used B-SeCRET to extract the foreground-cleaned CMB map after correcting the signal maps with the estimated angles. We proved that after this correction we obtain an unbiased estimation of the tensor-to-scalar ratio, r .

3.2.3 Foreground characterization

The importance of having a comprehensive understanding of the mechanisms and modeling of astrophysical foregrounds is twofold:

- i) to reduce residuals due to astrophysical foregrounds in the extracted CMB signal, and
- ii) to generate realistic sky simulations for forecast studies of future CMB experiments, such as in P. I., P. II and P. III.

In P. IV (de la Hoz et al., 2022b), we studied the diffuse polarized foregrounds, focusing on the polarized synchrotron emission, using the final data from the QUIJOTE-MFI instrument and ancillary data. The novelty of this study arises from the inclusion of the final data from the QUIJOTE-MFI instrument, which has measured the sky in the unique 10-20 GHz frequency range.

The QUIJOTE experiment (Rubiño-Martín et al., 2010) is a polarimetric ground-based CMB experiment whose main scientific goal is the characterization of the polarization of the CMB and other galactic and extragalactic physical processes in the frequency range 10-40 GHz and at large angular scales ($\gtrsim 1^\circ$). The experiment is located at the Teide Observatory (at ~ 2400 m above sea level) in Tenerife. It is composed of two telescopes equipped with three instruments: the Multi-Frequency Instrument (MFI), the Thirty-GHz Instrument (TGI), and the Forty-GHz Instrument (FGI), operating at 10-20 GHz, 26-36 GHz and 39-49 GHz, respectively. The MFI instrument operated from November 2012 to October 2018 and conducted two different surveys

- i) a shallow Galactic survey (called "wide survey") covering all the visible sky from Tenerife at elevations larger than 30° , and
- ii) a deep cosmological survey covering approximately 3000 deg^2 in three separated sky patches in the northern sky.

The wide survey provides an average sensitivity in polarization of $\sim 35\text{-}40 \mu\text{K}$ per 1-degree beam in four bands centred around 11, 13, 17 and 19 GHz (Rubiño-Martín et al., 2022).

Using the final data from the MFI's wide survey along with data from WMAP and *Planck*, we obtained the first detailed map of the polarized synchrotron's spectral index (β_s) in

the Northern Hemisphere and proved that its spatial variations are statistically significant. Moreover, we detected a uniform curvature parameter in four different sky regions. Finally, we showed that our results are prior independent in the regions where the synchrotron is significantly intense.

P. I: On the detection of CMB B-modes from the ground at low frequency

E. de la Hoz, P. Vielva, R. B. Barreiro, & E. Martínez-González. *Journal of Cosmology and Astroparticle Physics*, 2020(06), 006

© IOP Publishing. This is an author-created, un-copyedited version of an article accepted for publication/published in *Journal of Cosmology and Astroparticle Physics*. OP Publishing Ltd is not responsible for any errors or omissions in this version of the manuscript or any version derived from it. The Version of Record is available online at:
<https://doi.org/10.1088/1475-7516/2020/06/006>

On the Detection of CMB B-modes from Ground at Low Frequency

E. de la Hoz,^{a,b} P. Vielva,^a R. B. Barreiro^a and E. Martínez-González^a

^aInstituto de Física de Cantabria, CSIC-Universidad de Cantabria,
Avda. de los Castros s/n, E-39005 Santander, Spain

^bDpto. de Física Moderna, Universidad de Cantabria,
Avda. los Castros s/n, E-39005 Santander, Spain

E-mail: delahoz@ifca.unican.es, vielva@ifca.unican.es, barreiro@ifca.unican.es,
martinez@ifca.unican.es

Abstract. The primordial CMB B -mode search is on the spotlight of the scientific community due to the large amount of cosmological information that is encoded in the primeval signal. However, the detection of this signal is challenging from the data analysis point of view, due to the relative low amplitude compared to the foregrounds, the lensing contamination coming from the leakage of E -modes, and the instrumental noise. Here, we studied the viability of the detection of the primordial polarization B -mode with a ground-based telescope operating in the microwave low-frequency regime (i.e., from 10GHz-120GHz) in a handful of different scenarios: i. the instrument's channels distribution and noise, ii. the tensor-to-scalar ratio (r) detectability considering different possible r values and degrees of delensing, iii. the effect of including a possible source of polarized anomalous microwave emission (AME), iv. the strengths and weaknesses of different observational strategies and, v. the atmospheric and systematic noise impact on the recovery. We focused mainly on the removal of galactic foregrounds as well as noise contamination by applying a full-parametric pixel-based maximum likelihood component separation technique. Moreover, we developed a numerical methodology to estimate the residuals power spectrum left after component separation, which allow us to mitigate possible biases introduced in the primordial B -mode power spectrum reconstruction. Among many other results, we found that this sort of experiment is capable of detecting Starobinsky's r even when no delensing is performed or, a possible polarized AME contribution is taken into account. Besides, we showed that this experiment is a powerful complement to other on-ground or satellite missions, such as LiteBIRD, since it can help significantly with the low-frequency foregrounds characterization.

Contents

1	Introduction	1
2	Observational Configuration	3
3	Sky Model	4
4	Component Separation	9
5	Residual Power Spectra Estimation	11
5.1	Residuals Model Estimation	11
5.2	Cosmological Parameters Fit	13
5.3	Example: Default Scenario	13
6	Experiment Performance	16
6.1	Instrumental Setup	17
6.2	Primordial B -modes	19
6.3	Foreground Model	20
6.4	Observational Strategies	20
6.5	Atmospheric/Systematics Contamination	21
7	Complementarity to LiteBIRD	22
8	Conclusions	23
A	On the Residuals Model Estimation	26

1 Introduction

For several decades the scientific community has devoted a tremendous effort towards the improvement in the Cosmic Microwave Background (CMB) polarization detection. The interest arises due to the large amount of cosmological information comprised in it, e.g., the predicted primordial B -modes. Primordial B -modes are only sourced by non-scalar perturbations, hence a detection would constitute a definitive proof of the existence of primordial gravitational waves (PGWs) [1–3]. Even though PGWs are conjectured by most of inflationary models, their predictions differ in the PGWs’ amplitude. Current constraints on the tensor-to-scalar perturbations ratio r are $\lesssim 0.056$ at 95 % CL [4], which reveal the faintness of this signal. Unfortunately, there is no theoretical lower bound for this quantity so there is no warranty of detection. However, even in a non-detection case, all these endeavors would not be futile as more sensitive instruments can place stronger constraints in the PGWs’ amplitude and debunk a considerable number of inflationary models [4, 5].

Currently, there are many planned ground-based experiments, e.g., CMB-S4 [6], Simons Observatory [7], BICEP array [8], as well as satellite missions, e.g., LiteBIRD [9], PICO [10], which include the primordial B -mode search among their top scientific goals. Their primary objective is to be able to detect, or at least constrain r with a sensitivity $\sigma_r(r=0) \leq 10^{-3}$.

This work constitutes a preliminary study of the performance of a potential on-ground experiment encompassed in this international B -mode chase. This experiment is proposed in the context of the European Low Frequency Survey initiative. Here, we have studied a ground-based instrument to perform a Low Frequency Survey (LFS) with the following characteristics: operation in the low-frequency range covering approximately 10-120 GHz, full-sky coverage, and finally, capability of placing stringent constraints on r .

The main problem that the search of these primordial modes faces is the signal's weakness. Moreover, this elusive signal hides among other B -mode sources with rather different origins such as: E -modes converted to B -modes due to gravitational lensing along the photons path, foreground contaminants like the synchrotron or the thermal dust emissions, instrumental noise, etc. Therefore, special data treatment methods are required to disentangle the primeval signal from the nuisance signals. Here, we have focused mainly on component separation methods which deal with the foreground and noise contamination [11]. To conduct the instrument's forecasts we have applied a full-parametric pixel-based maximum-likelihood component separation method. Furthermore, we have developed an approach to estimate a model of the foregrounds and noise residuals. A residuals model allow us to correct possible biases induced in cosmological parameters due to insufficient foreground removal [12], as well as to forecast which values of r are detectable.

We have applied the aforementioned method to study the instruments performance in different situations: i. the instrument's channels distribution and noise, to determine the most optimal setup that fulfills the σ_r constraint, ii. the r detectability considering different possible r values and degrees of delensing, i.e., fraction of E -to- B modes removed, iii. the effect of including a possible source of polarized anomalous microwave emission (AME), iv. the strengths and weaknesses of different observational strategies, e.g., full-sky vs. small sky patches observation in the same observational time and, v. the atmospheric/systematic noise impact on the recovery.

In addition, this instrument is proposed to be a potential complement to other experiments, both on-ground and satellite. It has been shown [13] that different frequency coverage can affect the level of foreground residuals. Since this experiment studies the low-frequency regime with sensitivities never achieved before, it can help with the characterization of foregrounds dominant in this range, e.g., the synchrotron, and AME. Here, the reconstruction of the foreground components is analyzed in the case of LiteBIRD alone, and LiteBIRD with this telescope.

This work is structured as follows: in section 2 we describe the observational characteristics of this instrument; in section 3 the different contributions to the sky simulations, i.e., the astrophysical signals as well as the instrumental noise, are described; section 4 outlines the component separation approach followed; we explain the residuals model estimation methodology conducted in this work in section 5; in section 6 we compare the telescope performance under different scenarios, i.e., different experimental setups, noise scaling, etc.; section 7 studies the improvement on LiteBIRD's foreground characterization when combined with this experiment; finally, we draw some conclusions in section 8.

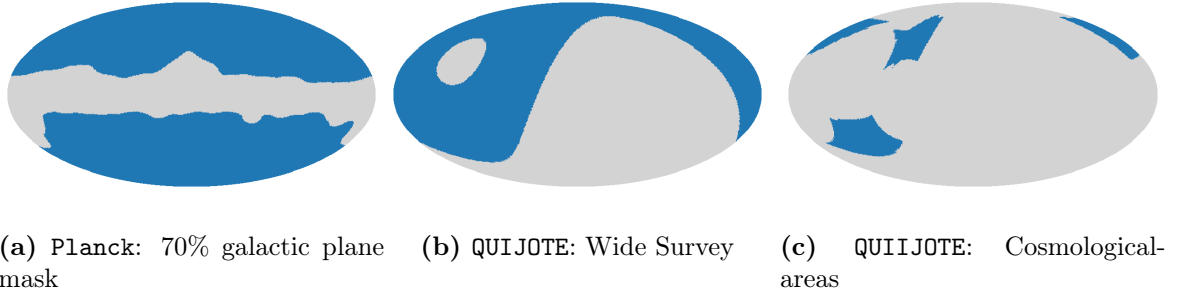


Figure 1: Sky observational masks.

2 Observational Configuration

In this section we highlight the basic observational characteristics of the propounded experiment, i.e., the instrument’s location, the sky coverage, and the frequency range covered.

Experiment location: This experiment is thought to be capable of measuring the whole sky. Therefore it requires at least two facilities, one located at the Northern Hemisphere (NH) and the other at the Southern Hemisphere (SH). A plausible choice for the NH location is Tenerife, in the Canary Islands, because there are precursor experiments successfully operating in the low-frequency regime like QUIJOTE [14]. On the other hand, Atacama is another realistic option for the SH since a handful of CMB experiments are already settled there, e.g., ACTPol [15], ABS [16], CLASS [17], POLARBEAR [18], the Simons Array [19], due to its sky quality.

Sky coverage: In this study we have applied three distinct observational masks in order to simulate different experiment locations and scanning strategies.

- In the case of two instruments located one at the NH and another at the SH, the full sky is available but we have applied a galactic disk mask to remove the foreground most contaminated areas. The mask is obtained from Planck Legacy Archive¹ [20].
- Another option is when the instrument is located only at NH, e.g., in Tenerife, hence, only a fraction of the sky is available. Thus, in this work we have considered the same observable sky as QUIJOTE [21]. Moreover, as in the previous situation we have applied a galactic mask to remove foreground dominated areas (same galactic area as in the previous Planck mask).
- Besides, instead of observing the whole accessible sky, one can observe small sky patches where the foregrounds are less dominant. An advantage of this strategy is the increase in the signal-to-noise ratio due to spending more time in a particular area within the same observational time. To study this option we have considered the QUIJOTE’s cosmological areas mask, i.e., sky patches where the foreground contamination is less harmful [21].

The observational masks described are shown in figure 1. In the NH case we apply a combined mask from figure 1a and figure 1b.

¹The $f_{sky} = 0.7$ (fraction of available sky) galactic mask from HFI_Mask_GalPlane-*apo0_2048_R2.00.fits* downloaded from <https://pla.esac.esa.int/#maps>

Frequency range: The LFS is designed to operate in the low-frequency regime, i.e., from 10 to 120 GHz, with its channels distributed among three frequency bands, where the atmospheric absorption is less significant. The bands are listed below:

- Low-frequency band (lb) from 10-20 GHz.
- Middle-frequency band (mb) from 26-46 GHz.
- High-frequency band (hb) from 75-120 GHz.

A telescope setup is defined by a 3-tuple $[n_{lb}, n_{mb}, n_{hb}]$ where n_b is the number of channels in the band b . The frequency channels within a band are distributed evenly as follows

$$\nu_{i,b} = \nu_{ini,b} + \frac{\Delta\nu_b}{2n_b}(2i - 1), \quad (2.1)$$

where $\nu_{i,b}$ is the i -th central frequency of the b band in a given experimental configuration, $\nu_{ini,b}$ is the lowest frequency within that band, and $\Delta\nu_b$ is the b band's bandwidth. For example, if the experimental setup is [5,5,5], the frequency channels centers are (11, 13, 15, 17, 19), (28, 32, 36, 40, 44), and (79.5, 88.5, 97.5, 106.5, 115.5) GHz in the lb, mb, and hb respectively.

3 Sky Model

Here, we describe the procedure adopted to generate the simulated maps used in the forecasts. Multi-frequency simulations are generated at a resolution of $n_{side} = 64$ (for observations of the whole available sky), and $n_{side} = 256$ (observations of small sky patches) using **HEALPix**². The frequencies selected depend on the telescope setup considered, and the effect of the detectors bandwidth is not taken into account, i.e., the channel's bandwidth is modeled as a δ -function.

Our sky simulations contain the following components: CMB, galactic foregrounds³, and other inevitable noise sources, such as instrumental or atmospheric/systematic noise.

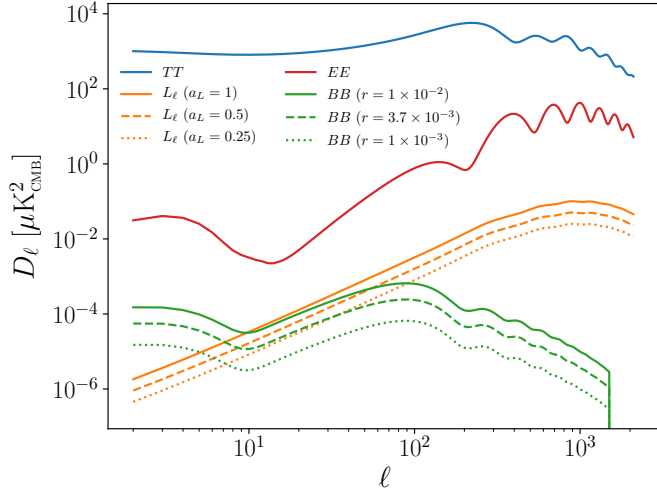
The Faraday Rotation effect at low frequencies is an interesting study by itself, but it is out of the scope of this work, and, therefore, we have not included this effect in our sky simulations. Let us remark that, given the frequency range considered in this work, one possibility would be to account its effect, as a first approximation, by relying on available models such as the one proposed in [23]. According to that model the sky signal in some pixels close to the border of the Planck galactic mask can be perturbed at the lowest frequency channels of the lb. However, this is left for future study.

CMB: CMB maps are drawn as Gaussian random realizations of theoretical power spectra. The power spectra are evaluated with the Boltzmann-solver **CAMB** [26] using the latest cosmological parameters from Planck [25]. Figure 2 shows the D_ℓ ⁴ of the primordial B -mode for different r values as well as the E -to- B lensing contamination modes, the EE and TT . With

²Hierarchical Equal Area isoLatitude Pixelization, <https://healpix.sourceforge.io/>, [22].

³Contamination due to point sources emission is neglected since its effect is not significant at the resolutions studied.

⁴ $D_\ell \equiv C_\ell \ell(\ell + 1)/(2\pi)$, where C_ℓ stands for the angular power spectrum.



$r \times 10^3$	a_L
0	1
0	0.5
3.7	1
3.7	0.5

Table 1: Cosmological values. Combinations of r and a_L values used for the CMB simulations. The value $r = 3.7 \times 10^{-3}$ is the expected Starobinsky [24] value according to the latest Planck results [25].

Figure 2: CMB spectra. TT , EE , BB and E -to- B lensing (L) contributions are displayed.

the lowest resolution, $n_{side} = 64$, multipoles as high as $\ell_{max} = 3n_{side} - 1 \sim 190$ are reached, hence both the re-ionization and recombination bumps could be observed.

In this work we have considered different scenarios with simulated CMB maps whose r and a_L (E -to- B lensing amplitude assuming a certain level of delensing) values, listed in table 1, differ. To allow meaningful comparisons among those scenarios, CMB maps were generated from template $a_{\ell m}$ realizations. The procedure followed to generate the simulated CMB maps is explained below.

1. Two sets of $a_{\ell m}$ were generated using the `synalm` routine of `healpy`, a python implementation of `HEALPix` [27]. One set $\{t_{\ell m}^{ul}, e_{\ell m}^{ul}, b_{\ell m}^{ul}\}$ is created from a collection of unlensed power spectra with $r = 1$, and another $\{t_{\ell m}^l, e_{\ell m}^l, b_{\ell m}^l\}$ from lensed power spectra with $r = 0$.
2. Then, CMB maps were generated using the `healpy` routine `alm2map` using the following set of $a_{\ell m}$

$$t_{\ell m} = t_{\ell m}^l, \quad e_{\ell m} = e_{\ell m}^l, \quad b_{\ell m} = \sqrt{r}b_{\ell m}^{ul} + \sqrt{a_L}b_{\ell m}^l. \quad (3.1)$$

These maps were smoothed with a FWHM = 1° or 15 arcmin for the $n_{side} = 64$, 256 resolutions respectively, and corrected with the appropriate pixel window function term. Note that the $t_{\ell m}$ and $e_{\ell m}$ terms do not have the contribution from the tensor fluctuations. However, since the tensor-to-scalar ratio is small, the possible errors that may arise from this mismatch are almost negligible.

Foregrounds: The polarized foreground contribution is composed primarily of synchrotron and thermal dust, as can be seen in figure 3. However, we have also included the AME in some realizations, as this contaminant might also emit in polarization [28]. The foreground contribution is simulated using parametric models since we want our model and sky simulations to be self-consistent. Below, we describe the procedure followed to create each foreground contribution. Only the Stokes parameters Q and U are considered since we are interested only in polarization.

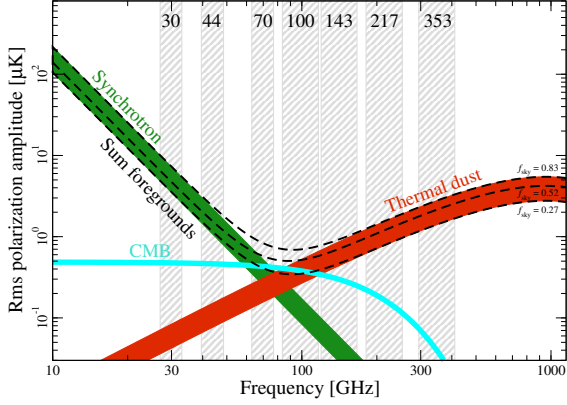


Figure 3: CMB and individual foreground contaminants signal as a function of frequency. Image courtesy of ESA and the Planck Collaboration [29].

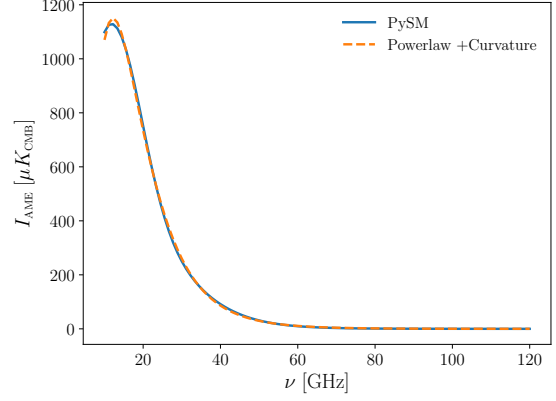


Figure 4: Comparison of the spectral behavior of the AME at a given sky direction, simulated with PySM (solid line), and fitted with a powerlaw with curvature model (dashed line) at the frequencies the LFS operates in.

- **Synchrotron.** This emission is originated from relativistic electrons spiralling around Galactic magnetic fields. Its spectral energy distribution (SED) can be modeled⁵ as a power-law [30]. Nevertheless, a model with a curved spectrum might be better suited since it can account for a steepening/flattening of the spectrum due to diverse effects such as: multiple synchrotron components along the line of sight, synchrotron self-absorption, cosmic ray's aging effect, etc. This extension of the model can be thought of as a natural SED's generalization following the approach of [31]. Thus, the model used is the following:

$$\begin{bmatrix} m_{\mathbf{n},s}^Q(\nu; \theta_{\mathbf{n},s}^Q) \\ m_{\mathbf{n},s}^U(\nu; \theta_{\mathbf{n},s}^U) \end{bmatrix} = \begin{bmatrix} a_{\mathbf{n},s}^Q \\ a_{\mathbf{n},s}^U \end{bmatrix} \left(\frac{\nu}{\nu_s} \right)^{\beta_{\mathbf{n},s} + c_{\mathbf{n},s} \log(\nu/\nu_s)}, \quad (3.2)$$

where \mathbf{n} is a unitary vector pointing in a given direction of the sphere, $m_{\mathbf{n},s}^X$ is the synchrotron signal in the X Stokes parameter ($X \in \{Q, U\}$) at the frequency ν given $\theta_{\mathbf{n},s}^X = \{a_{\mathbf{n},s}^X, \beta_{\mathbf{n},s}, c_{\mathbf{n},s}\}$ the set of the synchrotron's model parameters, where $a_{\mathbf{n},s}^X$ is the synchrotron's amplitude at $\nu_s = 23$ GHz, $\beta_{\mathbf{n},s}$ is the synchrotron's spectral index, and $c_{\mathbf{n},s}$ is the synchrotron's spectral curvature at ν_s .

The \mathbf{a}_s^X and β_s template maps at $n_{side} = 64$ and 256 were generated using the template maps of the Python Sky Model (PySM) [32]. The maps were degraded from $n_{side} = 512$ to 64 (256) through spherical harmonics, and smoothed with a beam of FWHM = 1° (15 arcmin), taking into account the pixel window function correction. Besides, latest studies of the galactic synchrotron contribution show that the spectral synchrotron dependence might have a non-negligible curvature ($c_s = 0.04 \pm 0.1$), [33]. Thus, we have

⁵The models provided here apply for antenna units. However, we have worked in thermodynamic units using the appropriate change of units where needed.

created a \mathbf{c}_s constant map whose value is 0.04⁶.

- **Thermal Dust.** General name to describe the thermal emission of microscopic matter left in the interstellar space. Dust grains, which are composed mainly of carbonaceous and silicate grains, are heated up by the interstellar radiation field yielding an emission at the microwave range. The dust component SED is well-approximated by a modified black-body [34]. However, at the frequencies under study, only the Rayleigh-Jeans part of the dust spectrum is detected, hence a power-law model is also suitable in this particular case:

$$\begin{bmatrix} m_{\mathbf{n},d}^Q(\nu; \theta_{\mathbf{n},d}^Q) \\ m_{\mathbf{n},d}^U(\nu; \theta_{\mathbf{n},d}^U) \end{bmatrix} = \begin{bmatrix} a_{\mathbf{n},d}^Q \\ a_{\mathbf{n},d}^U \end{bmatrix} \left(\frac{\nu}{\nu_d} \right)^{\beta_{\mathbf{n},d}}, \quad (3.3)$$

where $m_{\mathbf{n},d}^X$ is the dust signal of the Stokes parameter X at the frequency ν given $\theta_{\mathbf{n},d}^X = \{a_{\mathbf{n},d}^X, \beta_{\mathbf{n},d}\}$ the set of the dust's model parameters, where $a_{\mathbf{n},d}^X$ is the dust's amplitude at $\nu_d = 120$ GHz, and $\beta_{\mathbf{n},d}$ is the dust's spectral index.

The \mathbf{a}_d^X and β_d template maps at $n_{side} = 64$ and 256 were created in an analogous manner to the synchrotron's equivalent parameters.

- **AME.** It is a Galactic emission that cannot be explained with known foreground models. Spinning dust grains have been proposed as a mechanism for this emission since it is spatially correlated with dust [35, 36]. Although AME might not be polarized [28], we have studied some cases where AME contributes to the polarized sky with a 1% relative amplitude compared to the AME intensity. We have seen that the AME contribution is well-modelled by a power-law with curvature at the frequencies of operation, see figure 4. Therefore the model used is:

$$\begin{bmatrix} m_{\mathbf{n},a}^Q(\nu; \theta_{\mathbf{n},a}^Q) \\ m_{\mathbf{n},a}^U(\nu; \theta_{\mathbf{n},a}^U) \end{bmatrix} = \begin{bmatrix} a_{\mathbf{n},a}^Q \\ a_{\mathbf{n},a}^U \end{bmatrix} \left(\frac{\nu}{\nu_a} \right)^{\beta_{\mathbf{n},a} + c_{\mathbf{n},a} \log(\nu/\nu_a)}, \quad (3.4)$$

where $m_{\mathbf{n},a}^X$ is the AME signal of the Stokes parameter X at the frequency ν given $\theta_{\mathbf{n},a}^X = \{a_{\mathbf{n},a}^X, \beta_{\mathbf{n},a}, c_{\mathbf{n},a}\}$ the set of the AME's model parameters, where $a_{\mathbf{n},a}^X$ is the AME's amplitude at $\nu_a = 23$ GHz, $\beta_{\mathbf{n},a}$ the AME's spectral index, and $c_{\mathbf{n},a}$ is the AME's spectral curvature at ν_a .

We obtained maps of the AME's temperature parameters ($\mathbf{a}_a^I, \beta_a^I, \mathbf{c}_a^I$) at $n_{side} = 512$ by fitting the PySM default AME's I map to a powerlaw with curvature model. To construct the amplitudes maps in Q and U we have used the dust polarization angles γ_d map, since AME has been shown to be spatially correlated with dust. The amplitudes are then:

$$\mathbf{a}_a^Q = \eta \mathbf{a}_a^I \cos(2\gamma_d), \quad \mathbf{a}_a^U = \eta \mathbf{a}_a^I \sin(2\gamma_d), \quad (3.5)$$

where $\eta = 0.01$ is the considered AME's ratio of polarization to intensity. β_a and \mathbf{c}_a are the same both in intensity and polarization. Similar to the synchrotron and dust parameters case, the maps were degraded from $n_{side} = 512$ to 64 (256) through spherical

⁶Note that this assumption of a constant value for \mathbf{c}_s does not facilitate its estimation since the method works at the pixel level and spatial correlations are not taken into account.

harmonics, and smoothed with a beam of $\text{FWHM} = 1^\circ$ (15 arcmin), taking into account the pixel window function correction.

Note that we have assumed equal spectral parameters for polarization Q and U Stokes parameters.

Noise: We have included two different types of noise in our simulations: one that consists only of white noise, and another composed of white noise and a correlated noise that resembles the atmospheric and/or systematics contamination.

- **White noise.** The instrument's sensitivity is modeled as a white noise whose standard deviation follows a specific spectral law. The chosen law behaves as the sum of the main foregrounds contaminants in polarization:

$$s(\nu) = k_s \left(\frac{\nu}{100 \text{ GHz}} \right)^{-3} + k_d \left(\frac{\nu}{100 \text{ GHz}} \right)^{1.59}, \quad (3.6)$$

where we have applied the following constraints to fix k_s and k_d :

1. The sensitivity equals $1 \mu\text{K arcmin}$ at 100 GHz.
2. The dust-like and synchrotron-like contributions to the sensitivity are equal at 70 GHz.

The spectral law is represented in figure 5. With this noise behavior, the larger the number of channels the better the effective telescope sensitivity \bar{s} , which is defined as:

$$\bar{s}_{\mathcal{S}} = \left(\sum_{\nu \in \mathcal{S}} \frac{1}{s(\nu)^2} \right)^{-1/2}, \quad (3.7)$$

where \mathcal{S} is the set of frequencies in a given setup or band. The default instrument setup [10,10,15] is the largest setup, hence the rest of setups yield always worse results. In order to perform fair comparisons among setups, we have also studied the case where the sensitivity per frequency channel is scaled in the smaller setup to match the default's effective sensitivity. The scaling is conducted by applying the same correction factor ξ to each channels' sensitivity within a band b . After applying ξ , the smaller setup's effective sensitivity in the b band equals the default's effective sensitivity in the same band, hence

$$\xi_b = \sqrt{\frac{\bar{s}_b^{def}}{\bar{s}_b}}, \quad (3.8)$$

where \bar{s}_b^{def} and \bar{s}_b are the effective sensitivities of the default and smaller setup respectively.

- **White + Correlated noise.** In this case, a $1/f$ noise is added to the previously described white noise. This $1/f$ noise is included to mimic the correlated noise induced by the atmosphere as well as instrument's systematics. This contribution is obtained as a Gaussian random realization of the following power spectrum:

$$N_\ell = n_{corr} \left(\frac{\ell}{\ell_{\text{knee}}} \right)^\gamma \quad (3.9)$$

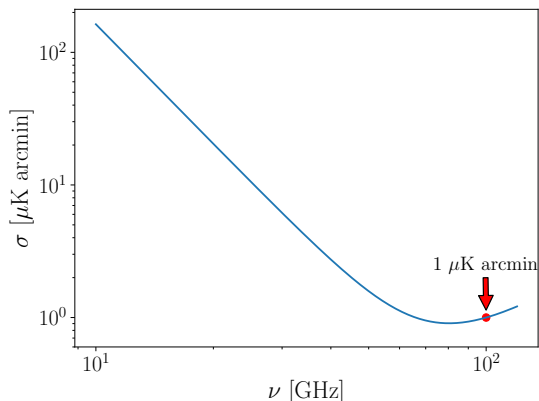


Figure 5: Spectral instrument's sensitivity.

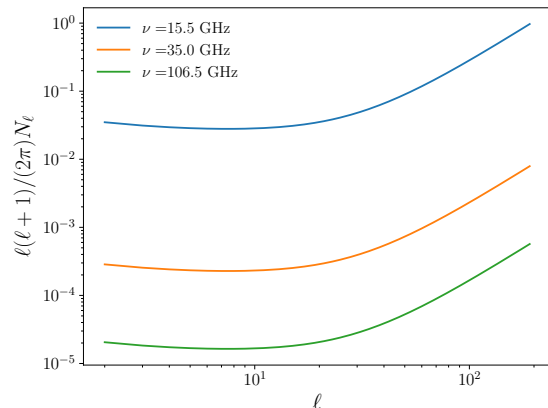


Figure 6: Total noise power spectra at different frequencies.

where n_{corr} is the variance per steradian at a given frequency channel, $\ell_{knee} = 30$ is the multipole until which the correlated noise is significantly larger than the white noise contribution, and $\gamma = -2.2, -2.4, -2.6$ if the frequency channel belongs to the lb, mb or hb respectively. The power spectrum parameters selected are similar to the values considered in [37]. The power spectrum of (3.9), along with the white noise contribution, is depicted in figure 6.

4 Component Separation

Our component separation approach grounds on a full-parametric pixel-based maximum likelihood method, which relies on an affine-invariant ensemble sampler for Markov Chain Monte Carlo (MCMC) [38], to retrieve the polarized CMB, as well as the foregrounds' parameters.

Parametric methods might be more advantageous than non-parametric methods since they provide a physical characterization of both the CMB and the foregrounds. On the other hand, incorrect modeling can lead to severe bias in the measurements in the most extreme cases [39–41]. Nevertheless, there are extensions to these parametric models that can cope with this setback [31]. As previously mentioned, our model and sky simulations are self-consistent, i.e., the simulations are generated from the models, hence our results are optimal.

Our method is more robust than other models [41, 42] since the pixel-based approach employed allows spatial variation of the spectral parameters. The method here is the limiting case considered in [12] of spatial variability in every single pixel. However, this robustness goes at expense of an increase in the statistical uncertainty of the parameters as less information is provided into the fit [43].

Hereunder, we outline the application and the fundamentals behind the bayesian inference method employed in this study.

Best-fit Parameter Estimates. To obtain sky maps of the most-likely model parameters we used a python implementation `emcee` [38] of an affine-invariant ensemble sampler for

MCMC [44]. MCMC methods are algorithms able to sample from a probability distribution, and hence provide an estimation of it. Therefore, we apply this algorithm to draw samples from the global posterior probability and obtain the best-fit parameters' map as the mean of each marginalized parameter posterior probability. The global posterior probability is given by:

$$\mathcal{P}(\theta_{\mathbf{n}}|\mathbf{d}_{\mathbf{n}}) \propto \mathcal{P}(\mathbf{d}_{\mathbf{n}}|\theta_{\mathbf{n}})\mathcal{P}(\theta_{\mathbf{n}}), \quad (4.1)$$

where $\theta_{\mathbf{n}}$ is a set whose elements are the Q and U model parameters in a given sky direction \mathbf{n} , $\mathbf{d}_{\mathbf{n}} = (\mathbf{d}_{\mathbf{n}}^Q, \mathbf{d}_{\mathbf{n}}^U)$ is a $2n_{\nu}$ vector where $\mathbf{d}_{\mathbf{n}}^X$ is a n_{ν} vector containing the sky signal X in the experimental setup's n_{ν} frequency channels, $\mathcal{L}(\theta_{\mathbf{n}}|\mathbf{d}_{\mathbf{n}}) \equiv \mathcal{P}(\mathbf{d}_{\mathbf{n}}|\theta_{\mathbf{n}})$ is the likelihood function, and $\mathcal{P}(\theta_{\mathbf{n}})$ is the prior information known about the parameters. In our approach, Q and U data are jointly fit since they share the spectral model parameters, hence the parameters' statistical uncertainties are reduced. Assuming Gaussian noise, the likelihood of the data can be expressed as

$$\mathcal{L}(\theta_{\mathbf{n}}|\mathbf{d}_{\mathbf{n}}) = \frac{1}{\sqrt{(2\pi)^{2n_{\nu}} \det(\mathbf{C})}} \exp\left(-\frac{1}{2}(\mathbf{d}_{\mathbf{n}} - \mathbf{m}(\nu; \theta_{\mathbf{n}}))^T \mathbf{C}^{-1}(\mathbf{d}_{\mathbf{n}} - \mathbf{m}(\nu; \theta_{\mathbf{n}}))\right), \quad (4.2)$$

where $\mathbf{C} = \text{diag}(\mathbf{C}^Q, \mathbf{C}^U)$ being \mathbf{C}^X the covariance matrix of the telescope's frequency channels for the Stokes parameter X ⁷⁸, and $\mathbf{m} = (\mathbf{m}^Q, \mathbf{m}^U)$ a $2n_{\nu}$ vector containing the model signal, and:

$$\mathbf{m}^X(\nu; \theta_{\mathbf{n}}^X) = c_{\mathbf{n}}^X + \sum_{f \in F} \mathbf{m}_{\mathbf{n},f}^X(\nu; \theta_{\mathbf{n},f}^X), \quad (4.3)$$

where $c_{\mathbf{n}}^X$ is the CMB X -contribution in the direction \mathbf{n} , F is the set of foregrounds included in a given model, e.g, $F = \{s, d\}$ in a model with only synchrotron and thermal dust, and $\mathbf{m}_{\mathbf{n},f}^X(\theta_{\mathbf{n},f}^X)$ is a vector whose elements are the f foreground model contribution at a given frequency obtained by evaluating the f foreground parametric model (3.2)-(3.4), using the set of model parameters $\theta_{\mathbf{n},f}^X$.

In the case of white noise, \mathbf{C}^X is a diagonal matrix whose elements are the squared telescope channels' sensitivities. With regard to the white + correlated noise case, \mathbf{C}^X is also a diagonal matrix but its elements are the sum of the squared telescope's sensitivities and the effective correlated noise variance s_{corr}^2 :

$$s_{corr}^2 = \frac{1}{4\pi} \sum_{\ell=2}^{\ell_{max}} (2\ell + 1) N_{\ell}, \quad (4.4)$$

where $\ell_{max} = 3n_{side} - 1$.

Priors are required in Bayesian inference and have been proven to help with convergence and computational time reduction. In this analysis we have used Gaussian priors:

Gaussian priors. We have applied Gaussian priors to the spectral parameters. Gaussian priors are given by:

$$\mathcal{P}(\theta_{\mathbf{n}}) = \exp\left(-\frac{1}{2} \frac{(\theta_{\mathbf{n}} - \mu_{\theta})^2}{\sigma_{\theta}^2}\right) \quad (4.5)$$

⁷In this work we have assumed $\mathbf{C}^Q = \mathbf{C}^U$.

⁸Notice that \mathbf{C}^X shows the correlation among frequency channels, not among pixels.

	β_s	β_d	β_a	c_s	c_a
μ_θ	-3.00	1.54	-2.5	0.04	-2.0
$3\sigma_\theta$	0.18	0.12	2.1	0.10	0.9

Table 2: Gaussian prior information. Displayed are the mean and the dispersion values of the spectral parameters employed in the Gaussian priors. μ_θ and σ_θ are the mean and the 3- σ value of θ template map respectively.

where θ is a given model parameter, and, μ_θ and σ_θ^2 are the mean and variance of the parameter θ . The means and standard deviations used are listed in table 2. Notice that we have used the spectral parameters template maps 3- σ values as σ_θ to loosen the priors.

5 Residual Power Spectra Estimation

In this study, we have developed a self-consistent approach to obtain an estimate of the combined foreground and instrumental model residuals power spectrum. Having a residuals model allow us to prevent possible biases in the fit due to an insufficient foreground removal, or to determine the range of detectable r values, given a specific experimental setup. Another advantage of this methodology is that it can be applied to real data. In this section, we describe the methodology followed to calculate the residuals model (section 5.1), explain the approach used to estimate the cosmological parameters (section 5.2), and show an example for the default scenario (section 5.3). A scenario is fixed when the following characteristics are set: i. the experimental setup, i.e., the 3-tuple $[n_{lb}, n_{mb}, n_{hb}]$; ii. the cosmological parameters that define the B -mode power spectrum (r, a_L); iii. the foreground model, i.e., the specific foregrounds that are included; iv. the noise type; and v. the maps' resolution, i.e., n_{side} . The scenarios characteristics are listed in table 3.

5.1 Residuals Model Estimation

We have tried several methodologies that rely on the sampling from the posterior to estimate the residuals model, but the estimates were not precise enough (see Appendix A for more details). The most accurate procedure to obtain the residuals model estimate is based on simulations derived using the best-fits of model parameters, and is as follows:

Let the data polarization signal be defined as $\mathbf{S} = (\mathbf{S}^Q, \mathbf{S}^U)$, where $\mathbf{S}^X = (\mathbf{s}_{\nu_1}^X \dots \mathbf{s}_{\nu_\nu}^X)$ is a $(n_{pix} \times n_\nu)$ matrix whose columns are the X -signal maps $\mathbf{s}_{\nu_j}^X$ at the frequency ν_j , being n_{pix} the number of map pixels. Let \mathbf{d}_p be a \mathbf{S} row, i.e., $\mathbf{d}_\mathbf{n}$ with \mathbf{n} pointing in the direction of the pixel p .

1. For each pixel p , the best-fit set of model parameters θ_p^{dat} is obtained by applying the Bayesian method explained in section 4 to \mathbf{d}_p . Eventually, we obtain Θ^{dat} a $(n_{pix} \times n_{par})$ matrix whose rows are the θ_p^{dat} and, its columns are the model parameters' maps. n_{par} is the number of model parameters.
2. Then, n_{sim} signal matrices $\{\mathbf{S}_j\}_{j \in \{1, \dots, n_{sim}\}}$ are generated using

$$\mathbf{d}_{p,j}^X(\nu) = c_{p,j}^X + \sum_{f \in F} \mathbf{m}_{p,f}^X(\nu; \theta_{p,f}^{X,dat}) + \mathbf{n}_{p,j}^X(\nu), \quad (5.1)$$

Scenario	setup	$r \times 10^3$	a_L	F	noise	n_{side}	sky
default	[10,10,15]	0	1	s,d	W	64	P70
558	[5,5,8]	0	1	s,d	W	64	P70
558-scaled	[5,5,8]	0	1	s,d	WS	64	P70
666	[6,6,6]	0	1	s,d	W	64	P70
666-scaled	[6,6,6]	0	1	s,d	WS	64	P70
default-delensed	[10,10,15]	0	0.5	s,d	W	64	P70
starobinsky	[10,10,15]	3.7	1	s,d	W	64	P70
starobinsky-delensed	[10,10,15]	3.7	0.5	s,d	W	64	P70
AME	[10,10,15]	0	1	s,d,a	W	64	P70
NH	[10,10,15]	0	1	s,d	W	64	Q(WS)
cosmoareas	[10,10,15]	0	1	s,d	$W(f_{sky})$	256	Q(CA)
correlated-noise	[10,10,15]	0	1	s,d	W+Corr	64	P70
LB	LB	0	1	s,d	W	64	P70
LB/LFS	LB+[10,10,0]	0	1	s,d	W	64	P70
LB-AME	LB	0	1	s,d,a	W	64	P70
LB/LFS-AME	LB+[10,10,0]	0	1	s,d,a	W	64	P70

Table 3: Scenarios. The different studied scenarios’ characteristics. The setup 3-tuple are the number of channels in each frequency band in the LFS, while LB stands for LiteBIRD’s frequency channels; r and a_L are the input tensor-to-scalar ratio and lensing amplitude; F is the set of foregrounds included in the sky signal simulation, where s , d , and a stands for synchrotron, thermal dust, and AME respectively; the noise included in the simulations are white noise (W), scaled white noise (WS), white plus correlated noise (W+Corr) and, white noise with a scaling factor to account for the longer observational time spent when only small patches of the sky are measured ($W(f_{sky})$); n_{side} is the resolution of the simulated signal maps; and finally sky specifies the observable sky studied in each scenario, P70, Q(WS) and Q(CA) are the sky left after applying the **Planck**, QUIJOTE wide survey combined with **Planck**, and QUIJOTE cosmological areas mask respectively.

where $c_{p,j}^X$ is the pixel p value of the j -th simulated CMB map \mathbf{c}_j^X , generated as a Gaussian random realization of a particular set of power spectra, the second term of the right-hand-side of (5.1) is a vector containing the foregrounds contribution obtained by evaluating the f foreground parametric model using the estimated $\theta_{p,f}^{X,dat}$ as model parameters, and $\mathbf{n}_{p,j}^X$ is the j -th noise vector obtained as a random realization of the noise model.

3. Step 1. is repeated for each \mathbf{S}_j to retrieve Θ_j^{sim} .
4. Next, the CMB X Stokes parameter residual maps are calculated for each j simulation as

$$\mathbf{c}_j^{X,res} = \mathbf{c}_j^X - \mathbf{c}_j^{X,sim}, \quad (5.2)$$

while the foreground residuals maps at a given frequency ν is given by

$$\mathbf{m}_{f,j}^{X,res} = \mathbf{m}_{f,j}^X(\nu; \theta_f^{X,dat}) - \mathbf{m}_{f,j}^X(\nu; \theta_{f,j}^{X,sim}). \quad (5.3)$$

5. Finally, for each j residual map, the power spectra is obtained using a pseudo- C_ℓ algorithm [45, 46]. Pseudo- C_ℓ algorithms are a technique to solve the E -to- B leakage due

to the scale spherical harmonics mixing in partial-sky maps⁹. Even though this method does not retrieve the minimum variance [47], it is the most broadly used approach since it is not computationally expensive. Moreover, there are techniques to reduce the B variance due to the overpowering E -to- B mode leakage, like the “pure” pseudo- C_ℓ mechanism [48]. This mechanism requires the mask to satisfy both the Neumann and Dirichlet conditions [49]. The latter is achieved by apodizing the mask, i.e., artificially making the mask’s edges less abrupt. In this work we have employed a “pure” pseudo- C_ℓ algorithm using the python implementation of the public software package **NaMaster** [49]. The residual model power spectrum estimate R_ℓ is calculated as the mean of the n_{sim} residuals power spectra.

5.2 Cosmological Parameters Fit

The cosmological parameters can be estimated by fitting the power spectrum of the cleaned map \mathbf{c}^{dat} to the theoretical primordial and lensing CMB power spectra as well as the residuals model power spectrum. In this work we are interested mainly in r , hence we only conduct the analysis on the BB power spectrum. Since only partial-sky maps are studied, the large scale multipoles cannot be accessed. Thus, in the limit of high enough multipoles, the likelihood of the cosmological parameters can be approximated to a Gaussian:

$$-\log \mathcal{L}(r, a_L, a_R) \propto \sum_{\ell} \frac{\left(C_\ell^{dat} - r B_\ell^{GW}(r=1) - a_L L_\ell - a_R R_\ell \right)^2}{\sigma_\ell^2}, \quad (5.4)$$

where C_ℓ^{dat} is the B -mode power spectrum of the best-fit CMB map, B_ℓ^{GW} is the B -mode primordial power spectrum at $r=1$, L_ℓ is the lensing contribution to the BB power spectrum, R_ℓ is the residuals model BB power spectrum, and σ_ℓ is the cosmic variance:

$$\sigma_\ell = \sqrt{\frac{C_\ell^2}{f_{sky}(\ell + \frac{1}{2})}} = \frac{r B_\ell^{GW}(r=1) + a_L L_\ell + a_R R_\ell}{f_{sky}^{1/2}(\ell + \frac{1}{2})^{1/2}}. \quad (5.5)$$

In order to maintain the same statistical properties as well as the binning (required to perform the Pseudo- C_ℓ algorithm), we have generated B_ℓ^{GW} and L_ℓ models as the mean of the mask corrected power spectra of 100 realizations of the theoretical B_ℓ^{GW} and L_ℓ respectively.

By minimizing (5.4) the best-fit r , a_L and, a_R parameters can be derived analytically, and their uncertainties can be evaluated from the Fisher matrix. It is worth noting that with this approach we marginalize over a_R and a_L which leads to more conservative results than fixing those parameters to unity.

5.3 Example: Default Scenario

In this section, the default scenario’s results are shown to: i. validate the method’s self-consistency, i.e., assess whether the residuals model obtained reproduces the true residuals, and ii. present some of the method’s results. In this analysis we have applied only a galactic disk mask, i.e., the Planck’s mask fig. 1a.

⁹Note that in this work, only partial sky maps are studied since we always apply a galactic mask.

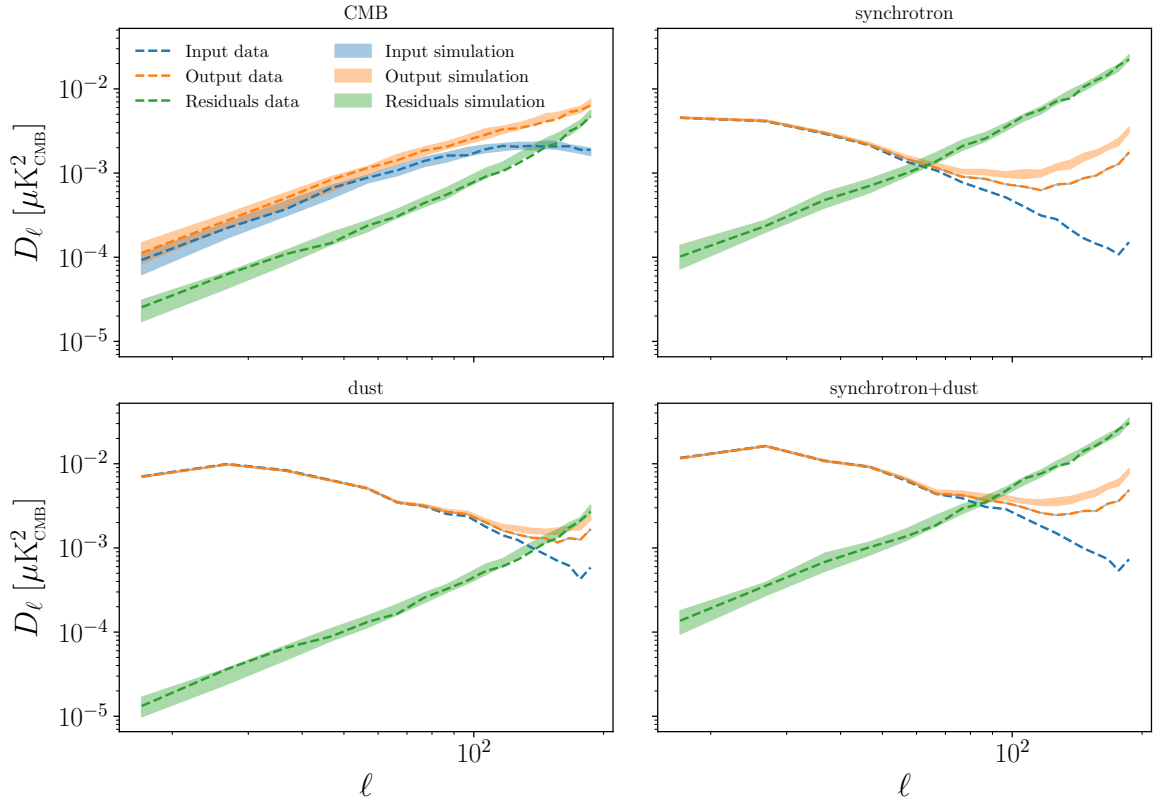


Figure 7: Power spectrum of the input, output, and residuals best-fit data versus simulation of different sky components. The simulation power spectra are represented as colored shaded areas, while the data are depicted with colored dashed lines. The foregrounds power spectra are evaluated at $\nu = 76.5$ GHz.

Self-consistency: To test the validity of our method we have compared the power spectra of the true residuals with the residuals obtained by simulations¹⁰. This is performed in figure 7 where the input, output, and residuals power spectra of both the data and the simulations are depicted together. Let us analyze the CMB and the foregrounds separately.

- **CMB.** We observe in figure 7 that the data and simulations input are very similar which is expected as they are generated in a similar fashion. In the case of real data, the true cosmological values are not known, but one can use $r = 0$ since the residuals left are substantially larger than the primordial signal. However, in this particular case we have used the same r for both the simulations and the data. Furthermore, we observe that the simulations output, and consequently, the residuals agree with the data output and residuals. Thus, we are confident that with this method coherent results can be obtained.
- **Foregrounds.** The input simulated foreground parameters are the best-fit parameters of the data. This is the reason why the input simulated power spectra overlap with the

¹⁰Notice that we have generated only one noise realization for each scenario (an equivalent situation to a real data analysis case), while each of the $n_{sim} = 50$ simulations performed for each scenario has its own unique noise realization.

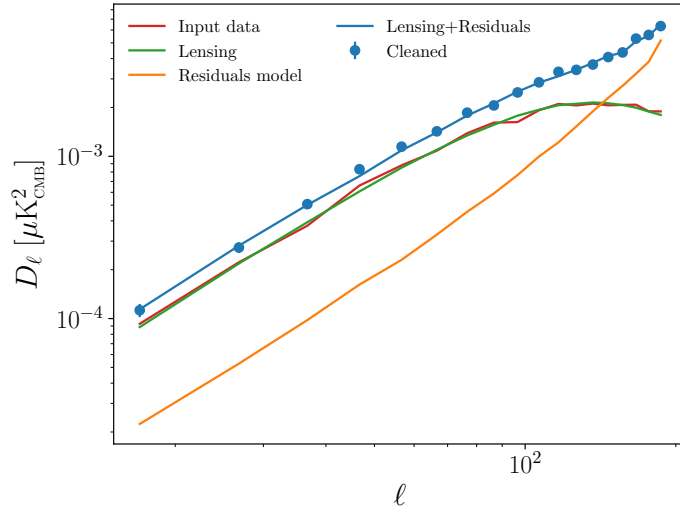


Figure 8: CMB B -mode power spectra contributions in the default case. Note that the primordial B -mode is not shown since $r = 0$ in the default scenario.

data output power spectrum. On the other hand, we observe in figure 7 that there is a slight increase in the simulated output power spectra at small scales. The data estimated foreground parameters already have an uncertainty since they are retrieved from noisy data. These foregrounds parameters are used to create new noisy sky simulations, hence the simulated output foreground parameters will have a larger uncertainty compared to the data foreground parameters. Regardless of this difference, the simulation residuals resembles the true residuals. Therefore, the mean simulation residuals is a suitable approximation of the true residuals.

Results: Once the default scenario residuals model R_ℓ is obtained we fit the BB power spectrum of the cleaned CMB map as described in section 5.2. In figure 8 we show the BB power spectra of the different components after correcting for the mask leakage. It is clear from figure 8 that, for this experimental configuration, the CMB lensing is the main source of uncertainty except at small scales, where the foreground residuals become dominant. Thus, if r is sufficiently small delensing would be mandatory in order to make a detection. This statement is limited to the assumptions made in this study, for instance, if the sky is more complex than current modelling, the foreground residuals could become the dominant source of error.

The Gaussian distributions and covariances among the parameters obtained from the fit are shown in figure 9, and the numerical results in table 4. r , a_L and a_R values are compatible with their true value and $\sigma_r \lesssim 10^{-3}$ which is the target value of most experiments. From the covariance matrices it is clear that each parameter is correlated with the rest. Therefore a bias on the r value could yield a mismatch between a_L and a_R from unity. If the residuals and lensing model are appropriate, a_L and a_R departures from the true value can be used to detect biases on the recovered r .

Moreover, given the residuals model an estimation of the r uncertainty can be obtained

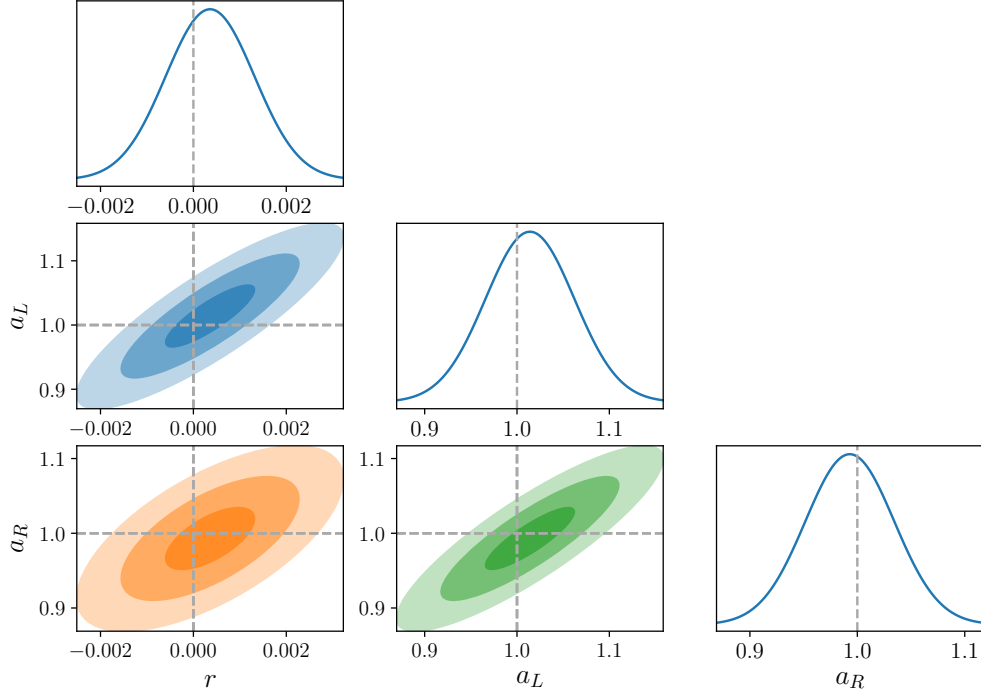


Figure 9: Marginalized Gaussian one and two dimensional projections of the posterior distribution of the fit parameters.

using the following equation:

$$\sigma_r = \left(\sum_{\ell} \frac{B_{\ell}^{GW^2}(r=1)}{\sigma_{\ell}^2} \right)^{-1/2}, \quad (5.6)$$

which is derived as the marginal uncertainty of the parameter r of the covariance matrix, calculated from the Fisher matrix. σ_r depends on the value of r , a_L and a_R through σ_{ℓ} . In figure 10 σ_r is depicted as a function of r and a_L having a_R fixed to unity.

From figure 10 we infer that within this scenario values of $r \lesssim 10^{-3}$ are not detectable, i.e., signal to noise ratio larger than 3σ , without performing any form of delensing.

6 Experiment Performance

In this section the LFS performance is analyzed in a handful of different scenarios where the following characteristics are tested: the experimental setup (section 6.1); different cosmologies (section 6.2); the inclusion of AME (section 6.3); different observation strategies (section 6.4); and the atmospheric/systematics contamination (section 6.5).

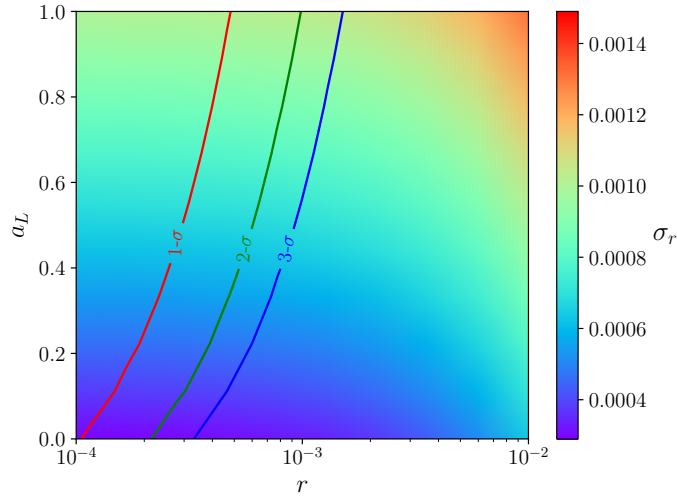


Figure 10: Density plot of σ_r as a function of r and a_L , for fixed $a_R = 1$ with the default’s residuals model. The 1,2,3- σ signal-to-noise contours are also represented.

Scenario	$\sigma_r \times 10^3$	a_L	σ_{a_L}	a_R	σ_{a_R}
default	1.0	1.01	0.05	0.99	0.04
558	1.2	1.02	0.06	0.98	0.03
558-scaled	1.0	0.91	0.05	1.07	0.04
666	1.2	0.92	0.07	1.04	0.03
666-scaled	1.0	0.96	0.05	1.04	0.05
default-delensed	0.7	0.53	0.04	0.94	0.04
starobinsky	1.1	0.92	0.05	1.06	0.05
starobinsky-delensed	0.8	0.50	0.04	0.99	0.04
AME	1.1	1.00	0.06	1.00	0.04
NH	1.5	0.99	0.08	1.01	0.07
cosmoareas	1.4	1.00	0.03	1.00	0.01
correlated-noise	1.0	0.99	0.05	1.02	0.04

Table 4: Fit Results. The tensor-to-scalar ratio uncertainty σ_r , as well as the a_L and a_R values and uncertainties obtained from the power spectrum fit for each scenario studied.

6.1 Instrumental Setup

Here, we have compared the instruments performance for three different telescope setups ([10,10,15], [5,5,8] and [6,6,6]) with both, their respective and scaled noise. The results from each setup are shown in table 4.

With regard to the r uncertainty, we observe a slight decrease when the noise is scaled. This is a result of the lensing being the principal error source as it is shown in figure 11. As a consequence, there is only an improvement at small scales, where the residuals are larger than the lensing.

In figure 11, the residuals model for each configuration is represented. When the noise is

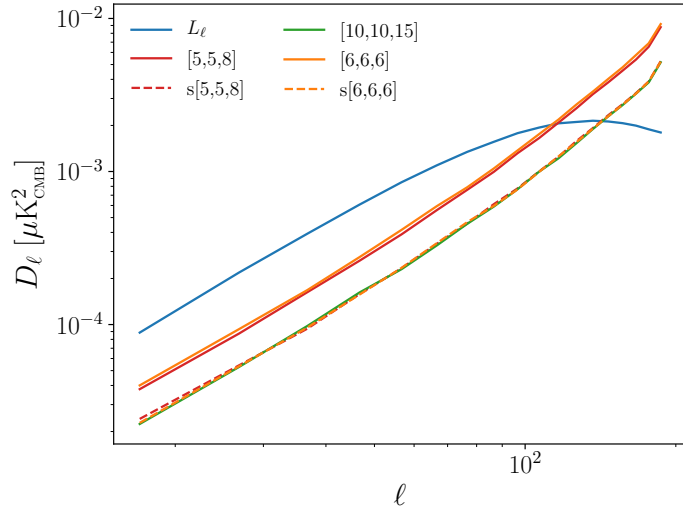


Figure 11: Residuals model power spectra for different telescope setups. The dashed (solid) lines correspond to a scenario where the instrument noise is (not) scaled.

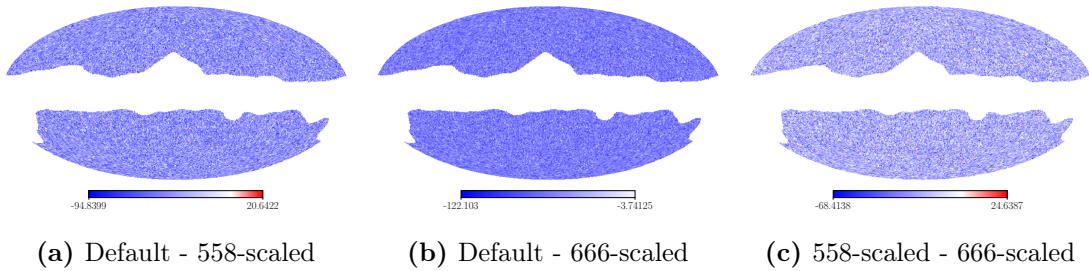


Figure 12: Difference BIC maps.

scaled the amount of residuals left is the same for all setups. In order to study if the distribution of frequency channels matters when the noise is scaled, we have applied a model selection prior independent criterion that takes into account the number of data points, the Bayesian Information Criteria (BIC) [50]:

$$\text{BIC} = -2 \log \mathcal{L} + p \log n_\nu, \quad (6.1)$$

where p is the number of model parameters. The smaller the BIC score, the better the fit. In figure 12 the difference BIC maps pair combination of the default, 558-scaled and, 666-scaled are displayed. It is clear that the default setup provides a superior fit than both the 558-scaled and, the 666-scaled. We infer that, given this instrumental noise, the best results are obtained when the number of channels is the largest, i.e., it is better to have more noisier signal channels than fewer more precise channels.

Moreover, the setup 558-scaled yields better results compared to the 666-scaled. To understand these results we have performed a simple study of the dependence of the CMB uncertainty estimation on the distribution of frequency channels among the available bands, given a fixed total number of channels. The CMB uncertainty is estimated using the Fisher

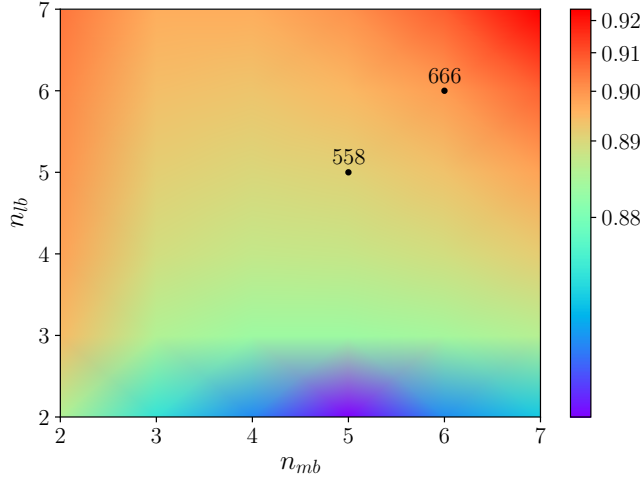


Figure 13: Fisher CMB uncertainty estimation for a typical pixel (Q Stokes parameter) as a function of the n_{lb} and n_{mb} . Results are normalized with respect to the maximum value. The number of channels at the hb is $n_{hb} = 18 - n_{lb} - n_{mb}$.

matrix obtained from (4.2). As an illustration, in figure 13 the CMB uncertainty for a typical pixel is shown as a function of n_{lb} and n_{mb} in a telescope with n_ν fixed to 18 channels and the instrumental noise scaled. We have verified that the behavior observed in the figure is independent of the particular pixel under study and, also the same for both Q and U Stokes parameters. From figure 13 it is inferred that the uncertainty on the CMB parameter is smaller in the 558-scaled scenario than in the 666-scaled, which can explain the results from figure 12c. Besides, according to this Fisher analysis, the best channel distribution with a fixed total number of channels is a distribution with a few channels at the lb , an optimal value at the mb (which in the particular case of $n_\nu = 18$ is five) and, most channels at the hb . The worst is obtained when the n_{hb} is the lowest. Thus, information from the hb is crucial in this analysis, since those are where the CMB and dust information is comprised.

6.2 Primordial B -modes

As previously mentioned, the success of an experiment relies on its ability to constrain r , since it has no lower limit. However, some of the preferred theoretical models predict r values that will be either detected or rejected with the target uncertainty ($\sigma_r \simeq 10^{-3}$). In this section we have studied if r is detectable considering the Starobinsky model. Moreover, we have studied the effect of applying a delensing of 50%, by simulating CMB maps with half the lensing power for $r = 0$ and $r = 3.7 \times 10^{-3}$ (Starobinsky's). The results for each scenario are shown in table 4.

First, we observe that within the Starobinsky scenario, r is detectable with more than 3σ even when no delensing is performed as was forecasted in figure 10. Moreover, when the default and Starobinsky scenarios are compared with their delensed version, we now observe a reduction of the uncertainty. This implies that in order to obtain a stringent constraint on r some sort of delensing will be required.

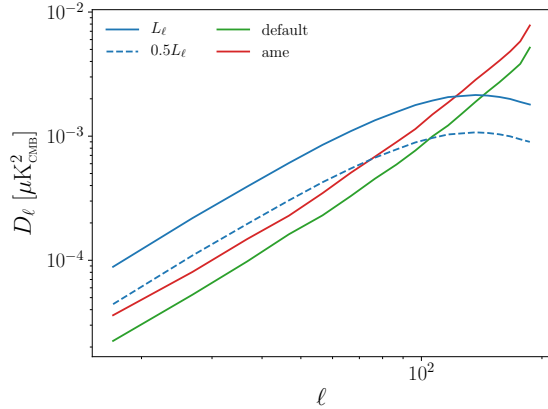


Figure 14: Residuals model power spectra for the default (s+d) and AME (s+d+a) scenario compared to the modeled lensing power spectrum when 0 and 50% delensing is performed.

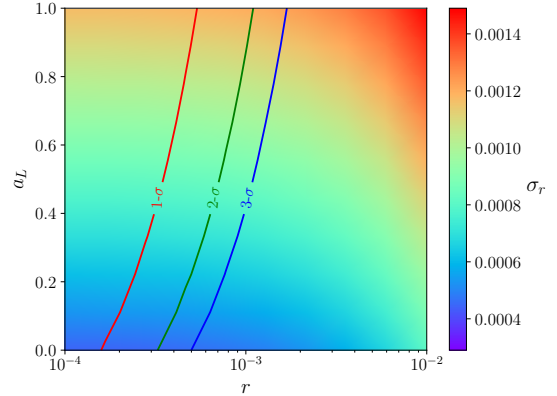


Figure 15: Density plot of σ_r as a function of r and a_L , for fixed $a_R = 1$ with the AME's residuals model. The 1,2,3- σ signal-to-noise contours are also represented.

6.3 Foreground Model

In this section, we have explored the possibility of a polarized AME emission and, its implications for the r detection. The results from the fit with this model are also displayed in table 4.

The uncertainty on r is slightly higher than in the default scenario mainly due to the increase in the number of model parameters. This is shown in figure 14, where the AME's residuals model is proven to be larger than the default's. Moreover, we see that the lensing continues to be the main contaminant, which yields a similar uncertainty in both scenarios. Only if a significant delensing is performed, e.g., reducing half or more the lensing contribution, we observe distinguishable differences between the two models.

The latter argument is confirmed in figure 15 where in the AME scenario σ_r is shown as a function of r and a_L with fixed $a_R = 1$. The results at large a_L are virtually unchanged from the results of figure 10, and shifts appear at low a_L . Despite this change, r values similar to Starobinsky's can still be detected if a possible AME polarization is taken into account.

6.4 Observational Strategies

In this section we compare the results obtained with the default, NH and, cosmoareas scenarios which correspond to three different observational strategies: i) Two experiments located at each hemisphere covering the full sky (default), ii) only one experiment located at the NH (NH), iii) an experiment at the NH exploring small sky patches (cosmoareas). In other words, we are studying whether a ground-based experiment can reach these scientific goals with just one instrument. An instrument can take measurements on its whole available sky view or, focus on the cleanest areas to achieve better sensitivities. Given the same observational time, the sensitivities of two different observational strategies (1) and (2) of a single telescope are

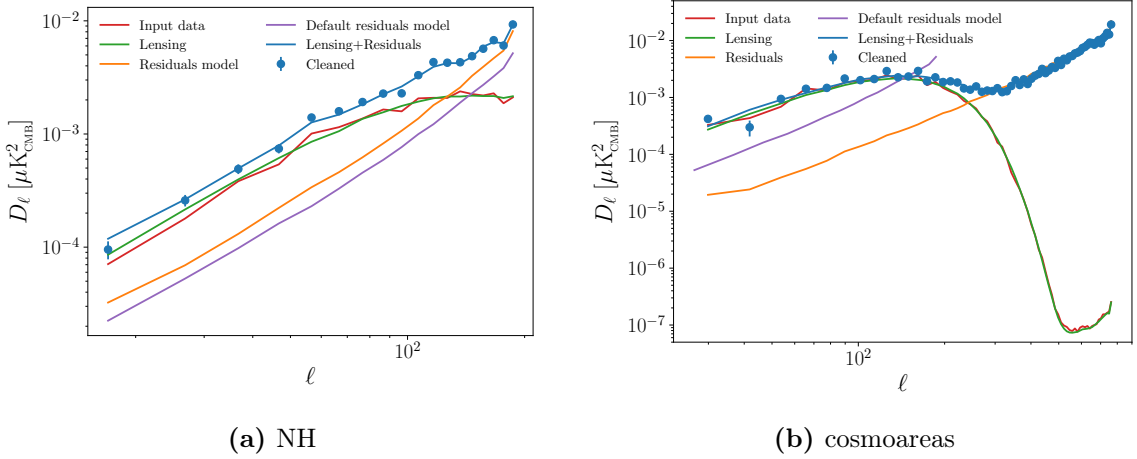


Figure 16: CMB B -mode power spectra contributions in a given scenario when the sensitivity accounts for the observed sky size. The default’s scenario residuals model is also plotted for comparison.

related by

$$s^{(1)} = \sqrt{\frac{f_{sky}^{(1)}}{f_{sky}^{(2)}}} s^{(2)}, \quad (6.2)$$

where $f_{sky}^{(l)}$ is the fraction of the sky covered by the strategy (l).

Therefore, the LFS’s sensitivity in the cosmoareas scenario is corrected by the factor with respect to the NH scenario defined in (6.2). The fraction of available observable sky is $f_{sky}^{(ca)} = 0.08$ ($f_{sky}^{(NH)} = 0.42$) in the cosmoareas (NH) scenario¹¹.

The fit results are shown in table 4. As expected the default scenario has a smaller r uncertainty compared to the NH scenario since it covers a wider sky area. On the other hand, if measurements are restricted to a particular hemisphere, we observe that it is better to cover smaller regions than the whole available sky, not only due to the smaller σ_r obtained but notably because the residuals foregrounds and lensing contributions are better characterized.

Figure 16a and figure 16b depict the power spectra results in the NH and cosmoareas scenarios respectively. We observe from the power spectra comparison of the cosmoareas scenario with the default (figure 8), that in the former strategy the residuals decrease at the recombination bump.

6.5 Atmospheric/Systematics Contamination

If atmospheric contamination in polarization is sufficiently large, its impact can have detrimental consequences on the uncertainty of r as it was shown in [51]. Here, we study the repercussions of including a correlated noise that mimics the atmosphere and/or systematics contribution. The results of the correlated-noise scenario is shown in table 4.

¹¹Notice that the f_{sky} considered in the NH scenario is the fraction of observable sky in the QUIJOTE Wide Survey mask, i.e., the galactic mask used in the analysis is not taken into account.

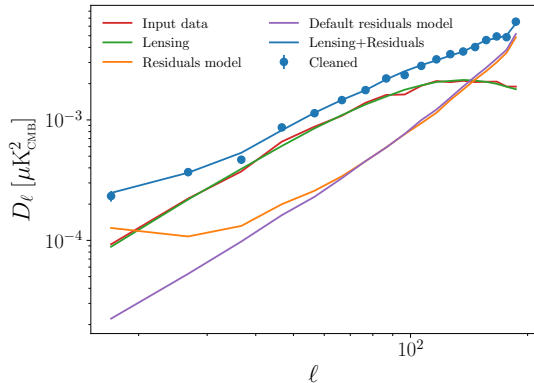


Figure 17: CMB B -mode power spectra contributions in the correlated-noise scenario.

Band [GHz]	$s[\mu\text{K arcmin}]$
40	37.5
50	24.0
60	19.9
68	16.2
78	13.5
89	11.7
100	9.2
119	7.6
140	5.9
166	6.5
195	5.8
235	7.7
280	13.2
337	19.5
402	37.5

Table 5: LiteBIRD’s characteristics. Channels’ central frequency and sensitivity [52].

From the results, we see that the uncertainty on r does not increase. Comparing the residuals model in the default and the atmosphere scenario we see that the increment only occurs at low ℓ where the residuals are at their lowest. Thus, the residuals contribution to the uncertainty comes primarily from the small scales where both scenarios have similar amount of residuals.

From figure 17, we observe that our methodology is able to recover the correlated noise introduced by the atmosphere at large scales. This yields a reduction on possible biases on r due to incorrect noise removal. On the other hand, if atmospheric noise is sufficiently large at the experiment’s location site, the residuals increment at low multipoles will increase. As a result, no information from the first bump could be gathered even in the default case where the whole observable sky is available.

7 Complementarity to LiteBIRD

LiteBIRD, Lite (Light) satellite for the studies of B -mode polarization and Inflation from cosmic background Radiation Detection, is a planned satellite mission whose primary objective is the detection of PGWs through the footprint left on the polarized CMB B -modes [52]. Recently, it has been selected by the Japan Aerospace Exploration Agency (JAXA) as a Strategic L-class mission and its launch is planned for 2027. Its design is optimized for CMB B -mode detection on large angular scales, and its principal scientific goal is reaching $\sigma_r(r=0) \leq 10^{-3}$.

LiteBIRD’s frequency coverage ranges from 40 to 402 GHz, as can be seen in table 5, where LiteBIRD’s observing frequency bands and sensitivities are shown. If AME has a polarized contribution, its detection by LiteBIRD would be extremely challenging (see figure 4), which may result in a potential bias for the primordial B -mode detection. A joint analysis with LFS could enhance LiteBIRD’s capabilities for the low-frequency foregrounds characterization. Even if the AME does not have a measurable polarized signal, LiteBIRD can benefit significantly from a joint analysis as our experiment covers smaller frequencies where the syn-

chrotron is considerably larger, see figure 3.

Below we analyze the improvement on the foreground characterization when both experiments are combined.

Foregrounds Characterization. We have studied an experiment’s ability to characterize foregrounds by studying the foregrounds residuals relative distributions at a given frequency, i.e., the ratio of the difference between the input modeled foregrounds and the retrieved ones over the input modeled foregrounds, using the corresponding models given by equations (3.2)-(3.4). In figure 18, the LB (LB-AME) and LB/LFS (LB/LFS-AME) scenarios’ foregrounds residuals distributions are compared. Notice from table 3 that the LFS considered here has only frequency channels at the lb and mb, since the frequencies at hb overlap with LiteBIRD’s frequency range.

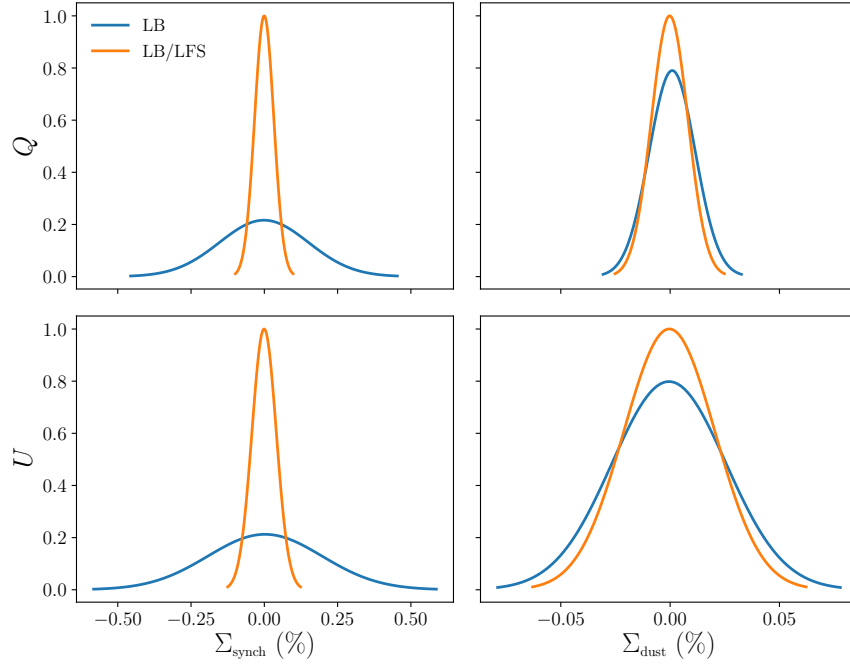
In figure 18a the synchrotron’s and dust’s residuals distributions are compared for the LB and LB/LFS scenarios at 70 GHz. We observe no significant difference in the dust residuals when LiteBIRD is combined with LFS, which is indeed expected as the latter focus mainly on low-frequencies where the thermal dust is insignificant. On the other hand, the inclusion of the ground-based experiment narrows considerably the synchrotron’s residuals distribution. Therefore, a joint analysis will reduce the uncertainties relative to the component separation. Moreover, if the actual synchrotron model is more complex than current models, more channels at the low-frequency spectrum regime might become essential to reconstruct properly the CMB.

Figure 18b compares the synchrotron’s and AME’s residuals distributions at 70 and 23 GHz respectively for the LB-AME and, LB/LFS-AME scenarios. Note that the synchrotron (AME) distributions in the LB-AME case are divided by a factor of 10 (50) for a better visualization. As in figure 18a the synchrotron is better recovered when both experiments are combined. However, the most outstanding improvement is observed in the AME’s residuals distribution. LiteBIRD’s frequency range does not overlap with the range where the AME is most dominant. If AME happens to be slightly polarized, a bias could be introduced in the CMB during the component separation. A combined analysis will help overcome this issue.

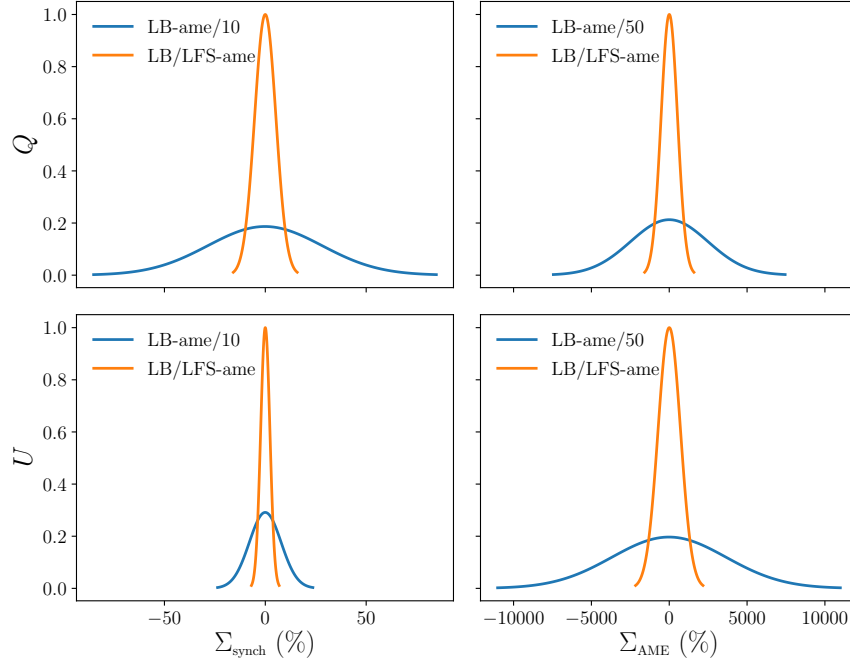
If current foreground modelling is a sufficiently good approximation of the diffuse sky, LiteBIRD can benefit from a joint analysis by reducing the uncertainties in the foregrounds recovery. Moreover, if current modelling lacks the low-frequency foregrounds’ inherent complexity, LiteBIRD could always employ data from low-frequency experiments such as the one proposed here.

8 Conclusions

We have studied whether a ground-based telescope operating in the low-frequency regime is able to detect or, at least, constrain r at the level of $\sigma_r(r=0) = 10^{-3}$. For this purpose, we have applied a full-parametric pixel-based maximum likelihood component separation method to obtain the CMB as well as the foregrounds parameters. Moreover, we developed a self-consistent approach to estimate the residuals left from the component separation methodology. Finally, with these techniques we have tested different scenarios that an experiment of this sort can face.



(a) Synchrotron and dust relative residuals at 70 GHz.



(b) Synchrotron and AME relative residuals at 70 and 23 GHz respectively.

Figure 18: Foregrounds relative residuals distributions in Q (top) and U (bottom) Stokes parameters for LiteBIRD alone (blue), and LiteBIRD combined with this instrument (orange). The distributions are normalized with respect to the the LB/LFS distribution's maximum.

First of all, we have compared different LFS’s frequency channels distributions with diverse telescope sensitivities, to obtain the most optimal telescope configuration. We have seen that given the same effective telescope sensitivity, it is preferable to have more noisier channels than a few channels with large sensitivities. Besides, it has been shown that the channels at the high frequency band help trace the thermal dust information.

We have found that r values within the Starobinsky’s range are detectable with this type of experiment even if no delensing is performed. However, some sort of delensing should be performed in order to reduce the r uncertainty, σ_r . This comes as a result of the lensing being the principal BB power spectrum contaminant in this experimental configuration. Similar conclusions are found in [53] where parametric foreground removal successfully mitigate bias induced due to contaminated CMB lensing reconstruction.

Since the foreground sky could be more complex than what current models predict, we have also studied the LFS’s performance when a polarized AME contribution is included. The results are virtually the same when no delensing is applied, as it constitutes the primary source of error. However, when a large fraction of lensing is removed, we estimated from the residuals left in the model with AME that the region where r is no longer detectable is larger than when AME is not taken into account.

In this study we have also considered different observational strategies related to the number of available telescope’s locations. For a experiment located at a given hemisphere, focusing on small sky patches yields smaller residuals at the small scales, and an overall smaller σ_r . However, we have shown that the tightest constraints on r are obtained when the largest amount of sky is covered, i.e., at least one instrument per hemisphere.

Furthermore, we have considered the contamination by the atmosphere and/or systematics in polarization measurements. These contributions introduce a correlated noise that masks the power spectrum at low multipoles, i.e., at large scales. With our residuals estimation method, we are able to recover the uncertainty generated by the correlated noise and avoid biases in the fit. Possible biases due to incorrect modelling is outside the scope of this work. Here, we reference a few studies that deal with this issue [39–41].

Finally, we have studied its potential complementarity with LiteBIRD. The LFS experiment explores the low-frequency range with a sensitivity never achieved before. Therefore, it significantly improves the characterization of the low-frequency foregrounds. Moreover, the need for a joint analysis will be more justified if the low-frequency sky is more complex than expected nowadays.

In conclusion, under the sky modelling assumptions made in this work, this type of experiment alone is capable of detecting r (in the Starobinsky model), or at least constrain it with $\sigma_r = 10^{-3}$ even when no delensing is performed. Additionally, it will help with the low-frequency foregrounds characterization as it reaches unprecedented sensitivities in this regime. The latter makes this instrument also a valuable complement to other satellite and on-ground experiments.

A On the Residuals Model Estimation

The methodology proposed here to estimate the residuals model relies on the simulations $\{\mathbf{S}_j\}_{j \in \{1, \dots, n_{sim}\}}$, derived using the best-fit set of model parameters in (5.1). However, we have tried to estimate the residuals models in other different manners. We have studied two different approaches, using the default scenario, which may be more intuitive but did not work in the end.

- **Sampling from the full posterior:** The MCMC technique adopted provides a large number of samples from the full posterior probability of the model parameters. Thus, one can consider using a collection of random samples from the ones obtained with that technique, instead of obtaining new best-fit model parameters from new simulations. This approach has the advantage of reducing significantly the computational time since only one fit is required. The residuals simulation are calculated as the difference between the best-fit CMB or the calculated best-fit foreground map and the CMB or the foreground map obtained randomly from the samples produced by the MCMC. The results for the default scenario are shown in figure 19.
- **Simulations with foregrounds sampled from the marginalized posteriors:** Instead of using $\theta_f^{X, dat}$ in (5.1), we can use $\theta_f^{X, sim}$ where the latter are generated as random realizations of the Gaussian marginalized posterior of the foreground parameters obtained from Bayesian method. This method introduces a variability in the simulations foreground component. The residuals are evaluated as in the methodology adopted in this work. The results for the default scenario are shown in figure 20.

As it can be seen from both figure 19 and 20 the estimated residual model are not consistent with the genuine residuals (these results are to be contrasted with those shown in figure 7 where the best-fit set of model parameters were used). In the first case, we believe that the discrepancy arises because those residuals not only take into account the foreground and noise left from methodology but also the uncertainty due to the spread of the full posterior distribution. In the latter method, another uncertainty is introduced in the simulations via the dispersion of $\theta_f^{X, sim}$ with respect to $\theta_f^{X, data}$. Due to this difference, the simulations no longer resemble enough the data signal and the residuals are overestimated. The latter method provides better results since the uncertainty of the marginalized posterior distributions of the foreground parameters is smaller than the uncertainty of the full posterior distribution.

Moreover, in figure 20, we observe that the discrepancy is larger in the dust's case compared to the synchrotron's. This may be a result of a worse characterization of the dust parameters, i.e., the dust's parameters' marginalized posterior distributions are more spread than the synchrotron's.

Acknowledgments

We would like to thank the referee for constructive comments which helped improve the quality of the manuscript. EdIH acknowledge partial financial support from the *Concepción Arenal Programme* of the Universidad de Cantabria. We acknowledge Santander Supercomputacion support group at the Universidad de Cantabria who provided access to the supercomputer Altamira Supercomputer at the Instituto de Física de Cantabria (IFCA-CSIC), member of

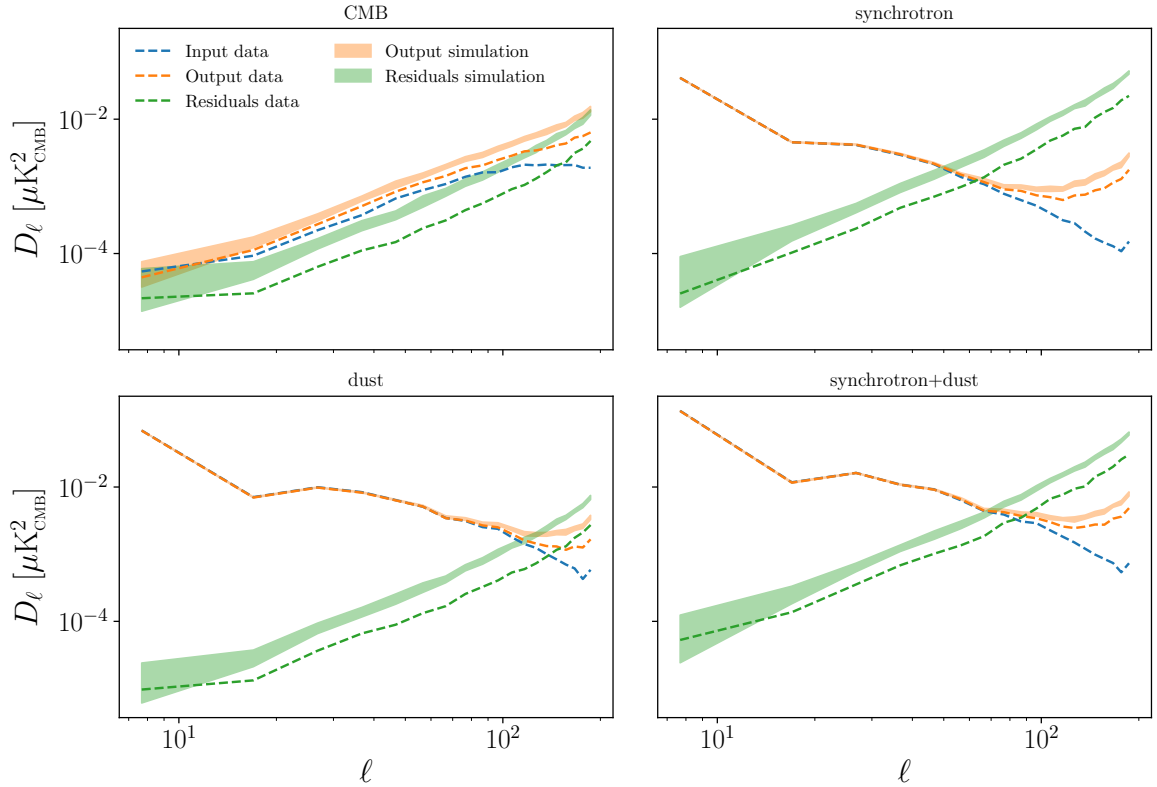


Figure 19: Sampling from full posterior. The input, output, and residuals best-fit versus random samples power spectra of different sky components are shown. The simulation power spectra are represented as colored shaded areas, while the data are depicted with colored dashed lines. The foregrounds power spectra are evaluated at $\nu = 76.5$ GHz.

the Spanish Supercomputing Network, for performing simulations/analyses. The authors would like to thank Spanish Agencia Estatal de Investigación (AEI, MICIU) for the financial support provided under the projects with references ESP2017-83921-C2-1-R and AYA2017-90675-REDC, co-funded with EU FEDER funds, and also acknowledge the funding from Unidad de Excelencia María de Maeztu (MDM-2017-0765). Some of the results in this paper have been derived using the `healpy` and `HEALPix` package.

References

- [1] Alan H Guth. Inflationary Universe: A Possible Solution to the Horizon and Flatness Problems. *Physical Review D*, 23(2):347, 1981.
- [2] Andrei D Linde. A new inflationary universe scenario: a possible solution of the horizon, flatness, homogeneity, isotropy and primordial monopole problems. *Physics Letters B*, 108(6):389–393, 1982.
- [3] Alexei A Starobinsky. Dynamics of phase transition in the new inflationary universe scenario and generation of perturbations. *Physics Letters B*, 117(3-4):175–178, 1982.
- [4] Y Akrami, F Arroja, M Ashdown, J Aumont, C Baccigalupi, M Ballardini, AJ Banday, RB Barreiro, N Bartolo, S Basak, et al. Planck 2018 results. X. Constraints on inflation. *arXiv preprint arXiv:1807.06211*, 2018.

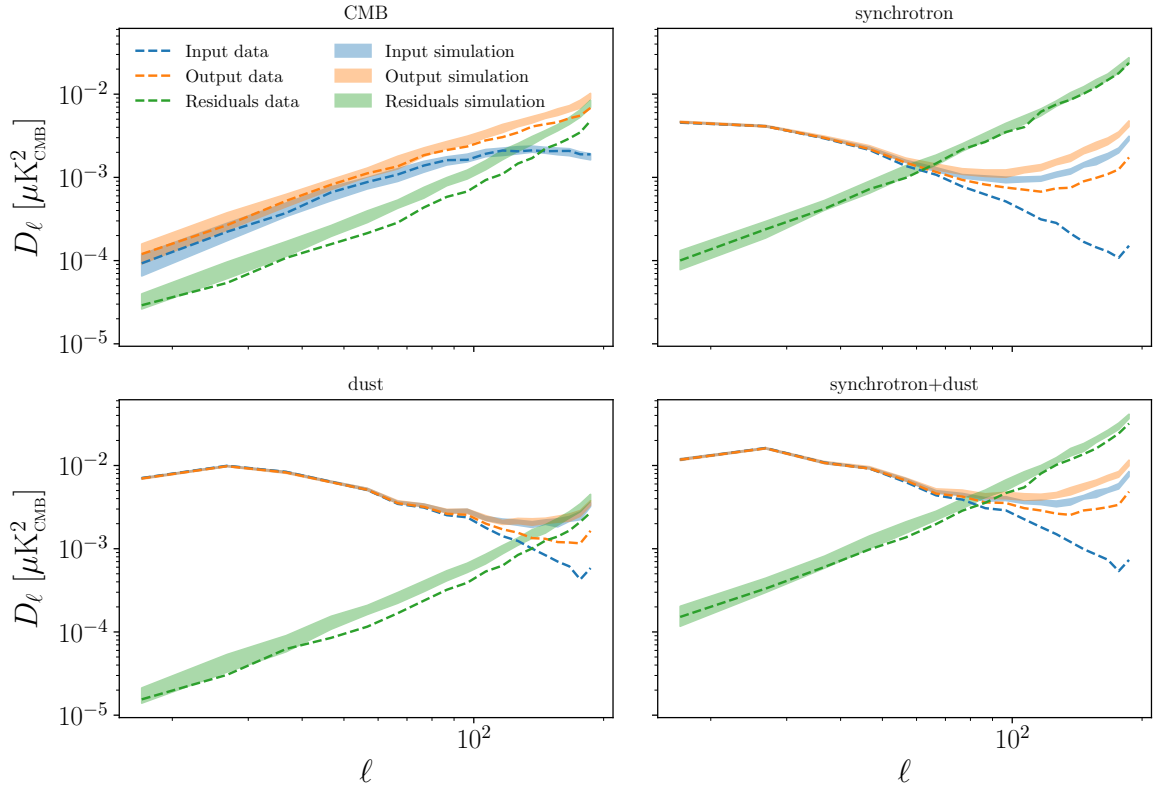


Figure 20: Simulations with foregrounds sampled from the marginalized posteriors. Power spectrum of the input, output, and residuals best-fit data versus simulation of different sky components. The simulation power spectra are represented as colored shaded areas, while the data are depicted with colored dashed lines. The foregrounds power spectra are evaluated at $\nu = 76.5$ GHz. dispersion

- [5] Jérôme Martin, Christophe Ringeval, Roberto Trotta, and Vincent Vennin. The best inflationary models after Planck. *Journal of Cosmology and Astroparticle Physics*, 2014(03):039, 2014.
- [6] Kevork N Abazajian, Peter Adshead, Zeeshan Ahmed, Steven W Allen, David Alonso, Kam S Arnold, Carlo Baccigalupi, James G Bartlett, Nicholas Battaglia, Bradford A Benson, et al. CMB-S4 Science Book. *arXiv preprint arXiv:1610.02743*, 2016.
- [7] Peter Ade, James Aguirre, Zeeshan Ahmed, Simone Aiola, Aamir Ali, David Alonso, Marcelo A Alvarez, Kam Arnold, Peter Ashton, Jason Austermann, et al. The Simons Observatory: Science goals and forecasts. *Journal of Cosmology and Astroparticle Physics*, 2019(02):056, 2019.
- [8] Howard Hui, PAR Ade, Z Ahmed, RW Aikin, KD Alexander, D Barkats, SJ Benton, CA Bischoff, JJ Bock, R Bowens-Rubin, et al. BICEP Array: a multi-frequency degree-scale CMB polarimeter. In *Millimeter, Submillimeter, and Far-Infrared Detectors and Instrumentation for Astronomy IX*, volume 10708, page 1070807. International Society for Optics and Photonics, 2018.
- [9] Tomotake Matsumura, Yoshiki Akiba, K Arnold, J Borrill, R Chendra, Yuji Chinone, A Cukierman, T de Haan, M Dobbs, A Dominjon, et al. LiteBIRD: Mission Overview and Focal Plane Layout. *Journal of Low Temperature Physics*, 184(3-4):824–831, 2016.

- [10] Shaul Hanany, Marcelo Alvarez, Emmanuel Artis, Peter Ashton, Jonathan Aumont, Ragnhild Aurlen, Ranajoy Banerji, R Belen Barreiro, James G Bartlett, Soumen Basak, et al. PICO: Probe of Inflation and Cosmic Origins. *arXiv preprint arXiv:1902.10541*, 2019.
- [11] Kiyotomo Ichiki. CMB foreground: A concise review. *Progress of Theoretical and Experimental Physics*, 2014(6), 2014.
- [12] Josquin Errard and Radek Stompor. Characterizing bias on large scale CMB B-modes after Galactic foregrounds cleaning. *Physical Review D*, 99(4):043529, 2019.
- [13] Federico Stivoli, J Grain, Samuel M Leach, M Tristram, Carlo Baccigalupi, and Radek Stompor. Maximum likelihood, parametric component separation and CMB B-mode detection in suborbital experiments. *Monthly Notices of the Royal Astronomical Society*, 408(4):2319–2335, 2010.
- [14] JA Rubiño-Martín, R Rebolo, M Aguiar, R Génova-Santos, F Gómez-Reñasco, JM Herreros, RJ Hoyland, C López-Caraballo, AE Pelaez Santos, V Sanchez de La Rosa, et al. The QUIJOTE-CMB experiment: studying the polarisation of the galactic and cosmological microwave emissions. In *Ground-based and Airborne Telescopes IV*, volume 8444, page 84442Y. International Society for Optics and Photonics, 2012.
- [15] Michael D Niemack, PAR Ade, J Aguirre, F Barrientos, JA Beall, JR Bond, J Britton, HM Cho, S Das, MJ Devlin, et al. ACTPol: A polarization-sensitive receiver for the Atacama Cosmology Telescope. In *Millimeter, Submillimeter, and Far-Infrared Detectors and Instrumentation for Astronomy V*, volume 7741, page 77411S. International Society for Optics and Photonics, 2010.
- [16] Tom Essinger-Hileman, JW Appel, JA Beal, HM Cho, J Fowler, M Halpern, Matthew Hasselfield, KD Irwin, TA Marriage, MD Niemack, et al. The Atacama B-Mode Search: CMB Polarimetry with Transition-Edge-Sensor Bolometers. In *AIP Conference Proceedings*, volume 1185, pages 494–497. AIP, 2009.
- [17] Thomas Essinger-Hileman, Aamir Ali, Mandana Amiri, John W Appel, Derek Araujo, Charles L Bennett, Fletcher Boone, Manwei Chan, Hsiao-Mei Cho, David T Chuss, et al. CLASS: The Cosmology Large Angular Scale Surveyor. In *Millimeter, Submillimeter, and Far-Infrared Detectors and Instrumentation for Astronomy VII*, volume 9153, page 91531I. International Society for Optics and Photonics, 2014.
- [18] Zigmund D Kermish, Peter Ade, Aubra Anthony, Kam Arnold, Darcy Barron, David Boettger, Julian Borrill, Scott Chapman, Yuji Chinone, Matt A Dobbs, et al. The polarbear experiment. In *Millimeter, Submillimeter, and Far-Infrared Detectors and Instrumentation for Astronomy VI*, volume 8452, page 84521C. International Society for Optics and Photonics, 2012.
- [19] A Suzuki, P Ade, Y Akiba, C Aleman, K Arnold, C Baccigalupi, B Barch, D Barron, A Bender, D Boettger, et al. The polarbear-2 and the simons array experiments. *Journal of Low Temperature Physics*, 184(3-4):805–810, 2016.
- [20] Peter AR Ade, N Aghanim, MIR Alves, C Armitage-Caplan, M Arnaud, M Ashdown, F Atrio-Barandela, J Aumont, H Aussel, C Baccigalupi, et al. Planck 2013 results. I. Overview of products and scientific results. *Astronomy & Astrophysics*, 571:A1, 2014.
- [21] F. Poidevin et al. The QUIJOTE Experiment: Prospects for CMB B-MODE polarization detection and foregrounds characterization. In *13th Rencontres du Vietnam: Cosmology 2017 Quy Nhon, Vietnam, July 9-15, 2017*, 2018.
- [22] K. M. Górski, E. Hivon, A. J. Banday, B. D. Wandelt, F. K. Hansen, M. Reinecke, and M. Bartelmann. HEALPix: A Framework for High-Resolution Discretization and Fast Analysis of Data Distributed on the Sphere. *Ast. Phys. J.*, 622:759–771, April 2005.
- [23] Sebastian Hutschenreuter and Torsten A Enßlin. The galactic faraday depth sky revisited. *Astronomy & Astrophysics*, 633:A150, 2020.

- [24] David H Lyth and Antonio Riotto. Particle Physics Models of Inflation and the Cosmological Density Perturbation. *Physics Reports*, 314(1-2):1–146, 1999.
- [25] N Aghanim, Y Akrami, M Ashdown, J Aumont, C Baccigalupi, M Ballardini, AJ Banday, RB Barreiro, et al. Planck 2018 results. VI. Cosmological parameters. *arXiv preprint arXiv:1807.06209*, 2018.
- [26] Antony Lewis and Anthony Challinor. CAMB: Code for Anisotropies in the Microwave Background. *Astrophysics Source Code Library*, 2011.
- [27] Andrea Zonca, Leo Singer, Daniel Lenz, Martin Reinecke, Cyrille Rosset, Eric Hivon, and Krzysztof Gorski. healpy: equal area pixelization and spherical harmonics transforms for data on the sphere in Python. *Journal of Open Source Software*, 4(35):1298, March 2019.
- [28] R Génova-Santos, JA Rubiño-Martín, R Rebolo, A Peláez-Santos, CH López-Caraballo, S Harper, RA Watson, M Ashdown, RB Barreiro, B Casaponsa, et al. Measurements of the Intensity and Polarization of the Anomalous Microwave Emission in the Perseus molecular complex with QUIJOTE. *arXiv preprint arXiv:1501.04491*, 2015.
- [29] Y Akrami, M Ashdown, J Aumont, C Baccigalupi, M Ballardini, AJ Banday, RB Barreiro, N Bartolo, S Basak, K Benabed, et al. Planck 2018 results. IV. Diffuse component separation. *arXiv preprint arXiv:1807.06208*, 2018.
- [30] George B Rybicki and Alan P Lightman. *Radiative Processes in Astrophysics*. John Wiley & Sons, 2008.
- [31] Jens Chluba, James Colin Hill, and Maximilian H Abitbol. Rethinking CMB foregrounds: systematic extension of foreground parametrizations. *Monthly Notices of the Royal Astronomical Society*, 472(1):1195–1213, 2017.
- [32] Ben Thorne, Joanna Dunkley, David Alonso, and Sigurd Naess. The Python Sky Model: software for simulating the Galactic microwave sky. *Monthly Notices of the Royal Astronomical Society*, 469(3):2821–2833, 2017.
- [33] N Krachmalnicoff, E Carretti, C Baccigalupi, G Bernardi, S Brown, BM Gaensler, M Haverkorn, M Kesteven, F Perrotta, S Poppi, et al. S-PASS view of polarized Galactic synchrotron at 2.3 GHz as a contaminant to CMB observations. *Astronomy & Astrophysics*, 618:A166, 2018.
- [34] R Adam, PAR Ade, N Aghanim, MIR Alves, M Arnaud, M Ashdown, J Aumont, C Baccigalupi, AJ Banday, RB Barreiro, et al. Planck 2015 results-X. Diffuse component separation: Foreground maps. *Astronomy & Astrophysics*, 594:A10, 2016.
- [35] Matthew A Stevenson. Derivation of an Analytical Approximation of the Spectrum of Spinning Dust Emission. *The Astrophysical Journal*, 781(2):113, 2014.
- [36] PAR Ade, N Aghanim, MIR Alves, M Arnaud, M Ashdown, J Aumont, C Baccigalupi, AJ Banday, RB Barreiro, JG Bartlett, et al. Planck 2015 results-XXV. Diffuse low-frequency Galactic foregrounds. *Astronomy & Astrophysics*, 594:A25, 2016.
- [37] Ben Thorne, Jo Dunkley, David Alonso, Maximilian H Abitbol, Josquin Errard, J Colin Hill, Brian Keating, Grant Teply, and Edward J Wollack. Removal of Galactic foregrounds for the Simons Observatory primordial gravitational wave search. *arXiv preprint arXiv:1905.08888*, 2019.
- [38] Daniel Foreman-Mackey, David W Hogg, Dustin Lang, and Jonathan Goodman. emcee: The MCMC hammer. *Publications of the Astronomical Society of the Pacific*, 125(925):306, 2013.
- [39] Charmaine Armitage-Caplan, Joanna Dunkley, Hans Kristian Eriksen, and Clive Dickinson. Impact on the tensor-to-scalar ratio of incorrect Galactic foreground modelling. *Monthly Notices of the Royal Astronomical Society*, 424(3):1914–1924, 2012.

- [40] M Remazeilles, C Dickinson, Hans Kristian Kamfjord Eriksen, and Ingunn Kathrine Wehus. Sensitivity and foreground modelling for large-scale cosmic microwave background B-mode polarization satellite missions. *Monthly Notices of the Royal Astronomical Society*, 458(2):2032–2050, 2016.
- [41] Y Fantaye, F Stivoli, J Grain, SM Leach, M Tristram, C Baccigalupi, and R Stompor. Estimating the tensor-to-scalar ratio and the effect of residual foreground contamination. *Journal of Cosmology and Astroparticle Physics*, 2011(08):001, 2011.
- [42] Nobuhiko Katayama and Eiichiro Komatsu. Simple foreground cleaning algorithm for detecting primordial B-mode polarization of the cosmic microwave background. *The Astrophysical Journal*, 737(2):78, 2011.
- [43] RDP Grunitt, Luke RP Jew, and C Dickinson. Hierarchical Bayesian CMB Component Separation with the No-U-Turn Sampler. *arXiv preprint arXiv:1910.14170*, 2019.
- [44] Jonathan Goodman and Jonathan Weare. Ensemble samplers with affine invariance. *Communications in applied mathematics and computational science*, 5(1):65–80, 2010.
- [45] Benjamin D Wandelt, Eric Hivon, and Krzysztof M Gorski. Cosmic microwave background anisotropy power spectrum statistics for high precision cosmology. *Physical Review D*, 64(8):083003, 2001.
- [46] Eric Hivon, Krzysztof M Górski, C Barth Netterfield, Brendan P Crill, Simon Prunet, and Frode Hansen. MASTER of the CMB Anisotropy Power Spectrum: A Fast Method for Statistical Analysis of Large and Complex CMB Data Sets. *arXiv preprint astro-ph/0105302*, 2001.
- [47] Max Tegmark. How to measure CMB power spectra without losing information. *Physical Review D*, 55(10):5895, 1997.
- [48] Emory F Bunn, Matias Zaldarriaga, Max Tegmark, and Angelica de Oliveira-Costa. E/B decomposition of finite pixelized CMB maps. *Physical Review D*, 67(2):023501, 2003.
- [49] David Alonso, Javier Sanchez, Anže Slosar, and LSST Dark Energy Science Collaboration. A unified pseudo- c_ℓ framework. *Monthly Notices of the Royal Astronomical Society*, 484(3):4127–4151, 2019.
- [50] Gideon Schwarz et al. Estimating the Dimension of a Model. *The annals of statistics*, 6(2):461–464, 1978.
- [51] David Alonso, Joanna Dunkley, Ben Thorne, and Sigurd Naess. Simulated forecasts for primordial B-mode searches in ground-based experiments. *Physical Review D*, 95(4):043504, 2017.
- [52] Masashi Hazumi, PAR Ade, Y Akiba, D Alonso, K Arnold, J Aumont, C Baccigalupi, D Barron, S Basak, S Beckman, et al. Litebird: A satellite for the studies of b-mode polarization and inflation from cosmic background radiation detection. *Journal of Low Temperature Physics*, 194(5-6):443–452, 2019.
- [53] Dominic Beck, Josquin Errard, and Radek Stompor. Impact of polarized galactic foreground emission on cmb lensing reconstruction and delensing of b-modes. *arXiv preprint arXiv:2001.02641*, 2020.

P. II: Determination of polarization angles in CMB experiments and application to CMB component separation analyses

E. de la Hoz, P. Diego-Palazuelos, E. Martínez-González, P. Vielva, R. B. Barreiro, & J. D. Bilbao-Ahedo. *Journal of Cosmology and Astroparticle Physics*, 2022(03), 032

© IOP Publishing. This is an author-created, un-copyedited version of an article accepted for publication in *Journal of Cosmology and Astroparticle Physics*. OP Publishing Ltd is not responsible for any errors or omissions in this version of the manuscript or any version derived from it. The Version of Record is available online at: <https://doi.org/10.1088/1475-7516/2022/03/032>

Determination of Polarization Angles in CMB Experiments and Application to CMB Component Separation Analyses

E. de la Hoz^{1, a, b}, P. Diego-Palazuelos,^{a, b} E. Martínez-González,^a
P. Vielva,^a R. B. Barreiro^a J. D. Bilbao-Ahedo^{a, b}

^aInstituto de Física de Cantabria (CSIC-Universidad de Cantabria),
Avda. de los Castros s/n, E-39005 Santander, Spain

^bDpto. de Física Moderna, Universidad de Cantabria,
Avda. los Castros s/n, E-39005 Santander, Spain

E-mail: delahoz@ifca.unican.es, diegop@ifca.unican.es, martinez@ifca.unican.es,
vielva@ifca.unican.es, barreiro@ifca.unican.es, bilbao@ifca.unican.es

Abstract. The new generation of CMB polarization experiments will reach limits of sensitivity never achieved before in order to detect the elusive primordial B -mode signal. However, all these efforts will be futile if we lack a tight control of systematics. Here, we focus on the systematic that arises from the uncertainty on the calibration of polarization angles. Miscalibrated polarization angles induce a mixing of E - and B -modes that obscures the primordial B -mode signal. We introduce an iterative angular power spectra maximum likelihood-based method to calculate the polarization angles ($\hat{\alpha}$) from the multi-frequency signal. The basis behind this methodology grounds on nulling the C_ℓ^{EB} power spectra. In order to simplify the likelihood, we assume that the rotation angles are small ($\lesssim 6^\circ$) and, the maximum likelihood solution for the rotation angles $\hat{\alpha}$ is obtained by applying an iterative process where the covariance matrix does not depend on $\hat{\alpha}$ per iteration, i.e., the rotation angles are fixed to the estimated $\hat{\alpha}$ in the previous iteration. With these assumptions, we obtain an analytical linear system which leads to a very fast computational implementation. We show that with this methodology we are able to determine the rotation angle for each frequency with sufficiently good accuracy. To prove the latter point we perform component separation analyses using the parametric component separation method B-SeCRET with two different approaches. In the first approach we apply the B-SeCRET pipeline to the signal de-rotated with the estimation of $\hat{\alpha}$, while in the second, the rotation angles are treated as model parameters using the estimation of $\hat{\alpha}$ as a prior information. We obtain that the rotation angles estimations improve after applying the second approach, and show that the systematic residuals due to the non-null calibration polarization angles are mitigated to the order of a 1% at the power spectrum level.

¹Corresponding author.

Contents

1	Introduction	1
2	Methodology	3
3	Simulations	7
3.1	Sky Signal	7
3.2	Rotation Angles	10
4	Methodology Performance	11
4.1	Building the Covariance Matrix from Observed Spectra	11
4.2	Convergence and Uncertainty Estimation	14
4.3	Telescope-by-telescope Analysis	16
4.4	Comparison among Different Likelihood Estimators	16
5	Component Separation	21
5.1	Component Separation Approaches	22
5.1.1	Approach 1	22
5.1.2	Approach 2	22
5.2	Polarization Rotation Angles Estimation Comparison	23
5.3	CMB Recovery Comparison	24
6	Conclusions	24

1 Introduction

With temperature data successfully characterized thanks to the Planck satellite [1], the next generation of cosmic microwave background (CMB) experiments will be focused on the measurement of the CMB polarization. Amongst other scientific objectives [see, e.g., 2–4], the CMB polarization would allow us to further constrain the Λ -CDM cosmological model and the inflation paradigm, map the distribution of matter in the universe, and probe the density of light relics from (and beyond) the Standard Model of particle physics. To accomplish these science goals, future CMB experiments will need to meet very demanding sensitivity requirements, and, more importantly, have a tight control on systematics.

One of the principal known sources of systematic uncertainty is the miscalibration of the polarization angle. A non-zero polarization angle of the polarimeter is one of the many systematics that lead to the mixing of the measured E - and B -modes, which, in turn, results in a leakage of E -modes into B -modes that can obscure the primordial B -mode signal from inflation [5–8]. To reach their sensitivity requirements of $\sigma_r \sim 10^{-3}$, future experiments can only afford uncertainties at the arcminute level on the determination of the polarization angle. Therefore, a very precise calibration is mandatory.

The common procedure for polarization angle calibration is to use an artificial calibrator (classically a thermal source behind a grid of linear polarizers), a natural astrophysical source of known polarization orientation (like, for example, the Crab Nebula [9]), or previous CMB measurements [10], to adjust the polarization angle of the detectors. Examples of

experiments that rely on artificial calibration sources are SPTPol [11] and BICEP [12], while POLARBEAR [13] and ACTPol [14] use instead the Crab Nebula as their calibration reference. However, this type of calibration has its limitations [15]. On the one hand, artificial calibration sources have spectral properties that are very different from those of the CMB, and they cannot always be placed and/or maintained in the antenna’s far-field during the whole observational campaign. However, new approaches have been proposed in the last years to place artificial calibration sources on stratospheric balloons [16], CubeSat on a low-Earth-orbit [17], and on a satellite following a formation-flight with the CMB master satellite [18]. On the other hand, the polarized emission of astrophysical sources needs to be very well constrained beforehand for it to serve as a calibration source, and even in that case, astrophysical sources suffer from time, frequency and spatial variability, and might not be visible from all CMB observatories. In addition, both astrophysical and artificial sources are much brighter than the CMB B -mode, which can make calibration more difficult by causing non-linearities in the response of the detectors. As a consequence, only a $\sim 0.5^\circ - 1^\circ$ uncertainty can be reached with this kind of calibration methodologies [11–15, 19].

Another possibility is to use our current understanding of the universe and the measured CMB itself as a calibration reference. The existence of a primordial magnetic field at the last scattering surface, or a hypothetical parity-violating field or process, could produce the rotation of the CMB polarization plane [20–22]. This rotation, quantified by the cosmic birefringence angle, would also produce mixing between E - and B -modes. Nevertheless, no parity-violating processes are contemplated in either the Λ -CDM cosmological model or the Standard Model of particle physics, and no evidence of a significant primordial magnetic field has been detected (see [23–25] for current constraints on cosmic birefringence), and, in the absence of such elements, the CMB is expected to have null TB and EB cross-correlations. In this way, if a zero birefringence angle is assumed, polarimeters can be calibrated by forcing the observed TB and EB angular power cross-spectra to be consistent with zero [15]. This methodology, known as self-calibration, is sometimes used in redundancy with other calibration methods to ensure consistency [13, 14], and, depending on the noise level of the experiment at hand, it can lead to uncertainties around the arcminute scale [15].

However, the existence of parity-violating physics or a primordial magnetic field cannot be probed through CMB data when measurements are calibrated by imposing the cancellation of the EB cross-correlation. To bypass this limitation, new algorithms have been proposed in recent years to simultaneously determine the uncertainty in the polarization angle and a possible non-zero EB cross-correlation¹ [27–29]. A simultaneous determination of both the polarization and birefringence angles is possible as the Galactic foreground photons are unaffected by the cosmic birefringence due to their small propagation length [27]. In this way, Galactic foreground emission can be used to break the degeneracy between cosmic birefringence and the polarization angle.

Here we present a new implementation of the in-flight calibration methodology to determine the rotation angle from CMB polarization measurements, under the assumption of a null birefringence angle, presented in [29]. In our approach we introduce two approximations that lead to an analytical linear system of equations, which leads to an efficient and fast-converging algorithm to calculate rotation angles. Building on the results from this methodology, we apply two component separation approaches to remove this systematic from the cleaned CMB map. In the first approach we apply the B-SeCRET (Bayesian-Separation of Components

¹In fact, an extension of the methodology proposed here which includes the determination of the birefringence angle will be presented in [26].

and Residuals Estimate Tool) method [30] to the signal after de-rotating with the estimation of the rotation angles. In the second approach, we incorporate the rotation angles into the component separation method itself as model parameters. Thus, the second approach constitutes an independent method to calculate the rotation angles. However, the information regarding the rotation angles from the previous method are used as prior information to help with convergence.

This work is structured as follows. A detailed explanation of our methodology to estimate rotation angles is presented in section 2. To test and validate our algorithm, we have produced sky simulations of a LiteBIRD-like experiment, which are described in section 3. The results of applying our methodology to those simulations are then shown in section 4. The interplay between our methodology and component separation is presented in section 5. Final comments and conclusions are left for section 6.

2 Methodology

Let N be the number of frequency channels of the experiment, and α_i the i -th channel's rotation angle. Assuming a null birefringence angle, the spherical harmonics coefficients of the observed E and B polarization fields of the i -th channels are rotated as follows [27]:

$$\begin{pmatrix} E_{i,\ell,m} \\ B_{i,\ell,m} \end{pmatrix} = \begin{pmatrix} c(2\alpha_i) & -s(2\alpha_i) \\ s(2\alpha_i) & c(2\alpha_i) \end{pmatrix} \begin{pmatrix} \tilde{E}_{i,\ell,m} \\ \tilde{B}_{i,\ell,m} \end{pmatrix}, \quad (2.1)$$

where $\tilde{E}_{i,\ell,m}$ and $\tilde{B}_{i,\ell,m}$ are the spherical harmonics coefficients of the non-rotated signal and, $c()$ and $s()$ stands for cosine and sine respectively. Thus, the observed angular power spectra are

$$\begin{pmatrix} C_\ell^{E_i E_j} \\ C_\ell^{E_i B_j} \\ C_\ell^{E_j B_i} \\ C_\ell^{B_i B_j} \end{pmatrix} = \begin{pmatrix} c(2\alpha_i)c(2\alpha_j) & -c(2\alpha_i)s(2\alpha_j) & -s(2\alpha_i)c(2\alpha_j) & s(2\alpha_i)s(2\alpha_j) \\ c(2\alpha_i)s(2\alpha_j) & c(2\alpha_i)c(2\alpha_j) & -s(2\alpha_i)s(2\alpha_j) & -s(2\alpha_i)c(2\alpha_j) \\ s(2\alpha_i)c(2\alpha_j) & -s(2\alpha_i)s(2\alpha_j) & c(2\alpha_i)c(2\alpha_j) & -c(2\alpha_i)s(2\alpha_j) \\ s(2\alpha_i)s(2\alpha_j) & s(2\alpha_i)c(2\alpha_j) & c(2\alpha_i)s(2\alpha_j) & c(2\alpha_i)c(2\alpha_j) \end{pmatrix} \begin{pmatrix} C_\ell^{\tilde{E}_i \tilde{E}_j} \\ C_\ell^{\tilde{E}_i \tilde{B}_j} \\ C_\ell^{\tilde{E}_j \tilde{B}_i} \\ C_\ell^{\tilde{B}_i \tilde{B}_j} \end{pmatrix}.$$

The spectra can be combined to obtain the following relationships:

$$C_\ell^{E_i E_j} + C_\ell^{B_i B_j} = \left(C_\ell^{\tilde{E}_i \tilde{E}_j} + C_\ell^{\tilde{B}_i \tilde{B}_j} \right) c(\phi) + \left(C_\ell^{\tilde{E}_i \tilde{B}_j} - C_\ell^{\tilde{E}_j \tilde{B}_i} \right) s(\phi), \quad (2.2)$$

$$C_\ell^{E_i E_j} - C_\ell^{B_i B_j} = \left(C_\ell^{\tilde{E}_i \tilde{E}_j} - C_\ell^{\tilde{B}_i \tilde{B}_j} \right) c(\psi) - \left(C_\ell^{\tilde{E}_i \tilde{B}_j} + C_\ell^{\tilde{E}_j \tilde{B}_i} \right) s(\psi), \quad (2.3)$$

$$C_\ell^{E_i B_j} + C_\ell^{E_j B_i} = \left(C_\ell^{\tilde{E}_i \tilde{E}_j} - C_\ell^{\tilde{B}_i \tilde{B}_j} \right) s(\psi) + \left(C_\ell^{\tilde{E}_i \tilde{B}_j} + C_\ell^{\tilde{E}_j \tilde{B}_i} \right) c(\psi), \quad (2.4)$$

$$C_\ell^{E_i B_j} - C_\ell^{E_j B_i} = -\left(C_\ell^{\tilde{E}_i \tilde{E}_j} + C_\ell^{\tilde{B}_i \tilde{B}_j} \right) s(\phi) + \left(C_\ell^{\tilde{E}_i \tilde{B}_j} - C_\ell^{\tilde{E}_j \tilde{B}_i} \right) c(\phi), \quad (2.5)$$

where $\psi = 2(\alpha_i + \alpha_j)$ and $\phi = 2(\alpha_i - \alpha_j)$. Substituting (2.2) and (2.3) in (2.5) and (2.4) respectively, and rearranging the terms we, get

$$\left(C_\ell^{E_i B_j} + C_\ell^{E_j B_i} \right) c(\psi) = \left(C_\ell^{E_i E_j} - C_\ell^{B_i B_j} \right) s(\psi) + C_\ell^{\tilde{E}_i \tilde{B}_j} + C_\ell^{\tilde{E}_j \tilde{B}_i}, \quad (2.6)$$

$$\left(C_\ell^{E_i B_j} - C_\ell^{E_j B_i} \right) c(\phi) = -\left(C_\ell^{E_i E_j} + C_\ell^{B_i B_j} \right) s(\phi) + C_\ell^{\tilde{E}_i \tilde{B}_j} - C_\ell^{\tilde{E}_j \tilde{B}_i}. \quad (2.7)$$

Summing (2.7) and (2.6) and isolating the $C_\ell^{\tilde{E}_i \tilde{B}_j}$

$$C_\ell^{\tilde{E}_i \tilde{B}_j} = (-c(2\alpha_i)s(2\alpha_j)C_\ell^{E_i E_j} + s(2\alpha_i)c(2\alpha_j)C_\ell^{B_i B_j} + c(2\alpha_i)c(2\alpha_j)C_\ell^{E_i B_j} - s(2\alpha_i)s(2\alpha_j)C_\ell^{E_j B_i}). \quad (2.8)$$

Taking ensemble averages² we obtain

$$\begin{aligned} \langle C_\ell^{E_i B_j} \rangle c(2\alpha_i)c(2\alpha_j) - \langle C_\ell^{E_j B_i} \rangle s(2\alpha_i)s(2\alpha_j) = \\ \langle C_\ell^{E_i E_j} \rangle c(2\alpha_i)s(2\alpha_j) - \langle C_\ell^{B_i B_j} \rangle s(2\alpha_i)c(2\alpha_j) \\ + \langle C_\ell^{\tilde{E}_i \tilde{B}_j, fg} \rangle + \langle C_\ell^{\tilde{E}_i \tilde{B}_j, CMB} \rangle. \end{aligned} \quad (2.9)$$

We neglect the $\langle C_\ell^{\tilde{E}_i \tilde{B}_j, CMB} \rangle$ contribution as Λ -CDM predicts a null CMB EB angular power spectrum. On the other hand, there is no theoretical model of the foregrounds' EB spectrum. Current measurements are compatible with a statistically null foregrounds' EB angular power spectrum. Thus, in this work, we have assumed $\langle C_\ell^{\tilde{E}_i \tilde{B}_j, fg} \rangle \approx 0$. Notice however, that this contribution could be taken into account with a proper model of the foregrounds' EB power spectrum [31, 32]. Finally, adding from (2.9) the resulting equation from exchanging the i and j indices in (2.9) times $s(2\alpha_i)s(2\alpha_j)/(c(2\alpha_i)c(2\alpha_j))$ and isolating the observed cross EB spectrum we find

$$C_\ell^{E_i B_j} = \frac{1}{c(4\alpha_i) + c(4\alpha_j)} (s(4\alpha_j)C_\ell^{E_i E_j} - s(4\alpha_i)C_\ell^{B_i B_j}). \quad (2.10)$$

Thus, the log-likelihood³ (assumed to be Gaussian) of all the possible EB -spectra is given in (2.11). The full log-likelihood contains an additional term proportional to the logarithm of the covariance determinant. In our methodology, this is assumed to be constant in each iteration, hence we can safely ignore it. However, this term is necessary in MCMC applications such as [29] as it is shown in [26].

$$-2 \log \mathcal{L} \propto \sum_{\ell=\ell_m}^{\ell_M} \left(\bar{C}_\ell^{EB} - \frac{s(4\bar{\alpha}_1)\bar{C}_\ell^{EE} - s(4\bar{\alpha}_2)\bar{C}_\ell^{BB}}{c(4\bar{\alpha}_1) + c(4\bar{\alpha}_2)} \right)^T \mathbf{C}_\ell^{-1} \left(\bar{C}_\ell^{EB} - \frac{s(4\bar{\alpha}_1)\bar{C}_\ell^{EE} - s(4\bar{\alpha}_2)\bar{C}_\ell^{BB}}{c(4\bar{\alpha}_1) + c(4\bar{\alpha}_2)} \right), \quad (2.11)$$

where \bar{C}_ℓ^{XY} , $\bar{\alpha}_1$ and $\bar{\alpha}_2$ are N^2 vectors given by

$$\bar{C}_\ell^{XY} = \left(C_\ell^{X_1 Y_1} \ C_\ell^{X_1 Y_2} \ \dots \ C_\ell^{X_1 Y_N} \ C_\ell^{X_2 Y_1} \ \dots \ C_\ell^{X_2 Y_N} \ \dots \ C_\ell^{X_N Y_1} \ \dots \ C_\ell^{X_N Y_N} \right)^T, \quad (2.12)$$

$$\bar{\alpha}_1 = (\alpha_1 \ \alpha_2 \ \dots \ \alpha_N \ \alpha_1 \ \dots \ \alpha_N \ \dots \ \alpha_1 \ \dots \ \alpha_N)^T, \quad (2.13)$$

$$\bar{\alpha}_2 = (\alpha_1 \ \alpha_1 \ \dots \ \alpha_1 \ \alpha_2 \ \dots \ \alpha_2 \ \dots \ \alpha_N \ \dots \ \alpha_N)^T, \quad (2.14)$$

ℓ_m and ℓ_M are the minimum and maximum multipoles involved in the likelihood, and \mathbf{C}_ℓ is the $N^2 \times N^2$ covariance matrix whose element $ijmn \equiv (i-1)N + j, (m-1)N + n$, i.e., the

²Notice that $\langle C_\ell^{\tilde{E}_i \tilde{B}_j} \rangle = \langle C_\ell^{\tilde{E}_i \tilde{B}_j, fg} \rangle + \langle C_\ell^{\tilde{E}_i \tilde{B}_j, CMB} \rangle$

³Notice that we are assuming no correlations among different multipoles since we saw that this assumption does not change the results.

element at the $(i-1)N + j$ row and $(m-1)N + n$ column, is given by

$$\begin{aligned}
C_{\ell,ijmn} = & \frac{1}{(2\ell+1)} \left[\langle C_{\ell}^{E_i E_m} \rangle \langle C_{\ell}^{B_j B_n} \rangle + \langle C_{\ell}^{E_i B_n} \rangle \langle C_{\ell}^{E_m B_j} \rangle \right. \\
& + \frac{s(4\alpha_m)}{c(4\alpha_m) + c(4\alpha_n)} \left(\langle C_{\ell}^{E_i B_m} \rangle \langle C_{\ell}^{B_j B_n} \rangle + \langle C_{\ell}^{E_i B_n} \rangle \langle C_{\ell}^{B_m B_j} \rangle \right) \\
& - \frac{s(4\alpha_n)}{c(4\alpha_m) + c(4\alpha_n)} \left(\langle C_{\ell}^{E_i E_m} \rangle \langle C_{\ell}^{B_j E_n} \rangle + \langle C_{\ell}^{E_i E_n} \rangle \langle C_{\ell}^{E_m B_j} \rangle \right) \\
& + \frac{s(4\alpha_i)}{c(4\alpha_i) + c(4\alpha_j)} \left(\langle C_{\ell}^{B_i E_m} \rangle \langle C_{\ell}^{B_j B_n} \rangle + \langle C_{\ell}^{B_i B_n} \rangle \langle C_{\ell}^{E_m B_j} \rangle \right) \\
& - \frac{s(4\alpha_j)}{c(4\alpha_i) + c(4\alpha_j)} \left(\langle C_{\ell}^{E_i E_m} \rangle \langle C_{\ell}^{E_j B_n} \rangle + \langle C_{\ell}^{E_i B_n} \rangle \langle C_{\ell}^{E_m E_j} \rangle \right) \\
& + \frac{s(4\alpha_j)s(4\alpha_n)}{(c(4\alpha_i) + c(4\alpha_j))(c(4\alpha_m) + c(4\alpha_n))} \left(\langle C_{\ell}^{E_i E_m} \rangle \langle C_{\ell}^{E_j E_n} \rangle + \langle C_{\ell}^{E_i E_n} \rangle \langle C_{\ell}^{E_m E_j} \rangle \right) \\
& + \frac{s(4\alpha_i)s(4\alpha_m)}{(c(4\alpha_i) + c(4\alpha_j))(c(4\alpha_m) + c(4\alpha_n))} \left(\langle C_{\ell}^{B_i B_m} \rangle \langle C_{\ell}^{B_j B_n} \rangle + \langle C_{\ell}^{B_i B_n} \rangle \langle C_{\ell}^{B_m B_j} \rangle \right) \\
& - \frac{s(4\alpha_j)s(4\alpha_m)}{(c(4\alpha_i) + c(4\alpha_j))(c(4\alpha_m) + c(4\alpha_n))} \left(\langle C_{\ell}^{E_i B_m} \rangle \langle C_{\ell}^{E_j B_n} \rangle + \langle C_{\ell}^{E_i B_n} \rangle \langle C_{\ell}^{B_m E_j} \rangle \right) \\
& \left. - \frac{s(4\alpha_i)s(4\alpha_n)}{(c(4\alpha_i) + c(4\alpha_j))(c(4\alpha_m) + c(4\alpha_n))} \left(\langle C_{\ell}^{B_i E_m} \rangle \langle C_{\ell}^{B_j E_n} \rangle + \langle C_{\ell}^{B_i E_n} \rangle \langle C_{\ell}^{E_m B_j} \rangle \right) \right]
\end{aligned} \tag{2.15}$$

Due to the lack of a reliable model of the foregrounds cross-spectra, we require a good estimator of it from the observed power spectra. In section 4.1 we study several estimators and show that binning the observed power spectrum leads to competent results.

Let us assume:

- The rotation angles are small, i.e., $\alpha \ll 1 \rightarrow s(\alpha) \sim \alpha$ and $c(\alpha) \sim 1$.
- The covariance matrix \mathbf{C} does not depend on α . To circumvent the mismatch induced by this approximation, we perform an iterative approach that updates the polarization angle in the covariance matrix with the one estimated in the previous step.

With these approximations, we achieve a linear system which enables us to obtain analytical equations from (2.11) to calculate the rotation angles. Moreover, the uncertainties can be evaluated from the Fisher matrix. This results in a very fast computational methodology.

In order to maximize the likelihood, we obtain N linear equations by taking the derivative of (2.11) with respect to each α , and equate each of them to zero. Thus, the rotation angles are the solution of the following linear system:

$$\mathbf{\Omega} \bar{\alpha} = \frac{1}{2} \bar{\eta}, \tag{2.16}$$

where $\mathbf{\Omega}$ is an $N \times N$ matrix and $\bar{\eta}$ is an N vector whose elements are:

$$\Omega_{ab} = \sum_{\ell=\ell_m}^{\ell_M} \left(\sum_{i=1}^N \sum_{m=1}^N C_{\ell}^{E_i E_a} \mathbf{C}_{\ell, iamb}^{-1} C_{\ell}^{E_m E_b} - \sum_{i=1}^N \sum_{m=1}^N C_{\ell}^{E_i E_a} \mathbf{C}_{\ell, iabm}^{-1} C_{\ell}^{B_b B_m} \right) \\ + \sum_{\ell=\ell_m}^{\ell_M} \left(\sum_{i=1}^N \sum_{m=1}^N C_{\ell}^{B_a B_i} \mathbf{C}_{\ell, aibm}^{-1} C_{\ell}^{B_b B_m} - \sum_{i=1}^N \sum_{m=1}^N C_{\ell}^{B_a B_i} \mathbf{C}_{\ell, aimb}^{-1} C_{\ell}^{E_m E_b} \right), \quad (2.17)$$

$$\eta_a = \sum_{\ell=\ell_m}^{\ell_M} \left(\sum_{i=1}^N \sum_{m=1}^N \sum_{n=1}^N C_{\ell}^{E_i E_a} \mathbf{C}_{\ell, iamn}^{-1} C_{\ell}^{E_m B_n} - \sum_{i=1}^N \sum_{m=1}^N \sum_{n=1}^N C_{\ell}^{B_a B_i} \mathbf{C}_{\ell, aimn}^{-1} C_{\ell}^{E_m B_n} \right). \quad (2.18)$$

The rotation angles' uncertainties are obtained from the Fisher matrix which is given as:

$$\mathbf{F} = 4\mathbf{\Omega} \quad (2.19)$$

Although the formalism exposed uses the information from all auto- and cross-spectra among all channels, one can limit the information to only cross-spectra or auto-spectra (i.e., no correlation among different channels). In the former case, the angles can be estimated using equation 2.16 and equations 2.17 and 2.18, excluding the terms where $i = a$, $m = b$ or $m = n$. In the latter case, with all the approximations made, the likelihood simplifies to

$$-2 \log \mathcal{L} \propto \sum_{\ell=\ell_m}^{\ell_M} (\bar{C}_{\ell,a}^{EB} - 2\bar{\alpha}(\bar{C}_{\ell,a}^{EE} - \bar{C}_{\ell,a}^{BB}))^T \mathbf{M}_{\ell}^{-1} (\bar{C}_{\ell,a}^{EB} - 2\bar{\alpha}(\bar{C}_{\ell,a}^{EE} - \bar{C}_{\ell,a}^{BB})), \quad (2.20)$$

where $\bar{C}_{\ell,a}^{XY}$ and $\bar{\alpha}$ are N vectors given by

$$\bar{C}_{\ell,a}^{XY} = \left(C_{\ell}^{X_1 Y_1} \ C_{\ell}^{X_2 Y_2} \ \dots \ C_{\ell}^{X_N Y_N} \right)^T, \quad (2.21)$$

$$\bar{\alpha} = (\alpha_1 \ \alpha_2 \ \dots \ \alpha_N)^T, \quad (2.22)$$

$$(2.23)$$

and the covariance matrix \mathbf{M}_{ℓ} is an $N \times N$ matrix whose elements are given as

$$M_{\ell,im} = \frac{1}{2\ell+1} \left[\langle C_{\ell}^{E_i E_m} \rangle \langle C_{\ell}^{B_i B_m} \rangle + \langle C_{\ell}^{E_i B_m} \rangle \langle C_{\ell}^{E_m B_i} \rangle \right. \\ + \tan(4\alpha_m) \left(\langle C_{\ell}^{E_i B_m} \rangle \langle C_{\ell}^{B_i B_m} \rangle - \langle C_{\ell}^{E_m B_i} \rangle \langle C_{\ell}^{E_i E_m} \rangle \right) \\ + \tan(4\alpha_i) \left(\langle C_{\ell}^{E_m B_i} \rangle \langle C_{\ell}^{B_i B_m} \rangle - \langle C_{\ell}^{E_i B_m} \rangle \langle C_{\ell}^{E_i E_m} \rangle \right) \\ + \frac{\tan(4\alpha_i) \tan(4\alpha_j)}{2} \left(\langle C_{\ell}^{E_i E_m} \rangle^2 + \langle C_{\ell}^{B_i B_m} \rangle^2 \right) \\ \left. - \frac{\tan(4\alpha_i) \tan(4\alpha_j)}{2} \left(\langle C_{\ell}^{E_i B_m} \rangle^2 + \langle C_{\ell}^{E_m B_i} \rangle^2 \right) \right]. \quad (2.24)$$

Analogous to the full spectra case, the rotation angles are obtained after solving the following linear system:

$$\mathbf{\Theta} \bar{\alpha} = \frac{1}{2} \bar{\xi}, \quad (2.25)$$

where Θ is an $N \times N$ matrix and $\bar{\xi}$ is an N vector whose elements are:

$$\Theta_{ab} = \sum_{\ell=\ell_m}^{\ell_M} \left(C_{\ell}^{EE_a} - C_{\ell}^{BB_a} \right) \mathbf{M}_{\ell,ab}^{-1} \left(C_{\ell}^{EE_b} - C_{\ell}^{BB_b} \right), \quad (2.26)$$

$$\xi_a = \sum_{m=1}^N \sum_{\ell=\ell_m}^{\ell_M} \left(C_{\ell}^{EE_a} - C_{\ell}^{BB_a} \right) \mathbf{M}_{\ell,am}^{-1} C_{\ell}^{EB_m}. \quad (2.27)$$

and the Fisher matrix is as

$$\mathbf{F}_a = 4\Theta. \quad (2.28)$$

In section 4.4 we study the differences among the results obtained when we use the total information available (cross and auto-spectra), only the cross-spectra information, or only the auto-spectra information.

3 Simulations

We have generated 100 simulations of the observed sky with LiteBIRD (see table 1). Each simulation has the following components: i) the sky signal, ii) the rotation angles and, iii) the instrumental noise. The sky signal is given as a collection of $N = 22$ (\mathbf{Q}, \mathbf{U}) pairs of frequency maps which contain the contribution of every significantly polarized physical emission. The rotation angles for a given simulation are generated from a distribution of zero mean and a covariance which correlates the angles within each instrument. Finally the instrumental noise is generated as white noise using sensitivities similar to LiteBIRD's (σ_{ν} column of table 1). For a given frequency ν the observed sky is calculated as follows:

$$\begin{pmatrix} \mathbf{Q}_{\nu}^{rot} \\ \mathbf{U}_{\nu}^{rot} \end{pmatrix} = \begin{pmatrix} \cos(2\alpha_{\nu}) & -\sin(2\alpha_{\nu}) \\ \sin(2\alpha_{\nu}) & \cos(2\alpha_{\nu}) \end{pmatrix} \begin{pmatrix} \mathbf{Q}_{\nu} \\ \mathbf{U}_{\nu} \end{pmatrix} + \begin{pmatrix} \mathbf{n}_{\nu}^Q \\ \mathbf{n}_{\nu}^U \end{pmatrix}, \quad (3.1)$$

where \mathbf{Q}_{ν} (\mathbf{U}_{ν}) is the map with the Q (U) sky signal, α_{ν} is the rotation angle at the ν channel and, \mathbf{n}_{ν}^Q and \mathbf{n}_{ν}^U are white noise maps. In the following subsections, we explain how the sky signal and the rotation angles are simulated.

3.1 Sky Signal

The multi-frequency sky signal maps are generated using the HEALPix⁴ scheme at a resolution of $N_{side} = 512$ (LiteBIRD's expected pixelization). The sky signal is composed of the CMB signal as well as the principal polarized foregrounds. Each component is simulated as follows:

CMB. CMB maps are drawn as Gaussian random realizations of theoretical angular power spectra. The power spectra are evaluated with the Boltzmann-solver CAMB [35] using the cosmological parameters from Planck18 results [36] and a null tensor-to-scalar ratio.

Polarized foregrounds. The primary polarized foreground sources are the synchrotron and the thermal dust emissions. We have generated three sets of multi-frequency maps of each foreground contaminant:

⁴Hierarchical Equal Area isoLatitude Pixelization, <https://healpix.sourceforge.io/> [34].

Instrument	ν (GHz)	FWHM (arcmin)	σ_ν ($\mu\text{K arcmin}$)
LFT	40	70.5	37.43
LFT	50	58.5	33.46
LFT	60	51.1	21.32
LFT	68a	41.6	19.91
LFT	68b	47.1	31.76
LFT	78a	36.9	15.56
LFT	78b	43.8	19.14
LFT	89a	33.0	12.28
LFT	89b	41.5	28.77
LFT	100	30.2	10.34
LFT	119	26.3	7.69
LFT	140	23.7	7.24
MFT	100	37.8	8.48
MFT	119	33.6	5.70
MFT	140	30.8	6.39
MFT	166	28.9	5.56
MFT	195	28.0	7.04
HFT	195	28.6	10.50
HFT	235	24.7	10.80
HFT	280	22.5	13.80
HFT	337	20.9	21.95
HFT	402	17.9	47.44

Table 1: LiteBIRD’s channels specifications: the instrument where the channel is located, ν the channel frequency, FWHM of the channel beam, σ_ν the sensitivity [33]. LFT, MFT and HFT refer to three LiteBIRD instruments and stand for Low, Medium and High Frequency Telescopes, respectively.

- Semi-realistic foregrounds (**s0d0**): the foregrounds are simulated using the **Python** software **PySM** [37]. In particular, we use the **s0** and **d0** models for the synchrotron and dust respectively. Both of these models assume constant spectral parameters over the sky. We have considered simple foreground models to avoid misidentifying residuals coming from improper foreground modelling as residuals from leftover rotation angles.
- Anisotropic Gaussian foregrounds (**AG**): we have generated anisotropic and Gaussian synchrotron and dust **Q** and **U** maps that satisfy the condition of having the same power spectra as the **s0d0** foregrounds⁵, see figure 1. The procedure is the following:
 - We calculate the **Q** and **U** local variance maps within 2° radius disks of the synchrotron and dust emission at 40 and 337 GHz respectively.
 - Then, we generate synchrotron and dust template maps as Gaussian samples from the former maps.
 - To obtain the synchrotron and thermal dust maps at LiteBIRD’s frequencies, we

⁵Note that these foregrounds do not need to follow the **s0d0** spectral laws.

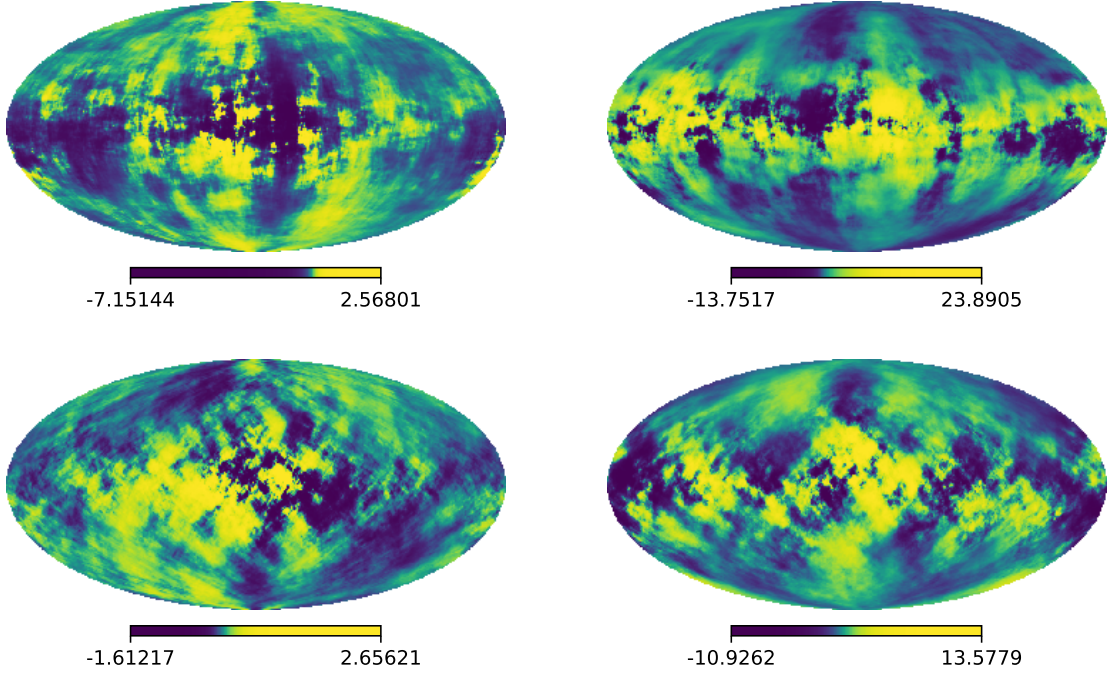


Figure 1: Synchrotron (left column) and thermal dust (right column) generated **AG** foregrounds at 100 GHz. The top and bottom rows corresponds to Q and U Stokes parameters respectively.

obtain the spherical harmonics $(e_{\ell m}, b_{\ell m})$, and re-scale them using:

$$\hat{e}_{\ell m, \nu} = \sqrt{\frac{E_{\ell, \nu}^{\text{s0d0}}}{E_{\ell}}} e_{\ell m},$$

$$\hat{b}_{\ell m, \nu} = \sqrt{\frac{B_{\ell, \nu}^{\text{s0d0}}}{B_{\ell}}} b_{\ell m}$$

where $X_{\ell, \nu}^{\text{s0d0}}$ is either the **s0d0** synchrotron or thermal dust $X \in \{E, B\}$ power spectrum at the frequency ν and X_{ℓ} is the power spectrum of the template maps.

- Isotropic Gaussian foregrounds (**IG**): we generated isotropic and Gaussian synchrotron and dust Q and U maps as follows:
 - We generated two Q and two U template maps by drawing Gaussian samples from the standard normal distribution.
 - Then, the Q and U synchrotron and thermal dust maps at LiteBIRD’s frequencies are obtained by re-scaling these template maps by the standard deviation of the corresponding **s0d0** foreground map.

To test the assumption of having a null EB foregrounds contribution, we have generated analogous versions of the **AG** and **IG** foregrounds with zero EB by removing their EB contribution. These foregrounds are denoted by **AGnEB** and **IGnEB**, respectively. For this purpose,

we modified the spherical harmonics coefficients of the B -mode ($b_{\ell m}$) as follows:

$$\hat{b}_{\ell m} = \beta_{\ell} b_{\ell m} + \gamma_{\ell} e_{\ell m}, \quad (3.2)$$

where $e_{\ell m}$ are the spherical harmonics coefficients of the E -mode and:

$$\beta_{\ell} = + \sqrt{\frac{C_{\ell}^{BB} C_{\ell}^{EE}}{C_{\ell}^{BB} C_{\ell}^{EE} - (C_{\ell}^{EB})^2}}, \quad (3.3)$$

$$\gamma_{\ell} = -\frac{C_{\ell}^{EB}}{C_{\ell}^{EE}} \beta_{\ell}. \quad (3.4)$$

These conditions satisfy:

$$\langle \hat{b}_{\ell m}, e_{\ell m} \rangle = C_{\ell}^{E\hat{B}} = \beta_{\ell} C_{\ell}^{EB} + \gamma_{\ell} C_{\ell}^{EE} = 0, \quad (3.5)$$

$$\langle \hat{b}_{\ell m}, \hat{b}_{\ell m} \rangle = C_{\ell}^{\hat{B}\hat{B}} = \beta_{\ell}^2 C_{\ell}^{BB} + \gamma_{\ell}^2 C_{\ell}^{EE} + 2\beta_{\ell} \gamma_{\ell} C_{\ell}^{EB} = C_{\ell}^{BB}. \quad (3.6)$$

Finally, both the CMB and foregrounds maps are convolved with Gaussian beams using the corresponding FWHM specified in table 1. Notice that the methodology described in section 2 is applied to full sky maps. It can also be applied to partial sky maps by calculating the angular power spectra using pseudo- C_{ℓ} algorithms such as [38]. The study of more realistic skies, i.e., more complex foregrounds and masking effects is studied in [26].

3.2 Rotation Angles

In this study, we have assumed that the rotation angles within a given telescope (e.g., the LFT) are correlated, but they are uncorrelated among different telescopes. In [39] they obtained the maximum uncertainty on the polarization angle calibration that does not introduce a bias in the r determination, taking into account possible correlations among different frequency channels, i.e., in the scenario we have assumed. We use values $(\sigma_{\alpha, \nu})$ compatible to those from Case 0 reported in [39] to obtain the distribution from which we sample the rotation angles.

The rotation angles distribution is a multi-variate Gaussian distribution with zero mean and the following covariance matrix:

$$\mathbf{C}_{\alpha} = \begin{pmatrix} M_{LFT} & 0 & 0 \\ 0 & M_{MFT} & 0 \\ 0 & 0 & M_{HFT} \end{pmatrix}, \quad (3.7)$$

where M_{ins} is the instrument covariance matrix whose elements are $M_{ins, ij} = \rho_{ij} \sigma_{\alpha, i} \sigma_{\alpha, j}$, $\sigma_{\alpha, i}$ is the miscalibration angle uncertainty of the i -th channel, and ρ_{ij} is the correlation coefficient among the channels i and j . Since we assumed full correlations among the channels at a given instrument $\rho_{ij} = 1 \forall i, j$. Note that the most stringent requirements are found when the channels are fully correlated. Therefore, the uncertainties are lower than in other cases leading to smaller rotation angles. However, it is worth mentioning that the requirements do not provide the actual calibration uncertainties. Moreover, the expected calibration uncertainties are smaller than the requirements for the least favourable scenario (i.e., no correlation among channels [39]).

One can generate samples with the covariance properties of \mathbf{C}_α using the Cholesky decomposition. \mathbf{C}_α is a real positive-definite symmetric matrix, hence the lower-triangular matrix \mathbf{L} that satisfies $\mathbf{C}_\alpha = \mathbf{L}\mathbf{L}^T$ can be obtained by applying the Cholesky decomposition. Then, if \bar{x} is an N vector whose components are independent random samples derived from the standard Gaussian distribution, $\mathbf{L}\bar{x}$ is a sample vector from the $\mathcal{N}(0, \mathbf{C}_\alpha)$ distribution. Thus, the rotation angles for a given simulation are obtained as

$$\bar{\alpha} = \mathbf{L}\bar{x}. \quad (3.8)$$

4 Methodology Performance

In this section, we study the performance of the methodology introduced in section 2 using the 100 multi-frequency simulations described in section 3. Unless stated otherwise, we use the LiteBIRD-like simulations i.e., CMB+s0d0+Noise. In particular, we discuss the difficulties that arise from computing the covariance matrix from the observed spectra, and how to alleviate this problem, in section 4.1, as well as checking the convergence of the algorithm and the compatibility of the Fisher uncertainties with the error bars that can be estimated from the dispersion of the simulations in section 4.2. As a consistency test, in section 4.3 we also compare the results that can be obtained from a telescope-by-telescope analysis with the ones coming from the full set of channels. Those studies are performed using only the information from the auto-spectra. Finally, in section 4.4, we compare the results recovered in the three information cases considered: i) when both the cross- and auto-spectra information is used, ii) when only the cross-spectra are taken into account and, iii) when only auto-spectra are considered.

4.1 Building the Covariance Matrix from Observed Spectra

As previously mentioned, in the absence of a reliable model of the angular power spectra of Galactic foregrounds, we must calculate the covariance matrix from the observed data. Although this might be seen as a positive outcome since it makes our methodology model-independent, in practice, building the covariance matrix from observed spectra can introduce significant uncertainty and numerical instability. We have explored several approaches to mitigate this problem, namely, adjusting the multipole range to avoid the contribution of noise-dominated angular scales as well as using different binning strategies.

The power of our methodology lies on the combination of information from various frequency channels. However, each of these frequency bands has associated a different instrumental beam and noise, and thus, although the smaller angular scales might be accessible for some channels, they will be completely noise-dominated in others. The inclusion of these noise-dominated scales will severely affect the calculation of the covariance matrix, consequently limiting the performance of the whole methodology. Therefore, the first action to take is to tune the multipole range to balance the contribution of each channel. Note that, although the discussion presented below is specific to LiteBIRD, the same optimization process can be applied to any other instrumental configuration.

Looking at the current configuration of LiteBIRD's frequency bands (see table 1), the FWHM of its beams varies between 70 to 18 arcmin, with a typical resolution across channels of around 30 arcmin. Angular scales below the beam size are severely suppressed. Therefore, although the multipole range allowed by the expected LiteBIRD map resolution is approximately $[3, 1500]$ ⁶, we have explored limiting the maximum multipole to $\ell_M =$

⁶We decided to omit $\ell = 2$ because it was problematic for the inversion of the covariance matrix

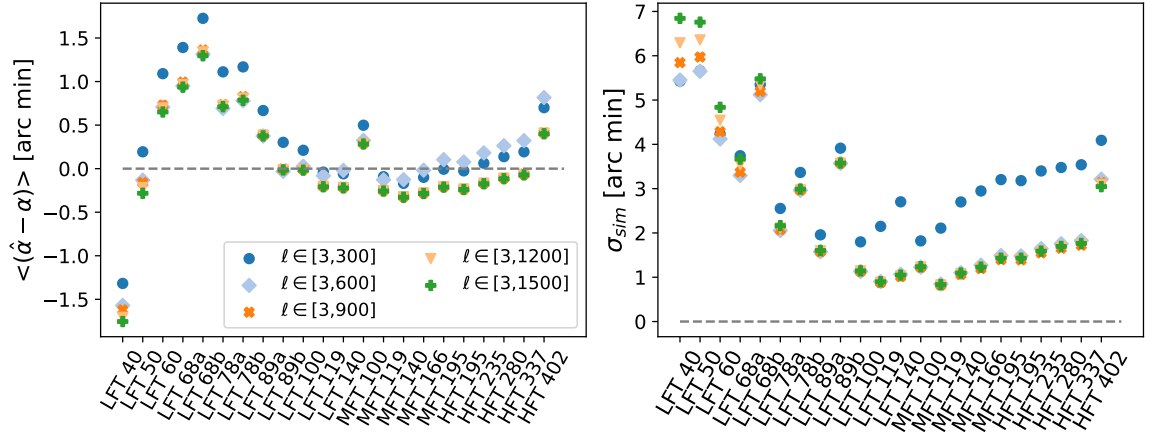


Figure 2: Left panel: Mean difference between the estimated and the genuine rotation angle per channel for different ℓ_M . Right panel: σ_{sim} uncertainty obtained as the simulations dispersion.

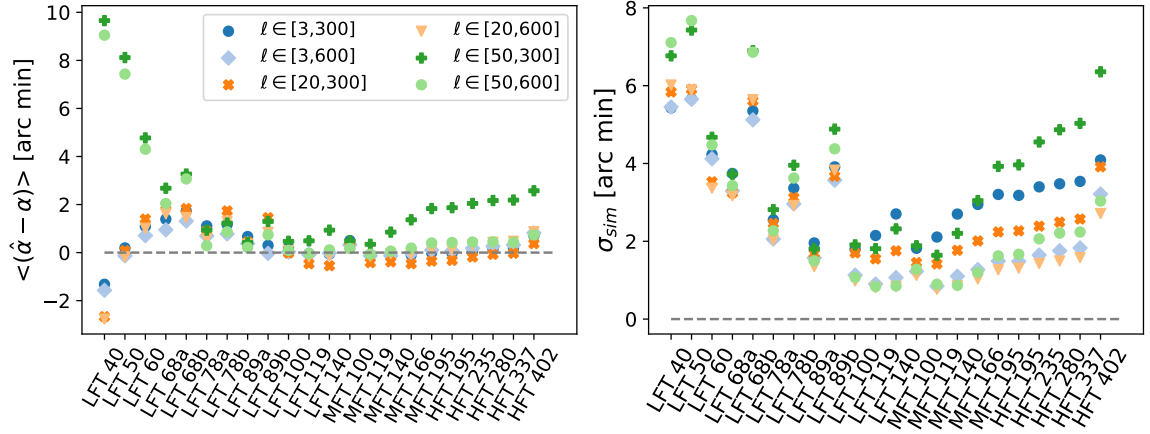


Figure 3: Left panel: Mean difference between the estimated and the genuine rotation angle per channel for different ℓ_m and ℓ_M cuts. Right panel: σ_{sim} uncertainty obtained as the simulations dispersion.

$\{300, 600, 900, 1200, 1500\}$. For completeness, we also evaluated the impact of applying $\ell_m = \{20, 50\}$ cuts to the performance of the estimation. Figures 2 and 3 show the effect that different combinations of these ℓ_m and ℓ_M intervals have on the bias per channel of the rotation angles estimates and on the σ_{sim} uncertainty calculated as the simulations' dispersion.

As can be seen in figure 2, exploiting the full multipole range allowed by the beam resolution is crucial to obtain a precise determination of rotation angles, but including information from scales beyond the beam resolution does not necessarily grant any additional signal-to-noise. In this way, fixing ℓ_M to match the angular resolution of the widest beam ($\ell_M = 600$) improves the performance on high-resolution channels without significantly deteriorating the results obtained for the low frequency bands of the LFT. In figure 3, we observe that cutting ℓ_m severely reduces the accuracy at the low frequency channels of the LFT. This is expected

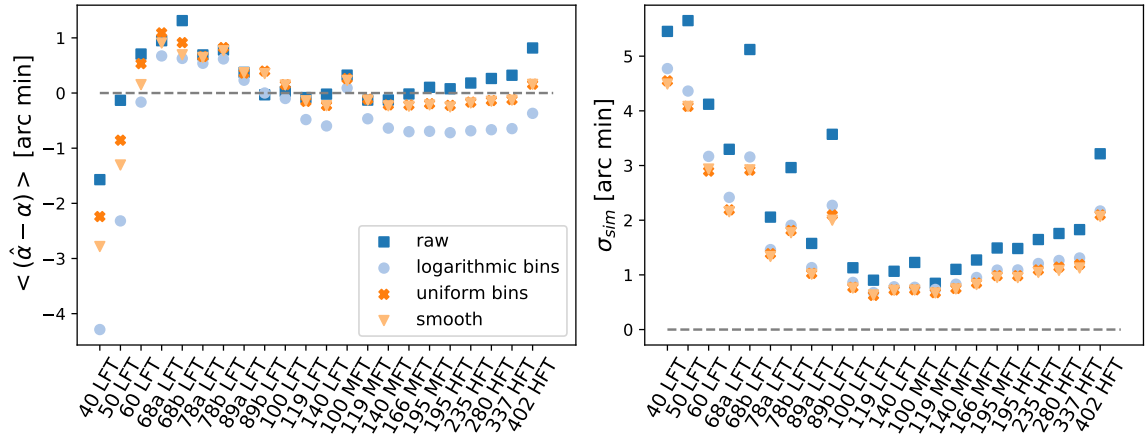


Figure 4: Left panel: Mean difference between the estimated and the genuine rotation angle per channel obtained using the raw power spectra (dark blue squares), smoothed power spectra (light orange triangles), logarithmically binned power spectra (light blue circles) and uniformly binned power spectra (orange crosses). Right panel: σ_{sim} uncertainty obtained as the simulations dispersion. The multipole range considered is $\ell \in [3, 600]$.

since, due to their lower resolution, most of the information from the LFT channels comes from the larger scales. On the contrary, the uncertainty on the rotation angle estimates from MFT bands is almost insensitive to ℓ_m cuts because, thanks to their narrower beams and better sensitivities, the main contribution comes from $\ell \gtrsim 150$ scales. Note that, because of their higher instrumental noises and broader beams, the lower frequencies of the LFT channels are expected to yield worse results. HFT channels behave as those from the MFT as they have narrow beams and share similar noise levels, except the 402 GHz channel where the sensitivity is worse, leading to larger uncertainties and less accurate estimates. Therefore, we decided to choose the multipole range that optimizes the rotation angle estimations at cosmological channels. According to these results, the best option would then be to work within the $\ell \in [3, 600]$ multipole interval. Hereinafter, the results will be obtained using this multipole interval.

So far, we have worked with the raw observed angular power spectra. In order to further reduce the noise in the calculation of the covariance matrix, and achieve an overall improvement of the results, we have also tried to smooth or bin the observed angular power spectra. To smooth the spectra, we have convolved the power spectra twice with two different square window functions, the first window function of 5ℓ length, and the second of 10ℓ length. We have also studied different binning schemes, e.g., using either uniform or logarithmically distributed bins (larger bins towards smaller angular scales). In figure 4 we show the optimal configuration for the uniform and logarithmic bins that we found (50 and 10 bins in the uniform and logarithm case respectively), as well as the results obtained by smoothing the spectra.

From figure 4 it is clear that either binning or smoothing the observed angular power spectra improves the uncertainty of the rotation angle estimates across all frequency bands. Although this improvement in precision does not necessarily translate into an improvement in accuracy (in fact, the mean errors obtained when applying a logarithmic binning tend to be greater than those obtained without applying any binning or smoothing), smoothing and

uniformly binning the observed spectra does indeed improve the overall performance of the methodology since, for cosmological channels, we obtain a better precision and comparable, or even slightly better, mean errors. Albeit smoothing the observed spectra seems to be a good option according to these results, it leads to larger discrepancies between Fisher uncertainties and the error bars that can be estimated from the simulations dispersion, aspects that will be discussed in the next subsection. Thus we favor uniformly binning the spectra over smoothing it. In the following all the results are obtained using the uniform binning scheme except as otherwise indicated.

4.2 Convergence and Uncertainty Estimation

One of the advantages that our method presents with respect to other similar methodologies [27–29] based on the same principles, but relying on MCMC implementations, is its speed. Although we have designed an iterative algorithm, once the input frequency maps are loaded and their spectra are calculated, each iteration only demands the inversion of the updated covariance matrix and solving the linear system. The inversion of the covariance matrix can be speeded up since the inversion of a $NN_\ell \times NN_\ell$ ⁷ matrix of diagonal $N_\ell \times N_\ell$ boxes is equivalent to the inversion of N_ℓ matrices of $N \times N$. In addition, as shown in figure 5, for the chosen binning configuration (50 uniformly distributed bins within $\ell \in [3, 600]$), the algorithm quickly converges to its final estimation after a couple of iterations. For some of the binning configurations and multipole intervals that lead to poorer angle estimates discussed in section 4.1, a larger number of iterations (of the order of tens) would be needed to converge to a stable solution. Therefore, the only time-consuming step is the initial reading and processing of frequency maps. This increase in speed does not entail a loss of accuracy since, as demonstrated in [40], both types of methodologies achieve comparable results.

As mentioned in section 2, our method can provide an estimate of the uncertainties associated to the best-fit values using the Fisher matrix approximation. Alternatively, the uncertainty can be characterized by applying the method to a set of simulations, and calculating the dispersion of the errors in the estimation of the rotation angles. If the likelihood is well behaved and posterior distributions are Gaussian-like, the σ obtained from the simulations dispersion and from the Fisher analysis should match. Checking the compatibility of these two estimates of the uncertainty is another of the tests we carried to evaluate the methodology performance.

In figure 6 we compare the σ obtained from the simulations dispersion and from a Fisher analysis for some of the binning and smoothing configurations discussed in section 4.1. As can be seen in this figure, although binning and smoothing slightly increases the Fisher uncertainties, it also helps to make both estimations more compatible. Given that uniformly binning the spectra, in addition to reducing the bias and the error bars estimated from simulations analysis (see section 4.1), also seems to yield the best agreement between Fisher uncertainties and the simulations dispersion, we chose this approach as our default configuration. Because of this good agreement we can trust that, when applied to different data, the Fisher matrix will give us a good estimate of the uncertainties associated to the best-fit values. We observe that, when the power spectra are either binned or smoothed, the simulations uncertainty is smaller than Fisher’s at low frequencies. These results seem to contradict the Cramer-Rao Bound. However, the Cramer-Rao Bound only applies when the likelihood is correctly defined. In our case, we do not have a model of the true covariance

⁷Notice that we are using auto-spectra, in the cross (total) spectra the covariance matrix is an $N(N-1)N_\ell \times N(N-1)N_\ell$ ($N^2N_\ell \times N^2N_\ell$) matrix.

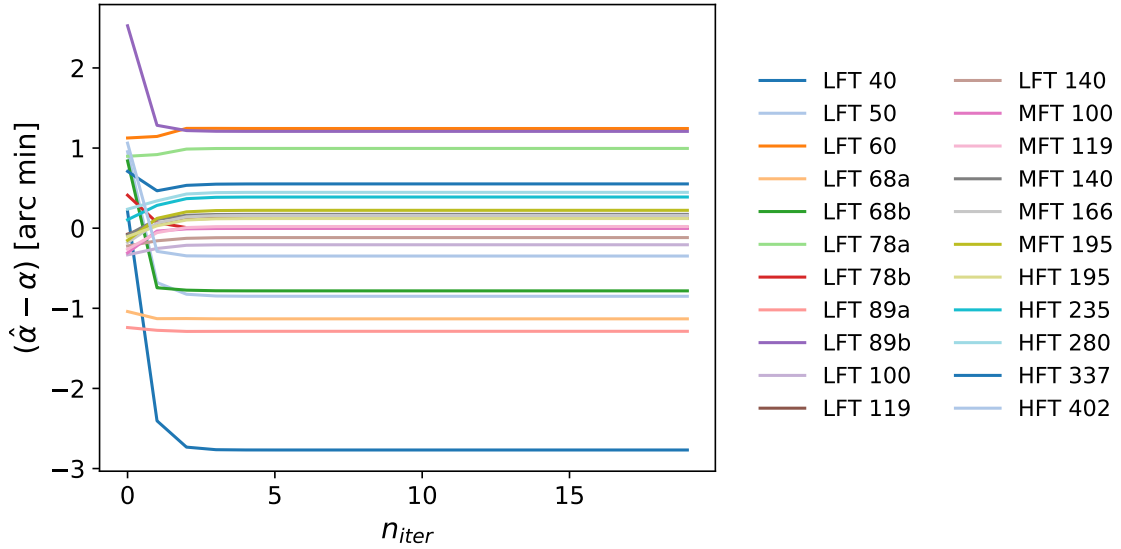


Figure 5: Difference between the estimated and the true rotation angle per iteration for one simulation using the default configuration (50 uniformly distributed bins within the $[3,600]$ multipole range). The results are shown for all LiteBIRD channels.

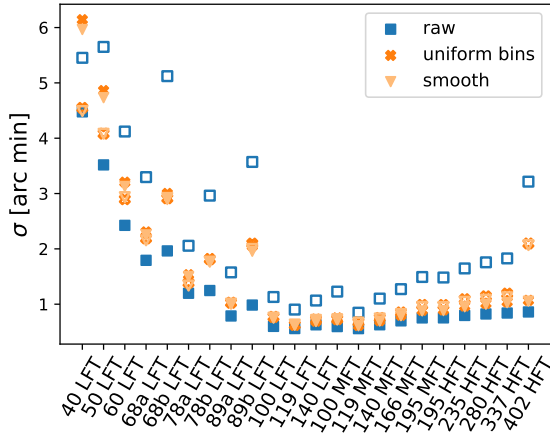


Figure 6: Comparison between the Fisher uncertainties (solid markers) and simulations uncertainties (empty markers) for some of the binning configurations and for the optimal multipole interval discussed in section 4.1.

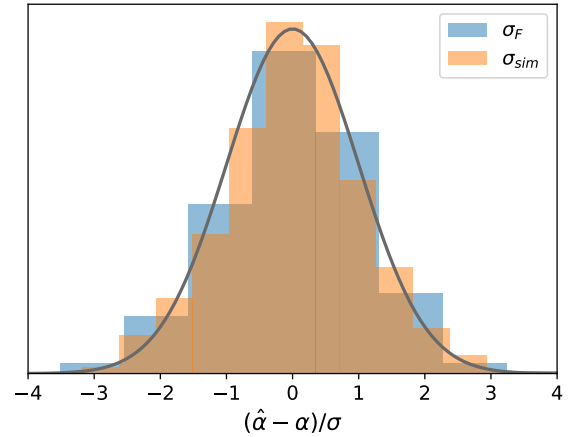


Figure 7: Distribution of the estimated and true rotation angles difference normalized by either the Fisher or the simulations uncertainty. The solid line shows the density function of the standard normal distribution.

matrix, and these results show that the approximations made in its calculations are not sufficient. In section 4.4 we analyze more in depth the role that the covariance matrix plays in the rotation angles estimations.

Figure 7 shows the distribution of the difference between the estimated and the genuine rotation angles normalized by either the Fisher or simulations uncertainty when the uniform binning scheme is used. All channels and simulations are included in the distribution. The

probability density function of the standard normal distribution is also shown for comparison. Both distributions have a mean and standard deviation compatible with the standard normal distribution showing that our results are unbiased and that Fisher provides a good estimation of the error. Furthermore, as can be seen in figure 8, Fisher confidence contours also reproduce correctly the correlations existing between different frequency bands (off-diagonal terms of the covariance matrix). As can be seen in this figure, in general, angle estimates are fairly independent across frequency channels, showing only a slight correlation between adjacent frequency bands, with the exception of dust-dominated bands ($\geq 100\text{GHz}$ channels of the LFT, MFT and HFT) where angles are strongly correlated amongst themselves.

4.3 Telescope-by-telescope Analysis

Until now we have estimated the rotation angles of all LiteBIRD’s frequency channels at once. However, a telescope-by-telescope determination of rotation angles will also be a reasonable approach since detectors are physically distributed in distinct telescopes, which might be systematically rotated in different orientations, and they target very different frequency ranges, each dealing with different weights of the Galactic foregrounds. Therefore, checking the compatibility of the results obtained from a telescope-by-telescope analysis with those from the joint analysis of all frequency bands will be, both a good consistency test, and a way to identify which telescope benefits more from the extra information coming from the others.

Figure 9 shows the comparison of the mean error and uncertainties in the estimation of rotation angles obtained from a telescope-by-telescope analysis with the previous results obtained from the joint analysis of all frequency bands (50 uniformly distributed bins between $\ell \in [3, 600]$). Like it was done in section 4.1 for the full set of channels, the multipole range and binning strategy has been tailored to optimize the performance of each individual telescope (LFT: $\ell \in [3, 600]$, MFT: $\ell \in [3, 1200]$ and, HFT: $\ell \in [20, 900]$ and uniform binning). This figure shows that the uncertainty in the estimation of rotation angles is slightly higher in the telescope-by-telescope analysis compared to the joint analysis. Regarding the bias, in the MFT and HFT the results are very similar but a small improvement is observed in the LFT channels. In light of these results, we conclude that a telescope-by-telescope analysis could constitute a good consistency test to check possible inconsistencies within a specific telescope.

4.4 Comparison among Different Likelihood Estimators

In section 2 we presented the formalism for three different estimators: i) when both the cross-spectra and auto-spectra information is used (total), ii) when only the cross-spectra is examined (cross) and, iii) when only the auto-spectra are considered (auto). Here, we have studied the accuracy of the rotation angles estimates and their uncertainties obtained in each case for the following sky models:

- CMB+N: 100 simulations of the sky with only CMB and white noise.
- CMB+s0d0+N: 100 simulations of the sky with CMB, the s0d0 foregrounds and white noise.
- CMB+s0d0+N \times 25: 100 simulations of the sky with CMB, the s0d0 foregrounds and white noise. The noise dispersion is scaled by a factor of 25.
- CMB+AG+N: 100 simulations of the sky with CMB, an anisotropic Gaussian foregrounds realization, and white noise.

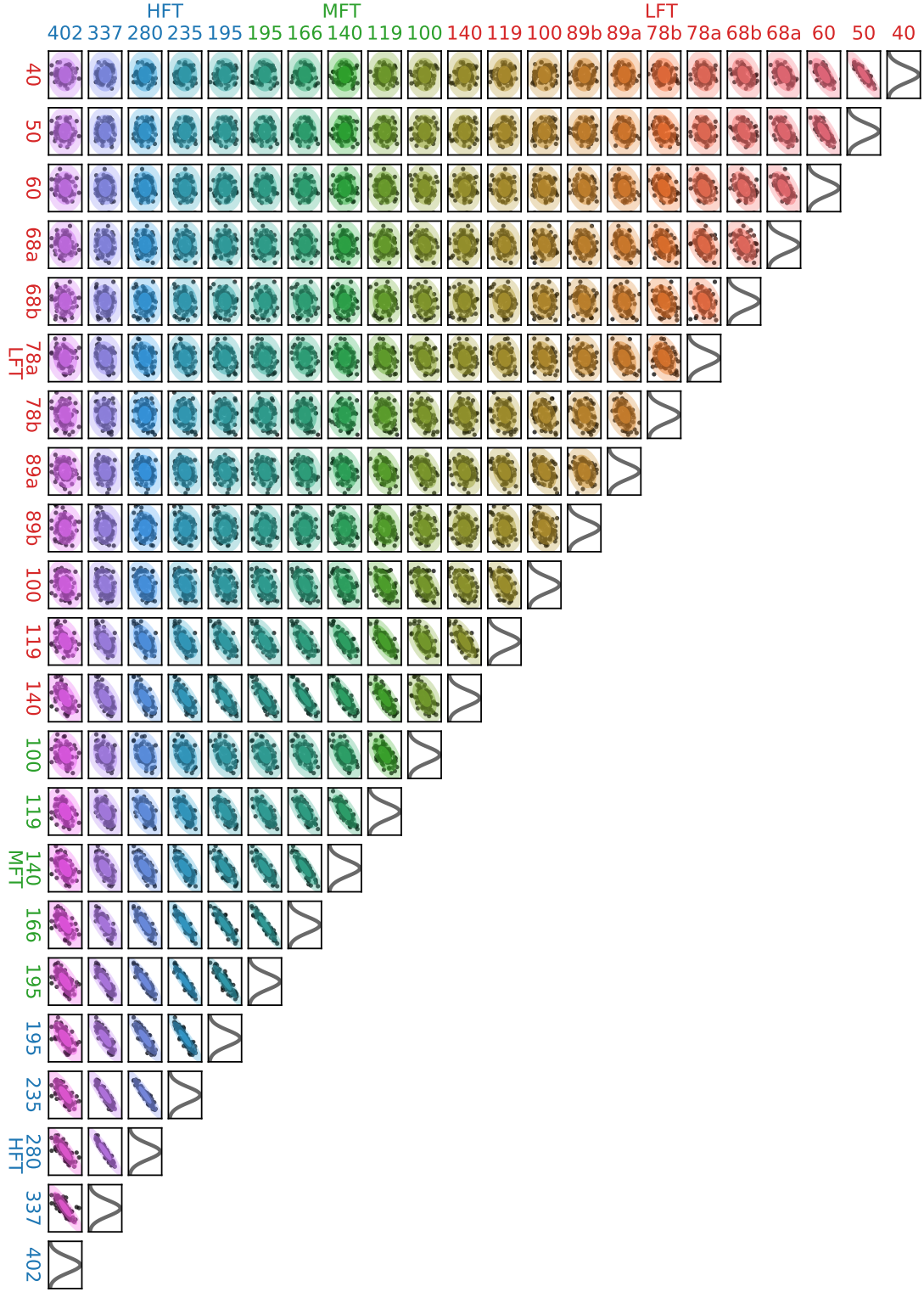


Figure 8: Correlation matrix of the rotation angles. On top of the point cloud from the simulations, we show the 1σ , 2σ and 3σ confidence contours obtained from the Fisher analysis.

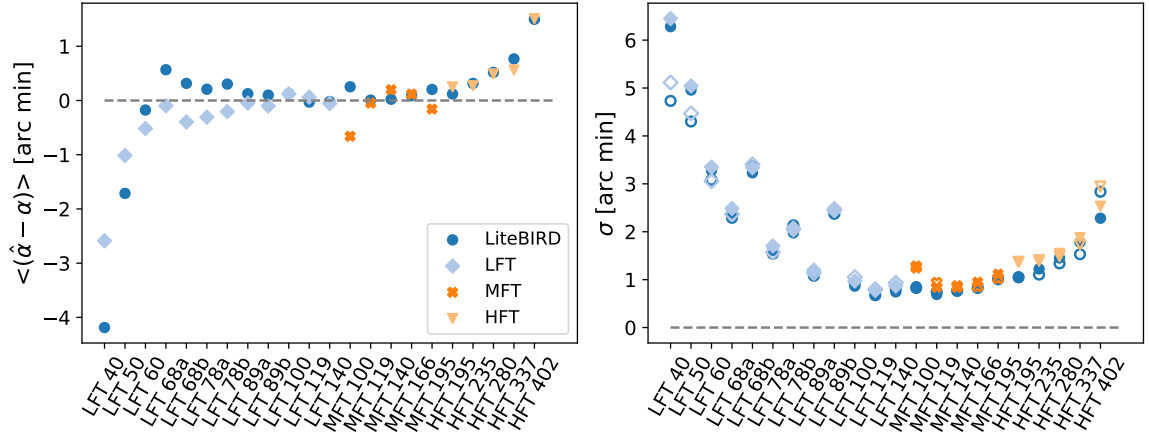


Figure 9: Left panel: Mean difference between the estimated and the genuine rotation angle per channel obtained from a telescope-by-telescope analysis compared to the previous results obtained from the joint analysis of all frequency bands. Right panel: Fisher (solid markers) and simulations (empty markers) uncertainties.

- CMB+AGnEB+N: 100 simulations of the sky with CMB, the previous anisotropic Gaussian foregrounds realization without its EB angular power spectrum contribution, and white noise.
- CMB+IG+N: 100 simulations of the sky with CMB, an isotropic Gaussian foregrounds realization, and white noise.
- CMB+IGnEB+N: 100 simulations of the sky with CMB, the previous isotropic Gaussian foregrounds realization without its EB angular power spectrum contribution, and white noise.

The results are shown in figures 10 and 11.

In the ideal scenario where there are no foregrounds (CMB+N, first row of figure 10) we find that the total, cross, and auto results show similar accuracies regarding the rotation angles estimates. Besides, the Fisher and simulations uncertainties agree in general quite well for the different cases. The uncertainties obtained in the cross and total cases are slightly lower at the lowest and highest frequencies with respect to the auto case. This is simply a consequence of having N times ($N - 1$ times) more information in the total (cross) case than in the auto case.

When s0d0 foregrounds are included (second row of figure 10) we observe that the estimates when the total information is used are biased. This effect arises due to numerical errors introduced by an improper characterization of the foregrounds in the covariance matrix, further enhanced after inverting the covariance matrix. Those numerical errors are significantly mitigated when either only the cross or the auto spectra are considered. However, the Fisher uncertainties obtained in the cross case underestimate considerably the uncertainty calculated from simulations. On the contrary, in the auto case the Fisher uncertainties resemble those computed from simulations and, they are smaller than the cross simulation uncertainties.

We have studied the same sky but scaling the noise by a factor of 25 (third row of figure 10). When the noise is the most important contribution instead of the foregrounds

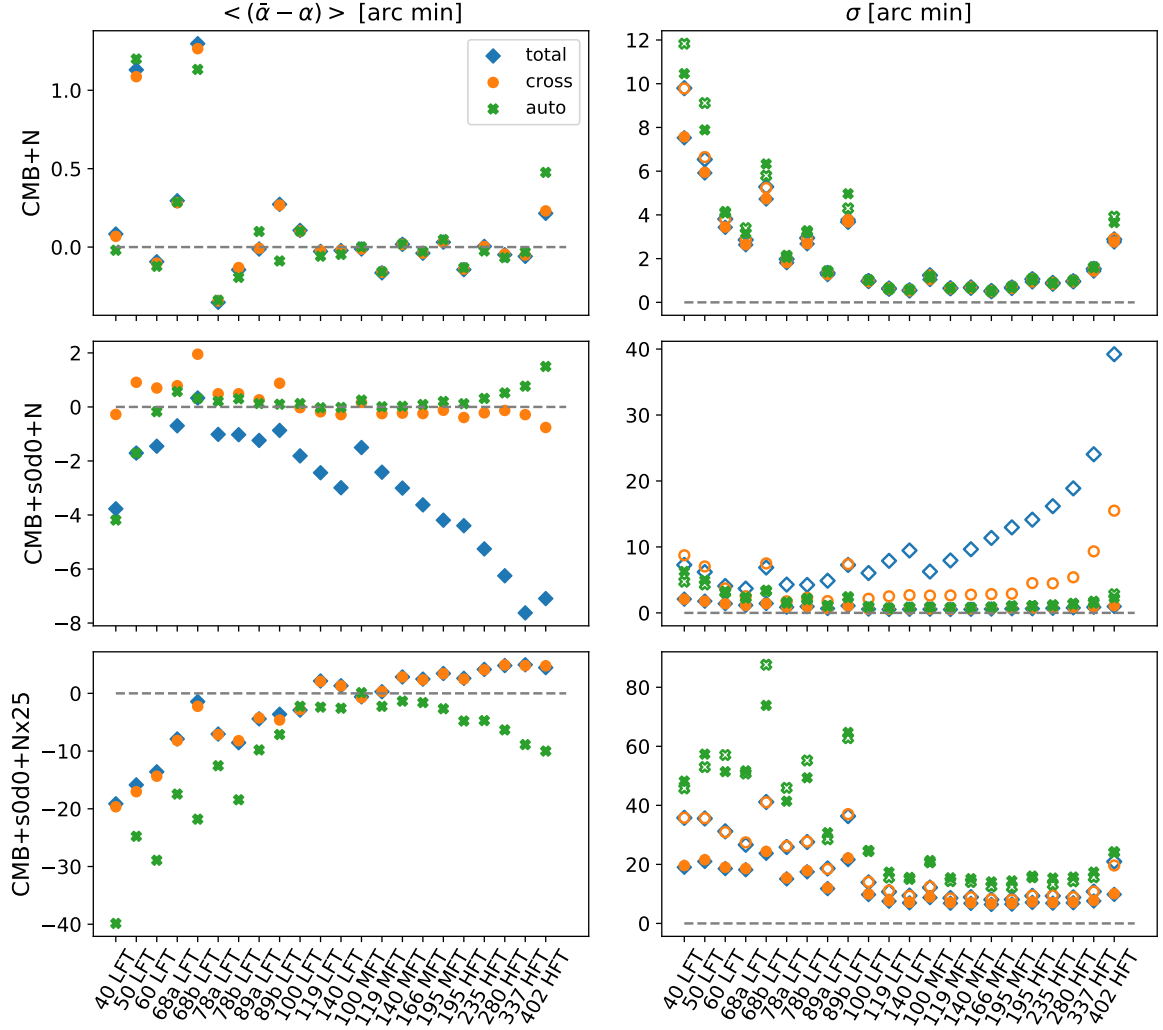


Figure 10: Estimations and uncertainties recovered when all spectra (total), only cross-spectra (cross), and only auto-spectra (auto) are considered in the CMB+N, CMB+s0d0+N and, CMB+s0d0+N \times 25 sky scenarios. Left panels: mean difference between the angle estimates and the genuine angles. Right panels: Fisher uncertainties (solid markers) and simulations uncertainties (empty markers).

the numerical errors are avoided and the results obtained using either the cross or the total information are very similar. The noise increment results in a poorer reconstruction of the polarization angles and larger uncertainties as expected. In this case the information from the auto spectra is very limited and the estimations and uncertainties are noticeably worse than in the cross and total cases. In comparison to the previous scenario, we find that for noise-dominated missions (e.g., Planck) the use of the cross or total information returns superior results. However, in the case of foregrounds-limit missions such as LiteBIRD the auto information retrieves accurate results with the lowest uncertainties. Thus, in the following sections, we limit the study to the auto case. Besides, this is the reason why only auto spectra are used in the previous subsections as well as in [40].

In addition, we have also analyzed two different skies, one where the foregrounds are

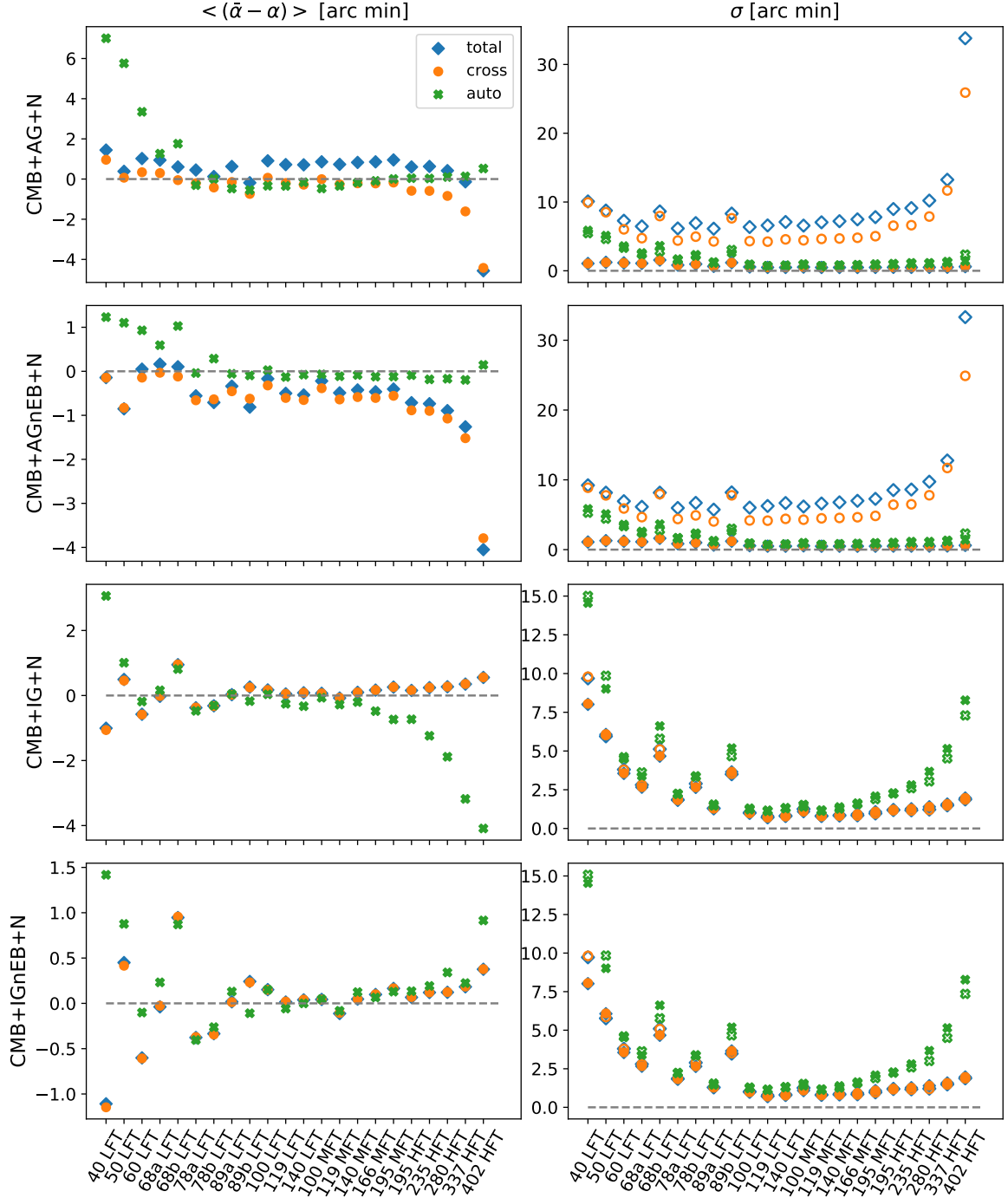


Figure 11: Estimations and uncertainties recovered when all spectra (total), only cross-spectra (cross), and only auto-spectra (auto) are considered in the CMB+AG+N, CMB+AGnEB+N, CMB+IG+N and, CMB+IGnEB+N sky scenarios. Left panels: mean difference between the angle estimates and the genuine angles. Right panels: Fisher uncertainties (solid markers) and simulations uncertainties (empty markers).

Gaussian and anisotropic, and the other Gaussian and isotropic (first and third row of figure 11 respectively). These cases were studied in order to understand the mismatch between the Fisher and simulations uncertainties in the cross case for the CMB+s0d0+N scenario. In the cross case, we find that this discrepancy arises due to the anisotropic nature of the foregrounds as it appears in the CMB+AG+N unlike in the CMB+IG+N. Besides, we observe that the total case is no longer biased. Therefore, we infer that the foregrounds anisotropy and non-gaussianity introduces some discrepancies in the recovered rotation angles since we are solving a Gaussian likelihood.

Finally, we have studied whether the assumption of having a zero EB foreground contribution could bias our results. This is performed by comparing the results of CMB+AG+N (CMB+IG+N) with those obtained using the CMB+AGnEB+N (CMB+IGnEB+N) skies. We find that the bias in the auto case is significantly reduced when there is no EB contribution in the simulated foregrounds, while the total and cross cases remain mostly the same. Thus, if the foregrounds EB is not negligible and not taken into account in the likelihood model, the auto solutions might be biased. However, as stated before, current measurements are compatible with a statistically zero foregrounds EB contribution. On the other hand, the removal of the EB foregrounds contribution does not impact the recovered Fisher and simulations uncertainty. This is a result of the contribution to the covariance matrix from the EB power spectrum terms being comparatively lower than those coming from the EE and BB power spectra.

5 Component Separation

The characterization of in-flight miscalibration angles is crucial to avoid systematics in CMB component separation analysis. Thus, one can use the results obtained with the above methodology to remove any possible bias introduced by a non-zero rotation angle. Here, we propose two different approaches to perform component separation adopting the information supplied by the above method. The component separation method B-SeCRET (Bayesian-Separation of Components and Residuals Estimate Tool) applied in this study is an improved version of the parametric Bayesian pixel-based methodology presented in [30]. The two approaches are the following:

- **Approach 1.** Component separation is applied to the signal maps after being de-rotated using the estimation of rotation angles. The parametric methodology is applied to estimate both the CMB and the foregrounds model parameters.
- **Approach 2.** Component separation is applied to the rotated signal maps. Thus, the rotation angles are included in the model parameters set. We include a Gaussian prior to help determine the rotation angles parameters. The prior's mean is fixed to the rotation angle estimate and the covariance matrix is the inverse of the calculated Fisher matrix obtained with auto-spectra.

It is relevant to highlight that the Approach 2 is also a map-based method to estimate the polarization rotation angles as opposed to the power spectrum-based method previously introduced.

This section is organized as follows. We describe the two component separation approaches used in section 5.1. We compare the polarization angle estimates from Approach 2 and from the power spectrum method in section 5.2. Finally, we contrast the CMB recovered using both approaches in section 5.3.

5.1 Component Separation Approaches

Here, we describe the two approaches used to perform component separation in section 5.1.1 and section 5.1.2. Both approaches are based on the parametric pixel-based method, B-SeCRET. Since we use a pixel-based method, a large computational time is needed to fit the simulated $N_{\text{side}} = 512$ maps. Thus, we have decided to downgrade the maps to $N_{\text{side}} = 64$ through spherical harmonics with a final resolution of 132 arc-minutes to perform the component separation analysis.

5.1.1 Approach 1

B-SeCRET is a Bayesian full-parametric pixel-based maximum likelihood method, which employs an affine-invariant ensemble sampler for Markov Chain Monte Carlo (MCMC) [41], to obtain the model parameters. Here we apply the methodology presented in [30] with the following modifications:

- Let θ be the set of model parameters. θ is the union of the disjoint sets of: 1) amplitudes parameters \mathcal{A} and, ii) spectral parameters \mathcal{B} . Instead of fitting both \mathcal{A} and \mathcal{B} at the same time, each set is fitted separately. First, the \mathcal{B} parameters are fixed to some initial values⁸ and the \mathcal{A} parameters are calculated. Then, the \mathcal{A} are fixed to the newly obtained values and the \mathcal{B} are fitted. This process is repeated iteratively until convergence is reached.
- Unlike the \mathcal{A} parameters which vary pixel-wise, the \mathcal{B} parameters can have a constant value within a sky region (i.e., clusters of pixels). Thus, we can obtain the value of \mathcal{B} in a given cluster of pixels instead of in a pixel. This procedure reduces significantly the statistical uncertainties of the methodology. Since the foregrounds are simulated using the s0d0 PySM model, that assumed constant spectral parameters over the sky, we have considered all the available sky as a cluster of pixels⁹.

The parametric models, $Q(\theta)$ and $U(\theta)$, that describe the Q and U signals at the pixel p are given by

$$\begin{pmatrix} Q(\theta) \\ U(\theta) \end{pmatrix}_p = \begin{pmatrix} c^Q \\ c^U \end{pmatrix}_p + \begin{pmatrix} a_s^Q \\ a_s^U \end{pmatrix}_p \frac{1}{u(\nu)} \left(\frac{\nu}{\nu_s} \right)^{\beta_s} + \begin{pmatrix} a_d^Q \\ a_d^U \end{pmatrix}_p \frac{1}{u(\nu)} \left(\frac{\nu}{\nu_d} \right)^{\beta_d-2} \frac{B(\nu, T_d)}{B(\nu_d, T_d)}, \quad (5.1)$$

where $\mathcal{A} = \{c^Q, c^U, a_s^Q, a_s^U, a_d^Q, a_d^U\}$ correspond to the Q and U amplitudes of the CMB, synchrotron and dust respectively, $\mathcal{B} = \{\beta_s, \beta_d, T_d\}$ are the spectral parameters, $u(\nu) = x(\nu)^2 \exp(x(\nu)) / (\exp(x(\nu)) - 1)^2$ and $x = h\nu / (KT_{\text{CMB}})$ is a unit conversion factor from thermodynamic to antenna units, $\nu_s = \nu_d = 150$ GHz are the synchrotron and dust pivot frequencies and $B(\nu, T)$ is Planck's law. The second (third) term on the RHS models the synchrotron (dust) contribution. Besides, we have applied Gaussian priors to the spectral parameters: $\beta_s \sim \mathcal{N}(-3.1, 0.3)$, $\beta_d \sim \mathcal{N}(1.56, 0.1)$, and $T_d \sim \mathcal{N}(21, 3)$.

5.1.2 Approach 2

In this approach the rotation angles α are included as models parameters as follows

$$\begin{pmatrix} Q \\ U \end{pmatrix}_p(\alpha, \theta) = \begin{pmatrix} \cos(2\alpha) & -\sin(2\alpha) \\ \sin(2\alpha) & \cos(2\alpha) \end{pmatrix} \begin{pmatrix} Q(\theta) \\ U(\theta) \end{pmatrix}_p. \quad (5.2)$$

⁸The initial values for the spectral parameters used are the most-likely values given in [42].

⁹The available sky considered is the one left by the galactic Planck mask with $f_{\text{sky}} = 0.60$, (HFI_Mask_GalPlane-apo0_2048_R2.00.fits downloaded from <https://pla.esac.esa.int/#maps> [43]).

Now, the model parameters are split in three categories, \mathcal{A} , \mathcal{B} and the rotation angles. As in Approach 1, the parameters are calculated iteratively:

1. First, the rotation angles α are set to the expected value of the prior, and the \mathcal{A} and \mathcal{B} parameters are calculated as in Approach 1. This step is equivalent to the Approach 1 if the expected value of the prior is equal to the rotation angles estimates.
2. Then, the sky signal parameters are fixed to the ones obtained in the previous step and the rotation angles are fitted.
3. The rotation angles are fixed to the results from the last step and this process is repeated until we reach convergence.

One can apply this procedure without using the prior information from the power spectrum based method. In that case, this approach is an independent method to estimate the polarization rotation angles. However, the use of priors helps significantly by speeding up the convergence of the MCMC since fewer iterations have to be performed in order to reach convergence. Thus, if there is no prior information regarding the calibration of the instrument, the results from the power spectrum based method can be used as prior information. Here we apply Gaussian priors on the rotation angles:

$$\pi(\alpha) = \frac{1}{\sqrt{(2\pi)^N |\mathbf{C}_a|}} \exp \left(-\frac{1}{2} (\alpha - \hat{\alpha})^T \mathbf{C}_a^{-1} (\alpha - \hat{\alpha}) \right)$$

where $\hat{\alpha}$ are the rotation angles estimated values and \mathbf{C}_a is the inverse of the rotation angles estimated Fisher matrix.

5.2 Polarization Rotation Angles Estimation Comparison

In this section we compare the rotation angle estimates obtained using the Approach 2 to those obtained with the power spectrum based method presented in section 2. For this purpose, we have applied the Approach 2 to the 100 rotated signal maps simulations. Figure 12 shows results using both methods.

We observe that the bias of the rotation angles estimates is reduced after applying Approach 2. These differences are further enhanced as the number of iterations increases. Besides, the right panel of figure 12 shows that the uncertainty of the rotation angles estimates obtained from simulations in the Approach 2 also decreases with the number of iteration. On the other hand, the uncertainties obtained with the power spectrum based method are slightly better than those recovered with Approach 2.

It is worth noting that, the rotation angles in Approach 2 are estimated using 60% of the sky unlike in the power spectrum method where the full sky was used in the analysis. On the one hand, larger sky fractions will lead to a reduction on the uncertainty of the rotation angles obtained with Approach 2. However, the inclusion of Galactic plane regions might yield biased estimates of the rotation angles due to incorrect foreground modelling. Moreover, the Approach 2 is computationally more expensive than the Approach 1 since there is an additional step involved in the fitting procedure. On the other hand, real data analyses of rotation angles with the power spectrum method will require at least a small mask to hide point sources and CO bright regions. Therefore, power spectra estimators algorithm's will be needed in order to obtain the true power spectra of the maps. This issue introduces more uncertainty on the rotation angles estimates from the power spectrum model. Hence both methods could be conceived as complementary and an useful consistency test.

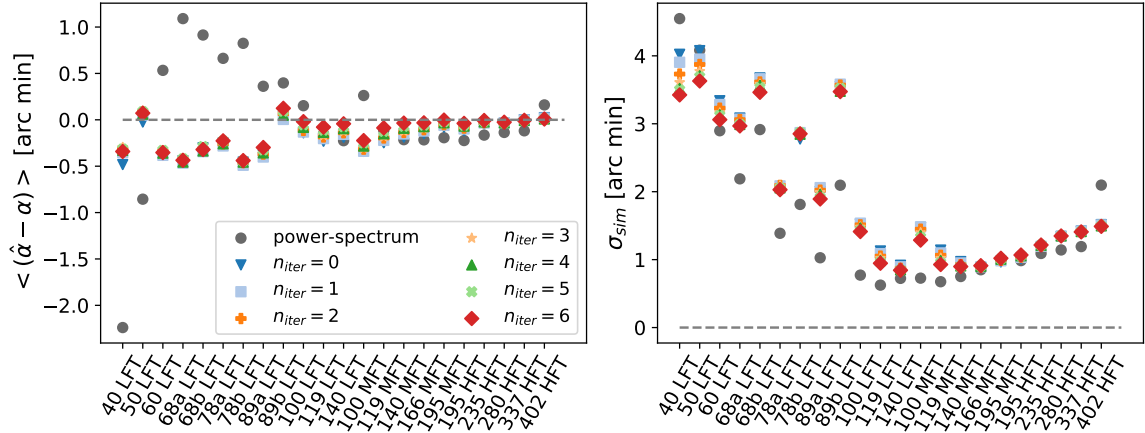


Figure 12: Left panel: Mean difference between the estimated and the actual rotation angle per channel obtained using the power spectrum method and the Approach 2. Right panel: σ_{sim} uncertainty obtained as the simulations dispersion. Since the Approach 2 is an iterative approach, the results from several iterations are displayed.

5.3 CMB Recovery Comparison

In this section, we compare the CMB maps recovered with both approaches, i.e., the CMB obtained after applying the Approach 1 to the de-rotated maps and the Approach 2 to the maps with this systematic (rotated maps). Moreover, we have applied the Approach 1 to the maps without the systematic (non-rotated maps), and the rotated map to study the improvement on the CMB cleaning after mitigating the effect of non-null polarization rotation angles. The angular power spectra is calculated using **ECLIPSE**, a fast Quadratic Maximum Likelihood estimator developed by [44]. The results from the 1st and 5th simulation are shown in figure 13 as representative examples of the results that we obtain.

From figure 13 it is clear that the worst results correspond to the Approach 1 applied to the rotated maps as expected since in this case we do not correct the effect induced by non-zero polarization angles. In order to study the systematic error left on the cleaned CMB maps, we show in the bottom panel the absolute relative residuals of the Approach 1 applied to the de-rotated maps as well as the Approach 2 applied to the rotated maps with respect to the non-rotated maps. The residuals of cleaned CMB maps using both Approach 1 and Approach 2 are of the order of a 1% and are compatible between them. Although the Approach 2 might provide a better estimation of the rotation angles, both approaches return similar systematic residuals. The rotation angle estimates from the power spectrum method are sufficiently accurate so as to mitigate most of the systematic induced in the CMB. The slight improvement in the angle estimation by Approach 2 does not lead to a better cleaning of the CMB. The systematic residuals left do not bias the tensor-to-scalar ratio r recovered from the cleaned CMB maps as shown in [40].

6 Conclusions

We have introduced an iterative angular power spectra maximum likelihood-based method to calculate the polarization rotation angles from the multi-frequency signal by nulling the EB power spectrum. Two major assumptions are made: i) the rotation angles are small ($\leq 6^\circ$),

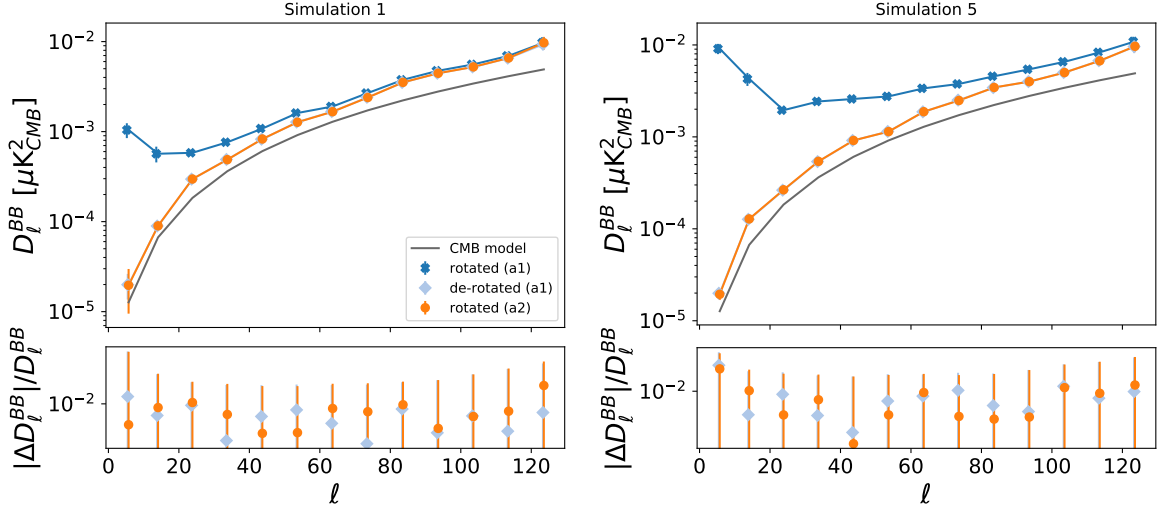


Figure 13: B -power spectrum from cleaned CMB maps obtained using the Approach 2 (orange circles) and the Approach 1 on the rotated (dark blue stars) and the de-rotated maps (light blue diamonds). The bottom panel displays the absolute relative residuals of the de-rotated (a1) as well as rotated (a2) with respect to the non-rotated case. The black line corresponds to the CMB B -power spectrum model. The difference between the model and the recovered power spectrum appears due to a non-removal of the noise bias.

and, ii) the covariance matrix does not depend on the rotation angles. Under this framework, we obtain analytical equations for both the angles and their uncertainties, which leads to a very fast computational method.

We have studied the performance of this methodology using sky simulations of a LiteBIRD-like experiment. These studies demonstrate that binning the observed spectra seems to be enough to overcome the lack of a reliable model for the angular power spectra of Galactic foregrounds for the calculation of the covariance matrix, and that, for the typical noise levels expected for next-generation experiments, the methodology will provide an unbiased estimation of rotation angles with a few arcminutes precision. The comparison of the full-instrument versus a telescope-by-telescope analysis also showed the power of our multi-frequency approach, since the overall uncertainties improve when information from different bands are combined.

Although the formalism is capable of exploiting all combinations of EB cross-spectra in combination with auto-spectra, we found that rotation angles estimated in this case are biased for typical sky simulations. This discrepancy comes from numerical errors that arise from approximating the theoretical power spectra in the covariance matrix calculation with the actual observed power spectra. We showed that these numerical instabilities disappear when the noise is larger than the foregrounds contribution. We found that for noise-dominated experiments it is better to use all available information (i.e., cross-spectra and auto-spectra) whereas, for foreground-dominated experiments such as LiteBIRD, limiting the information to only the auto-spectra provides results with smaller uncertainties.

Moreover, we have proposed two different approaches with which the rotation angles results from this methodology can be employed in the component separation analysis to remove any systematic error in the CMB cleaning. In Approach 1 we apply the B-SeCRET methodology to the signal maps de-rotated with the rotation angle estimates. In Approach

2, we include the rotation angles as model parameters and use the results from the power spectrum methodology as prior information. The Approach 2 can also be used as an independent method to calculate the rotation angles. However, the prior information from the power spectrum method helps significantly with the MCMC convergence. We found that the Approach 2 improves the accuracy in the estimation of the rotation angles, but returns slightly higher uncertainties. Finally, we have compared the CMB recovered using both Approach 1 and Approach 2 with the cleaned CMB obtained from signal maps without any rotation angles. We found that the residuals from both approaches are compatible and of the order of the 1% at the power spectrum level.

Acknowledgments

EdIH acknowledges financial support from the *Concepción Arenal Programme* of the Universidad de Cantabria. PDP acknowledges financial support from the *Formación del Profesorado Universitario (FPU) programme* of the Spanish Ministerio de Ciencia, Innovación y Universidades. We acknowledge Santander Supercomputación support group at the Universidad de Cantabria, member of the Spanish Supercomputing Network, who provided access to the Altamira Supercomputer at the Instituto de Física de Cantabria (IFCA-CSIC) for performing simulations/analyses. The authors would like to thank the Spanish Agencia Estatal de Investigación (AEI, MICIU) for the financial support provided under the projects with references PID2019-110610RB-C21, ESP2017-83921-C2-1-R and AYA2017-90675-REDC, cofunded with EU FEDER funds, and also acknowledge the funding from Unidad de Excelencia María de Maeztu (MDM-2017-0765). Some of the results in this paper have been derived using CAMB [35], ECLIPSE [44], and the healpy [34], emcee [41], PySM [37], and matplotlib [45] Python packages.

References

- [1] Planck Collaboration, N. Aghanim, Y. Akrami, F. Arroja, M. Ashdown, J. Aumont et al., *Planck 2018 results. I. Overview and the cosmological legacy of Planck*, *A&A* **641** (2020) [A1](#) [[1807.06205](#)].
- [2] P. Ade, J. Aguirre, Z. Ahmed, S. Aiola, A. Ali, D. Alonso et al., *The Simons Observatory: science goals and forecasts*, *J. Cosmology Astropart. Phys.* **2019** (2019) 056 [[1808.07445](#)].
- [3] K. Abazajian, G. Addison, P. Adshead, Z. Ahmed, S. W. Allen, D. Alonso et al., *CMB-S4 Science Case, Reference Design, and Project Plan*, *arXiv e-prints* (2019) [arXiv:1907.04473](#) [[1907.04473](#)].
- [4] S. Hanany, M. Alvarez, E. Artis, P. Ashton, J. Aumont, R. Aurlen et al., *PICO: Probe of Inflation and Cosmic Origins*, in *Bulletin of the American Astronomical Society*, vol. 51, p. 194, Sept., 2019, [1908.07495](#).
- [5] W. Hu, M. M. Hedman and M. Zaldarriaga, *Benchmark parameters for CMB polarization experiments*, *Phys. Rev. D* **67** (2003) 043004 [[astro-ph/0210096](#)].
- [6] M. Shimon, B. Keating, N. Ponthieu and E. Hivon, *CMB polarization systematics due to beam asymmetry: Impact on inflationary science*, *Phys. Rev. D* **77** (2008) 083003 [[0709.1513](#)].
- [7] A. P. S. Yadav, M. Su and M. Zaldarriaga, *Primordial B-mode diagnostics and self-calibrating the CMB polarization*, *Phys. Rev. D* **81** (2010) 063512 [[0912.3532](#)].
- [8] M. Hazumi et al., *Probing Cosmic Inflation with the LiteBIRD Cosmic Microwave Background Polarization Survey*, *Progress of Theoretical and Experimental Physics* (to be submitted) .

- [9] J. Aumont, J. F. Macías-Pérez, A. Ritacco, N. Ponthieu and A. Mangilli, *Absolute calibration of the polarisation angle for future CMB B-mode experiments from current and future measurements of the Crab nebula*, [*A&A* **634** \(2020\) A100](#) [[1911.03164](#)].
- [10] T. Matsumura, P. Ade, D. Barkats, D. Barron, J. O. Battle, E. M. Bierman et al., *Absolute polarization angle calibration using polarized diffuse Galactic emission observed by BICEP*, in *Millimeter, Submillimeter, and Far-Infrared Detectors and Instrumentation for Astronomy V*, vol. 7741 of *Society of Photo-Optical Instrumentation Engineers (SPIE) Conference Series*, p. 77412O, July, 2010, DOI [[1007.2874](#)].
- [11] J. T. Sayre, C. L. Reichardt, J. W. Henning, P. A. R. Ade, A. J. Anderson, J. E. Austermann et al., *Measurements of B -mode polarization of the cosmic microwave background from 500 square degrees of SPTpol data*, [*Phys. Rev. D* **101** \(2020\) 122003](#) [[1910.05748](#)].
- [12] H. C. Chiang, P. A. R. Ade, D. Barkats, J. O. Battle, E. M. Bierman, J. J. Bock et al., *Measurement of Cosmic Microwave Background Polarization Power Spectra from Two Years of BICEP Data*, [*ApJ* **711** \(2010\) 1123](#) [[0906.1181](#)].
- [13] S. Adachi, M. A. O. Aguilar Faúndez, K. Arnold, C. Baccigalupi, D. Barron, D. Beck et al., *A Measurement of the Degree Scale CMB B-mode Angular Power Spectrum with POLARBEAR*, *arXiv e-prints* (2019) arXiv:1910.02608 [[1910.02608](#)].
- [14] S. Naess, M. Hasselfield, J. McMahon, M. D. Niemack, G. E. Addison, P. A. R. Ade et al., *The Atacama Cosmology Telescope: CMB polarization at $200 < l < 9000$* , [*J. Cosmology Astropart. Phys.* **2014** \(2014\) 007](#) [[1405.5524](#)].
- [15] B. G. Keating, M. Shimon and A. P. S. Yadav, *Self-calibration of Cosmic Microwave Background Polarization Experiments*, [*ApJ* **762** \(2013\) L23](#) [[1211.5734](#)].
- [16] F. Nati, M. J. Devlin, M. Gerbino, B. R. Johnson, B. Keating, L. Pagano et al., *POLOCALC: A Novel Method to Measure the Absolute Polarization Orientation of the Cosmic Microwave Background*, [*Journal of Astronomical Instrumentation* **6** \(2017\) 1740008](#) [[1704.02704](#)].
- [17] B. R. Johnson, C. J. Vourch, T. D. Drysdale, A. Kalman, S. Fujikawa, B. Keating et al., *A CubeSat for Calibrating Ground-Based and Sub-Orbital Millimeter-Wave Polarimeters (CalSat)*, [*Journal of Astronomical Instrumentation* **4** \(2015\) 1550007](#) [[1505.07033](#)].
- [18] F. J. Casas, E. Martínez-González, J. Bermejo-Ballesteros, S. García, J. Cubas, P. Vielva et al., *L2-CalSat: A Calibration Satellite for Ultra-Sensitive CMB Polarization Space Missions*, [*Sensors* **21** \(2021\) 3361](#).
- [19] F. J. Casas, E. Martínez-González, J. Bermejo-Ballesteros, S. García, J. Cubas, P. Vielva et al., *L2-CalSat: A Calibration Satellite for Ultra-Sensitive CMB Polarization Space Missions*, [*Sensors* **21** \(2021\) 3361](#).
- [20] L. Pogosian, M. Shimon, M. Mewes and B. Keating, *Future CMB constraints on cosmic birefringence and implications for fundamental physics*, [*Phys. Rev. D* **100** \(2019\) 023507](#) [[1904.07855](#)].
- [21] A. Lue, L. Wang and M. Kamionkowski, *Cosmological Signature of New Parity-Violating Interactions*, [*Phys. Rev. Lett.* **83** \(1999\) 1506](#) [[astro-ph/9812088](#)].
- [22] A. Kosowsky and A. Loeb, *Faraday Rotation of Microwave Background Polarization by a Primordial Magnetic Field*, [*ApJ* **469** \(1996\) 1](#) [[astro-ph/9601055](#)].
- [23] T. Namikawa, Y. Guan, O. Darwish, B. D. Sherwin, S. Aiola, N. Battaglia et al., *Atacama Cosmology Telescope: Constraints on cosmic birefringence*, [*Phys. Rev. D* **101** \(2020\) 083527](#) [[2001.10465](#)].
- [24] F. Bianchini, W. L. K. Wu, P. A. R. Ade, A. J. Anderson, J. E. Austermann, J. S. Avva et al., *Searching for Anisotropic Cosmic Birefringence with Polarization Data from SPTpol*, *arXiv e-prints* (2020) arXiv:2006.08061 [[2006.08061](#)].

- [25] A. Gruppuso, D. Molinari, P. Natoli and L. Pagano, *Planck 2018 constraints on anisotropic birefringence and its cross-correlation with cmb anisotropy*, *Journal of Cosmology and Astroparticle Physics* **2020** (2020) 066.
- [26] P. Diego-Palazuelos et al., *Fast Analytical Maximum Likelihood Solution to the Simultaneous Determination of Cosmic Birefringence and Miscalibrated Polarization Angles*, Manuscript in preparation (2022) .
- [27] Y. Minami, H. Ochi, K. Ichiki, N. Katayama, E. Komatsu and T. Matsumura, *Simultaneous determination of the cosmic birefringence and miscalibrated polarisation angles from CMB experiments*, *arXiv e-prints* (2019) arXiv:1904.12440 [[1904.12440](#)].
- [28] Y. Minami, *Determination of miscalibrated polarization angles from observed cosmic microwave background and foreground EB power spectra: Application to partial-sky observation*, *Progress of Theoretical and Experimental Physics* **2020** (2020) 063E01 [[2002.03572](#)].
- [29] Y. Minami and E. Komatsu, *Simultaneous determination of the cosmic birefringence and miscalibrated polarization angles II: Including cross frequency spectra*, *arXiv e-prints* (2020) arXiv:2006.15982 [[2006.15982](#)].
- [30] E. de la Hoz, P. Vielva, R. B. Barreiro and E. Martínez-González, *On the detection of CMB B-modes from ground at low frequency*, *J. Cosmology Astropart. Phys.* **2020** (2020) 006 [[2002.12206](#)].
- [31] Planck Collaboration, R. Adam, P. A. R. Ade, N. Aghanim, M. Arnaud, J. Aumont et al., *Planck intermediate results. XXX. The angular power spectrum of polarized dust emission at intermediate and high Galactic latitudes*, *A&A* **586** (2016) A133 [[1409.5738](#)].
- [32] Planck Collaboration, Y. Akrami, M. Ashdown, J. Aumont, C. Baccigalupi, M. Ballardini et al., *Planck 2018 results. XI. Polarized dust foregrounds*, *A&A* **641** (2020) A11 [[1801.04945](#)].
- [33] M. Hazumi, P. A. R. Ade, A. Adler, E. Allys, K. Arnold, D. Auguste et al., *LiteBIRD satellite: JAXA's new strategic L-class mission for all-sky surveys of cosmic microwave background polarization*, in *Society of Photo-Optical Instrumentation Engineers (SPIE) Conference Series*, vol. 11443 of *Society of Photo-Optical Instrumentation Engineers (SPIE) Conference Series*, p. 114432F, Dec., 2020, DOI [[2101.12449](#)].
- [34] K. M. Górski, E. Hivon, A. J. Banday, B. D. Wandelt, F. K. Hansen, M. Reinecke et al., *HEALPix: A Framework for High-Resolution Discretization and Fast Analysis of Data Distributed on the Sphere*, *ApJ* **622** (2005) 759 [[arXiv:astro-ph/0409513](#)].
- [35] A. Lewis and A. Challinor, *CAMB: Code for Anisotropies in the Microwave Background*, Feb., 2011.
- [36] Planck Collaboration, N. Aghanim, Y. Akrami, M. Ashdown, J. Aumont, C. Baccigalupi et al., *Planck 2018 results. VI. Cosmological parameters*, *A&A* **641** (2020) A6 [[1807.06209](#)].
- [37] B. Thorne, J. Dunkley, D. Alonso and S. Næss, *The Python Sky Model: software for simulating the Galactic microwave sky*, *MNRAS* **469** (2017) 2821 [[1608.02841](#)].
- [38] D. Alonso, J. Sanchez, A. Slosar and L. D. E. S. Collaboration, *A unified pseudo- c_ℓ framework*, *Monthly Notices of the Royal Astronomical Society* **484** (2019) 4127.
- [39] P. Vielva, E. Martínez-González, F. J. Casas et al., *Polarization angle requirements for CMB B-mode experiments. Application to the LiteBIRD satellite*, *Journal of Cosmology and Astroparticle Physics* (to be submitted) .
- [40] N. Krachmalnicoff, T. Matsumura, E. de la Hoz, S. Basak, A. Gruppuso, Y. Minami et al., *In-flight polarization angle calibration using C_ℓ^{EB} for LiteBIRD: blind calibration challenge and cosmological impact*, *Journal of Cosmology and Astroparticle Physics* (to be submitted) .
- [41] D. Foreman-Mackey, D. W. Hogg, D. Lang and J. Goodman, *emcee: The MCMC Hammer*, *PASP* **125** (2013) 306 [[1202.3665](#)].

- [42] Planck Collaboration, Y. Akrami, M. Ashdown, J. Aumont, C. Baccigalupi, M. Ballardini et al., *Planck 2018 results. IV. Diffuse component separation*, [A&A **641** \(2020\) A4 \[1807.06208\]](#).
- [43] P. A. Ade, N. Aghanim, M. Alves, C. Armitage-Caplan, M. Arnaud, M. Ashdown et al., *Planck 2013 results. I. Overview of products and scientific results*, *Astronomy & Astrophysics* **571** (2014) A1.
- [44] J. D. Bilbao-Ahedo, R. B. Barreiro, P. Vielva, E. Martínez-González and D. Herranz, *ECLIPSE: a fast Quadratic Maximum Likelihood estimator for CMB intensity and polarization power spectra*, [J. Cosmology Astropart. Phys. **2021** \(2021\) 034 \[2104.08528\]](#).
- [45] J. D. Hunter, *Matplotlib: A 2D Graphics Environment*, [Computing in Science and Engineering **9** \(2007\) 90](#).

P. III: In-flight polarization angle calibration for LiteBIRD: blind challenge and cosmological implications

N. Krachmalnicoff, T. Matsumura, **E. de la Hoz**, S. Basak, A. Gruppuso, Y. Minami, C. Baccigalupi, E. Komatsu, E. Martínez-González, P. Vielva, & LiteBIRD collaboration. *Journal of Cosmology and Astroparticle Physics*, 2022(01), 039

© IOP Publishing. This is an author-created, un-copyedited version of an article accepted for publication in *Journal of Cosmology and Astroparticle Physics*. OP Publishing Ltd is not responsible for any errors or omissions in this version of the manuscript or any version derived from it. The Version of Record is available online at:
<https://doi.org/10.1088/1475-7516/2022/01/039>

In-flight polarization angle calibration for LiteBIRD: blind challenge and cosmological implications

N. Krachmalnicoff,^{1,2,3} T. Matsumura,⁴ E. de la Hoz,^{5,6} S. Basak,⁷
A. Gruppuso,^{8,9} Y. Minami,¹⁰ C. Baccigalupi,^{1,2,3} E. Komatsu,^{11,4}
E. Martínez-González,⁵ P. Vielva,⁵ J. Aumont,¹² R. Aurlen,¹³
S. Azzoni,^{14,4} A. J. Banday,¹² R. B. Barreiro,⁵ N. Bartolo,^{15,16}
M. Bersanelli,^{17,18} E. Calabrese,¹⁹ A. Carones,^{20,21} F. J. Casas,⁵
K. Cheung,^{22,23,24} Y. Chinone,^{25,4} F. Columbro,^{26,27}
P. de Bernardis,^{26,27} P. Diego-Palazuelos,^{5,6} J. Errard,²⁸
F. Finelli,^{8,9} U. Fuskeland,¹³ M. Galloway,¹³
R. T. Genova-Santos,^{29,30} M. Gerbino,³¹ T. Ghigna,^{14,4}
S. Giardiello,³² E. Gjerløw,¹³ M. Hazumi,^{33,34,4,35}
S. Henrot-Versillé,³⁶ T. Kisner,²⁴ L. Lamagna,^{26,27} M. Lattanzi,³¹
F. Levrier,³⁷ G. Luzzi,³⁸ D. Maino,¹⁷ S. Masi,^{26,27}
M. Migliaccio,^{20,21} L. Montier,¹² G. Morgante,⁸ B. Mot,¹²
R. Nagata,³⁴ F. Nati,^{39,40} P. Natoli,^{32,31} L. Pagano,^{32,31,41}
A. Paiella,^{26,27} D. Paoletti,^{8,9} G. Patanchon,²⁸ F. Piacentini,^{26,27}
G. Polenta,³⁸ D. Poletti,^{39,40} M. Remazeilles,⁴²
J. Rubino-Martin,^{29,30} M. Sasaki,⁴³ M. Shiraishi,⁴⁴ G. Signorelli,⁴⁵
S. Stever,^{46,4} A. Tartari,^{45,47} M. Tristram,³⁶ M. Tsuji,⁴⁴
L. Vacher,¹² I. K. Wehus,¹³ and M. Zannoni^{39,40}
LiteBIRD Collaboration.

¹International School for Advanced Studies (SISSA), Via Bonomea 265, 34136, Trieste, Italy

²INFN Sezione di Trieste, via Valerio 2, 34127 Trieste, Italy

³IFPU, Via Beirut, 2, 34151 Grignano, Trieste, Italy

⁴Kavli Institute for the Physics and Mathematics of the Universe (Kavli IPMU, WPI), UTIAS, The University of Tokyo, Kashiwa, Chiba 277-8583, Japan

⁵Instituto de Fisica de Cantabria (IFCA, CSIC-UC), Avenida los Castros SN, 39005, Santander, Spain

- ⁶Dpto. de Física Moderna, Universidad de Cantabria, Avda. los Castros s/n, E-39005 Santander, Spain
- ⁷School of Physics, Indian Institute of Science Education and Research Thiruvananthapuram, Maruthamala PO, Vithura, Thiruvananthapuram 695551, Kerala, India
- ⁸INAF - OAS Bologna, via Piero Gobetti, 93/3, 40129 Bologna (Italy)
- ⁹INFN Sezione di Bologna, Viale C. Berti Pichat, 6/2 – 40127 Bologna Italy
- ¹⁰Research Center for Nuclear Physics, Osaka University, Ibaraki, Osaka, 567-0047, Japan
- ¹¹Max-Planck-Institute for Astrophysics, Garching
- ¹²IRAP, Université de Toulouse, CNRS, CNES, UPS, (Toulouse), France
- ¹³Institute of Theoretical Astrophysics, University of Oslo, Blindern, Oslo, Norway
- ¹⁴Department of Physics, University of Oxford, Denys Wilkinson Building, Keble Road, Oxford OX1 3RH, United Kingdom
- ¹⁵Dipartimento di Fisica e Astronomia “G. Galilei”, Università degli Studi di Padova, via Marzolo 8, I-35131 Padova, Italy
- ¹⁶INFN Sezione di Padova, via Marzolo 8, I-35131, Padova, Italy
- ¹⁷Dipartimento di Fisica, Università degli Studi di Milano, Via Celoria 16 - 20133, Milano, Italy
- ¹⁸INFN Sezione di Milano, Via Celoria 16 - 20133, Milano, Italy
- ¹⁹Cardiff University, School of Physics and Astronomy, Cardiff CF10 3XQ, UK
- ²⁰Dipartimento di Fisica, Università di Roma Tor Vergata, Via della Ricerca Scientifica, 1, 00133, Roma, Italy
- ²¹INFN Sezione di Roma2, Università di Roma Tor Vergata, via della Ricerca Scientifica, 1, 00133 Roma, Italy
- ²²University of California, Berkeley, Department of Physics, Berkeley, CA 94720, USA
- ²³University of California, Berkeley, Space Science Laboratory, Berkeley, CA 94720, USA
- ²⁴Lawrence Berkeley National Laboratory (LBNL), Computational Cosmology Center, Berkeley, CA 94720, USA
- ²⁵University of Tokyo, School of Science, Research Center for the Early Universe, RESCEU
- ²⁶Dipartimento di Fisica, Università La Sapienza, P. le A. Moro 2, Roma, Italy
- ²⁷INFN Sezione di Roma, P.le A. Moro 2, 00185 Roma, Italy
- ²⁸AstroParticle and Cosmology (APC) - University Paris Diderot, CNRS/IN2P3, CEA/Irfu, Obs de Paris, Sorbonne Paris Cité, France
- ²⁹Instituto de Astrofísica de Canarias, E-38200 La Laguna, Tenerife, Canary Islands, Spain
- ³⁰Departamento de Astrofísica, Universidad de La Laguna (ULL), E-38206, La Laguna, Tenerife, Spain
- ³¹INFN Sezione di Ferrara, Via Saragat 1, 44122 Ferrara, Italy
- ³²Dipartimento di Fisica e Scienze della Terra, Università di Ferrara, Via Saragat 1, 44122 Ferrara, Italy
- ³³High Energy Accelerator Research Organization (KEK), Tsukuba, Ibaraki 305-0801, Japan
- ³⁴Japan Aerospace Exploration Agency (JAXA), Institute of Space and Astronautical Science (ISAS), Sagami-hara, Kanagawa 252-5210, Japan
- ³⁵The Graduate University for Advanced Studies (SOKENDAI), Miura District, Kanagawa 240-0115, Hayama, Japan
- ³⁶Université Paris-Saclay, CNRS/IN2P3, IJCLab, 91405 Orsay, France

- ³⁷Laboratoire de Physique de l'École Normale Supérieure, ENS, Université PSL, CNRS, Sorbonne Université, Université de Paris, 75005 Paris, France
- ³⁸Space Science Data Center, Italian Space Agency, via del Politecnico, 00133, Roma, Italy
- ³⁹University of Milano Bicocca, Physics Department, p.zza della Scienza, 3, 20126 Milan Italy
- ⁴⁰INFN Sezione Milano Bicocca, Piazza della Scienza, 3, 20126 Milano, Italy
- ⁴¹Université Paris-Saclay, CNRS, Institut d'Astrophysique Spatiale, 91405, Orsay, France.
- ⁴²University of Manchester, Manchester M13 9PL, United Kingdom
- ⁴³Remeis-Observatory and Erlangen Centre for Astroparticle Physics, FAU Erlangen-Nürnberg, Sternwartstr. 7, 96049 Bamberg, Germany
- ⁴⁴National Institute of Technology, Kagawa College
- ⁴⁵INFN Sezione di Pisa, Largo Bruno Pontecorvo 3, 56127 Pisa (Italy)
- ⁴⁶Okayama University, Department of Physics, Okayama 700-8530, Japan
- ⁴⁷Dipartimento di Fisica, Università di Pisa, Largo B. Pontecorvo 3, 56127 Pisa

E-mail: nkrach@sissa.it, tomotake.matsumura@ipmu.jp

Abstract. We present a demonstration of the in-flight polarization angle calibration for the JAXA/ISAS second strategic large class mission, *LiteBIRD*, and estimate its impact on the measurement of the tensor-to-scalar ratio parameter, r , using simulated data. We generate a set of simulated sky maps with CMB and polarized foreground emission, and inject instrumental noise and polarization angle offsets to the 22 (partially overlapping) *LiteBIRD* frequency channels. Our in-flight angle calibration relies on nulling the EB cross correlation of the polarized signal in each channel. This calibration step has been carried out by two independent groups with a blind analysis, allowing an accuracy of the order of a few arc-minutes to be reached on the estimate of the angle offsets. Both the corrected and uncorrected multi-frequency maps are propagated through the foreground cleaning step, with the goal of computing clean CMB maps. We employ two component separation algorithms, the Bayesian-Separation of Components and Residuals Estimate Tool (B-SeCRET), and the Needlet Internal Linear Combination (NILC). We find that the recovered CMB maps obtained with algorithms that do not make any assumptions about the foreground properties, such as NILC, are only mildly affected by the angle miscalibration. However, polarization angle offsets strongly bias results obtained with the parametric fitting method. Once the miscalibration angles are corrected by EB nulling prior to the component separation, both component separation algorithms result in an unbiased estimation of the r parameter. While this work is motivated by the conceptual design study for *LiteBIRD*, its framework can be broadly applied to any CMB polarization experiment. In particular, the combination of simulation plus blind analysis provides a robust forecast by taking into account not only detector sensitivity but also systematic effects.

Contents

1	Introduction	1
2	Simulated maps	4
2.1	Sky models	4
2.2	Polarization angle offsets	6
3	Polarization angle calibration	8
3.1	Methods	9
3.2	Results	9
4	Component Separation	12
4.1	B-SeCRET	14
4.2	NILC	16
4.3	Impact on CMB maps	19
5	Discussion and conclusions	20
A	Methods to estimate the polarization angle offset	23
A.1	Implementation A	23
A.2	Implementation B	24
B	Component Separation Methodologies	25
B.1	B-SeCRET	26
B.2	NILC	27

1 Introduction

The measurement of temperature and polarization anisotropies in the cosmic microwave background (CMB) plays a crucial role in modern cosmology [1–7]. In recent years, the *Planck* satellite has observed the CMB signal over the entire celestial sphere in both total intensity and polarization, returning a picture of our Universe in excellent agreement with the standard cosmological constant (Λ) + Cold Dark Matter (CDM) cosmological model [8].

The focus has now shifted primarily to the measurement of the imprint of primordial gravitational waves [9, 10] predicted by the inflationary paradigm on the CMB polarized signal [11, 12]. The theory of cosmic inflation, which assumes a period of accelerated expansion in the very early evolution of the Universe, was originally proposed to explain unresolved problems in cosmology [13–16]; it also predicts that, if primordial perturbations were generated from vacuum fluctuations in the early Universe, their wavelength would be stretched to macroscopic length scales by an exponential expansion phase [17–21], thus leaving an imprint on the CMB signal. In particular, tensor perturbations in the metric (gravitational waves) would generate a curl component in the CMB polarized signal, called *B* modes, at angular scales larger than about 1° . There has been no detection of this faint primordial *B*-mode signal yet. Its amplitude is parameterized by the tensor-to-scalar ratio, r , the amplitude of which is directly related to the energy scale of inflation [22]. The current upper limit, $r < 0.036$ (95% C.L.),

has been obtained from the combination of the *Planck* and BICEP/Keck Array data [7, 23]. This corresponds to a B -mode signal of amplitude ~ 50 nK.

The ongoing effort in the CMB community to reach the instrumental sensitivity needed to probe the primordial B -mode signal is driving significant advancement in focal-plane technology. Current operational ground-based experiments, including SPTpol, the advanced ACTpol, BICEP/Keck, and POLARBEAR, employ focal planes of about 10^3 superconducting detector arrays [24–27]. The next generation of ground-based projects, such as the Simons Observatory, the South Pole Observatory, and eventually CMB Stage IV (CMB-S4) experiment, will employ a total of $\sim 10^4$ and $> 10^5$ detectors, respectively [28–30]. In space, *LiteBIRD*[31], the second strategic large-class mission selected by the Institute of Space and Astronautical Science (ISAS)/Japan Aerospace Exploration Agency (JAXA), is scheduled to observe the sky from the second Lagrangian (L2) point of the Earth-Sun system, in the late 2020s with ~ 5000 detectors. These experiments will achieve a sensitivity on the order of a few to several $\mu\text{K}\cdot\text{arcmin}$ with multi-frequency coverage, reaching a statistical noise level comparable to, or lower than, the B -mode signal of the weak gravitational lensing effect on the CMB E -mode polarization [32]. Such experiments could enable the first ever detection of the signature of primordial gravitational waves with $r \gtrsim 10^{-3}$ in the CMB.

Pushing instrumental sensitivities to these levels, by installing complex focal planes on telescopes, leads to new challenges in the control of instrumental systematic effects. In particular, one of the major possible systematics is related to the need for accurate calibration of the intrinsic polarization angles of the detectors. The Stokes parameters of linear polarization can be written as $Q \pm iU = P \exp(\pm 2i\gamma)$, where P and γ are the polarization intensity and angle, respectively. If the polarization angle of a detector has an uncalibrated offset α , the observed angle, γ^o , would shift from the true value γ to an incorrect one, $\gamma^o = \gamma + \alpha$. The observed Stokes parameters would then be related to the true ones by $Q^o \pm iU^o = (Q \pm iU) \exp(\pm 2i\alpha)$.

Following Refs. [33, 34], we use spin-2 spherical harmonics to expand the Stokes parameters in the \hat{n} direction as $Q(\hat{n}) \pm iU(\hat{n}) = -\sum_{\ell m} (E_{\ell m} \pm iB_{\ell m})_{\pm 2} Y_{\ell m}(\hat{n})$. It then follows trivially that the observed E - and B -mode spherical harmonic coefficients are given by $E_{\ell m}^o \pm iB_{\ell m}^o = (E_{\ell m} \pm iB_{\ell m}) \exp(\pm 2i\alpha)$, or

$$E_{\ell m}^o = E_{\ell m} \cos(2\alpha) - B_{\ell m} \sin(2\alpha), \quad (1.1)$$

$$B_{\ell m}^o = E_{\ell m} \sin(2\alpha) + B_{\ell m} \cos(2\alpha). \quad (1.2)$$

Thus, any uncertainty associated with the polarization angle with respect to the sky coordinates leads to a mixing of E - and B -mode polarization signals [35, 36]. For example, even if the true sky contained no B -mode signal, we would observe a spurious B -mode power spectrum of $C_{\ell}^{B,0} = \sin^2(2\alpha) C_{\ell}^{EE}$. This leakage of the bright E -mode to the much weaker B -mode signal is a major source of systematic uncertainty, and can introduce a possible bias in the tensor-to-scalar ratio measurement [37, 38], since the required accuracy in the knowledge of the detector polarization angle to achieve a sensitivity of $r = 10^{-3}$ can be as demanding as a few arcminutes [39].

Miscalibration of the instrumental polarization angle is not the only instrumental systematic effect that can cause mixing of polarization modes. A similar effect can arise, for example, from the presence of non-ideality in the optical beam shape [35, 36], which therefore should also be known to high accuracy. In this paper, however, we focus on the implementation of a strategy to mitigate the impact of the former effect. The conventional approach for calibrating the detector polarization angle has been to employ an external polarized source, e.g., a polarizing grid with a known polarization orientation with respect to the polarimeters.

Such a device is placed in either the near or far field from a telescope, and is used to calibrate the polarization angles prior to or during the observing campaign. However, this strategy can be employed only if the required accuracy is at the level of 1° degree [40], unless we can substantially improve upon the precision of the current generation of calibrators. Detailed modeling of the optics system can also help to improve knowledge of the instrumental polarization [41, 42]. Another possibility to calibrate the absolute polarization angle is to use a polarized sky source, e.g., Tau A and the Galactic diffuse emission [43–45]. The current measurement accuracy of these sources, however, is not sufficiently high to allow the calibration of the absolute polarization angle at the targeted sensitivity for the tensor-to-scalar ratio. While we do not exclude these options when observational data from future ground-based and balloon-borne CMB telescopes is available, we do not rely on them in this paper.

An alternative approach to calibrating the absolute polarization angle with sub-degree accuracy is to null the EB cross-correlation, C_ℓ^{EB} . This approach can be used either under the assumption that no cosmological EB signal is present [46], or generalized to the case where intrinsic EB correlation exists in the sky signal [47–49]. In this paper we carry out analysis under the first assumption. Even if there were no intrinsic EB correlation (which is the case in the standard model of cosmology), the miscalibration angle would yield a spurious EB power spectrum given by

$$C_\ell^{EB,o} = \frac{1}{2}(C_\ell^{EE} - C_\ell^{BB}) \sin(4\alpha), \quad (1.3)$$

as derived from Eqs. (1.1) and (1.2). Thus, we can use $C_\ell^{EB,o}$ to solve for α given the prior knowledge of the intrinsic $C_\ell^{EE} - C_\ell^{BB}$, with an accuracy limited by cosmic variance and the noise level of the experiments. This approach, called “self-calibration”, has been applied to BICEP1, BICEP2/Keck, POLARBEAR, and SPTpol data sets [50–53]. In this paper, we further study the feasibility of polarization angle calibration by this method. Due to the stringent requirement on the uncertainty in the knowledge of α for future experiments such as *LiteBIRD* and CMB-S4, establishing a reliable calibration method will solidify the overall calibration strategy and could potentially reduce the required accuracy at the hardware level. Although in this work we assumed non-zero

To increase the reliability of our study, we carry out the analysis in a blind fashion. Moreover, in this paper we restrict ourselves to the EB field as a tracer of the spurious correlation induced by the rotation angle. In principle, one could also consider the TB channel as complementary, though not totally independent, information. In this way we are conservative, by considering the main source of information, postponing the full exploitation of other sets of data to a future work. In all previous work using the EB self-calibration technique, the polarized CMB was assumed to be the dominant sky signal, and the effect of polarized foreground emission was ignored [50–53]. In the absence of foregrounds, the technique is straightforward to implement. As demonstrated in Ref. [47], it is possible to extend the EB self-calibration method in the foreground-dominated channel (see section 3 for details). However, it is important to check whether this successful demonstration was a special case or if the method would be successful in general. It is particularly important to avoid tuning the details of the method to mitigate the impact of foreground emission in the simulations. To avoid this potential human bias, we have decided to carry out our analysis in a blind fashion. Specifically, two independent groups use independently developed tools to analyze the simulated data, without knowing the values of the offset angles injected into

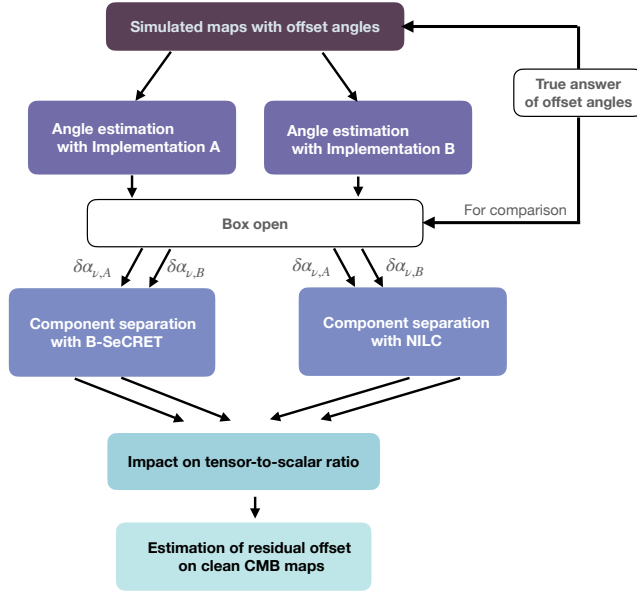


Figure 1: Block diagram of the data analysis steps presented in this paper.

them. We then “open the box” and compare the results with the true answer only after the completion of both independent analyses.

We also propagate the residual errors after calibration in the analysis pipeline through to the determination of r . While this exercise is applicable to any CMB polarization experiment, we specifically apply it to the *LiteBIRD* satellite as a test case. Figure 1 shows a block diagram describing the steps in our analysis.

The remainder of the paper is organized as follows. In section 2, we describe the preparation of the simulated maps including polarization angle offsets. In section 3, we summarize two implementations (Implementation A and B) of the self-calibration method for determining the offset angles, and compare the results. In section 4, we study the impact of the calibration errors on the estimate of r by propagating them in the component separation analysis step. In section 5, we discuss the validity and limitations of the study framework and conclude. In appendix A, we provide the details of the two calibration algorithms and in appendix B, we describe our component separation methods (NILC and B-SeCRET).

2 Simulated maps

We assess the feasibility of *EB*-based in-flight polarization angle calibration on a set of simulated multi-frequency maps. These maps include the sky emission, from both the CMB and Galactic foreground signals, instrumental noise, and the injected polarization angle offsets. In this study we use the instrumental specifications of the *LiteBIRD* satellite, as reported in table 1 [54].

2.1 Sky models

We generate the CMB signal as a set of Gaussian realizations of the *Planck* 2018 best-fit Λ CDM model without tensor modes ($r = 0$) [2]. The polarized Galactic foreground maps are

Table 1: Instrumental specification used to produce the simulations in this work.

Channel name	Frequency [GHz]	FWHM [arcmin]	Pol. sensitivity $\mu\text{K-arcmin}$
LFT-40	40	69.3	59.29
LFT-50	50	56.8	32.78
LFT-60	60	49.0	25.76
LFT-68a	68	41.6	21.60
LFT-68b	68	44.5	23.53
LFT-78a	78	36.9	18.59
LFT-78b	78	40.0	18.45
LFT-89a	89	33.0	16.95
LFT-89b	89	36.7	15.03
LFT-100	100	30.2	12.93
LFT-119	119	26.3	9.79
LFT-140	140	23.7	9.55
MFT-100	100	37.8	9.67
MFT-119	119	33.6	6.41
MFT-140	140	30.8	7.02
MFT-166	166	28.9	5.81
MFT-195	195	28.0	7.12
HFT-195	195	28.6	15.66
HFT-235	235	24.7	15.16
HFT-280	280	22.5	17.98
HFT-337	337	20.9	24.99
HFT-402	402	17.9	49.90

generated through the Python Sky Model package (PySM) [55]. In particular, we consider the presence of polarized thermal dust and synchrotron emission. The polarized dust template implemented in PySM, based on the **Commander** results from the *Planck* 2015 data release [56], was smoothed to an angular resolution of 2° , then Gaussian fluctuations added on smaller angular scales. The template at 353 GHz is scaled in frequency as a modified blackbody with spatially uniform spectral parameters: $\beta_d = 1.54$ and $T_d = 20$ K (the so-called model *d0* in PySM). The synchrotron template corresponds to the *WMAP* 9 year Stokes *Q* and *U* maps [38] at 23 GHz, smoothed to an angular resolution of 3° , to which Gaussian fluctuations were again added on small scales; the synchrotron spectral index is also spatially uniform with $\beta_s = -3$ (model *s0* in PySM). The templates adopted for both synchrotron and thermal dust emission do not show a detectable signal in the *EB* correlation. We emphasize that, although updated templates exist for foreground emission, including information coming from new data [57] or developed with new algorithms [58], they have not been fully validated yet nor interfaced with the PySM library. Therefore, since the main analysis of this work is not related to the evaluation of the optimal strategy for component separation, we simply retain the models already implemented in PySM that are widely used by the community [28].

Moreover, the assumption of spatially uniform spectral parameters is a simplification

Case	Source	Range of injected offset angles
1	Global	≤ 5 arcmin
2	Telescope	$\leq 1^\circ$ for each of LFT, MFT, and HFT, with no correlation
3	Observational band	$\leq 2^\circ$ for each 22-band unit with, no correlation

Table 2: Summary of the ranges for absolute values of random offset angles. In all cases, we assume a uniform probability distribution within the stated range.

of the expected properties of the foreground emission. Recent observations at low and high frequencies have shown that both synchrotron and thermal dust emission show spatial variations in their spectral energy distributions (SEDs) for both polarization and total intensity, measured with varying levels of significance depending on the sky region [56, 59, 60]. However, we stress that, in this work, we focus on assessing the level of precision that can be reached in the estimation of polarization angle offsets through the nulling of the EB correlation. The methods presented in section 3 would not be affected by the spatial variation of the foreground SED, although the component separation step would be rendered significantly more complicated. We therefore choose to use the simplified sky model to separate the two problems.

The simulations are produced for each of the 22 (partially overlapping) *LiteBIRD* frequency channels, and the total signal (CMB plus foregrounds) is smoothed to the corresponding angular resolution (see table 1). Noise is simulated as homogeneous Gaussian fluctuations corresponding to the sensitivity values reported in table 1. No correlated noise is considered, this choice is made under the assumption of the use of a continuously rotating half-wave plate (HWP), which can up-covert the signal bandwidth above the low-frequency noise. The description of the polarimeter configuration is detailed in the next section. Note that we include the potential polarization angle miscalibration originating from the HWP. We produce 10 different sets of simulations. In each set, we change the CMB and noise realization, as well as the polarization angle offsets, generated as described in the following section.

2.2 Polarization angle offsets

As already mentioned, we use the *LiteBIRD* instrument configuration as a test case for this study. *LiteBIRD* consists of three telescopes - the Low-Frequency Telescope (LFT), Mid-Frequency Telescope (MFT), and High-Frequency Telescope (HFT). These three telescopes are cooled to a temperature of 5 K. Structurally, LFT, MFT and HFT will be separately assembled, and each telescope will be integrated on the frame of a payload module that is supported by the rest of the satellite structure. Figure 2 shows an overview of the payload module. The overall mission concepts and configurations can be found in Refs. [61].

Each telescope consists of a continuously rotating HWP, an optical system (cross-Dragone for LFT, and two two-lens refractor systems for MFT and HFT), thermal filters, and a focal plane [62, 63]. Each focal plane contains an array of wafers and each wafer contains multiple beam-forming elements. LFT and MFT employ a lenslet as the beam-forming element, with each lenslet containing six (three bands and two polarization states) transition-edge sensor (TES) bolometers. Similarly, HFT employs a feed-horn coupled antenna, each containing four TES bolometers (two bands and two polarization states) [64]. As a result, the combination of the detectors at each band achieves the sensitivity listed in table 1.

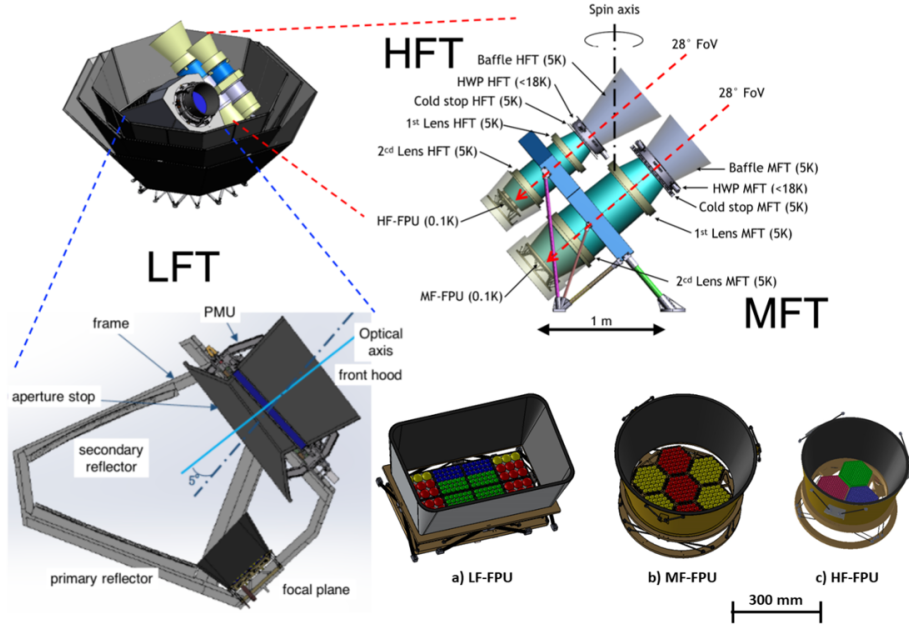


Figure 2: Overview of the *LiteBIRD* satellite, the three telescopes (LFT, MFT, HFT), and the three focal planes for LFT (a), MFT (b), and HFT (c).

In the following, we describe potential sources of polarization angle offset in the *LiteBIRD* polarimeters assumed in this study. We define an offset angle as the shift of the projected polarization-sensitive angle of the polarimeter on the sky from the designed orientation. We have considered three different sources of offset, as summarized in table 2. For Case 1, the simplest example is a global misalignment between the sky and satellite coordinates, which can be described by a single offset angle. A candidate physical origin for this effect is the misalignment and/or miscalibration of a star tracker on the satellite frame with respect to the telescope mount. For Case 2, each of the LFT, MFT, and HFT can have its own independent offset angle, e.g., a misalignment of each telescope with respect to the common frame. A potential physical origin for this is the uncertainty of the HWP position angle reconstruction in each telescope [65, 66]. For Case 3, we apply independent offset angles to the 22 observational frequency band units. Although there are 15 frequencies, the observational bands are divided into 22 units, so there are partial overlaps in frequency coverage between the three different telescopes. In addition, there are two types of lenslet, with two different diameters, for the same observational frequency in LFT. The lenslet diameter changes the optical coupling, thus leading to different sensitivity. As a result, we treat them separately, labeled *a* and *b* in table 1. Any wobbling effect caused by the sinuous antenna and a frequency-dependent polarization sensitive axis from the achromatic HWP can yield a rotational angle offset [67–69]. Additionally, ignorance of the polarization angle rotation induced by the optical system itself can rotate the polarization angle over the focal plane by a few degrees [70]. The focal plane position and the observational frequency are coupled, and thus this can also be a source of an offset angle due to miscalibration.

We assume that all of these effects will be either calibrated or modeled with some imperfections at the component level prior to the observations, thus leading to the presence of offsets. For each case, we draw offset angles randomly from a uniform probability distribution

in the ranges reported in table 2, and for each channel we sum the three contributions to obtain the final angle. We generate 10 different sets of miscalibrated maps, simulated by directly rotating the Stokes Q and U maps in pixel space.

While we limit the scope of our study to these three sources of miscalibration in this paper, we are aware that more cases could be considered in a more realistic polarimeter model. For example, sinuous antenna and achromatic HWPs have a frequency-dependent polarization angle effect [67–69], which adds further complications. Detailed modeling of the *LiteBIRD* polarimeter will be addressed in a future study. Precision construction of polarimeters on a wafer allows us to accurately know the relative angles within one wafer in the same observational band. Therefore, we assume that the relative angles within a given wafer are well calibrated prior to the final calibration analysis using the EB self-calibration method.

3 Polarization angle calibration

In previous work [50–53], eq. (1.3) was used for calibrating the polarization angles with prior knowledge of $C_\ell^{EE} - C_\ell^{BB} \simeq C_\ell^{EE}$ of the CMB signal given by the best-fitting cosmological model. However, eq. (1.3) can be rewritten using only the *observed* difference of E - and B -mode power spectra, $C_\ell^{EE,o} - C_\ell^{BB,o}$ [47, 71, 72]. We use this formulation in this paper.

While we assume throughout this paper that there is no EB correlation in either the primordial or foreground signals, a new algorithm has been developed to constrain the non-zero intrinsic C_ℓ^{EB} and the instrumental polarization angle offsets simultaneously [47–49]. Specifically, if we add prior knowledge of the CMB power spectra, we can determine α and an intrinsic EB signal, perhaps due to the “cosmic birefringence” effect [73], simultaneously [47]. Our analysis can be simply extended to this case by replacing eq. (3.3) below with Eq. (9) in Ref. [47], but here we prefer to focus only on the determination of α . For the simultaneous determination of α and the cosmic birefringence, as well as a discussion on the effect of the intrinsic foreground EB correlation, see Refs. [74–77].

Using the relationships between the observed E - and B -mode polarization and the intrinsic values, $E_{\ell m}^o = E_{\ell m} \cos(2\alpha) - B_{\ell m} \sin(2\alpha)$ (eq. (1.1)) and $B_{\ell m}^o = E_{\ell m} \sin(2\alpha) + B_{\ell m} \cos(2\alpha)$ (eq. (1.2)), the observed E - and B -mode power spectra are related to the intrinsic ones as

$$C_\ell^{EE,o} = \cos^2(2\alpha) C_\ell^{EE} + \sin^2(2\alpha) C_\ell^{BB}, \quad (3.1)$$

$$C_\ell^{BB,o} = \sin^2(2\alpha) C_\ell^{EE} + \cos^2(2\alpha) C_\ell^{BB}, \quad (3.2)$$

in the absence of any physical EB correlation. Combining these with eq. (1.3), we obtain [47, 71, 72]¹

$$C_\ell^{EB,o} = \frac{1}{2} (C_\ell^{EE,o} - C_\ell^{BB,o}) \tan(4\alpha). \quad (3.3)$$

This expression no longer requires any prior knowledge of the intrinsic E - and B -mode power spectra, but the observed difference between them can be used to solve for α . This allows us to retrieve the angle α not only in the presence of the CMB power spectra, which are known accurately, but also foreground emission or any other sky components for which the theoretical power spectra are not available.

¹Also see [78] for earlier work, which used the observed EE and BB power spectra but with $\sin(4\alpha)$ instead of $\tan(4\alpha)$, which would be the same in the limit $|\alpha| \ll 1$.

In this paper, we explore two different ways of implementing the estimation of α using eq. (3.3). We summarize them briefly in the following section, and provide details in appendix A. Our results are reported in section 3.2.

3.1 Methods

We implemented the self-calibration technique in two ways (Implementations A and B) to estimate the polarization angle offsets in our simulated data. Both implementations use eq. (3.3) to solve for α by nulling the EB cross correlation in the observed power spectra at different frequencies. In this section, we highlight the common assumptions of the two implementations as well as their differences. Detailed descriptions of the formalisms are given in appendix A.

Both implementations use a maximum likelihood approach, building the likelihood function from the observed power spectra, $C_\ell^{XY,o}$, which are considered to follow a Gaussian distribution. In the case of Implementation A, only the auto-frequency power spectra of BB , EE and EB are considered, while in Implementation B all the possible frequency cross-spectra of the 22 channels (see table 1) are included. Moreover, Implementation A makes the assumption of small angles for the α offsets, i.e., $\tan(\alpha) \rightarrow \alpha$. This approximation is not used in Implementation B. The covariance matrices are computed differently (see appendix A), with the assumption of being independent from the α parameter for Implementation A; in both cases the correlation between multipoles is neglected. The maximum of the likelihood function is found analytically and the uncertainties on α are estimated by the Fisher matrix for Implementation A, whereas for Implementation B the full posterior distribution is sampled with the publicly available Markov chain Monte Carlo (MCMC) algorithm EMCEE [79], with the marginalized 1σ uncertainties taken as errors on α .

It is important to highlight that the two methods, corresponding to independent implementations by two different groups, also differ in details related to the computation of the power spectra, such as the multipole binning and the maximum ℓ value considered in the analysis. However, as already stressed, we carried out our analysis in a blind fashion, with the exact goal of avoiding the fine tuning of nuisance parameters in the implementations, in order to demonstrate that useful results can be achieved independently of those details.

3.2 Results

We generated ten different sets of sky simulations, changing, in each of them, the noise and CMB realizations as well as the polarization angle offsets for each frequency channel. The values of the angle offsets were not revealed to the two analysis teams. Here we summarize the results of the angle calibration challenge.

In figure 3, we show an example comparison of the true (α_{true} ; black solid lines) and estimated (α_{est} ; filled circles) angles, for one of the ten realizations (results for the other cases are similar). We find that both implementations perform similarly, leading to estimated values for the offset angles close to the true ones for all frequency channels. The uncertainties are small (note that the figure reports 3σ uncertainties), with the error bars being visible only for the lowest frequency channels.

To better characterize and compare the results, figure 4 shows histograms of all of the angle realizations and frequency channels (for a total of 220 estimations). The top panels show the distribution of the injected offsets (α_{true} ; yellow histograms in the left panel) and those of the residuals, $\alpha_{\text{true}} - \alpha_{\text{est}}$, after the self-calibration (coloured histograms in both panels). For Implementation A, the maximum absolute residual offset is at the level of $23'$,

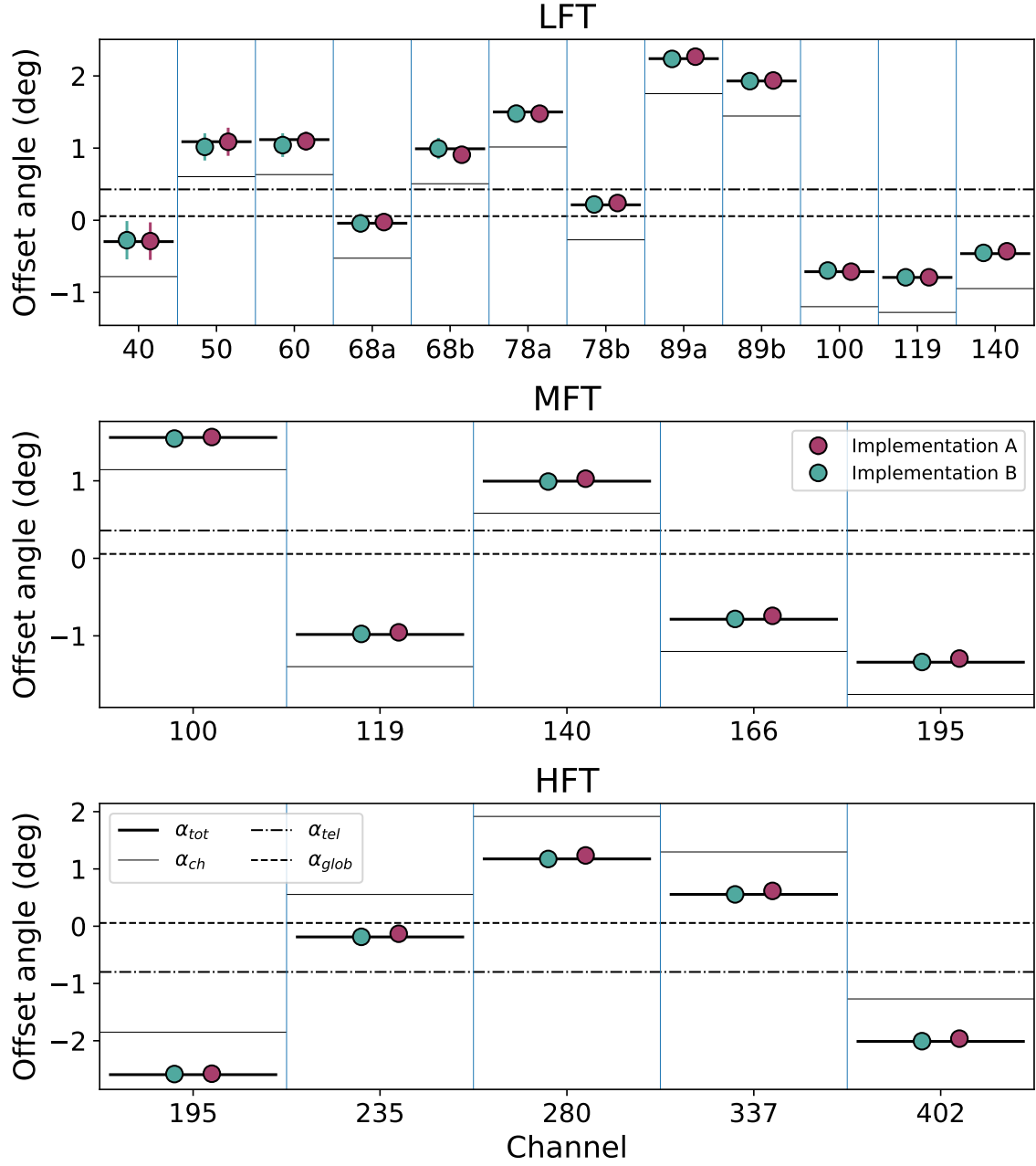


Figure 3: Comparison of the polarization angle estimates from Implementations A and B (filled circles) and the true injected offsets (black solid lines) for all the considered frequency channels and for one realization of the simulated maps. The error bars show the 3σ uncertainties, which are smaller than the size of the filled circles except in the lowest frequency channels. The total true injected offset is obtained as the sum of the three possible sources considered: global misalignment (dashed lines), telescope offset (dashed-dotted lines) and wafer offsets (solid thin lines).

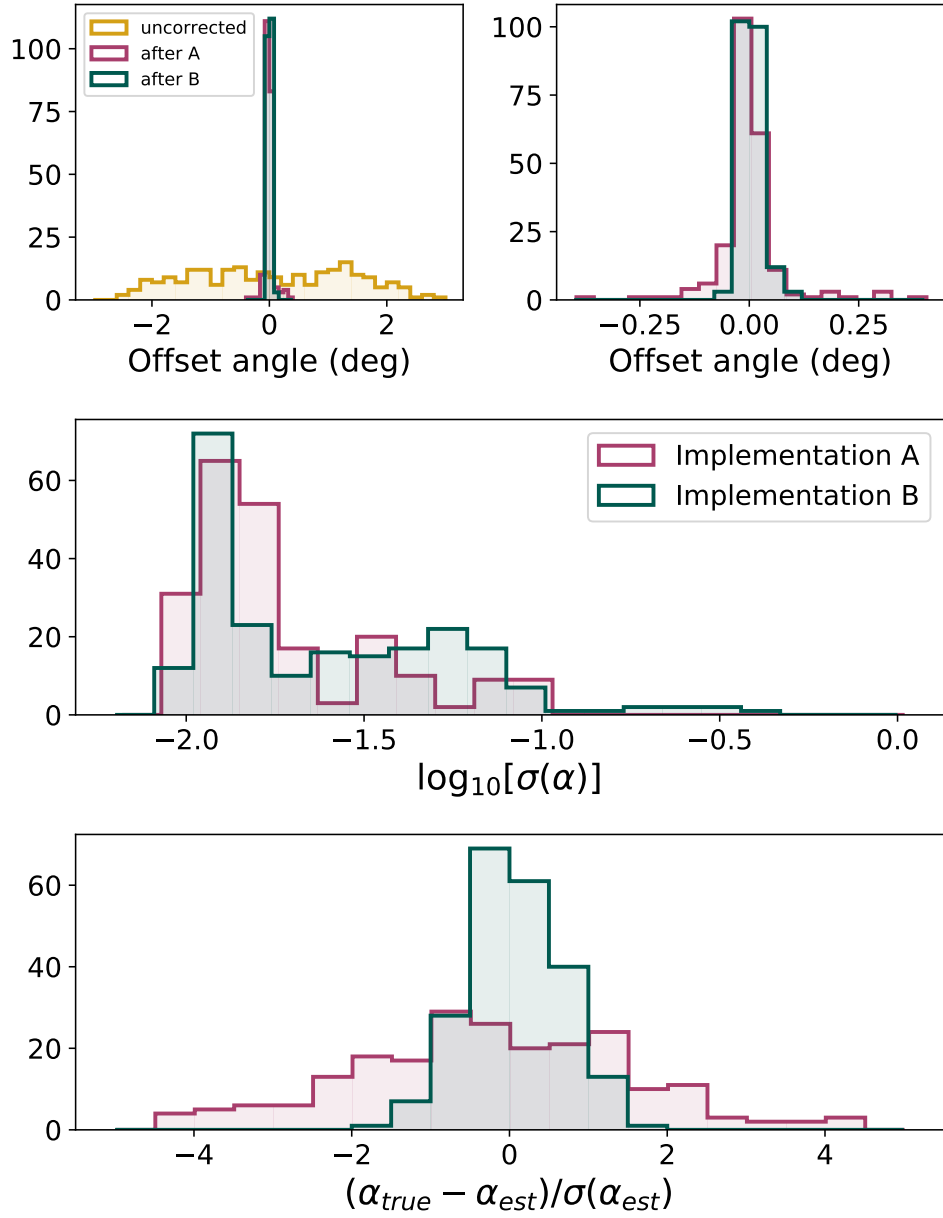


Figure 4: Summary of the results for the estimation of the polarization angles with the two implementations presented in section 3.1. Histograms are computed from all the 10 different sets of simulated maps and the 22 frequency channels (i.e., a total of 220 realizations). The top panels show the distribution of the offset angles before (yellow histogram in the left panel) and after (pink and green histograms) corrections; the right figure shows a zoom on the relevant offset interval after correction. The middle panel shows the distribution of uncertainties in the estimated angles α_{est} . The bottom panel shows the distribution of the bias over the uncertainty of the estimation.

with 90% of the cases below $6'$. For Implementation B, the absolute errors are smaller, lower than $2'$ in 90% of the cases, and reach a maximum of around $6'$.

In the middle panel of figure 4, we show the distributions of the estimated uncertainties on the reconstructed angles. We find that they are similar, which indicates that Implementation A may underestimate the uncertainties. This is confirmed in the bottom panel, where the distributions of $\alpha_{\text{true}} - \alpha_{\text{est}}$ in units of the estimated uncertainties are shown. For Implementation B all the estimated angles are within 2σ of the true ones, while the distribution is broader for Implementation A, with some outliers at more than 4σ . During the post-processing following the unblinding of the challenge results, we found that the Fisher uncertainties used in Implementation A were underestimated due to the use of a non-optimal estimator of the ensemble average power spectra involved in the calculation of the likelihood's covariance matrix. This estimator did not properly model the foreground contribution, leading to an underestimation of the uncertainty especially at the lowest/highest frequency channels, where the foreground contribution is larger.

In the following sections, we describe how we propagate the residual angle offsets into the data analysis pipeline and evaluate their impact on the measurements of r .

4 Component Separation

The goal of our in-flight polarization angle calibration task is to reduce systematic errors in the determination of the tensor-to-scalar ratio, r . Here, we test the improvement on the measurements when Implementations A and B of the self-calibration technique are used to correct the miscalibration angles α in multi-frequency maps, and the residual offsets are propagated through the component separation step, with the goal of obtaining clean CMB maps. We apply component separation strategies to the following sets of maps, in order to characterize our results.

- **Non-rotated maps:** the original signal plus noise maps without any injected rotation of the polarization angle.
- **Rotated maps:** the previous maps with the corresponding rotation offsets applied to the sky signal.
- **Derotated maps:** the maps after derotating the rotated maps with the solutions obtained from Implementations A and B. We derotate the sum of the signal and noise maps.

We adopt two complementary foreground-cleaning techniques that provide a complete framework for analyzing the propagation of rotation angle errors to the cosmological parameter estimation. The first is a map-based algorithm that adopts, and fits for, a parameterized model for the frequency dependence of the sky components. The SED parameters and the amplitudes of the different sky signals are fitted in each resolution element by exploiting the multi-frequency observations. Several implementations of this procedure have been studied in the literature (see Ref. [57] and references therein), such as **Commander**² and **FGBuster**³. In this paper, we use the procedure called **B-SeCRET** (Bayesian-Separation of Components and Residuals Estimate Tool) [80], described in detail in appendix B.1.

²<https://github.com/Cosmoglobe/Commander>

³<https://fgbuster.github.io/fgbuster/index.html>

The second component separation procedure, based on an internal linear combination (ILC) algorithm [81–83], does not assume any prior knowledge of the foreground SED, but rather minimizes the variance of a linear mixture of the multi-frequency data with the constraint of retaining the black body frequency scaling for the CMB. In the implementation used in this work, called Needlet Internal Linear Combination (NILC), the variance minimization is performed in both the spatial and harmonic domains. This allows us to take into account the non-uniform behavior of foregrounds, captured by the variation of the ILC coefficients over the sky and as a function of angular scale. In this work, we adopt the implementation used in the three data releases of the *Planck* experiment [57, 84], as described in detail in appendix B.2.

In the following, we summarize the results of the analysis, on the sets of simulated maps described above, with **B-SeCRET** (section 4.1) and **NILC** (section 4.2). Before this, let us first discuss the expected impacts of the polarization angle miscalibration on the component separation process. When the foreground SED is uniform, we can approximate the component separation procedure as a weighted linear sum of the frequency channel maps, with coefficients that do not depend on sky location, but can depend on the multipole scale because of the different beams and noise levels of the frequency channels. We emphasize that this assumption is only adopted here to simplify the discussion: both **B-SeCRET** and **NILC** allow for spatially-varying SEDs. In the limit of small angles ($|\alpha_i| \ll 1$ for each i th channel), we write the spherical harmonic coefficients of the clean CMB E and B modes as

$$E_{\ell m}^{\text{clean}} = \sum_{i=1}^{N_{\text{ch}}} \omega_{\ell,i}^E E_{\ell m}^{o,i} \approx E_{\ell m}^{\text{CMB}} + \sum_{i=1}^{N_{\text{ch}}} \omega_{\ell,i}^E \left[E_{\ell m}^{\text{FG},i} - 2\alpha_i \left(B_{\ell m}^{\text{CMB}} + B_{\ell m}^{\text{FG},i} \right) \right], \quad (4.1)$$

$$B_{\ell m}^{\text{clean}} = \sum_{i=1}^{N_{\text{ch}}} \omega_{\ell,i}^B B_{\ell m}^{o,i} \approx B_{\ell m}^{\text{CMB}} + \sum_{i=1}^{N_{\text{ch}}} \omega_{\ell,i}^B \left[B_{\ell m}^{\text{FG},i} + 2\alpha_i \left(E_{\ell m}^{\text{CMB}} + E_{\ell m}^{\text{FG},i} \right) \right], \quad (4.2)$$

where $N_{\text{ch}} = 22$ is the number of frequency channels and $\omega_{\ell,i}^X$ are the linear weights of the i th channel map of $X = (E, B)$ satisfying $\sum_i \omega_{\ell,i}^X = 1$. Ignoring the intrinsic CMB EB correlation and the noise bias, the ensemble average of the EB and BB power spectra of the clean map up to first order in α_i is given by

$$C_{\ell}^{EB,\text{clean}} = 2 \left(\alpha_{\text{eff},\ell}^B C_{\ell}^{EE,\text{CMB}} - \alpha_{\text{eff},\ell}^E C_{\ell}^{BB,\text{CMB}} \right) + \sum_{ij} \omega_{\ell,i}^E \omega_{\ell,j}^B \left[C_{\ell}^{E_i B_j, \text{FG}} + 2 \left(\alpha_j C_{\ell}^{E_i E_j, \text{FG}} - \alpha_i C_{\ell}^{B_i B_j, \text{FG}} \right) \right], \quad (4.3)$$

$$C_{\ell}^{BB,\text{clean}} = C_{\ell}^{BB,\text{CMB}} + \sum_{ij} \omega_{\ell,i}^B \omega_{\ell,j}^B \left(C_{\ell}^{B_i B_j, \text{FG}} + 4\alpha_i C_{\ell}^{E_i B_j, \text{FG}} \right), \quad (4.4)$$

where we have defined the new effective (ℓ -dependent) angle, $\alpha_{\text{eff},\ell}^X \equiv \sum_i \omega_{\ell,i}^X \alpha_i$. We thus expect, even in the absence of the EB correlation intrinsic to the foreground ($C_{\ell}^{E_i B_j, \text{FG}} = 0$), that:

1. The clean CMB map will have a non-zero EB correlation, unless the angle miscalibration is corrected prior to the component separation;
2. the BB power spectrum of the clean CMB map will be affected by the angle miscalibration, if the presence of α_i affects the component separation (i.e., $\omega_{\ell,i}^X$).

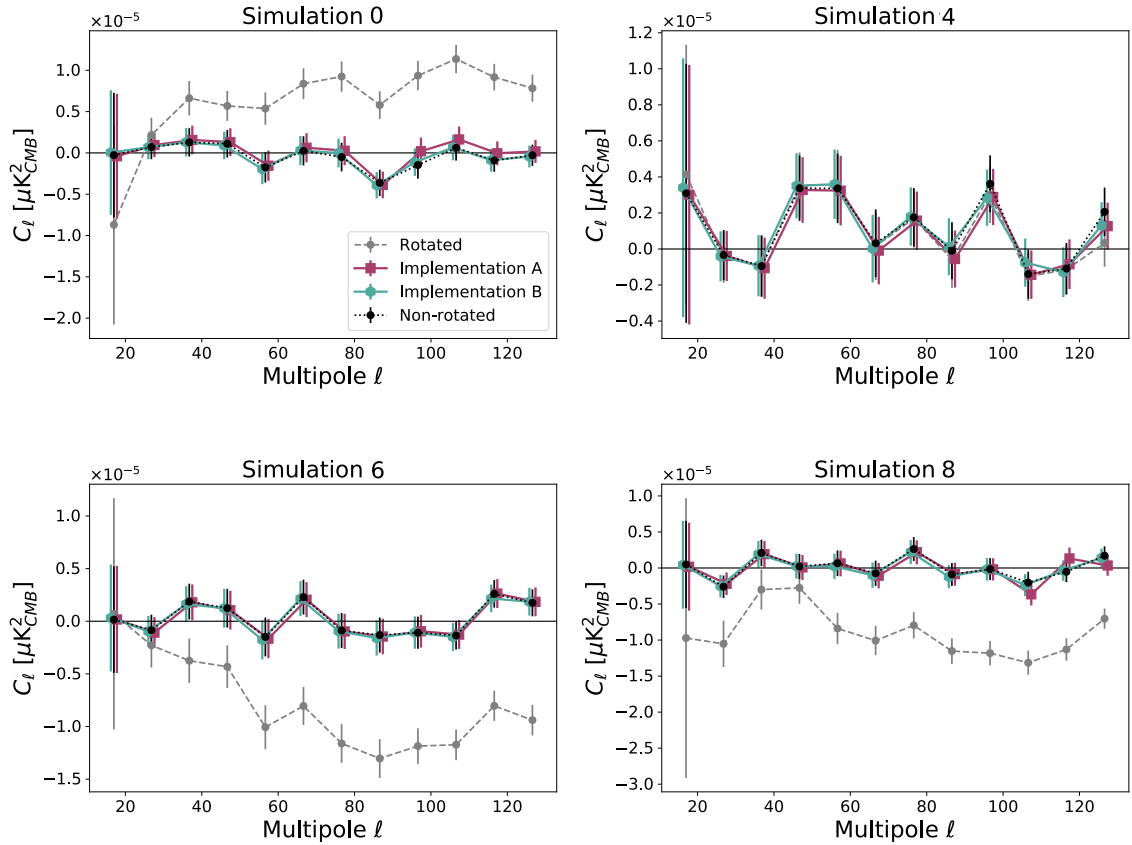


Figure 5: CMB EB power spectra for all cases considered (non-rotated, rotated, and derotated maps with Implementations A and B), after the application of the B-SeCRET algorithm to perform component separation.

While the first is a trivial statement, the second is an interesting one. As we find below, the impact of α_i on the BB power spectrum depends on the specific component separation method applied.

Moreover we note that the ℓ dependence of $\alpha_{\text{eff},\ell}^X$ could potentially compromise the method described in [85] to cancel the angle miscalibration by comparing EB from the reionization and recombination bumps.

4.1 B-SeCRET

We apply the B-SeCRET parametric component separation algorithm to the multi-frequency non-rotated, rotated and derotated maps, for each of ten different sets of simulations. We fit a parametric model that includes seven parameters. Specifically, the thermal dust emission is parameterized with a modified blackbody SED, while the synchrotron radiation is parametrized with a power-law SED with spectral curvature. The details of the parametric model are reported in appendix B.1. Since the maps are simulated with spatially uniform SED parameters, we perform the fit on the whole sky jointly for Q and U maps, assuming that they share the same spectral parameters.

Given the clean CMB map obtained using B-SeCRET, we calculate angular power spectra

using a pseudo- C_ℓ estimator [86, 87], as implemented in the python **NaMaster** package [88]. The power spectra are computed on 60% of the sky defined by the publicly available *Planck* mask⁴, in 10 multipole bins from $\ell = 12$ to $\ell = 132$. We have applied a non-uniform weighting scheme to account for the cosmic variance. Let b be a bin, then the weight applied to $\ell_q \in b$ is

$$w_{\ell_q} = \frac{\ell_q + \frac{1}{2}}{\sum_{\ell \in b} \left(\ell + \frac{1}{2} \right)}. \quad (4.5)$$

Thus, the binned power spectrum is $C_b = \sum_{\ell \in b} w_\ell C_\ell$, and the binned covariance between the i -th and j -th bins is

$$C_{i,j} = \sum_{\ell_i \in b_i} \sum_{\ell_j \in b_j} w_{\ell_i} w_{\ell_j} C_{\ell_i, \ell_j}, \quad (4.6)$$

where C_{ℓ_i, ℓ_j} is the covariance between the i -th and j -th multipoles.

The results of the component separation procedure are reported in figures 5 and 6, which show the EB and BB power spectra of the recovered CMB signal, respectively. As expected, figure 5 shows a non-null C_ℓ^{EB} contribution in the rotated maps, in agreement with eq. (4.3). On the other hand, the C_ℓ^{EB} of the non-rotated and derotated maps are compatible with zero.

Figure 6 shows the excess in the BB power spectra in the rotated maps compared to those in the non-rotated ones, that do not include any primordial B -mode signal. As the rotated maps carry frequency-dependent polarization angle offsets, which are not taken into account in the parametric model, the component separation fails and yields large residuals. We find that the amount of systematic residuals left in the rotated maps are realization dependent. For example, the systematic residuals in the 4th realization are negligible, while those in the 8th realization are significant, especially at low multipoles.

On the other hand, the BB power spectra of the non-rotated and derotated maps are similar, showing that the in-flight calibration methods proposed here are able to remove the systematic errors induced by the miscalibration of the polarization angles. Note that the correction of the polarization angle systematics is achieved in all realizations, regardless of whether the systematics are large (8th realization) or small (4th). Thus, the main goal of the present study is achieved.

In order to assess the biases introduced in the r parameter by the residual systematic effect, we compare the recovered r values from each set of maps to those from the non-rotated maps. We fit the cleaned CMB BB power spectrum for each case (C_ℓ^{out}) to a linear combination of the theoretical primordial B -mode power spectrum (B_ℓ^{gw}), the lensing B -mode power spectrum (L_ℓ) and the power spectrum of the component separation residuals plus noise of non-rotated maps R_ℓ^{non} (parametrized by the a_R coefficient):

$$-2 \ln \mathcal{L}(r, a_R) = \left(C_b^{\text{out}} - r B_b^{\text{gw}} - L_b - a_R R_b^{\text{non}} \right)^T \mathbf{C}_{b,b'}^{-1} \left(C_{b'}^{\text{out}} - r B_{b'}^{\text{gw}} - L_{b'} - a_R R_{b'}^{\text{non}} \right), \quad (4.7)$$

where b denotes a bin and $\mathbf{C}_{b,b'}$ is the covariance between the power spectra at the bins b and b' . The covariance matrix is calculated using the **gaussian_covariance** subroutine in the **NaMaster** package. This subroutine calculates the covariance matrix of the pseudo- C_ℓ power-spectra estimated as $\mathbf{C} = \mathbf{K}^{-1} \tilde{\mathbf{C}} (\mathbf{K}^{-1})^T$ where $\tilde{\mathbf{C}}$ is the covariance of the pseudo power-spectra and, \mathbf{K} is the mode coupling matrix [89, 90]. The results are shown in table 3. We find that the recovered r of the derotated maps with Implementations A and B are

⁴We use `HFI_Mask_GalPlane-apo0_2048_R2.00.fits` available in <https://pla.esac.esa.int/#maps>

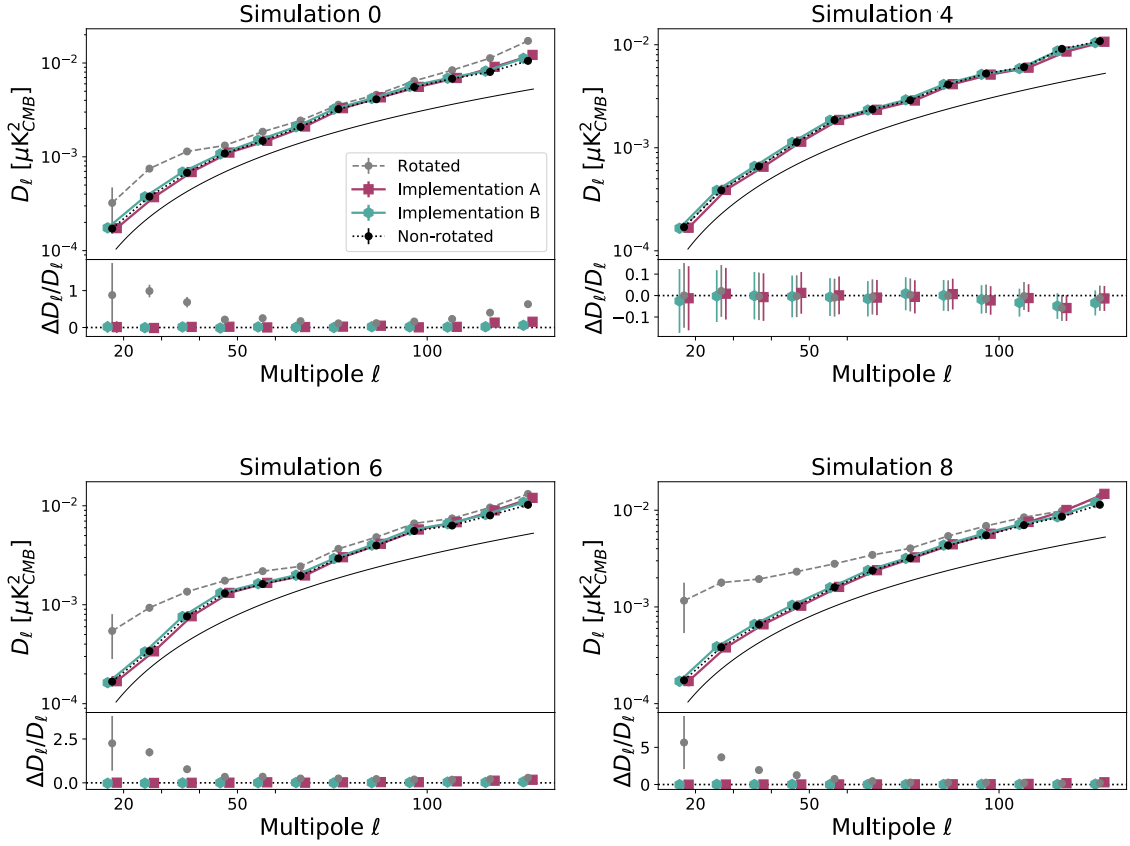


Figure 6: CMB BB power spectra for the non-rotated, rotated, and derotated maps derived by Implementations A and B after application of the B-SeCRET component separation algorithm. The solid black line in the upper section of each panel shows the theoretical CMB lensing BB power spectrum, L_ℓ . The difference between L_ℓ and the data for non-rotated and derotated maps is due to the noise power spectrum, while that for rotated maps is also due to the component separation residual. The lower sections show the relative difference between the recovered BB power spectra in the rotated and derotated cases with respect to the non-rotated case.

consistent with those of the non-rotated maps. We also find that the uncertainty on the recovered r is approximately the same. On the other hand, there is a significant bias in r of the rotated maps with higher uncertainties in those simulations where the impact of the systematic effect is higher. This mismatch between the rotated and non-rotated results arises because the non-rotated residuals, R_ℓ^{non} , account only for foregrounds and noise residuals; thus, the excess in the BB power spectrum due to the angle miscalibration leads to a bias in r . We conclude that correcting the polarization angle miscalibration *prior to* the parametric component separation is crucial for an unbiased inference of r .

4.2 NILC

Next, we use the NILC algorithm to obtain clean CMB maps. As was done previously in the B-SeCRET case, we perform component separation on the non-rotated, rotated, and derotated

Rotated				Correction with Implementation A			Correction with Implementation B		
nsim	$r \times 10^4$	$\frac{r - r^{\text{non}}}{\sigma_r^{\text{non}}}$	$\frac{\sigma_r}{\sigma_r^{\text{non}}}$	$r \times 10^4$	$\frac{r - r^{\text{non}}}{\sigma_r^{\text{non}}}$	$\frac{\sigma_r}{\sigma_r^{\text{non}}}$	$r \times 10^4$	$\frac{r - r^{\text{non}}}{\sigma_r^{\text{non}}}$	$\frac{\sigma_r}{\sigma_r^{\text{non}}}$
0000	10.14	0.80	1.46	-18.53	-2.02	1.03	-5.62	-0.75	1.01
0001	81.91	8.37	1.39	-29.14	-2.16	1.02	-14.26	-0.75	0.98
0002	42.78	4.67	1.24	-26.46	-2.52	1.02	16.30	1.92	0.97
0003	100.18	11.35	1.42	8.37	1.28	0.95	13.78	1.88	0.94
0004	21.92	0.46	1.00	22.31	0.50	0.99	23.07	0.57	0.97
0005	139.48	14.99	1.23	21.84	2.56	0.98	22.76	2.66	0.94
0006	99.26	8.81	1.47	-20.48	-2.35	1.01	-5.71	-0.97	0.99
0007	51.22	3.08	1.09	4.20	-1.59	1.03	25.59	0.53	1.00
0008	246.19	24.06	1.84	-38.68	-3.85	1.06	-4.51	-0.50	1.02
0009	26.35	1.99	1.31	-16.42	-2.28	1.09	-21.71	-2.81	1.06

Table 3: Comparison of r estimation after the application of the B-SeCRET algorithm to the rotated and derotated maps with respect to r from the non-rotated maps. The quantity $(r - r^{\text{non}})/\sigma_r^{\text{non}}$ shows the “number of σ ” of the difference with respect to the non-rotated case while $\sigma_r/\sigma_r^{\text{non}}$ is the ratio of the uncertainty calculated for a given case with respect to the non-rotated case. We recall that the input non-rotated simulations do not include any CMB primordial B -mode signal.

Rotated				Correction with Implementation A			Correction with Implementation B		
nsim	$r \times 10^4$	$\frac{r - r^{\text{non}}}{\sigma_r^{\text{non}}}$	$\frac{\sigma_r}{\sigma_r^{\text{non}}}$	$r \times 10^4$	$\frac{r - r^{\text{non}}}{\sigma_r^{\text{non}}}$	$\frac{\sigma_r}{\sigma_r^{\text{non}}}$	$r \times 10^4$	$\frac{r - r^{\text{non}}}{\sigma_r^{\text{non}}}$	$\frac{\sigma_r}{\sigma_r^{\text{non}}}$
0	-2.07	-0.77	1.04	-6.23	-1.22	1.02	-7.17	-1.32	1.02
1	-1.77	-1.07	1.07	-4.42	-1.35	1.00	-4.37	-1.34	1.00
2	19.28	2.28	1.00	1.40	0.40	0.98	0.74	0.33	0.98
3	16.98	1.68	1.11	-0.48	-0.18	1.01	-1.96	-0.34	1.01
4	18.79	2.99	1.02	13.05	2.38	1.01	10.84	2.14	1.01
5	-2.55	-1.06	1.28	-10.80	-1.94	1.00	-10.54	-1.92	1.00
6	3.67	0.38	1.13	-1.49	-0.17	1.01	-1.87	-0.21	1.01
7	32.74	3.37	1.01	16.83	1.67	1.00	16.85	1.67	1.00
8	18.68	2.17	1.13	4.05	0.61	1.00	2.76	0.47	1.00
9	33.31	3.52	1.11	21.53	2.27	0.99	20.50	2.16	0.99

Table 4: Same as table 3 but for the NILC algorithm.

maps for the ten sets of simulations. Before applying the algorithm, the simulated sky maps are first convolved and deconvolved in harmonic space to a common angular resolution. Here, we adopt the smallest beam, i.e., $17.9'$, as the common resolution.

The NILC algorithm, as currently implemented, is applicable to scalar fields on the

sphere; thus, we construct sky maps of the E and B modes from the input maps of the Q and U Stokes parameters on the full sky. The NILC weights used to combine the multi-frequency input data to determine the CMB signal are computed separately for the E - and B -mode sky maps. The derived full mission weights are also applied to the “half-split maps”, two splits of a map sharing the same sky signal but with uncorrelated noise enhanced by a factor of $\sqrt{2}$ with respect to the sensitivity levels reported in table 1. These are subsequently used for both the power spectrum and noise estimation.

The needlet weights are mostly determined by the Galactic contamination, which dominates on large angular scales, and by the noise, which dominates on small angular scales. The reconstructed CMB E - and B -mode maps cannot be free of contamination by residual foregrounds and noise. Therefore, for further analysis, a set of conservative masks are derived from the variance of the residual foreground maps as follows. First, the variance of the residual foreground maps are smoothed with a 9° Gaussian beam. We then set thresholds appropriate for the desired sky fraction. We pick the mask with a 60% sky fraction for the B -mode map.

Given the CMB sky obtained using NILC, we calculate angular power spectra using a pseudo- C_ℓ estimator [87, 91–93]. Although the NILC weights are computed from full mission sky maps, the impact of the instrumental noise residuals on the angular power spectra is avoided by evaluating cross-power spectra of the NILC half-split maps. Each data point of the angular power spectra is then obtained from the average of all possible cross half-split angular power spectra. To compute the covariance of our measurements, we follow the method described in Ref. [93].

Figure 7 shows the EB power spectra of the clean CMB maps of the non-rotated, rotated, and derotated maps with Implementations A and B. We find that the NILC EB power spectra of rotated maps are not consistent with a null result, in agreement with eq. (4.3). However they become compatible with zero in the derotated case (i.e., after correcting the polarization angle offsets), similar to the results of the parametric component separation. Note that, since we apply the correction to noisy maps, the noise realizations on the rotated and the derotated multi-frequency maps is different, and therefore the EB spectra of the cleaned maps after the application of the NILC algorithm are not expected to fully correlate, but only to be compatible with zero.

Interestingly, the BB power spectra shown in figure 8 are compatible with those of the non-rotated maps, as well as with the theoretical lensing BB power spectrum L_ℓ , not only for the derotated maps but also for the rotated maps. This shows that, by being applied directly to the B -mode maps and by minimizing the variance of the CMB signal, the NILC algorithm is also able to minimize the impact of the injected systematic effect. This property is fundamentally different from the outcome of the parametric component separation process.

Table 4 reports the comparison of the estimation of r for the different cases considered. The methodology to estimate r and its error from the measured angular power spectra and covariance is the same as that for the parametric component separation described in section 4.1. The multipole range and binning are also the same. As we estimate the power spectrum from half-split maps, we do not need to marginalize over the noise power spectrum; thus, we set $a_R = 0$ in eq. (4.7). A qualitatively different result compared to that from B-SeCRET is that the impact of the in-flight correction of the angle miscalibration is less evident, reflecting the fact that the CMB BB power spectra do not show any excess due to the presence of the systematic effect. Nonetheless, the uncertainties on r are reduced when the angle offset in the multi-frequency maps is corrected prior to the NILC component separation.

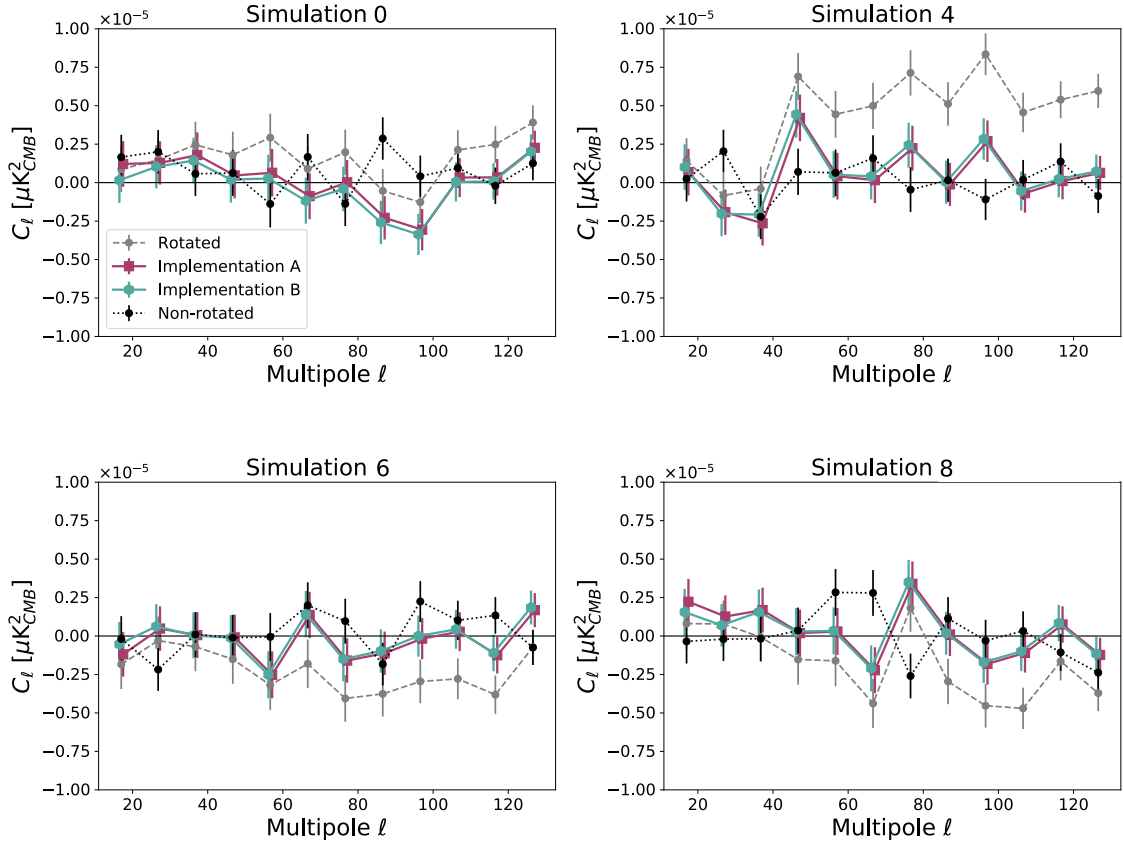


Figure 7: Same as figure 5 but for the NILC algorithm.

4.3 Impact on CMB maps

We can further assess the impact of the polarisation angle offset and its residual before and after self-calibration by estimating the miscalibration angle α from the clean CMB maps. We estimate α by minimizing $\mathcal{D}_\ell^{EB}(\alpha)$ defined as

$$\mathcal{D}_\ell^{EB}(\alpha) = C_\ell^{EB} \cos(4\alpha) - \frac{1}{2} \left(C_\ell^{EE} - C_\ell^{BB} \right) \sin(4\alpha), \quad (4.8)$$

where C_ℓ^{EB} , C_ℓ^{EE} and C_ℓ^{BB} are the power spectra of the CMB solutions, through a standard χ^2 -approach where the first 200 multipoles are considered. The sky fraction used to evaluate the CMB power spectra is $f_{\text{sky}} = 0.6$ for both component separation methods. We have also checked that the estimated angles are stable when we consider a smaller portion of the sky with $f_{\text{sky}} = 0.4$. Further details about the properties of $\mathcal{D}_\ell^{EB}(\alpha)$ can be found in Refs. [72, 94].

In figure 9, we show the angles α estimated from each of the ten realizations considered: the estimates from the non-rotated maps are shown in black, those from the rotated maps in grey, and those from the derotated maps are shown in purple for Implementation A and in cyan for B. The left and right panels show α of the CMB solutions found by B-SeCRET and NILC algorithms, respectively. We find that α estimated from the B-SeCRET and NILC rotated maps are different for most of the realizations. This is expected because the effective

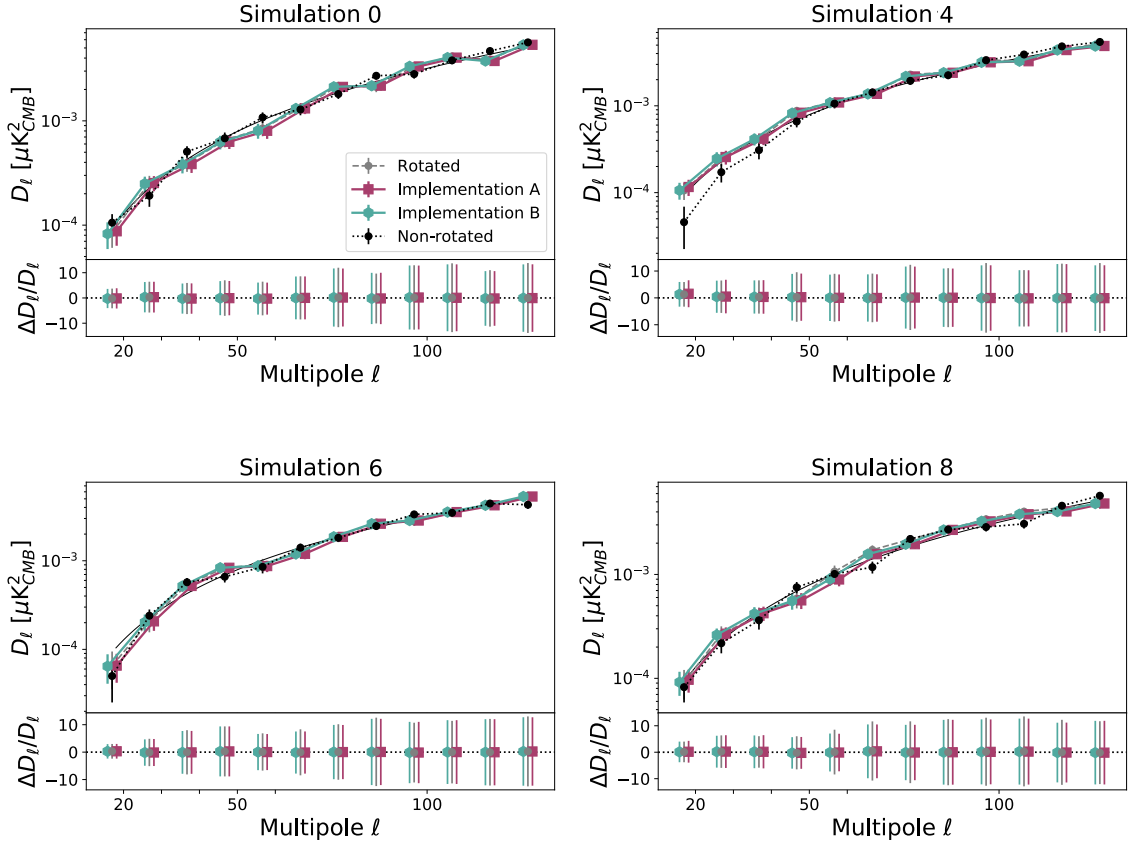


Figure 8: Same as figure 6 but for the NILC algorithm. Here, the noise power spectra are not seen because the BB power spectra are estimated from half-split maps.

angles appearing in the EB power spectrum of the clean CMB map ($\alpha_{\text{eff},\ell}^E$ and $\alpha_{\text{eff},\ell}^B$ in eq. 4.3) depend on the weights obtained for specific component separation algorithms. The right panel shows that, although the angle offsets of the magnitudes assumed in this work do not lead to a large bias in r from the NILC CMB map, they still impact the EB CMB cross-correlation, showing up with values of α significantly different from null, in agreement with eq. (4.3). On the other hand, when derotated with either Implementation A or B, we find excellent compatibility with zero for all realizations.

5 Discussion and conclusions

In this paper, we have presented the results of a blind analysis to study the impact of possible polarization angle offsets (miscalibration of linear polarization angles) on the measurements of the CMB polarized signal, with particular emphasis on the detection of the faint signal of the primordial B -mode polarization. We have used a set of simulated sky maps, where a rotation of the polarization angle was manually injected, generated by three different instrumental sources. As a test case we have considered the instrumental specification of the *LiteBIRD* mission, with 22 (partially overlapping) frequency channels, each with a different polarization offset. As is well known, this systematic effect can cause a spurious B -mode

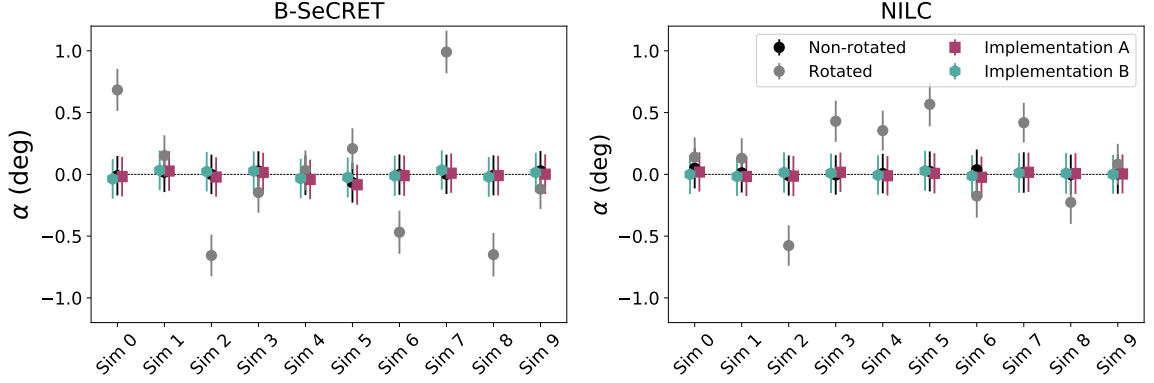


Figure 9: Polarization angle estimated through minimization of $D_\ell^{EB}(\alpha)$ given in eq. (4.8), for each of the 10 realizations considered. This is performed on the CMB solutions found by B-SeCRET (left panel) and NILC (right panel) algorithms. The black and gray points are for the non-rotated and rotated maps, respectively, whereas the purple and cyan points are for the derotated maps with Implementations A and B, respectively. The error bars are evaluated as the 99% C.L. of $\exp(-\chi^2/2)$.

signal, arising from the mixing of polarization states, with an amplitude potentially higher than the cosmological target range.

We have applied, in an independent manner, two different implementations of the self-calibration technique for correcting the polarization angle offset in each frequency channel, estimated by zeroing the EB correlation. All of the frequency channels were analyzed jointly. The offset angles were recovered with an accuracy at the level of few arc-minutes. By propagating the residual angle miscalibration error to the component separation step, here represented by parametric fitting and ILC algorithms, we have estimated the impact on the measurement of the tensor-to-scalar ratio parameter, r . Results are reported in tables 3 and 4.

Table 3 summarizes the impact of the angle miscalibration on r using the parametric method B-SeCRET, showing that uncorrected offsets lead to a large bias in r . This is expected because the sky signal is rotated differently at each frequency channel and the parametric model of the sky emission is no longer adequate for the rotated maps. In the case of derotated maps, this effect is reduced significantly, the sky model is valid and r from clean CMB maps of the derotated maps are consistent with those of the non-rotated maps. On the other hand, table 4 shows that the impact of the angle miscalibration on the angular power spectrum of CMB B modes obtained using NILC is small and is not prominently reflected in any bias on r . This is a consequence of the fact that the method makes no assumptions about the foreground emission, but finds a solution by minimizing the variance of the clean CMB map. It is only mildly affected by incorrect modelling of the sky, and is capable of dealing with the extra complication introduced by this systematic. However, we still find an increase in the uncertainty on r compared to the derotated cases.

The additional analysis of the recovered CMB maps, presented in section 4.3 shows that the presence of residual polarization angle offsets is detectable as a non-zero signal in the clean CMB EB power spectra, even in the NILC case where the impact on the cosmological parameter r is small. The spectra are found to be compatible with zero when corrections are

applied.

In conclusion, we have shown how the interplay between errors on the calibration of the instrumental polarization angles and component separation method can lead to a bias in r when clean CMB maps are retrieved with parametric methods without correcting the angle miscalibration. Component separation methods that do not make any assumptions about the foreground emission, such as NILC, are less affected by miscalibration. In both cases, the clean CMB maps of rotated maps show non-null EB power spectra. The EB self-calibration method to correct the polarization angle offsets can efficiently restore the correct instrument orientation and mitigate their impacts, if applied prior to the component separation (especially for the parametric method, but also for non-parametric ones, leading to smaller uncertainties).

Acknowledgments

This work is supported in Japan by ISAS/JAXA for Pre-Phase A2 studies, by the acceleration program of JAXA research and development directorate, by the World Premier International Research Center Initiative (WPI) of MEXT, by the JSPS Core-to-Core Program of A. Advanced Research Networks, and by JSPS KAKENHI Grant Numbers JP15H05891, JP17H01115, and JP17H01125. The Italian LiteBIRD phase A contribution is supported by the Italian Space Agency (ASI Grants No. 2020-9-HH.0 and 2016-24-H.1-2018), the National Institute for Nuclear Physics (INFN) and the National Institute for Astrophysics (INAF). The French LiteBIRD phase A contribution is supported by the Centre National d’Etudes Spatiales (CNES), by the Centre National de la Recherche Scientifique (CNRS), and by the Commissariat à l’Energie Atomique (CEA). The Canadian contribution is supported by the Canadian Space Agency. The US contribution is supported by NASA grant no. 80NSSC18K0132. Norwegian participation in LiteBIRD is supported by the Research Council of Norway (Grant No. 263011). The Spanish LiteBIRD phase A contribution is supported by the Spanish Agencia Estatal de Investigación (AEI), project refs. PID2019-110610RB-C21 and AYA2017-84185-P. Funds that support the Swedish contributions come from the Swedish National Space Agency (SNSA/Rymdstyrelsen) and the Swedish Research Council (Reg. no. 2019-03959). The German participation in LiteBIRD is supported in part by the Excellence Cluster ORIGINS, which is funded by the Deutsche Forschungsgemeinschaft (DFG, German Research Foundation) under Germany’s Excellence Strategy (Grant No. EXC-2094 - 390783311). This research used resources of the Central Computing System owned and operated by the Computing Research Center at KEK, as well as resources of the National Energy Research Scientific Computing Center, a DOE Office of Science User Facility supported by the Office of Science of the U.S. Department of Energy. TM’s work is supported by JSPS KAKENHI Grant Number JP18KK0083. EdIH acknowledges partial financial support from the *Concepción Arenal Programme* of the Universidad de Cantabria. EdIH, EMG and PV acknowledge the Santander Supercomputación support group at the Universidad de Cantabria, a member of the Spanish Supercomputing Network, who provided access to the Altamira Supercomputer at the Instituto de Física de Cantabria (IFCA-CSIC) for performing simulations and analyses. They also acknowledge funding from Unidad de Excelencia María de Maeztu (MDM-2017-0765). YM’s work was supported in part by the Japan Society for the Promotion of Science (JSPS) KAKENHI, Grants No. JP20K14497. NK, CB and AG acknowledge financial support from the INFN InDark project and from the COSMOS network (www.cosmosnet.it) through

the ASI (Italian Space Agency) Grants 2016-24-H.0 and 2016-24-H.1-2018. EK’s work was supported in part by the JSPS KAKENHI Grant Number JP20H05850 and JP20H05859.

A Methods to estimate the polarization angle offset

In section 3.1, we provided a high-level summary of two implementations of the self-calibration technique for estimating the polarization angle offsets from the multi-frequency simulated maps, which we called “Implementation A” and “Implementation B”. Here, we describe the details.

A.1 Implementation A

This is a computationally fast implementation of the methodology to estimate the parameter α from the observed power spectra. We make two assumptions that enable us to obtain analytic formulae for both the rotation angles and their uncertainties in terms of the EE , BB and EB power spectra. The formalism of this implementation is explained in [95]. We build our likelihood function considering only the auto-frequency power spectra, which are computed on the full sky with the `anafast` function within the `healpy` library. Despite this limitation in the information used, the accuracy of the recovered polarized angles is sufficiently competitive.

The main assumptions made for simplifying the likelihood are the following:

- Small angle approximation: $\tan(\alpha) \rightarrow \alpha$.
- We do not vary α in the covariance matrix of the power spectra when estimating α . To correct the mismatch induced by this approximation, we perform an iterative approach that updates α in the covariance matrix with the one estimated in the previous step.

We ignore correlations between different multipoles in the likelihood, since we work with the full-sky data and thus the correlation is negligible. With these approximations, we obtain a linear system from which the analytical equations to calculate the rotation angles as well as the Fisher error bars are derived. The analyticity of the problem yields a fast computational implementation.

After applying the aforementioned approximations, the likelihood is given by

$$-2 \ln \mathcal{L} = \sum_{i=1}^{N_{\text{ch}}} \sum_{j=1}^{N_{\text{ch}}} \sum_{\ell=\ell_{\text{min}}}^{\ell_{\text{max}}} \left(C_{\ell}^{E_i B_i, o} - 4\alpha_i \xi_{\ell}^i \right) \left(\mathbf{M}^{-1} \right)_{\ell, ij} \left(C_{\ell}^{E_j B_j, o} - 4\alpha_j \xi_{\ell}^j \right), \quad (\text{A.1})$$

where N_{ch} is the number of frequency channels and α_i is the i -th channel’s polarization angle offset. We find that $\ell_{\text{min}} = 10$ and $\ell_{\text{max}} = 300$ are the optimal multipole range for a *LiteBIRD*-like instrument. Here, ξ_{ℓ}^i ⁵ is given by

$$\xi_{\ell}^i = \frac{1}{2} \left(C_{\ell}^{E_i E_i, o} - C_{\ell}^{B_i B_i, o} \right). \quad (\text{A.2})$$

⁵Notice that this is valid only if the noise bias is null. Otherwise, the noise bias could be taken into account.

The elements of the covariance matrix \mathbf{M} are given by

$$M_{\ell,ij} = \frac{1}{2\ell+1} \left\{ \tilde{C}_\ell^{E_i E_j, \circ} \tilde{C}_\ell^{B_i B_j, \circ} + \tilde{C}_\ell^{E_i B_j, \circ} \tilde{C}_\ell^{B_i E_j, \circ} \right. \\ - 4\alpha_j \left(\tilde{C}_\ell^{E_i E_j, \circ} \tilde{C}_\ell^{B_i E_j, \circ} - \tilde{C}_\ell^{E_i B_j, \circ} \tilde{C}_\ell^{B_i B_j, \circ} \right) \\ - 4\alpha_i \left(\tilde{C}_\ell^{E_i E_j, \circ} \tilde{C}_\ell^{E_i B_j, \circ} - \tilde{C}_\ell^{B_i E_j, \circ} \tilde{C}_\ell^{B_i B_j, \circ} \right) \\ \left. + 8\alpha_i \alpha_j \left[\left(\tilde{C}_\ell^{E_i E_j, \circ} \right)^2 + \left(\tilde{C}_\ell^{B_i B_j, \circ} \right)^2 - \left(\tilde{C}_\ell^{E_i B_j, \circ} \right)^2 - \left(\tilde{C}_\ell^{B_i E_j, \circ} \right)^2 \right] \right\}, \quad (\text{A.3})$$

where \tilde{C}_ℓ^{XY} are the power spectra smoothed by convolving C_ℓ^{XY} with a $5\text{-}\ell$ width box of unity area.

The rotation angles can then be obtained analytically by solving the following linear system,

$$\sum_{j=1}^{N_{\text{ch}}} \Omega_{ij} \alpha_j = \frac{1}{4} \eta_i, \quad (\text{A.4})$$

where

$$\Omega_{ij} = \sum_{\ell=\ell_{\min}}^{\ell_{\max}} \xi_\ell^i \left(\mathbf{M}^{-1} \right)_{\ell,ij} \xi_\ell^j, \quad (\text{A.5})$$

$$\eta_i = \sum_{j=1}^{N_{\text{ch}}} \sum_{\ell=\ell_{\min}}^{\ell_{\max}} \xi_\ell^i \left(\mathbf{M}^{-1} \right)_{\ell,ij} C_\ell^{E_j B_j}. \quad (\text{A.6})$$

In this implementation, the uncertainties on the rotation angles are obtained from the Fisher matrix, whose elements are given by

$$F_{ij} = \frac{1}{2} \frac{\partial^2 (-2 \ln \mathcal{L})}{\partial \alpha_i \partial \alpha_j} = 16 \sum_{\ell=\ell_{\min}}^{\ell_{\max}} \xi_\ell^i \left(\mathbf{M}^{-1} \right)_{\ell,ij} \xi_\ell^j. \quad (\text{A.7})$$

A.2 Implementation B

In this implementation, we extend eq. (3.3) to include all the possible observed EB cross power spectra from N_{ch} frequency channels to estimate α_i , allowing us to retrieve the values of the parameters with more precision. We include the approximate covariance between all the observed EB , EE , and BB power spectra assuming Gaussian statistics. The methodology used for this implementation and its validation are detailed in Ref. [49]. We briefly review the methodology below.

When we ignore the intrinsic EB cross power spectra of the CMB and the Galactic foregrounds, we can relate the observed power spectra of the i th and j th channels at each ℓ as [49],

$$\left(-\vec{R}^\top(\alpha_i, \alpha_j) \mathbf{R}^{-1}(\alpha_i, \alpha_j) \ 1 \right) \begin{pmatrix} C_\ell^{E_i E_j, \circ} \\ C_\ell^{B_i B_j, \circ} \\ C_\ell^{E_i B_j, \circ} \end{pmatrix} = 0, \quad (\text{A.8})$$

where \mathbf{R} and \vec{R} are a rotation matrix and rotation vector of power spectra, respectively. The explicit forms are

$$\mathbf{R}(\theta_i, \theta_j) = \begin{pmatrix} \cos(2\theta_i) \cos(2\theta_j) & \sin(2\theta_i) \sin(2\theta_j) \\ \sin(2\theta_i) \sin(2\theta_j) & \cos(2\theta_i) \cos(2\theta_j) \end{pmatrix}, \quad (\text{A.9})$$

$$\vec{R}(\theta_i, \theta_j) = \begin{pmatrix} \cos(2\theta_i) \sin(2\theta_j) \\ -\sin(2\theta_i) \cos(2\theta_j) \end{pmatrix}. \quad (\text{A.10})$$

Using eq. (A.8), we construct a log-likelihood function as [49],

$$-2 \ln \mathcal{L} = \sum_{\ell=\ell_{\min}}^{\ell_{\max}} \left(\mathbf{A} \vec{C}_{\ell}^{\text{o}} \right)^{\text{T}} \mathbf{C}^{-1} \left(\mathbf{A} \vec{C}_{\ell}^{\text{o}} \right), \quad (\text{A.11})$$

where $\ell_{\min} = 2$, $\ell_{\max} = 1024$, $\vec{C}_{\ell}^{\text{o}}$ is an array of the observed power spectra, $\left(C_{\ell}^{E_i E_j, \text{o}} \ C_{\ell}^{B_i B_j, \text{o}} \ C_{\ell}^{E_i B_j, \text{o}} \right)^{\text{T}}$, with i, j in ${}_{22}\text{C}_2 + {}_{22}\text{C}_2 = 253$ combinations, \mathbf{A} is a block diagonal matrix of $\left(-\vec{R}^{\text{T}}(\alpha_i, \alpha_j) \mathbf{R}^{-1}(\alpha_i, \alpha_j) \ 1 \right)$, and $\mathbf{C} = \mathbf{A} \text{Cov}(\vec{C}_{\ell}^{\text{o}}, \vec{C}_{\ell}^{\text{oT}}) \mathbf{A}^{\text{T}}$. The explicit form of $\text{Cov}(\vec{C}_{\ell}^{\text{o}}, \vec{C}_{\ell}^{\text{oT}})$ is

$$\begin{aligned} & \text{Cov}(\vec{C}_{\ell}^{\text{o}, ij}, \vec{C}_{\ell}^{\text{o}, pq\text{T}}) \\ &= \begin{pmatrix} \text{Cov}(C_{\ell}^{E_i E_j, \text{o}}, C_{\ell}^{E_p E_q, \text{o}}) & \text{Cov}(C_{\ell}^{E_i E_j, \text{o}}, C_{\ell}^{B_p B_q, \text{o}}) & \text{Cov}(C_{\ell}^{E_i E_j, \text{o}}, C_{\ell}^{E_p B_q, \text{o}}) \\ \text{Cov}(C_{\ell}^{B_i B_j, \text{o}}, C_{\ell}^{E_p E_q, \text{o}}) & \text{Cov}(C_{\ell}^{B_i B_j, \text{o}}, C_{\ell}^{B_p B_q, \text{o}}) & \text{Cov}(C_{\ell}^{B_i B_j, \text{o}}, C_{\ell}^{E_p B_q, \text{o}}) \\ \text{Cov}(C_{\ell}^{E_i B_j, \text{o}}, C_{\ell}^{E_p E_q, \text{o}}) & \text{Cov}(C_{\ell}^{E_i B_j, \text{o}}, C_{\ell}^{B_p B_q, \text{o}}) & \text{Cov}(C_{\ell}^{E_i B_j, \text{o}}, C_{\ell}^{E_p B_q, \text{o}}) \end{pmatrix}, \end{aligned} \quad (\text{A.12})$$

where we use an approximate covariance for each element [49]:

$$\text{Cov}(C_{\ell}^{X, Y, \text{o}}, C_{\ell}^{Z, W, \text{o}}) \approx \frac{1}{(2\ell + 1)} (C_{\ell}^{X, Z, \text{o}} C_{\ell}^{Y, W, \text{o}} + C_{\ell}^{X, W, \text{o}} C_{\ell}^{Y, Z, \text{o}}). \quad (\text{A.13})$$

Thus, we estimate α_i only with the observed power spectra. We do not include $\ln |\mathbf{C}|$ term in the log-likelihood function of eq. (A.11), following the method validated in Ref. [49]. We confirm that including the $\ln |\mathbf{C}|$ term does not change the results for the instrument specification given in table 1.

Here, to remove biases from statistical fluctuations, we neglect the off-diagonal elements in eq. (A.12) and adopt the binned power spectra and the corresponding covariance [49]:

$$\begin{aligned} C_b^{X, Y} &= \frac{1}{\Delta \ell} \sum_{\ell \in b} C_{\ell}^{X, Y}, \\ \text{Cov}(C_b^{X, Y}, C_b^{Z, W}) &= \frac{1}{\Delta \ell^2} \sum_{\ell \in b} \text{Cov}(C_{\ell}^{X, Y}, C_{\ell}^{Z, W}), \end{aligned} \quad (\text{A.14})$$

where we use $\Delta \ell = 20$. Using these binned variables in the log-likelihood (A.11) we estimate all α_i by sampling the posterior distribution with the MCMC algorithm EMCEE [79] and evaluating the errors on the retrieved maximum likelihood α_i parameters at 1σ .

B Component Separation Methodologies

In this section, we describe the component separation methods **B-SeCRET** [80] and **NILC** [96–98] adopted to obtain clean CMB maps from the multi-frequency simulated sky maps.

B.1 B-SeCRET

The first component separation method is based on a modified version of the Bayesian parametric pixel-based maximum likelihood method described in [80]. Given a set of sky maps observed at different frequencies, the multi-frequency signal at a given pixel p is fitted to a parametric model given by

$$m^X(\nu; \theta_p^X) = c_p^X + \frac{a_{s,p}^X}{u(\nu)} \left(\frac{\nu}{\nu_s} \right)^{\beta_s + c_s \log(\nu/\nu_s)} + \frac{a_{d,p}^X}{u(\nu)} \left(\frac{\nu}{\nu_d} \right)^{\beta_d - 2} \frac{B(\nu, T_d)}{B(\nu_d, T_d)}, \quad (\text{B.1})$$

where X denotes a Stokes parameter (Q or U). We use an MCMC algorithm EMCEE [79] to sample the posterior of $\theta_p^X = \{c_p^X, a_{s,p}^X, a_{d,p}^X, \beta_s, \beta_d, c_s, T_d\}$. Here, $u(\nu) = x^2 e^x / (e^x - 1)^2$ with $x = h\nu / (k_B T_{\text{CMB}})$ is a unit conversion factor from thermodynamic to antenna temperature units, $\nu_s = \nu_d = 150\text{GHz}$ are the synchrotron and dust pivot frequencies, and $B(\nu, T)$ is Planck's law. The second and third terms on the right hand side are the synchrotron and dust contributions, respectively. We use Gaussian priors for the foreground SED parameters: $\beta_s \sim \mathcal{N}(-3.1, 0.3)$, $\beta_d \sim \mathcal{N}(1.56, 0.1)$, $c_s \sim \mathcal{N}(0, 0.1)$, and $T_d \sim \mathcal{N}(21, 3)$.

The posterior probability density is given by the product of the data likelihood and the priors on the model parameters. The likelihood for each pixel p is given by

$$\mathcal{L}(\theta_p | \bar{d}_p) = \frac{1}{\sqrt{(2\pi)^{2N_{\text{ch}}} \det(\mathbf{C})}} \exp \left[-\frac{1}{2} \left(\bar{d}_p - m(\bar{\nu}; \theta_p) \right)^\top \mathbf{C}^{-1} \left(\bar{d}_p - m(\bar{\nu}; \theta_p) \right) \right], \quad (\text{B.2})$$

where $N_{\text{ch}} = 22$ is the number of frequency channels, $\bar{\nu}$ is a N_{ch} vector whose elements are *LiteBIRD*'s frequency channels, $\bar{d}_p = (\bar{d}_p^Q, \bar{d}_p^U)$ with \bar{d}_p^Q (\bar{d}_p^U) being a N_{ch} vector with the Q (U) multi-frequency signal in the pixel p , θ_p is the set of model parameters in the pixel p , $m(\bar{\nu}, \theta_p) = (m^Q(\bar{\nu}, \theta_p), m^U(\bar{\nu}, \theta_p))$ with $m^Q(\bar{\nu}, \theta_p^Q)$ ($m^U(\bar{\nu}, \theta_p^U)$) being a vector whose elements are the result of evaluating the model given the parameters θ_p^Q (θ_p^U) in the pixel p , and $\mathbf{C} = \text{diag}(\mathbf{C}^Q, \mathbf{C}^U)$ with \mathbf{C}^X being a $N_{\text{ch}} \times N_{\text{ch}}$ noise covariance matrix for the X Stokes parameter. We assume $\mathbf{C}^Q = \mathbf{C}^U$. The matrix \mathbf{C} depends in general on p , but we assume it to be independent of it, i.e., homogeneous noise across the sky. \mathbf{C}^X is assumed to be diagonal, i.e., no correlation among different frequencies. The Q and U signals are fitted jointly since we assume that they share the same SED model parameters. Since the foregrounds have been simulated using the uniform SED parameters, we also assume uniform spectral parameters across the available sky.

Due to the large computational time required to fit the maps at $N_{\text{side}} = 512$, we downgrade them to $N_{\text{side}} = 64$ and convolve them to a common beam resolution. The map processing proceeds as follows: (i) the original maps at $N_{\text{side}} = 512$ are converted to a spherical harmonic representation; (ii) beam deconvolution is applied in the harmonic domain for the beam full-width-at-half-maximum (FWHM) of each frequency channel as reported in table 1; (iii) the spherical harmonic coefficients of each channel are convolved with a Gaussian beam of FWHM = $132'$; and (iv) we transform the spherical harmonic coefficients to $N_{\text{side}} = 64$ maps.

To estimate the effective noise per channel, we have generated 100 noise simulations per *LiteBIRD* channel and downgraded them using the same process. The i -th diagonal element of \mathbf{C}^X is the effective variance calculated from the 100 pre-processed noise simulation maps.

We perform the parameter fitting in a two-step process, as in Ref. [80]. First, the model parameters are split into two categories: the amplitudes and the SED parameters. Each set of

the parameters is fitted in an iterative manner, i.e., in the first iteration the SED parameters are fixed to the initial values of $\beta_s = -3.0$, $\beta_d = 1.54$, $c_s = 0$ and $T_d = 20$ K, and the amplitudes are fitted. Then, the amplitudes are fixed to the values obtained from this fit and the SED parameters are calculated. In the next step, the SED parameters are fixed to the values determined in the first iteration, and the amplitudes are fitted. This process is repeated until it converges. We find that convergence is achieved typically by the second iteration.

B.2 NILC

The second component separation technique that we apply, NILC [96–98], is based on the ILC method [81–83]. It is based on the construction of the linear mixture of frequency channel maps that minimizes the variance on a frame of spherical wavelets called needlets, allowing localised filtering in both pixel space and harmonic space. It is designed to recover the CMB as the component scaling as a blackbody in the linear mixture, assuming only that it is uncorrelated with foregrounds, with no other prior information. See Refs. [57, 84] for the application to the *Planck* data.

NILC estimates the CMB, \hat{S} , as a weighted linear combination of multi-frequency sky maps such that (1) the variance of the estimate is minimum, with (2) unit response to the flat CMB frequency spectrum,

$$\hat{S} = w^\top X = \frac{a^\top \hat{R}^{-1}}{a^\top \hat{R}^{-1} a} X = \frac{a^\top \hat{R}^{-1}}{a^\top \hat{R}^{-1} a} (aS + F + N). \quad (\text{B.3})$$

Here, X is the vector of frequency channel maps, a the constant frequency spectrum of the CMB signal S , F the total foreground signal, N the instrumental noise for the different frequency channels, and \hat{R} the covariance matrix across frequencies. The condition (1) guarantees minimum contamination by foregrounds and instrumental noise, while condition (2) guarantees that the CMB signal is conserved without bias. The weights, w , result from a trade-off between minimising the foregrounds and the instrumental noise contributions in the reconstructed CMB map [96, 99–102]. They are computed in needlet space, i.e., for different regions of the sky or for different angular scales, respectively, which allows for variations of the data covariance matrix in either space. This technique has already been applied broadly in CMB data analysis [96–98, 103–107].

The needlet decomposition allows the ILC weights to vary smoothly on large angular scales and rapidly on small angular scales. The needlet windows in harmonic space, h_ℓ^j , are defined as follows

$$h_\ell^j = \begin{cases} \cos \left[\left(\frac{\ell_{\text{peak}}^j - \ell}{\ell_{\text{peak}}^j - \ell_{\text{min}}^j} \right) \frac{\pi}{2} \right] & \text{for } \ell_{\text{min}}^j \leq \ell < \ell_{\text{peak}}^j, \\ 1 & \text{for } \ell = \ell_{\text{peak}}, \\ \cos \left[\left(\frac{\ell - \ell_{\text{peak}}^j}{\ell_{\text{max}}^j - \ell_{\text{peak}}^j} \right) \frac{\pi}{2} \right] & \text{for } \ell_{\text{peak}}^j < \ell \leq \ell_{\text{max}}^j \end{cases}. \quad (\text{B.4})$$

Table 5: List of needlet bands used in the present analysis.

Band index	ℓ_{\min}	ℓ_{peak}	ℓ_{\max}	N_{side}
1	0	0	50	32
2	0	50	100	64
3	50	100	200	128
4	100	200	300	128
5	200	300	400	256
6	300	400	500	256
7	400	500	600	512
8	500	600	700	512
9	600	700	800	512
10	700	800	900	512
11	800	900	1000	512

In terms of h_ℓ^j , the spherical needlets are defined as

$$\Psi_{jk}(\hat{n}) = \sqrt{\lambda_{jk}} \sum_{\ell=\ell_{\min}^j}^{\ell_{\max}^j} \sum_{m=-\ell}^{\ell} h_\ell^j Y_{\ell m}^*(\hat{n}) Y_{\ell m}(\hat{\xi}_{jk}), \quad (\text{B.5})$$

where the $\{\xi_{jk}\}$ denote a set of cubature points on the sphere for scale j . In practice, we identify these points with the pixel centers of the HEALPix pixelization scheme [92]. Each index k corresponds to a particular HEALPix pixel, at a resolution parameter $N_{\text{side}}(j)$ specific to that scale j . The cubature weights λ_{jk} are inversely proportional to the number N_j of pixels used for the needlet decomposition, i.e., $\lambda_{jk} = \frac{4\pi}{N_j}$. Given a set of needlet functions, any sky map of a spin-0 field $X(\hat{n})$ (such as the CMB temperature anisotropy or the E and B modes) can be expressed as

$$X(\hat{n}) = \sum_{\ell=0}^{\ell_{\max}} \sum_{m=-\ell}^{\ell} X_{\ell m} Y_{\ell m}(\hat{n}) = \sum_j \sum_k \beta_{jk}^X \Psi_{jk}(\hat{n}), \quad (\text{B.6})$$

where the needlet coefficients, β_{jk}^X , of the sky map are denoted as

$$\beta_{jk}^X = \langle X, \Psi_{jk} \rangle = \sqrt{\lambda_{jk}} \sum_{\ell=0}^{\ell_{\max}} \sum_{m=-\ell}^{\ell} h_\ell^j X_{\ell m} Y_{\ell m}(\xi_{jk}). \quad (\text{B.7})$$

For each scale j , the NILC filter has compact support between the multipoles ℓ_{\min}^j and ℓ_{\max}^j with a peak at ℓ_{peak}^j . The values of ℓ_{\min}^j , ℓ_{peak}^j and ℓ_{\max}^j for different needlet bands used in the analysis are listed in table 5. The needlet coefficients, β_{jk}^X , are computed on the HEALPix grid points, ξ_{jk} , with a resolution parameter, N_{side} , equal to the smallest power of 2 larger than $\ell_{\max}^j/2$.

References

- [1] E. Komatsu et al., PTEP, **2014**, 06B102 (2014), arXiv:1404.5415.

- [2] Planck Collaboration VI, *Astron. Astrophys.*, **641**, A6 (2020), arXiv:1807.06209.
- [3] S. Adachi et al., *Astrophys. J.*, **904**(1), 65 (2020), arXiv:2005.06168.
- [4] S. Aiola et al., *JCAP*, **12**, 047 (2020), arXiv:2007.07288.
- [5] J. T. Sayre et al., *Phys. Rev. D*, **101**(12), 122003 (2020), arXiv:1910.05748.
- [6] D. Dutcher et al., *Phys. Rev. D*, **104**(2), 022003 (2021), arXiv:2101.01684.
- [7] P. A. R. Ade et al., *Phys. Rev. Lett.*, **127**(15), 151301 (2021), arXiv:2110.00483.
- [8] Planck Collaboration I, *Astron. Astrophys.*, **641**, A1 (2020).
- [9] L. P. Grishchuk, *Sov. Phys. JETP*, **40**, 409–415 (1975).
- [10] A. A. Starobinsky, *JETP Lett.*, **30**, 682–685 (1979).
- [11] U. Seljak and M. Zaldarriaga, *Phys. Rev. Lett.*, **78**, 2054–2057 (1997), astro-ph/9609169.
- [12] M. Kamionkowski, A. Kosowsky, and A. Stebbins, *Phys. Rev. Lett.*, **78**, 2058–2061 (1997), astro-ph/9609132.
- [13] A. Guth, *Phys. Rev. D*, **23**, 347–356 (Jan 1981).
- [14] K. Sato, *Mon. Not. Roy. Astron. Soc.*, **195**(3), 467–479 (07 1981).
- [15] A. D. Linde, *Phys. Lett. B*, **108**, 389–393 (1982).
- [16] A. Albrecht and P. J. Steinhardt, *Phys. Rev. Lett.*, **48**, 1220–1223 (1982).
- [17] V. F. Mukhanov and G. V. Chibisov, *JETP Lett.*, **33**, 532–535 (1981).
- [18] S. W. Hawking, *Phys. Lett. B*, **115**, 295 (1982).
- [19] A. A. Starobinsky, *Phys. Lett. B*, **117**, 175–178 (1982).
- [20] A. H. Guth and S. Y. Pi, *Phys. Rev. Lett.*, **49**, 1110–1113 (1982).
- [21] J. M. Bardeen, P. J. Steinhardt, and M. S. Turner, *Phys. Rev. D*, **28**, 679 (1983).
- [22] M. Kamionkowski and E. D. Kovetz, *Annual Review of Astronomy and Astrophysics*, **54**(1), 227–269 (2016).
- [23] M. Tristram et al., *Astron. Astrophys.*, **647**, A128 (2021), arXiv:2010.01139.
- [24] J. Hubmayr et al., *J. Low Temp. Phys.*, **167**(5), 904–910 (2012).
- [25] R. J. Thornton et al., *Astrophys. J. Suppl.*, **227**(2), 21 (2016), arXiv:1605.06569.
- [26] J. A. Grayson et al., BICEP3 performance overview and planned Keck Array upgrade, In Wayne S. Holland and Jonas Zmuidzinas, editors, *Millimeter, Submillimeter, and Far-Infrared Detectors and Instrumentation for Astronomy VIII*, volume 9914, pages 157 – 173. International Society for Optics and Photonics, SPIE (2016).
- [27] D. Kaneko et al., *J. Low Temp. Phys.*, **199**(3), 1137–1147 (May 2020).
- [28] Simons Observatory Collaboration, *JCAP*, **02**, 056 (2019), arXiv:1808.07445.
- [29] L. Moncelsi et al., Receiver development for BICEP Array, a next-generation CMB polarimeter at the South Pole, In Jonas Zmuidzinas and Jian-Rong Gao, editors, *Millimeter, Submillimeter, and Far-Infrared Detectors and Instrumentation for Astronomy X*, volume 11453, pages 189 – 206. International Society for Optics and Photonics, SPIE (2020).
- [30] CMB-S4 Collaboration, *ArXiv e-prints* (2020), arXiv:2008.12619.
- [31] M. Hazumi et al., *J. Low Temp. Phys.*, **194**(5-6), 443–452 (2019).
- [32] M. Zaldarriaga and U. Seljak, *Phys. Rev. D*, **58**, 023003 (1998), astro-ph/9803150.
- [33] M. Zaldarriaga and U. Seljak, *Phys. Rev. D*, **55**, 1830–1840 (1997), astro-ph/9609170.

- [34] M. Kamionkowski, A. Kosowsky, and A. Stebbins, *Phys. Rev. D*, **55**, 7368–7388 (1997), astro-ph/9611125.
- [35] M. Shimon, B. Keating, N. Ponthieu, and E. Hivon, *Phys. Rev. D*, **77**, 083003 (2008), arXiv:0709.1513.
- [36] N. J. Miller, M. Shimon, and B. G. Keating, *Phys. Rev. D*, **79**, 103002 (2009), arXiv:0903.1116.
- [37] W. Hu, M. M. Hedman, and M. Zaldarriaga, *Phys. Rev. D*, **67**, 043004 (Feb 2003).
- [38] C. L. Bennett et al., *Astrophys. J. Suppl.*, **208**, 20 (2013), arXiv:1212.5225.
- [39] P. Vielva, E. Martínez-González, F. J. Casas, et al., In prep. (2021).
- [40] Y. D. Takahashi et al., *Astrophys. J.*, **711**(2), 1141–1156 (feb 2010).
- [41] B. J. Koopman,
Detector Development and Polarization Analyses for the Atacama Cosmology Telescope,
PhD thesis, Cornell U. (2018).
- [42] S. K. Choi et al., *JCAP*, **12**, 045 (2020), arXiv:2007.07289.
- [43] T. Matsumura et al., *Millimeter, Submillimeter, and Far-Infrared Detectors and Instrumentation for Astronomy V* (Jul 2010).
- [44] J. Aumont, J. F. Macías-Pérez, A. Ritacco, N. Ponthieu, and A. Mangilli, *Astron. Astrophys.*, **634**, A100 (2020), arXiv:1805.10475.
- [45] Silvia Masi, Paolo de Bernardis, Fabio Columbro, Alessandro Coppolecchia, Giuseppe D’Alessandro, Lorenzo Mele, Alessandro Paiella, and Francesco Piacentini, *Astrophys. J.*, **921**(1), 34 (2021), arXiv:2106.04841.
- [46] B. G. Keating, M. Shimon, and A. P. S. Yadav, *Astrophys. J.*, **762**(2), L23 (dec 2012).
- [47] Y. Minami, H. Ochi, K. Ichiki, N. Katayama, E. Komatsu, and T. Matsumura, *PTEP*, **2019**(8), 083E02 (2019), arXiv:1904.12440.
- [48] Y. Minami, *PTEP*, **2020**(6), 063E01 (2020), arXiv:2002.03572.
- [49] Y. Minami and E. Komatsu, *PTEP*, **2020**(10), 103E02 (2020), arXiv:2006.15982.
- [50] J. P. Kaufman et al., *Phys. Rev. D*, **89**, 062006 (Mar 2014).
- [51] BICEP2 Collaboration, *Phys. Rev. Lett.*, **112**, 241101 (Jun 2014).
- [52] Polarbear Collaboration, *Astrophys. J.*, **794**(2), 171 (oct 2014).
- [53] F. Bianchini et al., *Phys. Rev. D*, **102**(8), 083504 (2020), arXiv:2006.08061.
- [54] H. Sugai et al., *J. Low Temp. Phys.*, **199**(3), 1107–1117 (May 2020).
- [55] B. Thorne, J. Dunkley, D. Alonso, and S. Naess, *Mon. Not. Roy. Astron. Soc.*, **469**(3), 2821–2833 (August 2017), arXiv:1608.02841.
- [56] Planck Collaboration X, *Astron. Astrophys.*, **594**, A10 (September 2016), 1502.01588.
- [57] Planck Collaboration IV, *Astron. Astrophys.*, **641**, A4 (September 2020), arXiv:1807.06208.
- [58] N. Krachmalnicoff and G. Puglisi, *Astrophys. J.*, **911**(1), 42 (2021), arXiv:2011.02221.
- [59] Planck Collaboration Int. XLVIII, *Astron. Astrophys.*, **596**, A109 (December 2016), arXiv:1605.09387.
- [60] N. Krachmalnicoff, E. Carretti, C. Baccigalupi, G. Bernardi, S. Brown, B. M. Gaensler, M. Haverkorn, M. Kesteven, F. Perrotta, S. Poppi, and L. Staveley-Smith, *Astron. Astrophys.*, **618**, A166 (October 2018), arXiv:1802.01145.

- [61] M. Hazumi et al., LiteBIRD satellite: JAXA’s new strategic L-class mission for all-sky surveys of cosmic microwave background polarization, In Makenzie Lystrup, Marshall D. Perrin, Natalie Batalha, Nicholas Siegler, and Edward C. Tong, editors, Space Telescopes and Instrumentation 2020: Optical, Infrared, and Millimeter Wave, volume 11443, pages 431 – 450. International Society for Optics and Photonics, SPIE (2020).
- [62] Y. Sekimoto et al., Concept design of low frequency telescope for CMB B-mode polarization satellite LiteBIRD, In Jonas Zmuidzinas and Jian-Rong Gao, editors, Millimeter, Submillimeter, and Far-Infrared Detectors and Instrumentation for Astronomy X, volume 11453, pages 189 – 209. International Society for Optics and Photonics, SPIE (2020).
- [63] L. Montier et al., Overview of the medium and high frequency telescopes of the LiteBIRD space mission, In Makenzie Lystrup, Marshall D. Perrin, Natalie Batalha, Nicholas Siegler, and Edward C. Tong, editors, Space Telescopes and Instrumentation 2020: Optical, Infrared, and Millimeter Wave, volume 11443, pages 451 – 471. International Society for Optics and Photonics, SPIE (2020).
- [64] B. Westbrook et al., Detector fabrication development for the LiteBIRD satellite mission, In Makenzie Lystrup, Marshall D. Perrin, Natalie Batalha, Nicholas Siegler, and Edward C. Tong, editors, Space Telescopes and Instrumentation 2020: Optical, Infrared, and Millimeter Wave, volume 11443, pages 915 – 936. International Society for Optics and Photonics, SPIE (2020).
- [65] S. Sugiyama et al., Evaluation of reconstructed angular error of a continuous rotating HWP for LiteBIRD, In Makenzie Lystrup, Marshall D. Perrin, Natalie Batalha, Nicholas Siegler, and Edward C. Tong, editors, Space Telescopes and Instrumentation 2020: Optical, Infrared, and Millimeter Wave, volume 11443, pages 1099 – 1112. International Society for Optics and Photonics, SPIE (2020).
- [66] F. Columbro, P. de Bernardis, L. Lamagna, S. Masi, A. Paiella, F. Piacentini, and G. Pisano, A polarization modulator unit for the mid- and high-frequency telescopes of the LiteBIRD mission, In Makenzie Lystrup, Marshall D. Perrin, Natalie Batalha, Nicholas Siegler, and Edward C. Tong, editors, Space Telescopes and Instrumentation 2020: Optical, Infrared, and Millimeter Wave, volume 11443, pages 1113 – 1128. International Society for Optics and Photonics, SPIE (2020).
- [67] A. Suzuki, Multichroic Bolometric Detector Architecture for Cosmic Microwave Background Polarimetry Experiments, PhD thesis, University of California, Berkeley (January 2013).
- [68] K. Komatsu, T. Matsumura, H. Imada, H. Ishino, N. Katayama, and Y. Sakurai, *Journal of Astronomical Telescopes, Instruments, and Systems*, **5**(4), 1 – 14 (2019).
- [69] C. Bao, B. Gold, C. Baccigalupi, J. Didier, S. Hanany, A. Jaffe, B. R. Johnson, S. Leach, T. Matsumura, A. Miller, and D. O’Dea, *Astrophys. J.*, **747**(2), 97 (feb 2012).
- [70] S. Kashima, M. Hazumi, H. Imada, N. Katayama, T. Matsumura, Y. Sekimoto, and H. Sugai, *Appl. Opt.*, **57**(15), 4171–4179 (May 2018).
- [71] G.-B. Zhao, Y. Wang, J.-Q. Xia, M. Li, and X. Zhang, *JCAP*, **07**, 032 (2015), arXiv:1504.04507.
- [72] A. Gruppuso, G. Maggio, D. Molinari, and P. Natoli, *JCAP*, **05**, 020 (2016), arXiv:1604.05202.
- [73] S. M. Carroll, *Phys. Rev. Lett.*, **81**, 3067–3070 (1998), astro-ph/9806099.
- [74] L. Pagano et al., *Phys. Rev. D*, **80**(4), 043522 (August 2009), arXiv:0905.1651.
- [75] Y. Minami and E. Komatsu, *Phys. Rev. Lett.*, **125**(22), 221301 (2020), arXiv:2011.11254.
- [76] M. H. Abitbol et al., *JCAP*, **05**, 032 (2021), arXiv:2011.02449.

- [77] S. E. Clark, C.-G. Kim, J. C. Hill, and B. S. Hensley, *Astrophys. J.*, **919**(1), 53 (2021), arXiv:2105.00120.
- [78] E. Y. S. Wu et al., *Phys. Rev. Lett.*, **102**, 161302 (2009).
- [79] D. Foreman-Mackey, D. W. Hogg, D. Lang, and J. Goodman, *Publications of the Astronomical Society of the Pacific*, **125**(925), 306 (2013).
- [80] E. de la Hoz, P. Vielva, R. B. Barreiro, and E. Martínez-González, *JCAP*, **2020**(06), 006 (2020).
- [81] M. Tegmark and G. Efstathiou, *Mon. Not. Roy. Astron. Soc.*, **281**(4), 1297–1314 (August 1996), arXiv:astro-ph/9507009.
- [82] C. Bennett et al., *Astrophys. J. Suppl.*, **148**, 97 (2003), astro-ph/0302208.
- [83] M. Tegmark, A. de Oliveira-Costa, and A. J. Hamilton, *Phys. Rev. D*, **68**(12), 123523 (December 2003), arXiv:astro-ph/0302496.
- [84] Planck Collaboration IX, *Astron. Astrophys.*, **594**, A9 (September 2016), arXiv:1502.05956.
- [85] B. D. Sherwin and T. Namikawa, *ArXiv e-prints* (8 2021), arXiv:2108.09287.
- [86] B. D. Wandelt, E. Hivon, and K. M. Gorski, *Phys. Rev. D*, **64**(8), 083003 (2001).
- [87] E. Hivon, K. M. Górski, C. B. Netterfield, B. P. Crill, S. Prunet, and F. Hansen, *Astrophys. J.*, **567**(1), 2–17 (March 2002), arXiv:astro-ph/0105302.
- [88] D. Alonso, J. Sanchez, A. Slosar, and LSST Dark Energy Science Collaboration, *Mon. Not. Roy. Astron. Soc.*, **484**(3), 4127–4151 (2019).
- [89] G. Efstathiou, *Mon. Not. Roy. Astron. Soc.*, **349**(2), 603–626 (April 2004), arXiv:astro-ph/0307515.
- [90] F. Couchot, S. Henrot-Versillé, O. Perdureau, S. Plaszczyński, B. Rouillé d’Orfeuil, M. Spinelli, and M. Tristram, *Astron. Astrophys.*, **602**, A41 (June 2017), arXiv:1609.09730.
- [91] G. Chon, A. Challinor, S. Prunet, E. Hivon, and I. Szapudi, *Mon. Not. Roy. Astron. Soc.*, **350**(3), 914–926 (May 2004), arXiv:astro-ph/0303414.
- [92] K. M. Górski, E. Hivon, A. J. Banday, B. D. Wandelt, F. K. Hansen, M. Reinecke, and M. Bartelmann, *Astrophys. J.*, **622**(2), 759–771 (April 2005), arXiv:astro-ph/0409513.
- [93] M. Tristram, J. F. Macías-Pérez, C. Renault, and D. Santos, *Mon. Not. Roy. Astron. Soc.*, **358**(3), 833–842 (April 2005), arXiv:astro-ph/0405575.
- [94] Planck Collaboration Int. XLIX, *Astron. Astrophys.*, **596**, A110 (2016), arXiv:1605.08633.
- [95] E. de la Hoz, P. Diego-Palazuelos, E. Martínez-González, P. Vielva, R. B. Barreiro, and J. D. Bilbao-Ahedo, *ArXiv e-prints* (10 2021), arXiv:2110.14328.
- [96] J. Delabrouille, J. F. Cardoso, M. Le Jeune, M. Betoule, G. Fay, and F. Guilloux, *Astron. Astrophys.*, **493**(3), 835–857 (January 2009), arXiv:0807.0773.
- [97] S. Basak and J. Delabrouille, *Mon. Not. Roy. Astron. Soc.*, **419**(2), 1163–1175 (January 2012), arXiv:1106.5383.
- [98] S. Basak and J. Delabrouille, *Mon. Not. Roy. Astron. Soc.*, **435**(1), 18–29 (October 2013), arXiv:1204.0292.
- [99] T. Souradeep, R. Saha, and P. Jain, *New Astronomy Review*, **50**(11-12), 854–860 (December 2006), arXiv:astro-ph/0608199.
- [100] R. Saha, S. Prunet, P. Jain, and T. Souradeep, *Phys. Rev. D*, **78**(2), 023003 (July 2008), arXiv:0706.3567.
- [101] R. Saha, *Astrophys. J. Lett.*, **739**(2), L56 (October 2011), arXiv:1105.6298.

- [102] J. Dick, M. Remazeilles, and J. Delabrouille, *Mon. Not. Roy. Astron. Soc.*, **401**(3), 1602–1612 (January 2010), [arXiv:0907.3105](#).
- [103] M. Remazeilles, J. Delabrouille, and J.-F. Cardoso, *Mon. Not. Roy. Astron. Soc.*, **410**(4), 2481–2487 (February 2011), [arXiv:1006.5599](#).
- [104] M. Remazeilles, J. Delabrouille, and J.-F. Cardoso, *Mon. Not. Roy. Astron. Soc.*, **418**(1), 467–476 (November 2011), [arXiv:1103.1166](#).
- [105] M. Remazeilles, N. Aghanim, and M. Douspis, *Mon. Not. Roy. Astron. Soc.*, **430**(1), 370–385 (March 2013), [arXiv:1207.4683](#).
- [106] F. J. Narcowich, P. Petrushev, and J. D. Ward, *SIAM Journal on Mathematical Analysis*, **38**(2), 574–594 (2006), <https://doi.org/10.1137/040614359>.
- [107] D. Marinucci, D. Pietrobon, A. Balbi, P. Baldi, P. Cabella, G. Kerkycharian, P. Natoli, D. Picard, and N. Vittorio, *Mon. Not. Roy. Astron. Soc.*, **383**(2), 539–545 (January 2008), [arXiv:0707.0844](#).

P. IV: QUIJOTE scientific results - VIII. Diffuse polarized foregrounds from component separation with QUIJOTE-MFI

E. de la Hoz, R. B. Barreiro, P. Vielva, E. Martínez-González, J. A. Rubiño-Martín, B. Casaponsa, F. Guidi, M. Ashdown, R. T. Génova-Santos, & QUIJOTE collaboration. *Monthly Notices of the Royal Astronomical Society*. In press.

QUIJOTE scientific results – VIII. Diffuse polarized foregrounds from component separation with QUIJOTE-MFI

E. de la Hoz^{1,2★}, R. B. Barreiro,¹ P. Vielva,¹ E. Martínez-González,¹ J. A. Rubiño-Martín^{3,4},
B. Casaponsa,¹ F. Guidi^{3,4,5}, M. Ashdown,^{6,7} R. T. Génova-Santos,^{3,4} E. Artal,⁸ F. J. Casas,¹
R. Fernández-Cobos,⁹ M. Fernández-Torreiro,^{3,4} D. Herranz¹, R. J. Hoyland,^{3,4} A. N. Lasenby,^{6,7}
M. López-Caniego,^{10,11} C. H. López-Caraballo,^{3,4} M. W. Peel^{3,4}, L. Piccirillo,¹² F. Poidevin^{3,4},
R. Rebolo,^{3,4,13} B. Ruiz-Granados,^{3,4,14} D. Tramonte,^{3,4,15,16} F. Vansyngel^{3,4} and R. A. Watson.¹²

Affiliations are listed at the end of the paper

Accepted 2022 October 14. Received 2022 October 14; in original form 2022 July 27

ABSTRACT

We derive linearly polarized astrophysical component maps in the Northern Sky from the QUIJOTE-MFI data at 11 and 13 GHz in combination with the Wilkinson Microwave Anisotropy Probe *K* and *Ka* bands (23 and 33 GHz) and all *Planck* polarized channels (30–353 GHz), using the parametric component separation method B-SeCRET. The addition of QUIJOTE-MFI data significantly improves the parameter estimation of the low-frequency foregrounds, especially the estimation of the synchrotron spectral index, β_s . We present the first detailed β_s map of the Northern Celestial Hemisphere at a smoothing scale of 2° . We find statistically significant spatial variability across the sky. We obtain an average value of -3.08 and a dispersion of 0.13 , considering only pixels with reliable goodness of fit. The power-law model of the synchrotron emission provides a good fit to the data outside the Galactic plane but fails to track the complexity within this region. Moreover, when we assume a synchrotron model with uniform curvature, c_s , we find a value of $c_s = -0.0797 \pm 0.0012$. However, there is insufficient statistical significance to determine which model is favoured, either the power law or the power law with uniform curvature. Furthermore, we estimate the thermal dust spectral parameters in polarization. Our cosmic microwave background, synchrotron, and thermal dust maps are highly correlated with the corresponding products of the PR4 *Planck* release, although some large-scale differences are observed in the synchrotron emission. Finally, we find that the β_s estimation in the high signal-to-noise synchrotron emission areas is prior-independent, while, outside these regions, the prior governs the β_s estimation.

Key words: cosmology: observations – methods: data analysis – polarization – cosmic microwave background.

1 INTRODUCTION

Currently, most of the efforts of the cosmic microwave background (CMB) community are devoted to the search for primordial B modes. These predicted B modes at large scales can only be produced by tensor modes, and their detection would constitute compelling evidence of an inflationary phase. The intensity of this primordial signal is determined by the tensor-to-scalar ratio r , the relative amplitude between the tensor and scalar modes at a given pivot scale. The current best upper bound on the tensor-to-scalar ratio is $r < 0.032$ at 95 percent CL, set by the combination of *Planck*, BICEP2/KeckArray, and baryon-acoustic-oscillation data (Tristram et al. 2022).

The weakness of the primordial B modes makes its detection a tremendous experimental challenge, requiring high-sensitivity experiments as well as an exquisite control of systematics. Indeed, a large effort is currently on-going with the aim to detect, or at least to

constrain, r with a sensitivity $\sigma_r(r=0) \leq 10^{-3}$. This includes many planned ground-based experiments, e.g. GroundBIRD (Lee et al. 2020), LSPE-Strip (Lamagna et al. 2020), CMB-S4 (Abazajian et al. 2016), Simons Observatory (Ade et al. 2019), and BICEP array (Hui et al. 2018), as well as satellite missions [e.g. LiteBIRD (LiteBIRD Collaboration et al. 2022) and PICO (Hanany et al. 2019)].

The detectability of the primordial B modes could be improved by removing the secondary B-mode component induced by weak gravitational lensing. Several delensing procedures have been proposed in the literature (Planck Collaboration 2016b; Millea, Anderes & Wandelt 2019) and have been applied to data from current CMB experiments (Planck Collaboration 2016b; Carron, Lewis & Challinor 2017; BICEP/Keck Collaboration 2021), and in forecasts of future CMB experiments (Diego-Palazuelos et al. 2020; Namikawa et al. 2022).

It is necessary to disentangle the CMB polarization signal from those coming from other microwave emissions, such as Galactic synchrotron, thermal dust, and extragalactic point sources. Thus, the problem of component separation is a crucial step in order to detect the primordial B mode of CMB polarization. This process

* E-mail: delahoz@ifca.unican.es

benefits from the characterization of foreground emissions, using complementary frequency ranges that provide unique information about the contaminants.

The main diffuse polarized contaminants are the synchrotron emission (at low frequencies) and the thermal dust emission (at high frequencies). The best characterization of these diffuse foregrounds has been done by *Planck* (Planck Collaboration IV 2020d), using a data set covering frequencies from 30 to 353 GHz. This frequency range limited strongly the estimation of the synchrotron spectral parameters. In Planck Collaboration IV (2020d), it is shown that, with *Planck* data only, one cannot test the spatial variability of the synchrotron spectral index due to limited sensitivity and frequency coverage. The data only allows a measurement of a global spectral index of $\beta_s = -3.1 \pm 0.1$. The synchrotron spectral index has also been estimated using other data sets (e.g. Fuskeland et al. 2014; Krachmalnicoff et al. 2018; Fuskeland et al. 2021).

The Q-U-I JOint Tenerife Experiment (QUIJOTE; Rubiño-Martín et al. 2010) is a polarimetric ground-based CMB experiment whose main scientific goal is the characterization of the polarization of the CMB and other Galactic and extragalactic physical processes in the frequency range of 10–40 GHz and at large angular scales ($\gtrsim 1^\circ$). The experiment is located at the Teide Observatory (at ~ 2400 m above sea level) in Tenerife. It is composed of two telescopes equipped with three instruments: the Multi-Frequency Instrument (MFI), the Thirty-GHz Instrument (TGI), and the Forty-GHz Instrument (FGI), operating at 10–20, 26–36, and 39–49 GHz, respectively.

The MFI instrument has been operating from 2012 November to 2018 October. It conducted two different surveys: (i) a shallow Galactic survey (called ‘wide survey’) covering all the visible sky from Tenerife at elevations larger than 30° , and (ii) a deep cosmological survey covering approximately 3000 deg^2 in three separated sky patches in the northern sky. In this work we use the QUIJOTE-MFI wide survey maps. This survey provides an average sensitivity in polarization of $\sim 35\text{--}40 \text{ }\mu\text{K}$ per 1-deg beam in four bands centred around 11, 13, 17, and 19 GHz (Rubiño-Martín et al. 2022). Those frequencies are crucial to achieving a better characterization of the low-frequency foregrounds. In intensity, this additional information helps breaking degeneracies between the synchrotron, free-free, and anomalous microwave emissions (AMEs) while, in polarization, the QUIJOTE-MFI channels are key to characterize the synchrotron spectral dependence.

In this work, we perform a component separation analysis to obtain more information about the polarized sky using the QUIJOTE-MFI data¹ (Rubiño-Martín et al. 2022) in combination with the publicly available *Planck* (Planck Collaboration I 2020a; Planck Collaboration LVII 2020f) and Nine-Year Wilkinson Microwave Anisotropy Probe (WMAP; Bennett et al. 2013) data. To perform component separation analysis, we use B-SeCRET (Bayesian-Separation of Components and Residual Estimation Tool), a parametric maximum-likelihood method described in de la Hoz et al. (2020).

The paper is organized as follows. In Section 2, we provide details of the main components in the polarized microwave sky and the corresponding parametric models used to characterize them. Section 3 describes briefly the B-SeCRET method. The data used in the analysis are presented in Section 4. Then, the main component separation results obtained are shown in Section 5. Finally, the main conclusions from the analysis are given in Section 6. In Appendix A, we provide maps of the synchrotron spectral index obtained from independent fits in linear Stokes parameters Q and U . Appendix B

compares the variations on the synchrotron spectral index due to rotations of the polarized angle with Faraday rotation.

2 THE MICROWAVE SKY MODEL

The polarized microwave sky is composed primarily of photons from the CMB, synchrotron, and thermal dust. As stated before, the synchrotron emission dominates at low-frequencies while the thermal dust is the principal component at higher frequencies. The contribution from other components, discussed in Section 2.5, is expected to be insignificant and not taken into account. Apart from these astronomical signals, the measured sky signal maps have another contribution from the instrumental noise. The characteristics of this noise depend on the specifications of the experiment. Furthermore, contaminants such as the atmosphere and artificial signals from satellites also contribute to the microwave sky, see Rubiño-Martín et al. (2022) for more details. Thus, the measured polarized sky signal for a given ν channel can be expressed as the following sum:

$$\begin{pmatrix} Q \\ U \end{pmatrix}_\nu = \begin{pmatrix} Q_{\text{cmb}} \\ U_{\text{cmb}} \end{pmatrix}_\nu + \begin{pmatrix} Q_s \\ U_s \end{pmatrix}_\nu + \begin{pmatrix} Q_d \\ U_d \end{pmatrix}_\nu + \begin{pmatrix} Q_n \\ U_n \end{pmatrix}_\nu, \quad (1)$$

where X_{cmb} , X_s , and X_d are the CMB, synchrotron, and thermal dust signals, respectively, and X_n is the instrumental noise ($X \in \{Q, U\}$). In the subsequent subsections, we describe the main physical components that encompass the sky signal as well as some effects that alter this signal. Moreover, we present the parametric models that we use in the component separation analysis for each polarized astronomical component.

2.1 Synchrotron

The synchrotron emission arises from relativistic particles (cosmic rays) passing through the Galactic magnetic field. Its emissivity depends both on the magnetic field strength and energy distribution of the relativistic particles (generally electrons). These quantities are not uniform in the Galactic disc. For instance, the free electrons are more predominant in compact regions as supernovae remnants. On the other hand, the magnetic field is amplified in some compact regions and can have different strength and direction across the sky.

The synchrotron spectral energy distribution (SED) is generally described as a power law (Rybicki & Lightman 2008):

$$\begin{pmatrix} Q_s \\ U_s \end{pmatrix}_\nu = \begin{pmatrix} A_s^Q \\ A_s^U \end{pmatrix} \left(\frac{\nu}{\nu_s} \right)^{\beta_s}, \quad (2)$$

where A_s is the amplitude in brightness temperature at the pivot frequency $\nu_s = 30 \text{ GHz}$ and β_s is the spectral index which is assumed to be equal for both Q and U Stokes parameters.

Previous works dedicated to the estimation of the spectral index, found values around $\beta_s \simeq -3.1$ (Planck Collaboration IV 2020d). However, the spectral index is expected to vary spatially due to its dependence on the energy distribution of the cosmic rays $N(E)$. Studies such as Fuskeland et al. (2014), Vidal et al. (2015), Krachmalnicoff et al. (2018), Martire, Barreiro & Martínez-González (2022), and Weiland et al. (2022) indicate that different polarized regions present different spectral indices. Here, we conduct a more detailed analysis of the β_s spatial variations in the Northern Hemisphere by performing a pixel-by-pixel component separation analysis using the QUIJOTE MFI polarized maps.

The S-PASS survey (Carretti et al. 2019) has provided the most sensitive reconstruction of the β_s variations of the South Celestial Hemisphere (Krachmalnicoff et al. 2018). They found large variability over the sky, and a mean value of -3.22 ± 0.08 . Those results

¹This is one of the papers which are part of the MFI wide survey data release.

were further confirmed in the analysis of Fuskeland et al. (2021) that estimated the spectral index taking into account the Faraday Rotation effect. They also studied the Galactic plane and found compatible results to those where only WMAP data were used, finding a flatter index in the Galactic plane than at high Galactic latitudes.

We have also considered an extension of equation (2), where we include a possible curvature in the synchrotron's SED:

$$\left(\frac{Q_s}{U_s}\right)_\nu = \left(\frac{A_s^Q}{A_s^U}\right)_\nu \left(\frac{\nu}{\nu_s}\right)^{\beta_s + c_s \log\left(\frac{\nu}{\nu_s}\right)}, \quad (3)$$

where c_s is the parameter that represents the curvature. This extension is worth studying since a curved spectrum can account for steepening or flattening of the SED due to different effects, e.g. cosmic ray aging effect or multiple synchrotron components along the line of sight. This model could also account for the presence of polarized AME.

2.2 Thermal dust

The thermal dust radiation comes from dust grains present in the interstellar medium. Those grains absorb ultraviolet light and re-emit as a grey body. In general, these dust grains are not perfectly spherical and typically have their minor axis aligned with the direction of the local magnetic field. This effect yields polarized thermal dust emission. The SED of this radiation is often described as a modified blackbody with emissivity index β_d and dust temperature T_d :

$$\left(\frac{Q_d}{U_d}\right)_\nu = \left(\frac{A_d^Q}{A_d^U}\right)_\nu \left(\frac{\nu}{\nu_d}\right)^{\beta_d + 1} \frac{e^{\gamma \nu_d} - 1}{e^{\gamma \nu} - 1}, \quad (4)$$

where A_d is the amplitude of the dust in brightness temperature evaluated at the pivot frequency $\nu_d = 143$ GHz and $\gamma = \frac{h}{k_B T_d}$.² The amplitude is well characterized by the higher frequency channels, where the other components are clearly subdominant. The current temperature map of the dust grains (T_d) is obtained from temperature analysis and has values mostly between 14 and 26 K. The polarized dust emissivity evaluated with *Planck* data is $\beta_d = 1.55 \pm 0.05$ (Planck Collaboration IV 2020d).

Several works support the idea that a single component dust model is too simplistic and more components might be required to fully characterize this emission (e.g. McBride, Bull & Hensley 2022; Ritacco et al. 2022). None the less, since this paper is focused on the low frequency foregrounds, we keep the model used in Planck Collaboration VI (2020d) which seems to provide a good description at the *Planck* polarized frequencies (30 GHz $< \nu < 353$ GHz).

2.3 CMB

The CMB radiation has a thermal blackbody spectrum with a temperature of $T_o = 2.7255 \pm 0.0006$ K (Fixsen 2009). CMB photons are linearly polarized due to the Thomson scattering experienced with the hot electron gas at the last scattering surface. Unlike in intensity, where the CMB can be the dominant contribution at intermediate frequencies (70–150 GHz) and high Galactic latitudes, in polarization, the foreground contribution cannot be overlooked. Thus, in order to detect the primordial B -mode, experiments with very high sensitivity, exquisite control of systematics and a careful removal of foregrounds are mandatory.

The CMB signal at each pixel is given by its amplitude A_{cmb} , which is the only free parameter for this component. Since the rest

of the components are given in brightness temperature, we convert the thermodynamic temperature of the CMB to the same units:

$$\left(\frac{Q_{\text{cmb}}}{U_{\text{cmb}}}\right)_\nu = \left(\frac{A_{\text{cmb}}^Q}{A_{\text{cmb}}^U}\right)_\nu \frac{x^2 e^x}{(e^x - 1)^2}, \quad (5)$$

where $x = \frac{h\nu}{k_B T_o}$.

2.4 Faraday rotation

Another issue intrinsic to the polarization signal is the Faraday rotation effect, i.e. the rotation of the plane of polarization that occurs when light passes through the interstellar medium in the presence of a magnetic field. The magnitude of this effect scales with the square of the wavelength; hence, its repercussions are more significant at low frequencies. To properly account for this effect we require a broad knowledge of the Galactic magnetic field as well as the interstellar medium, in order to recognize the regions where the effect is more significant. Moreover, since the instrumental beam has a finite size, the measured signal is an average of the emission from various directions within the beam with slightly different rotation angles. This results in a ‘beam depolarization’ of the signal.

Hutschenreuter et al. (2022) show that the possible Faraday Rotation effects at the QUIJOTE-MFI frequencies (10–20 GHz) are very small in most of the sky, and particularly at high Galactic latitudes. Thus, in this work we have not considered any Faraday Rotation effect. Nevertheless, in Appendix B we study variations on the synchrotron spectral index due to rotations of the polarized angle and compare it to Faraday Rotation models such as the one proposed in Hutschenreuter et al. (2022).

2.5 Other contributions

It is well known that there are other foreground components whose emissions are important for intensity analyses. In particular, at low frequencies, one needs to consider two additional Galactic emission components: the bremsstrahlung radiation generated from electron-ion scattering in interstellar plasma (free-free), and AME, whose physical origin still is not fully clear. At high frequencies, in addition to thermal dust, we find an isotropic extragalactic emission called the cosmic infrared background (CIB), coming from different sources, e.g. dusty star-forming galaxies, quasars, intergalactic stars, and intercluster dust in the Local group. We also have other contributions such as CO line emission or Sunyaev–Zeldovich effect (SZ) from clusters of galaxies (Sunyaev & Zeldovich 1972) that should be taken into account in intensity analyses (Planck Collaboration 2016a). In addition, emission from extragalactic point sources, both at radio and infrared frequencies is an important contaminant at small scales. In polarization the problem is simplified since several of these emissions (free-free, CIB, SZ) are not expected to be polarized (at least significantly); therefore, we do not consider them.

The polarization of the AME is still under study because its nature is still uncertain (Dickinson et al. 2018). Several models have been proposed such as spinning dust particles (Ali-Haïmoud 2013), magnetic dipole emission (Draine & Lazarian 1999), or more recently the proposal of spinning nano-diamonds (Greaves et al. 2018). The predicted polarization fraction of the AME emission for most of these models is below 5 per cent. From the data analysis point of view, no evidence of polarization has been found in compact region studies [the most stringent constraints on the polarization fraction, Π , have been provided by Génova-Santos et al. (2017), $\Pi < 0.22$ per cent at 41 GHz]. Due to this lack of evidence, we do not take into account the AME component in this work.

² h and k_B are Planck and Boltzmann constants, respectively.

On the other hand, point sources present some degree of polarization, which is in general small (a few percent). However, at the resolutions considered in this work, they are subdominant with respect to Galactic foregrounds. Thus, we do not include them in our analysis. We note however that in the data, a few polarized point sources are present that are not taken into account in the component separation analysis (see Herranz et al. 2022).

3 COMPONENT SEPARATION METHODOLOGY

In this work, we apply the parametric component separation method B-SeCRET to extract the polarized astrophysical signals. Parametric methods are very powerful since they provide physical information of each sky component. However, they require a profound theoretical understanding of the nature of the foregrounds and accurate knowledge of the experiment’s characteristics to avoid biases in the analysis.

Below, in Section 3.1, we outline the component separation technique applied in this work. Then, in Section 3.2, we describe the prior information that is used in the Bayesian analyses.

3.1 Bayesian analyses

The B-SeCRET methodology is a parametric pixel-based maximum-likelihood method, which relies on an Affine-Invariant Markov Chain Monte Carlo Ensemble sampler to draw samples from a posterior distribution (Foreman-Mackey et al. 2013). This methodology has already been applied in previous studies (e.g. de la Hoz et al. 2020, 2022).

B-SeCRET applies Bayesian inference to determine the best-fitting model parameters given some prior information. In Bayesian statistics, the probability of the set of model parameters θ_p given the signal data \mathbf{d}_p at the pixel p is proportional to the probability of the \mathbf{d}_p given θ_p times the probability of θ_p , i.e.

$$\mathcal{P}(\theta_p|\mathbf{d}_p) \propto \mathcal{P}(\mathbf{d}_p|\theta_p)\mathcal{P}(\theta_p). \quad (6)$$

$\mathcal{P}(\theta_p)$ is commonly known as the prior information, whereas $\mathcal{P}(\mathbf{d}_p|\theta_p)$ is usually referred to as the likelihood. Assuming Gaussian noise, the likelihood of the data can be expressed as

$$\mathcal{P}(\mathbf{d}_p|\theta_p) = \frac{\exp\left(-\frac{1}{2}(\mathbf{d}_p - \mathbf{S}_p)^T \mathbf{C}^{-1}(\mathbf{d}_p - \mathbf{S}_p)\right)}{\sqrt{(2\pi)^N \det(\mathbf{C})}}, \quad (7)$$

where \mathbf{C} is the noise covariance matrix, N is the number of elements in the \mathbf{d}_p array, and \mathbf{S}_p is the parametric model considered, which has been described in detail in Section 2.

To draw samples from the posterior probability, we use the PYTHON implementation EMCEE (Foreman-Mackey et al. 2013) of an affine-invariant ensemble sampler for Markov chain Monte Carlo (MCMC; Goodman & Weare 2010). In each pixel, the best-fitting parameters and their uncertainties are obtained as the median and the standard deviation of their respective marginalized posterior probability.

3.2 Priors

In this work, we benefit from prior information about astrophysical foregrounds to help with convergence and computational time reduction. For example, the synchrotron spectral index is known to be around -3.1 , although experiments such as S-PASS found a more negative value. Here, we use the estimated value obtained with *Planck* polarization data by the SMICA method, $\beta_s = -3.1 \pm 0.06$ (Planck



Figure 1. QUIJOTE observed sky after removing the geostationary satellite band and the region around the north celestial pole, which is affected by high atmospheric air-mass [$f_{\text{sky}} = 51$ percent, Galactic coordinates centred on (0,0)].

Collaboration IV 2020d) and use a broad Gaussian distribution $\mathcal{N}(-3.1, 0.3)^3$ as a prior on β_s . When we include a curvature in the synchrotron model we apply a Gaussian prior $\mathcal{N}(0, 0.1)$ on c_s . Moreover, we apply Gaussian priors $\mathcal{N}(1.55, 0.1)$ and $\mathcal{N}(21, 3)$ on both β_d and T_d , respectively. Finally, flat priors are used in the characterization of the amplitude parameters.

4 DATA

The aim of this work is to obtain a better characterization of the low-frequency foregrounds by including the newly released QUIJOTE-MFI maps in component separation analyses. In this section, we summarize the basic details of these maps as well as those from the other experiments used in the analysis, i.e. the *K* and *Ka* bands from WMAP and *Planck*’s third and fourth public releases (PR3 and PR4, respectively). We also discuss some technical issues related to the instruments such as the estimated noise, RFI, and the colour corrections.

4.1 Data sets

In this analysis, we have used the data from the following experiments:

(i) QUIJOTE: We have used the low frequency QUIJOTE MFI 11 and 13 GHz channels (MFI) (Rubiño-Martín et al. 2022) due to their better signal-to-noise ratio. Although QUIJOTE has observed 70 percent of the sky there are regions with poorer sensitivity due to the presence of artificial satellites and high atmospheric masses in some directions. Thus, in this analysis we have considered the mask shown in Fig. 1, as the observable sky. This mask (satband + NCP) is described in Rubiño-Martín et al. (2022).

(ii) WMAP: We have used the low-frequency Nine-Year WMAP *K* (22.8 GHz) and *Ka* (33.1 GHz) bands (Bennett et al. 2013).⁴

(iii) *Planck*: We have used the full set of *Planck* polarization maps, i.e. the low-frequency instrument (LFI) 30, 44, and 70 GHz frequency maps and the high-frequency instrument (HFI) 100, 143, 217, and 353 GHz maps. We have obtained results from both PR3⁵ (Planck

³ $\mathcal{N}(x, \sigma)$ represents a normal distribution with mean x and variance σ^2 .

⁴The other bands were not included since they have a much lower synchrotron signal-to-noise ratio and do not contribute to the determination of the synchrotron characteristics.

⁵We used the Planck maps corrected from bandpass leakage.

Collaboration II 2020b; Planck Collaboration III 2020c) and PR4 (Planck Collaboration LVII 2020f) data releases.

Before component separation analyses, the frequency maps are all convolved (taking appropriately into account the beam window function of each particular frequency map) with a common beam, a Gaussian beam of full width at half-maximum (FWHM) = 2° , and downgraded to the same resolution through spherical harmonics, given by the `HEALPIX` parameter $N_{\text{side}} = 64$. The procedure followed is described below:

- (i) We calculate the spherical harmonics coefficients ($t_{\ell m}, e_{\ell m}, b_{\ell m}$) using the `healpy` routine `map2alm`.
- (ii) To convolve all channels with the same beam we multiply the ($t_{\ell m}, e_{\ell m}, b_{\ell m}$) by $b_\ell(2^\circ) p_\ell(64)/(b_{i,\ell} p_\ell(N_{\text{side}}))$, where $b_\ell(\alpha)$ is a Gaussian beam window function whose FWHM is α , $b_{i,\ell}$ is the i th channel beam window function, and $p_\ell(N_{\text{side}})$ is the pixel window function at the resolution N_{side} .
- (iii) We obtain the downgraded maps at $N_{\text{side}} = 64$, applying the `healpy` routine `alm2map` to the new ($t_{\ell m}, e_{\ell m}, b_{\ell m}$).

Several combinations of the previous data sets have been tested. Each configuration's name is given by the 'sum' of the sets of maps included in the analysis. For example, the configuration composed of PR4 channels in combination with WMAP's K and Ka bands is referred as $K/Ka+PR4$, or MFI-QUIJOTE low-frequency channels in combination with PR4 and WMAP channels is specified as $MFI+K/Ka+PR4$.

4.2 Instrumental effects

Real data present different instrumental effects that need to be accounted for. For example, an important contribution to the observed signal is the noise produced by the detectors of each experiment. A proper characterization of the noise levels is key for component separation analyses. In this work, we have calculated the covariance matrix among the frequency channels per pixel, required by the parametric component separation method, using realistic noise simulations specific to each instrument. Each experiment's noise simulations are obtained as follows:

- (i) QUIJOTE: We have used the correlated noise simulations described in Rubiño-Martín et al. (2022). They account for the $1/f$ noise present in the maps, and the correlated noise component between 11 and 13 GHz.
- (ii) WMAP: We have generated a set of white noise simulations using the RMS noise per pixel provided by the WMAP collaboration (Hinshaw et al. 2003). The RMS noise σ is calculated as $\sigma = \sigma_0/\sqrt{N_{\text{obs}}}$.⁶
- (iii) Planck: For PR3, we have used the FFP10 simulations generated by the Planck Collaboration (Planck Collaboration I 2020a). In the case of the PR4, we have employed the noise simulations described in Planck Collaboration LVII (2020f).⁷

While the frequency channels of different experiments are uncorrelated, there might be correlations between channels of a given instrument. This is the case for the 11 and 13 GHz low-frequency MFI channels. On the other hand, we have assumed no correlations between frequency channels for WMAP and Planck. Thus, for a

given pixel p , the Planck and WMAP frequency covariance matrices are diagonal while QUIJOTE's has non-zero off-diagonal terms. For a given configuration, the covariance matrix is obtained as a block matrix, where each block corresponds to the frequency covariance matrix of each instrument included in that configuration.

To obtain the experiments' frequency covariance matrices, first we pre-process the noise simulations in the same manner as the data maps. Then, for Planck and WMAP, the diagonal terms are calculated as the variance of the noise simulations at the corresponding pixel for each frequency. Each pixel covariance matrix between QUIJOTE 11 and 13 GHz is calculated as the sample covariance matrix using the values of the 11 and 13 GHz noise simulations at that specific pixel.

One test to verify that our covariance matrices are well estimated is the following. We obtained a distribution of $\chi^2_{n,i}$ values as

$$\chi^2_{n,i} = \mathbf{n}_i^T \mathbf{C}_i^{-1} \mathbf{n}_i, \quad (8)$$

where \mathbf{n}_i is a noise simulated map⁸ at the frequency i and \mathbf{C}_i is the noise covariance matrix described above. The $\chi^2_{n,i}$ distributions should have the expected form with N_{pix} degrees of freedom (dof). This is consistent with the values obtained for Planck and WMAP. In the case of QUIJOTE, the distribution deviates slightly from the expected N_{pix} dof χ^2 -distribution, since they are not end-to-end noise simulations and hence not as accurate (see Rubiño-Martín et al. 2022 for details). However, as subsequent analyses will show, we find that when the astrophysical emission is included, the obtained χ^2 is correct as expected, i.e. in the regions where the model properly explains the data (outside the Galactic plane). Thus, QUIJOTE's noise simulations are accurate enough to perform scientific analyses.

We explored the possibility of including correlations among neighbouring pixels within a 1 deg radius.⁹ The smoothing process of the maps induces noise correlations among different pixels and, although this does not affect our pixel-by-pixel analyses, it can affect analyses where we assume a uniform parameter value within one region. Therefore, for each pixel, we calculated the covariance matrix among its neighbouring pixels from noise simulations. Then we generated a sparse covariance matrix where the only non-zero values in each row were the diagonal element and the correlation with the neighbouring pixels. In this case, the distribution does not follow a N_{pix} degrees-of-freedom χ^2 distribution as one would expect. The recovered values were smaller than expected, more notably for Planck maps. This is a consequence of not having enough noise simulations, which prevents us from obtaining a good characterization of the noise correlations. Therefore, we use the covariance matrices that do not take into account possible noise correlations among neighbouring pixels in the following.

As explained in Rubiño-Martín et al. (2022), in order to correct residual RFI signals emerging after co-adding all data in the map-making process of the QUIJOTE-MFI data, the polarization maps are corrected using a function of the declination (FDEC). This correction is equivalent to applying a filter to QUIJOTE data, which removes the zero mode in lines of constant declination. In Appendix C, we studied whether this correction affects the recovery of foregrounds spectral parameters such as β_s . We found that if only QUIJOTE maps are filtered with FDEC the recovered β_s map is biased in regions such as the North Polar Spur. When all data maps are

⁶ σ_0 and N_{obs} are given in <https://lambda.gsfc.nasa.gov/product/wmap/dr5/skymap.info.html>.

⁷ Simulations available at NERSC under `/global/cfs/cdirs/cmb/data/planck2020`.

⁸ The noise simulations used in this test are different from the noise simulations used to calculate the noise covariance matrices.

⁹ The pixels contained within this radius are the ones with the largest correlations induced by the smoothing process.

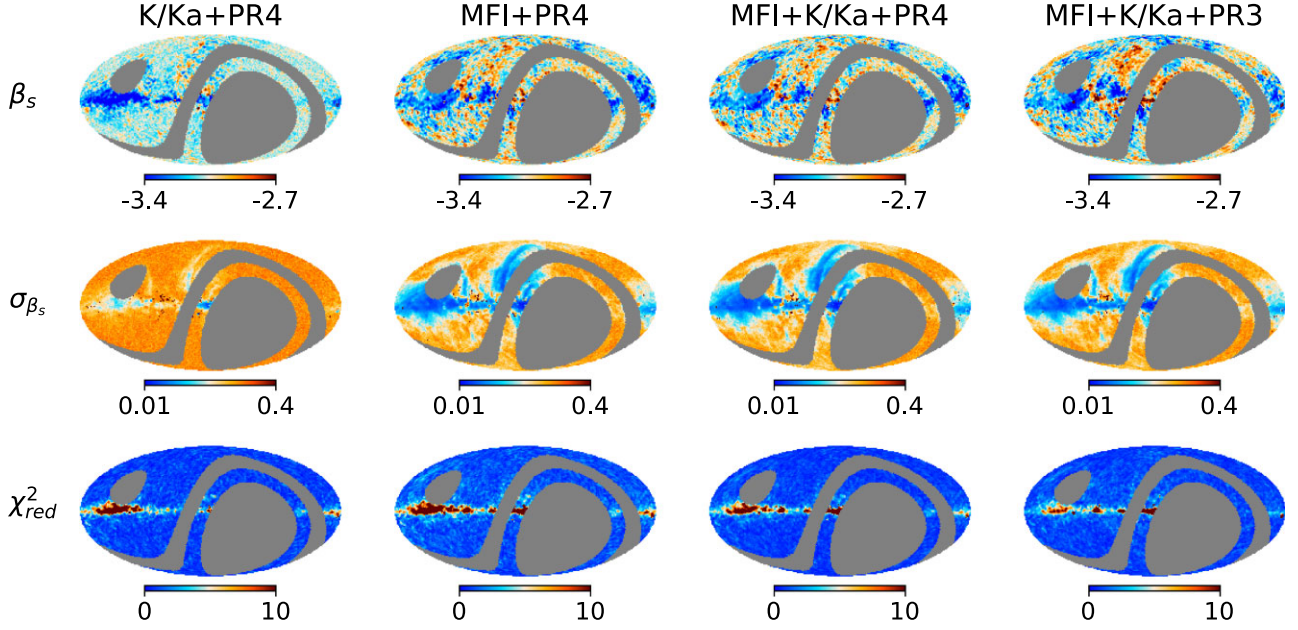


Figure 2. Synchrotron spectral index (top row) and uncertainty maps (middle row) obtained after component separation with four different data sets. The synchrotron emission is modelled with a power law. Bottom row: Reduced χ^2 map obtained for each data set.

filtered in the same way this bias disappears. Thus, for this analysis we have filtered all signal maps with their corresponding FDEC function.

Another important instrumental effect arises from detectors having a finite bandwidth. This issue has to be taken into account when dealing with foreground components whose amplitude varies within that frequency band. This effect can be corrected by adding a multiplicative factor, called colour correction, to the signal that depends on the spectral behaviour. We have used the `fastcc` PYTHON code (Peel et al. in preparation; Genova-Santos et al. in preparation) to obtain the colour corrections of each experiment considered here. Therefore, our model for the sky signal presented in Section 2 is corrected as follows:

$$X_\nu = X_{\nu,\text{cmb}} + \frac{X_{\nu,s}}{C_s(\alpha, \nu)} + \frac{X_{\nu,d}}{C_d(\beta_d, T_d, \nu)}, \quad (9)$$

where X is either Q or U , $C_s(\alpha, \nu)$ is synchrotron colour correction whose spectral behaviour is modelled as a power law with $\alpha = \beta_s + 2$. The spectral behaviour of dust colour correction $C_d(\beta_d, T_d, \nu)$ is assumed to be a modified blackbody and it is determined by its β_d and T_d parameters. The colour correction values are updated in each MCMC iteration.

5 RESULTS

In this section, we present the component separation products obtained using the recently released QUIJOTE low-MFI data along with the already available *Planck* and WMAP data. We have focused primarily on the synchrotron spectral parameters since those are the parameters where a greater improvement is found (see Sections 5.1 and 5.2). Moreover, we show the recovered amplitudes of the CMB, synchrotron and thermal dust and, compare them with those obtained by Commander using PR4 data in Section 5.3. In Section 5.4, we present the spectral parameters of the thermal dust. Finally, we evaluate the robustness of these results in Section 5.5.

5.1 Synchrotron spectral index

The major improvement obtained from including the low-frequency QUIJOTE-MFI channels is having the sufficient sensitivity to study the synchrotron spectral index with great accuracy. Here, we have conducted a deep study on several aspects with regard to this parameter. First, we have compared the recovered β_s maps using different combinations of the available data sets (Section 5.1.1). Section 5.1.2 studies the spatial variability of β_s . Finally, we compare our results to the available β_s models that are often exploited in simulations used in CMB science forecasts in Section 5.1.3.

5.1.1 Data sets

We have obtained different β_s maps from component separation analyses using the four following data sets: WMAP K and Ka bands with PR4 (K/Ka +PR4); QUIJOTE-MFI 11 and 13 GHz channels with PR4 (MFI+PR4); QUIJOTE-MFI 11 and 13 GHz channels, WMAP K and Ka bands and PR4 (MFI+ K/Ka +PR4) and QUIJOTE-MFI 11 and 13 GHz channels, WMAP K and Ka bands and PR3 (MFI+ K/Ka +PR3). The results are shown in Fig. 2. It is clear from the comparison of the synchrotron spectral index uncertainty maps obtained in the K/Ka +PR4 case (first column) with respect to the MFI+ K/Ka +PR4 case (third column), that the inclusion of QUIJOTE channels significantly improves the estimation of β_s . Moreover, we observe that, outside the Galactic plane, the estimation of β_s is very close to the mean value of the prior set on this parameter, in this case -3.1 . In other words, the information contained in that fraction of the data, i.e. the likelihood, is very poor and the estimation is driven by the prior.

This improvement does not come from the inclusion of more channels, but from channels where the synchrotron contribution is larger. This is evident from the comparison of the results from K/Ka +PR4 with respect to MFI + PR4, where the number of frequency channels is the same but the results are significantly better for the latter.

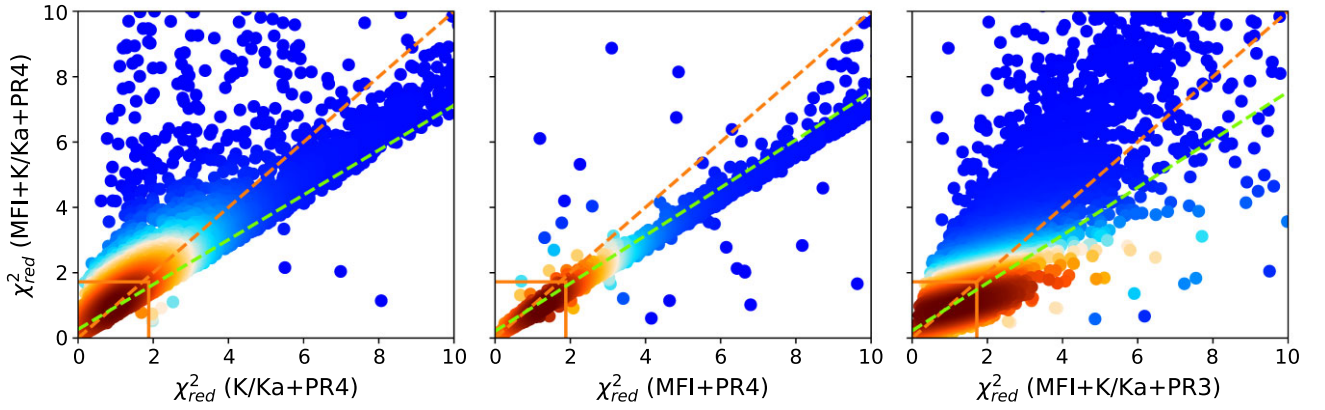


Figure 3. Reduced χ^2 , χ^2_{red} , obtained using the MFI+K/Ka+PR4 data set versus the χ^2_{red} obtained using K/Ka+PR4 (left), MFI+PR4 (centre), and MFI+K/Ka+PR3 (right). The colour scale is related to the density of points; redder (bluer) corresponds to denser (sparser) regions. The orange rectangle shows the χ^2_{red} within a 95 percent confidence region. The slope calculated with the points within this 95 percent confidence region is $m = 0.686 \pm 0.004$ (left column), $m = 0.732 \pm 0.003$ (centre column), and $m = 0.731 \pm 0.003$ (right column), shown with a green dashed line. The orange dashed line shows the one-to-one line. The synchrotron emission is modelled with a power law.

Finally, we have compared also the results obtained with MFI+K/Ka+PR3 and MFI+K/Ka+PR4 (fourth and third columns, respectively). In this case, the recovered uncertainty maps are virtually the same but there are some distinct differences between the β_s maps that should be ascribed to changes in *Planck* maps.

One of the advantages of using a parametric component separation method is that we can evaluate the goodness of the fit with certain estimators. In this work, we use the reduced χ^2 estimator, whose value at a given pixel p is calculated as

$$\chi^2_{\text{red},p} = \frac{1}{N_{\text{dof}}} \sum_{i \in \{Q,U\}} (\mathbf{d}_{p,i} - \mathbf{S}_{p,i}) \mathbf{C}_{p,i}^{-1} (\mathbf{d}_{p,i} - \mathbf{S}_{p,i}), \quad (10)$$

where the sum is over all Q and U frequency channels, and N_{dof} is the number of dof. The bottom row of Fig. 2 shows the χ^2_{red} maps obtained for each data set combination. These maps show that our default model, i.e. a power law and a modified blackbody to model the synchrotron and thermal dust emission, respectively, provides a good fit (low values of χ^2_{red}) outside the Galactic plane. Within the Galactic plane, this model is not able to capture all the physical complexity and the χ^2_{red} values are quite large. However, we note that in this analysis we have considered statistical uncertainties but not calibration errors, which in QUIJOTE are of 5 per cent. Apart from the higher complexity of the Galactic plane emission, the higher χ^2_{red} in this region could also be due, in part, to having neglected calibration errors.

We have also used the χ^2_{red} estimator to select the data set that is used as the default for further tests between the MFI+K/Ka+PR3 and the MFI+K/Ka+PR4 data sets, i.e. the only combinations that include all the channels considered. In Fig. 3, the χ^2_{red} obtained using the MFI+K/Ka+PR4 data set is plotted against the χ^2_{red} obtained with K/Ka+PR4, MFI+PR4, and MFI+K/Ka+PR3. The 95 per cent confidence regions are delimited by orange lines. These lines indicate the χ^2 values, from the reduced χ^2 -distribution with N_{dof} dof,¹⁰ that satisfy that the normalized area covered to their left is equal to 0.95. We have also fitted the points within this confidence regions to a straight line to determine which data set has more pixels with smaller χ^2_{red} . If the slope is larger than unity, the data set on the horizontal axis has more pixels with smaller χ^2 . If the slope is smaller than

unity, the data set on the vertical axis is the one which satisfies that condition.

Although it is not clear from the left plot of Fig. 3 that data set is better, the slope $m = 0.686 \pm 0.004$ indicates that the MFI+K/Ka+PR4 data set provides a better fit. Moreover, the K/Ka+PR4 data set has larger uncertainties which can mask model inconsistencies. On the other hand, from the middle plot of Fig. 3, we observe that the inclusion of the K and Ka WMAP bands to the MFI+PR4 data set improves the goodness of the fit. Finally, comparing MFI+K/Ka+PR4 with MFI+K/Ka+PR3, we see that PR3 provides a better fit in the Galactic plane, while PR4 fits better outside the Galactic plane (Fig. 2). Since the fit in the Galactic plane is bad in both cases we have chosen the MFI+K/Ka+PR4 as our default data set, as it retrieves better fits within the 95 per cent confidence regions (pixels outside the Galactic plane, Fig. 4).

5.1.2 Spatial variability

We have also studied the spatial variability of the synchrotron spectral index in several high signal-to-noise regions of the sky (see Fig. 5). These connected regions satisfy the condition that β_s is estimated with a signal-to-noise ratio larger than 15. In particular, R1 is associated with the North Polar Spur (NPS), and R2 encompasses the Galactic plane. R3, R4, and R5 are other sky regions where the polarized synchrotron intensity has a large signal-to-noise ratio.

Fig. 6 shows the estimated synchrotron spectral index against the uncertainty on the estimation of all the pixels within a given region. We have limited this study to those pixels with a χ^2_{red} within the 95 per cent confidence region. The area delimited by the dotted lines contains the values that are consistent within 3σ with the weighted mean in each region. The top left-hand panel indicates that β_s has a large spatial variability across the whole available QUIJOTE-MFI sky (QS). Therefore, a constant value of β_s is not a good model of the synchrotron emission. On the contrary, the R1, R3, R4, and R5 pixels values are well within those lines, i.e. a uniform β_s value could be a good model for all pixels within each region. Finally, R2 (the top right-hand panel) shows a significant spatial variability which is consistent with the large heterogeneity observed in the β_s map.

¹⁰The χ^2 -distribution with N_{dof} divided by N_{dof} .

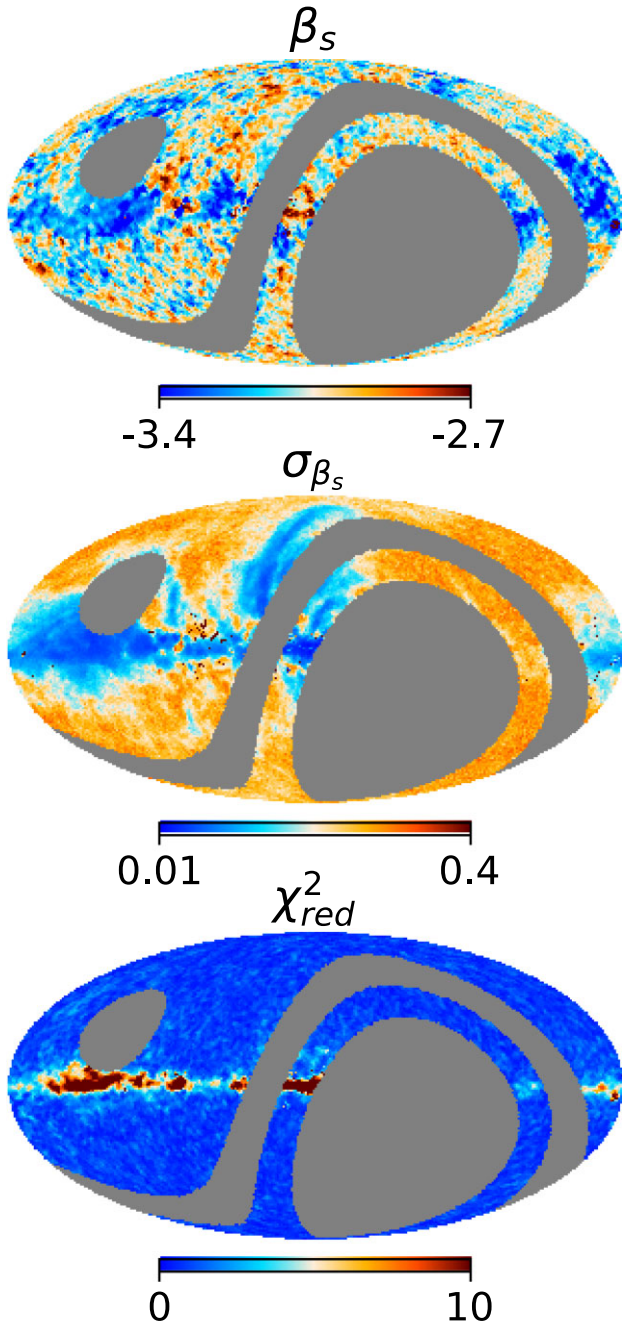


Figure 4. Synchrotron spectral index (top), its uncertainty (middle), and reduced χ^2 (bottom) maps obtained after component separation with the default data set MFI+K/Ka+PR4. The synchrotron emission is modelled with a power law.

The study of regions with uniform β_s values helps with improving the detectability of primordial B modes. Allowing spatial variations of the spectral parameters at the pixel level results in a very robust parametrization of the signal sky. However, this robustness comes at the expense of an increase in the statistical uncertainty of the parameters as less information is provided in the fit (Errard & Stompór 2019). Thus, several approaches have been proposed in the literature to define sky regions with uniform spectral parameters. For example, in Errard & Stompór (2019), these regions are chosen

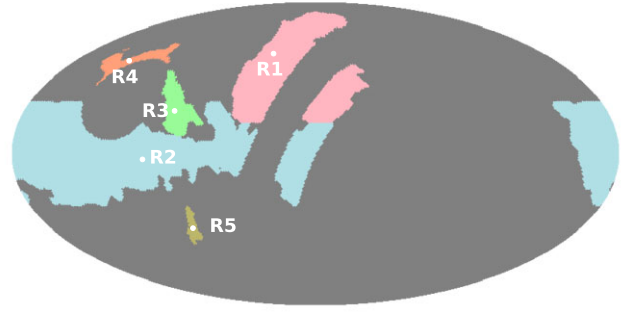


Figure 5. R1, R3, R4, and R5 are sky regions where β_s is assumed uniform in Section 5.1.2 and R2, which encompasses the Galactic plane seen by QUIJOTE, is a very heterogeneous region. These regions satisfy that β_s is recovered with a signal-to-noise ratio larger than 15.

as super-pixels at a lower HEALPix maps resolution, whereas in Grumitt, Jew & Dickinson (2020), the regions are obtained using clustering algorithms such as the mean-shift clustering algorithm. Recently, Puglisi et al. (2022) has presented a new methodology based on spectral clustering to define geometrical affine regions with similar spectral parameters. It is worth noting that if the assumption of uniform spectral parameters within those regions does not hold, the modelling errors introduced might bias cosmological parameters measurements obtained from the output CMB map after component separation, as well as foreground model parameters.

We have calculated the value of β_s in some of these regions assuming a constant value within each region. We have performed the fit in the following manner:

- (i) First, we fix β_s to a given value and fit the rest of the model parameters in each pixel of the region.
- (ii) Then, the rest of the parameters are fixed to the estimation from the previous fit, and we fit β_s assuming a unique value in the whole region under study.
- (iii) β_s is fixed to the new obtained value and the process is repeated until it reaches convergence.

We have chosen the median of the β_s values (obtained pixel-wise) within that region as the initial guess of β_s . The results are shown in Table 1. Notice that the uncertainty on the recovered β_s has dramatically decreased. This is simply a result of having N_{pix}^R (the number of pixels contained within the region R) times more information to fit the parameter. The β_s values recovered in each region (R1, R3, R4, and R5) are not consistent among them. These results further showcase the spatial variability of the synchrotron’s spectral parameter.

5.1.3 Comparison with current β_s models

In this section, we compare our β_s map with the currently most used β_s template,¹¹ the ‘Model 4’ Miville-Deschenes et al. template, which was constructed with Haslam and WMAP observations in temperature (Miville-Deschênes et al. 2008). Fig. 7 shows the distribution of the spectral index value for this model (blue) and for our analysis (orange), considering only those QUIJOTE-MFI pixels

¹¹Used for example in the *Planck* Sky Model (Ashdown et al. 2012), or in the Python Sky Model (PYSM) a PYTHON library to simulate foregrounds (Thorne et al. 2017).

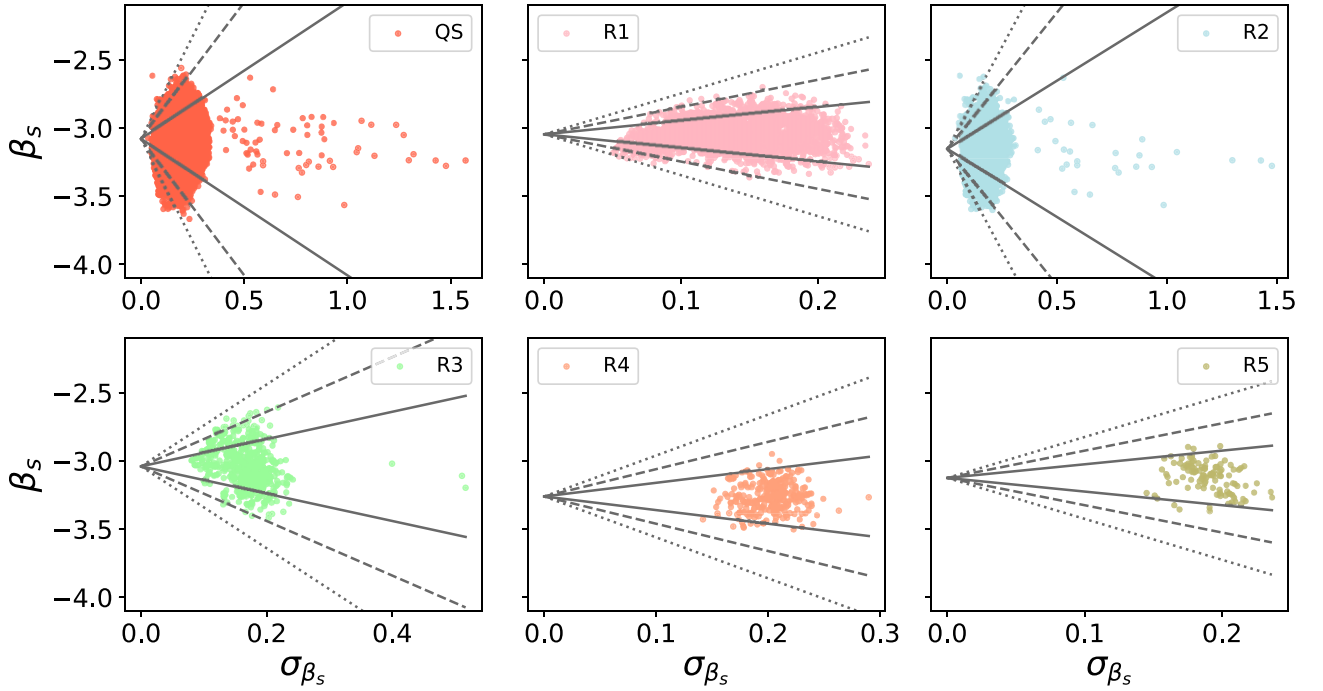


Figure 6. Synchrotron spectral index estimate against its uncertainty within different sky regions: QUIJOTE-MFI sky (QS) (Fig. 1); R1, R2, R3, R4, and R5 are shown in Fig. 5. The solid, dashed, and dotted lines enclose the values of β_s within 1σ , 2σ , and 3σ of the weighted mean, respectively. The study is limited to those pixels whose χ^2_{red} lies within the 95 per cent confidence region.

Table 1. Synchrotron spectral index estimation β_s^R and its uncertainty $\sigma(\beta_s^R)$ obtained, assuming uniform value across the regions R1, R3, R4, and R5 shown in Fig. 5.

Region	f_{sky} (per cent)	β_s^R	$\sigma(\beta_s^R)$
R1	4.84	-3.028	0.002
R3	0.96	-2.945	0.008
R4	0.56	-3.319	0.011
R5	0.21	-3.228	0.019

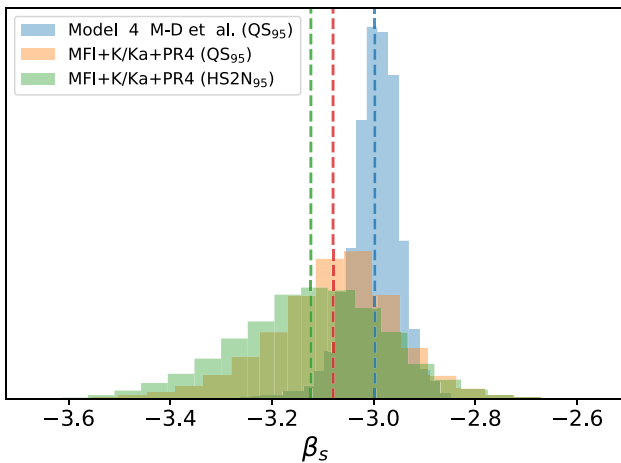


Figure 7. Distribution of the synchrotron spectral index from ‘Model 4’ of Miville-Deschênes et al. (2008) and from our estimation using the MFI+K/Ka+PR4 data set. Vertical dashed lines indicate the mean value for each distribution.

that lie within the 95 per cent confidence region of the χ^2 (QS_{95}). In the QS_{95} region, the mean and the standard deviation from the ‘Model 4’ of Miville-Deschênes et al. (2008) template are -3.00 ± 0.05 while those from our estimate are -3.08 ± 0.13 . It is interesting to note that the variability observed in our analysis is significantly larger. A direct comparison of the dispersion of both maps (using the same mask) indicates an increment of the spatial variability in our study around a factor of 2.6, i.e. $\sigma(\beta_s^{\text{MFI+K/Ka+PR4}})/\sigma(\beta_s^{\text{Model 4}}) \sim 2.6$.

One may wonder if this result can be affected by the considered prior, since the estimated spectral indices for low signal-to-noise pixels are significantly constrained by it (see Section 5.5.2). In order to test this point, we have repeated the previous analysis considering only those pixels satisfying that the recovered β_s values have a signal-to-noise larger than 15 (i.e. where the synchrotron signal-to-noise ratio is high and thus the results are not driven by the prior) and lie within the 95 per cent confidence region of the χ^2 ($HS2N_{95}$). In this case, we find that the mean value and dispersion of the distribution of β_s are -3.12 ± 0.15 for our analysis (see green histogram in Fig. 7) versus -3.00 ± 0.05 for ‘Model 4’ in the same region, confirming our finding. Although our estimations can be affected by the presence of noise, the results show that the variability of the synchrotron spectral index assumed in current templates is underestimated. A similar increment in the variability was also noted by analysing the S-PASS data in the Southern hemisphere (Krachmalnicoff et al. 2018).

Recently, Weiland et al. (2022) published a composite map of β_s , using publicly available data covering approximately 44 per cent of the sky. In the region covered in our study, they obtained β_s estimates in the Galactic plane and the North Polar Spur using information from WMAP K and Ka band, and estimates at latitudes larger than 40° using K , Ka , and DRAO 1.41 GHz map (Wolleben et al. 2006). From a visual inspection, our results are compatible within the North Polar Spur. We find that our derived spectral indices are steeper at the

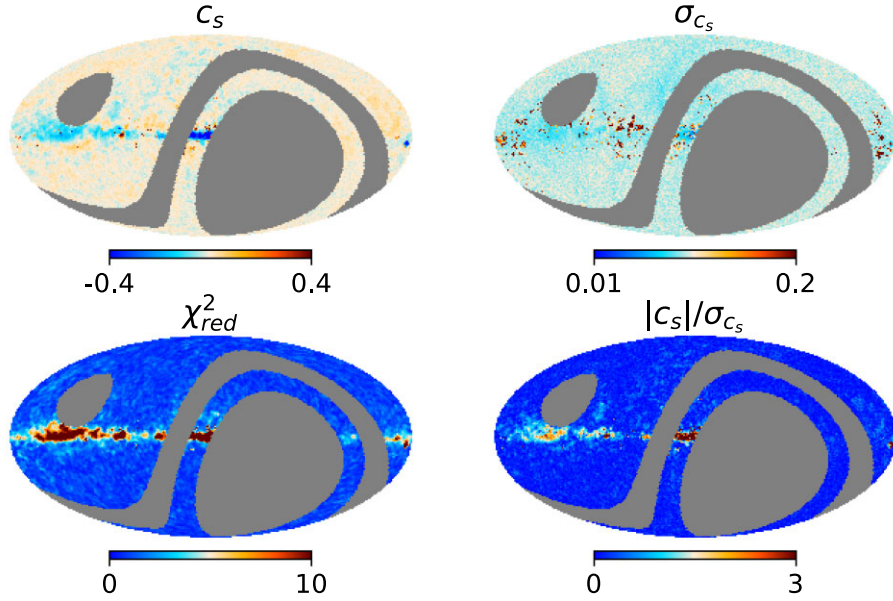


Figure 8. Top row: Synchrotron curvature estimate (left) and uncertainty (right) maps obtained after component separation using the default data set (MFI+K/Ka+PR4). The synchrotron emission is modelled using a power law with spatially varying curvature (pixel-wise). Bottom row: Reduced χ^2 map (left) and c_s signal-to-noise map (right).

Galactic plane. Weiland et al. (2022) found discrepancies between the β_s values obtained in the Fan Region when they performed the analysis using WMAP *K* and *Ka* band versus WMAP *K* band and Planck LFI 30 GHz channel. In the latter case, the recovered β_s were significantly steeper. We repeated our analysis excluding the PR4 30 GHz channel and did not observe a discrepancy concerning the β_s recovered from the default analysis in Fan Region. This results from the fact that the β_s recovery is mainly driven by QUIJOTE-MFI data. At high latitudes, we cannot make a reasonable comparison since our β_s estimates are driven by the prior. They also show that DRAO data have some unexplained systematics and can be affected by Faraday rotation depolarization.

Other studies, such as those presented in Vidal et al. (2015), Fuskeland et al. (2014, 2021), Martire et al. (2022), also find variability of the spectral index analysing different regions of the sky. However, it is difficult to compare the same regions in our map, since they compute a global spectral index for large areas, while we work pixel by pixel. For example, near the centre of the Galactic plane we see a fair amount of structure that cannot be accounted for in the T–T scatter plots analyses carried out in some of the cited papers, that use several pixels to obtain a single β_s value. In that sense, the methodology followed here is more complete given that we perform a full component separation in each pixel, retrieving information at smaller scales for a large fraction of the sky.

Rubiño-Martín et al. (2022) obtain an estimate of the synchrotron spectral index map directly from the comparison of the QUIJOTE-MFI 11 GHz map with the WMAP *K*-band map. The results obtained there are fully consistent with the ones from this work.

5.2 Synchrotron curvature

We have also explored a synchrotron model with curvature, i.e. the model presented in equation (3), using the MFI+K/Ka+PR4 data set. Fig. 8 shows the estimation and uncertainty maps of the curvature parameter as well as the χ^2_{red} map and the c_s signal-to-noise map.

We observe from the signal-to-noise map that curvature is detected at more than 3σ in the Galactic plane, in regions where the fit is not good as it can be seen from the χ^2_{red} map. Even though the inclusion of a curvature parameter is not able to explain the complexity of this region, this parameter can account for some effects along the Galactic plane, e.g. Faraday rotation.

Outside the Galactic plane the estimated c_s values are close to zero and their uncertainties are around 0.1, which are the expected value and the spread of the prior set on c_s . Moreover, the recovered β_s map in this case is very similar to the one obtained when the synchrotron is model with a power law. This means that we do not have enough sensitivity to detect a spatially varying curvature. Hopefully, joint analyses with future releases of the Northern celestial hemisphere data like the new MFI2 instrument and C-BASS at 5 GHz (Jones et al. 2018) might elucidate more details on changes of the power-law spectrum.

In Fig. 9, we compare the goodness of fit using a power law versus a power law with curvature as the synchrotron model. We see that there are more points located below the bisector. Besides, the slope 0.9227 ± 0.0005 calculated at the 95 percent confidence region, shows that, given the current data, the power-law model is slightly preferred over the power law plus curvature model.

Furthermore, we have considered modelling the synchrotron emission with a power law with uniform curvature. We have assumed a constant c_s in four regions: RC1, RC2, and the Haze and North bubble (Fig. 10). The recovered curvature values are shown in Table 2. RC1 encompasses all the pixels whose χ^2_{red} is within 95 per cent confidence region. RC2 is composed of the RC1 pixels that also satisfy that the synchrotron polarized intensity signal-to-noise ratio at 30 GHz is larger than 5. We detect curvature in all regions. The detection is more evident in RC1 and RC2, mostly due to the higher sensitivity (lower σ_c) in these regions. However, it is important to highlight that there is no physical reasoning behind the definition of RC1 and RC2, and the assumption of uniform curvature in all synchrotron

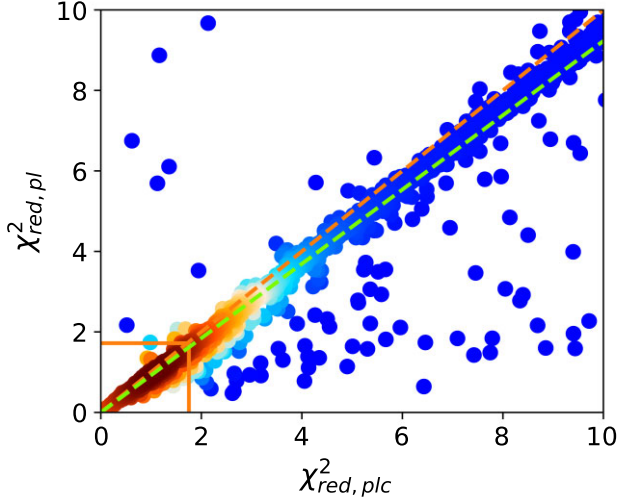
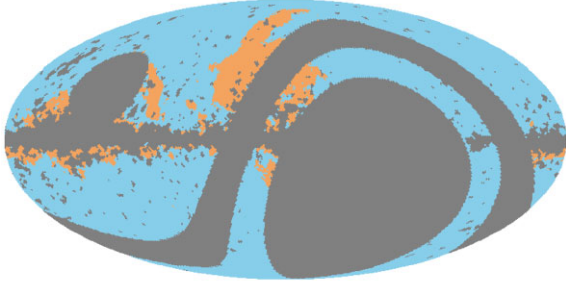
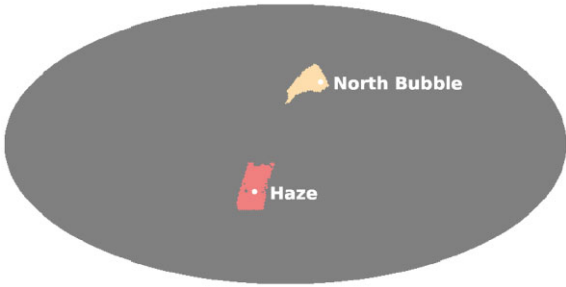


Figure 9. Reduced χ^2 calculated using a power law as a model of the synchrotron emission ($\chi^2_{\text{red,pl}}$) versus χ^2_{red} when the model is a power law with spatially varying curvature ($\chi^2_{\text{red,plc}}$). The colour scale is related to the density of points, redder (bluer) corresponds to denser (sparser) regions. The red rectangle shows the χ^2_{red} within a 95 per cent confidence region. The slope at the 95 per cent confidence region is $m = 0.9227 \pm 0.0005$, shown with a green dashed line. The orange dashed line shows the one-to-one line.



(a) RC1 (coloured) and RC2 (orange) regions.



(b) Haze and North bubble regions.

Figure 10. Regions where c_s has been assumed to be uniform.

Table 2. Estimated values of the curvature and its uncertainty obtained assuming the curvature is uniform within the region.

Region	$f_{\text{sky}} (\%)$	c_s^R	$\sigma_{c_s^R}$	$ c_s^R /\sigma_{c_s^R}$
RC1	45.48	-0.0797	0.0012	63.75
RC2	5.93	-0.2768	0.0017	161.57
Haze	0.94	0.041	0.010	4.23
North bubble	0.63	-0.083	0.007	11.43

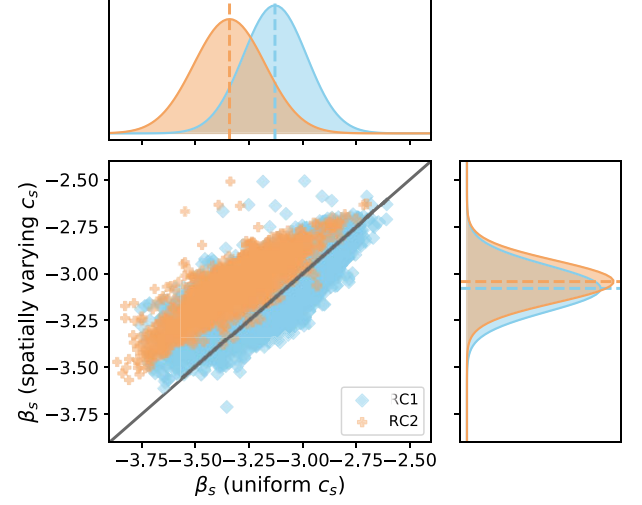


Figure 11. Comparison between the pixel β_s values obtained when fitting the synchrotron emission with a spatially varying curvature model (y-axis) versus with a model with uniform curvature (x-axis) in the regions RC1 and RC2 using the MFI+K/Ka+PR4 data set.

high signal-to-noise regions is arbitrary.¹² In the Haze and North bubble, we find a curvature value different from zero at more than 3σ . These regions are studied in greater detail in Guidi et al. (2022).

We have studied how β_s changes when we impose the constraint of having a uniform c_s value within each region. The results are displayed in Fig. 11. For RC2, we observe that β_s steepens considerably. The weighted mean value of β_s in RC2 is $\langle \beta_s \rangle = -3.022 \pm 0.011$ in the pixel-wise analysis and, $\langle \beta_s \rangle = -3.375 \pm 0.002$ when c_s is imposed to be uniform in RC2. For RC1, this effect is not as considerable. The weighted mean values are $\langle \beta_s \rangle = -3.079 \pm 0.002$ and $\langle \beta_s \rangle = -3.1651 \pm 0.0014$ when c_s varies pixel-wise and is uniform, respectively. The steepening of β_s leads to values of the exponent $\beta_s + c_s \log(\nu/\nu_s)$ within $[-3.04, -3.10]$ at 11 GHz which are compatible with the average value of β_s when we fit to a power-law model. From these results, we infer that the β_s and c_s parameters are not independent. More sensitive data at the QUIJOTE frequencies and at lower and/or higher frequencies are required to break the degeneracy.

In order to test which model provides a better goodness of fit, we calculate the reduced χ^2 of a given region R as follows:

$$\chi^2_{\text{red},R} = \frac{1}{N_{\text{dof}}} \sum_{p=1}^{N_{\text{pix}}^R} \sum_{l \in \{Q,U\}} (d_{p,i} - S_{p,i}) \mathbf{C}_{p,i}^{-1} (d_{p,i} - S_{p,i}), \quad (11)$$

where we sum over all pixels N_{pix}^R within R . The dof are given as $N_{\text{dof}} = N_{\text{pix}}^R (2N - N_{\theta})$ when all model parameters are allowed to vary pixel-wise, and $N_{\text{dof}} = N_{\text{pix}}^R (2N - (N_{\theta} - 1)) - 1$ when c_s is assumed uniform in the analysis, where N_{θ} is the number of model parameters. We calculated the value of this estimator in three cases: (i) when the model parameters are allowed to vary spatially using a power-law model for the synchrotron component, (ii) when the model parameters vary from pixel-to-pixel using a power law with curvature model, (iii) when we fit the data assuming uniform curvature using a power law with curvature model. The results are given in Table 3.

¹²Any curvature will be more easily detected in high signal-to-noise regions than in low signal-to-noise regions.

Table 3. Reduced χ^2 obtained using either a power law or a power law with curvature model in different regions, R . We have considered two curvature models: one where c_s varies spatially (spatial) and other where c_s is assumed constant in R .

Model	Curvature	Region	$\chi_{red,R}^2$
Power law	–	RC1	0.892
Power law + curvature	Spatial	RC1	0.965
Power law + curvature	Uniform	RC1	0.936
Power law	–	RC2	1.010
Power law + curvature	Spatial	RC2	1.088
Power law + curvature	Uniform	RC2	1.081
Power law	–	Haze	0.845
Power law + curvature	Spatial	Haze	0.936
Power law + curvature	Uniform	Haze	0.885
Power law	–	North bubble	0.961
Power law + curvature	Spatial	North bubble	1.041
Power law + curvature	Uniform	North bubble	0.986

The χ_{red}^2 results show that the models we used, i.e. power law and power law with curvature, are compatible with the data. However, there is not enough statistical significance to discern which model suits better the data. Especially, considering that we have not been able to take into account possible correlations between pixels and that the power law with curvature model is degenerate.¹³

5.3 Recovered amplitudes and comparison with *Planck* results

We have compared our baseline results, i.e. using the MFI+K/Ka+PR4 data set and a power law as the synchrotron model, to those obtained from the Commander pipeline (Eriksen et al. 2008) applied to PR4 data.¹⁴ We have only considered this pipeline among those used by *Planck*, since it is the reference method with regard to the recovery of foreground components. In Figs 12–14, we show a comparison of the CMB, the synchrotron emission at 30 GHz, and the thermal dust emission at 353 GHz between Commander and our results. In order to perform a direct comparison we have filtered Commander results with FDEC. The left column shows the Q and U Commander amplitudes, the centre column our amplitudes and the right column the corresponding uncertainties. A visual inspection shows that both estimates are very similar, especially the synchrotron and thermal dust emissions that are the dominant contributions in polarization.

5.3.1 CMB

Regarding CMB, the left column of Fig. 15 shows the pixel-to-pixel comparison for the recovered CMB map from our analysis and from Commander both in Q and U . We have applied a combination of the QUIJOTE observed sky and the common polarization confidence mask provided by the *Planck* Collaboration¹⁵ (Planck Collaboration IV 2020d).

We observe from the maps that there is a discrepancy. We found that the application of the FDEC filter, before the component

separation process, leads to a decrease of the amplitude in the power spectra of our recovered CMB map. This power reduction appears only when *Planck* and WMAP are filtered with FDEC, since the CMB information is extracted mainly from those channels. Instead of applying the FDEC filter, one could apply a filter that suppresses the large scales. This would be equivalent to applying a linear function to the CMB and there would not be a reduction of power. However, since we want to study all scales we decided to apply the FDEC filter. Since the aim of this work is the study of the foregrounds, we keep the results obtained with all the data filtered with FDEC to recover the β_s map without any bias. One can in principle recover the unbiased CMB following one of the approaches described below:

(i) Perform the component separation analysis without filtering the data with FDEC and including the FDEC correction in QUIJOTE-MFI data as part of the model; or

(ii) Given the unbiased β_s map¹⁶ and *Planck* data, one can construct a template with the modes that QUIJOTE-MFI data are missing after being filtered with FDEC. Then perform the analysis with the reconstructed QUIJOTE-MFI maps.

Since the estimation of the CMB is out of the scope of this paper, we leave this analysis for future works.

5.3.2 Synchrotron

Fig. 16 shows the difference between the synchrotron amplitude maps obtained using the MFI+K/Ka+PR4 and the Commander reconstruction using the PR4 data. The largest differences observed are located in the Galactic plane where the model fails to reproduce the sky signal. We also observe large-scale structures in the difference map. These structures can originate from the fact that we have obtained a more accurate estimation of the scaling law, as our fit is performed using additional frequencies. However, overall, the correlation between both methods is very good.

This can also be seen in the centre column of Fig. 15, where a pixel-to-pixel comparison is given, showing that both methods present a synchrotron amplitude at 30 GHz highly correlated for Q and U except in some pixels where the synchrotron emission is very large. Those pixels are located primarily in the Galactic plane. These discrepancies are likely to arise from differences in the amplitude of the polarized intensity instead of from differences in the polarization angles. In Fig. 15, we observe that both the slopes, in the Q and U plots, are higher than unity. If the discrepancies were originated from differences in the polarization angle, one slope would be higher than unity and the other lower.

5.3.3 Dust

Regarding thermal dust emission, this foreground strongly dominates the 353 GHz *Planck* frequency map and, therefore, the recovered amplitude is very much determined by this channel. This was also the case in the Commander analysis done by the *Planck* Collaboration. Thus, our recovered Q and U components of the thermal dust are strongly correlated with those obtained using Commander, see the right column of Fig. 15.

¹³We considered applying other statistics such as the Bayesian evidence to do model selection. However, since the QUIJOTE-MFI noise simulations are not end-to-end and the Bayesian evidence is very computationally expensive we did not perform any model selection analysis. This is left for future work.

¹⁴Data available at NERSC under /cmb/daa/planck20.

¹⁵Available at <https://pla.esac.esa.int/#maps>.

¹⁶Obtained in the component separation analysis using the data filtered with FDEC.

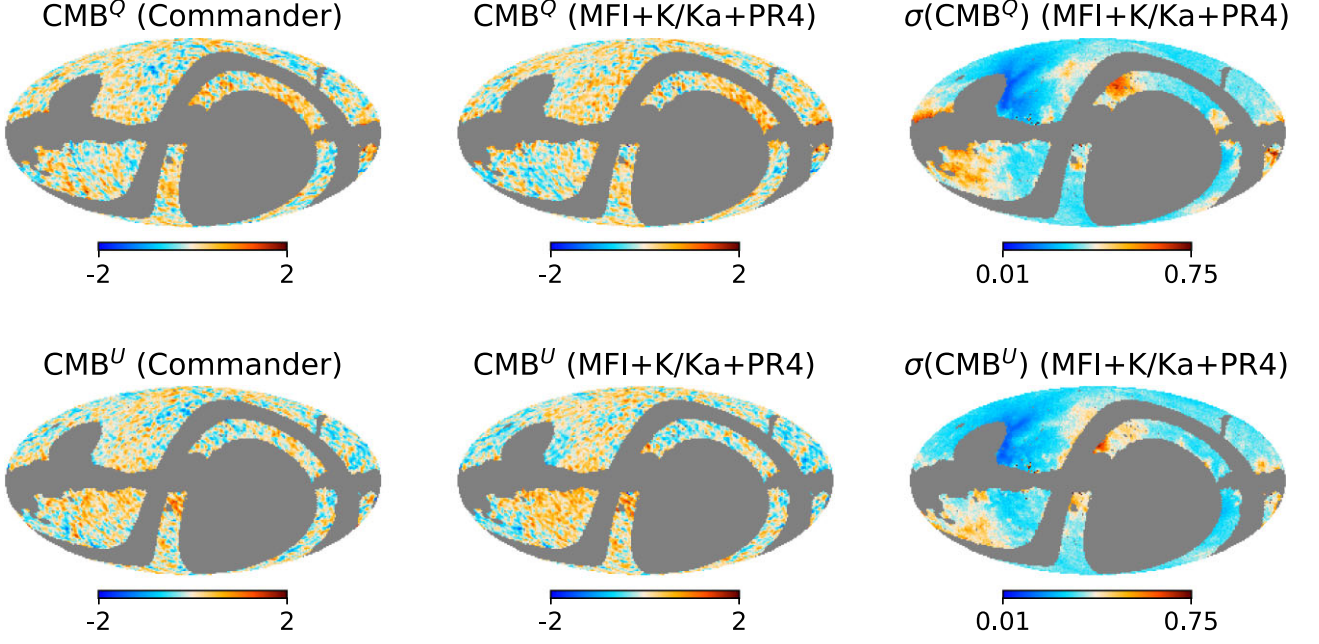


Figure 12. Left column: Commander Q (top) and U (bottom) CMB maps at $N_{\text{side}} = 64$, smoothed with a Gaussian beam to a final resolution of $\text{FWHM} = 2^\circ$. Centre column: CMB Q and U maps using the MFI+K/Ka+PR4 data set. Right column: Uncertainty of the CMB maps. Maps are in thermodynamic temperature (μK). We apply the common polarization confidence mask provided by *Planck*.

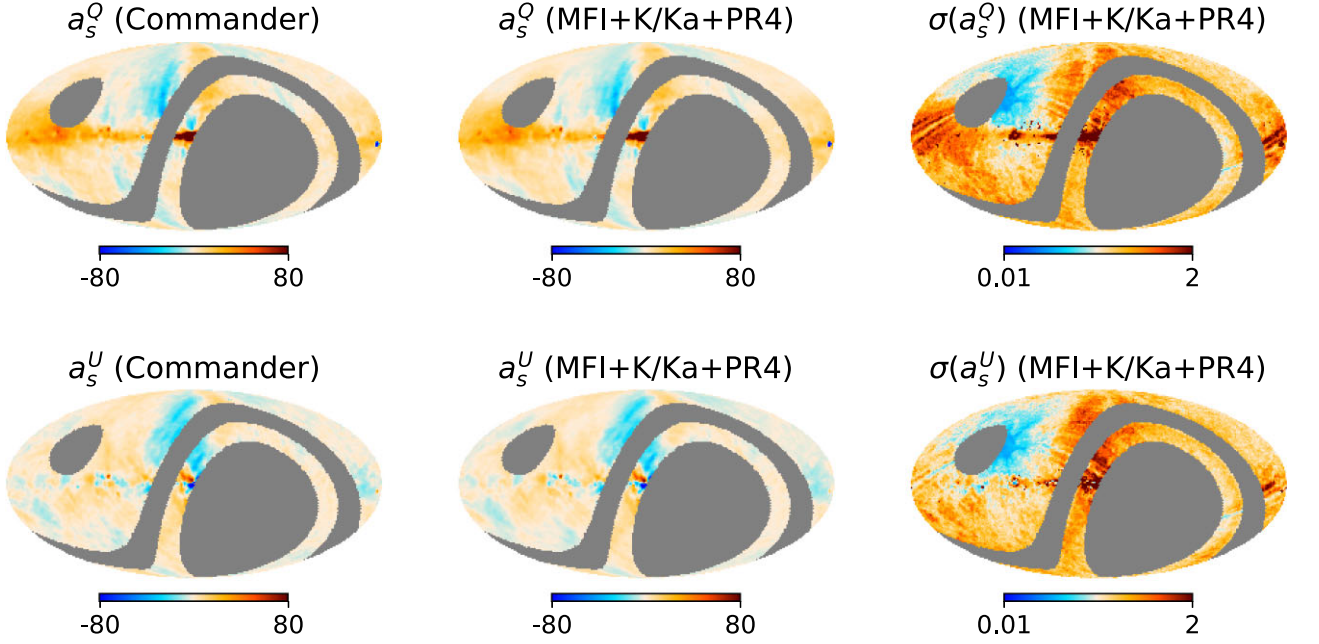


Figure 13. Left column: Commander Q (top) and U (bottom) synchrotron amplitude maps at 30 GHz at $N_{\text{side}} = 64$, smoothed with a Gaussian beam to a final resolution of $\text{FWHM} = 2^\circ$. Centre column: Our estimate of the synchrotron amplitude at 30 GHz, using the MFI+K/Ka+PR4 data set. Right column: Uncertainty of the estimated synchrotron amplitude. Maps are in antenna temperature (μK).

5.4 Dust spectral parameters

Although the frequencies of QUIJOTE-MFI do not overlap with the spectral range where the thermal dust is more dominant, we have studied whether the inclusion of this data set in the analysis can help with the thermal dust characterization due to an improvement on the determination of the rest of the polarized foreground parameters. Fig. 17 shows the thermal dust spectral index β_d recovered with the

default data set, modelling the synchrotron emission as a power law, in two cases:

- (i) T_d is included as a model parameter.
- (ii) T_d is fixed to Commander's estimation of the thermal dust temperature from the component separation analysis in intensity (Planck Collaboration 2016a) like Commander did in their polarization analysis. Fixing T_d helps breaking its degeneracy with β_d in

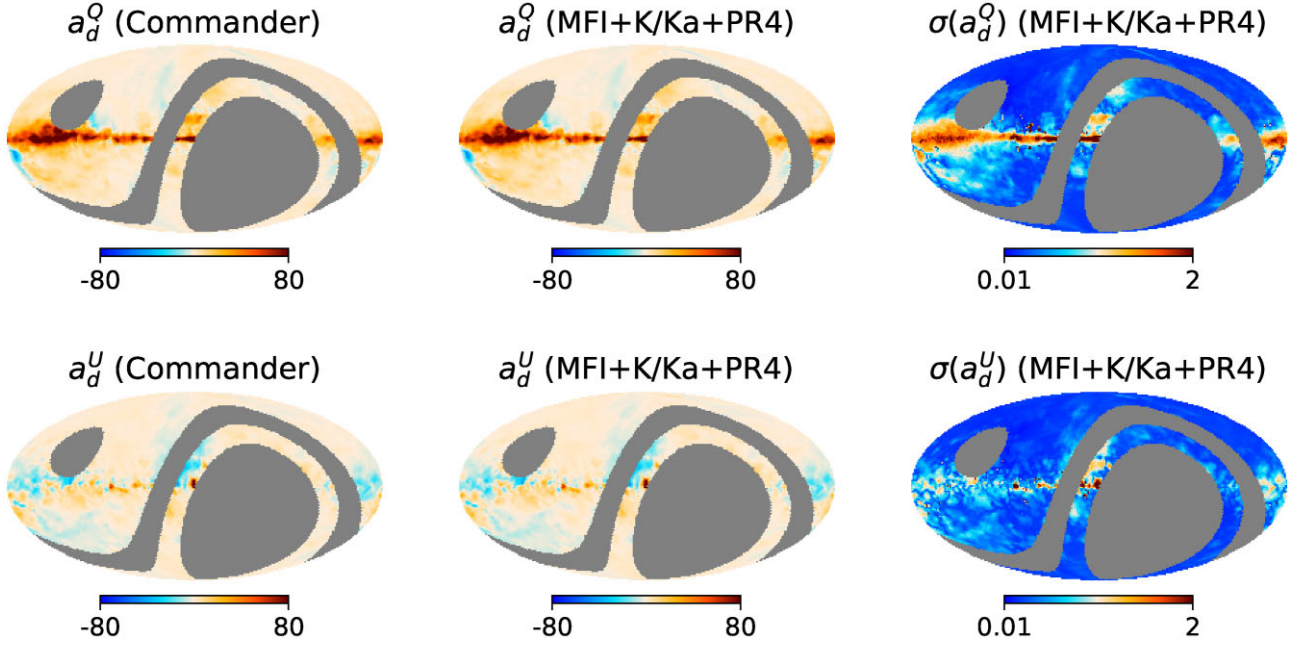


Figure 14. Left column: Commander Q (top) and U (bottom) thermal dust amplitude maps at 353 GHz at $N_{\text{side}} = 64$, smoothed with a Gaussian beam to a final resolution of $\text{FWHM} = 2^\circ$. Centre column: Our estimate of the thermal dust amplitude at 353 GHz, using the MFI+K/Ka+PR4 data set. Right column: Uncertainty of the estimated thermal dust amplitude. Maps are in antenna temperature (μK).

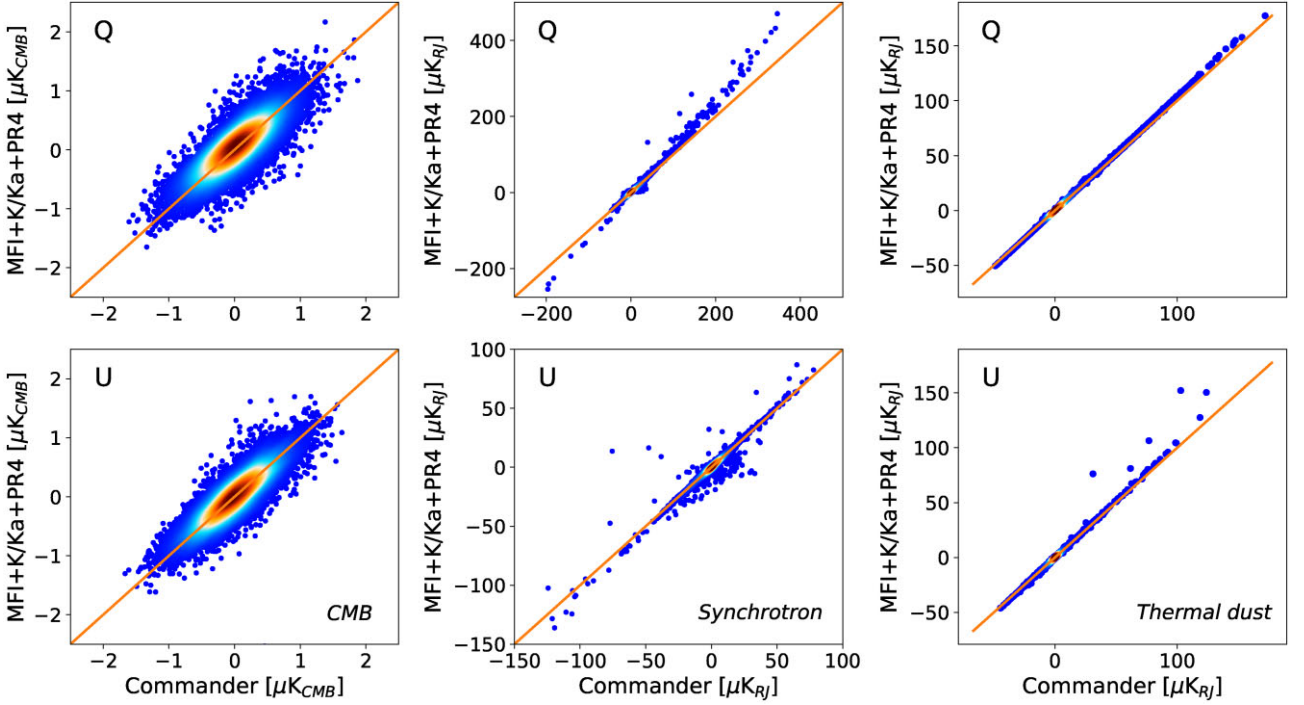


Figure 15. Comparison of CMB (left), synchrotron at 30 GHz (centre), and thermal dust at 353 GHz (right) amplitudes recovered using the MFI+K/Ka+PR4 data set and the ones obtained by Commander using PR4 data. The correlation factors are $\rho^Q = 0.543$ and $\rho^U = 0.817$ (CMB), $\rho^Q = 0.992$ and $\rho^U = 0.973$ (synchrotron), and $\rho^Q = 1.000$ and $\rho^U = 0.997$ (thermal dust).

the Rayleigh–Jeans part of the thermal dust spectrum, which is the one observed with *Planck* in polarization.

In both maps, we find that the recovered β_d values are close to the expected value of the prior, i.e. 1.55, except close to the Galactic

plane where the thermal dust signal is larger.¹⁷ The results differ

¹⁷Notice that the uncertainty does not improve in the regions where the β_d values are close to the mean value of the prior when we fix one parameter. The uncertainty in those pixels is the spread of the prior.

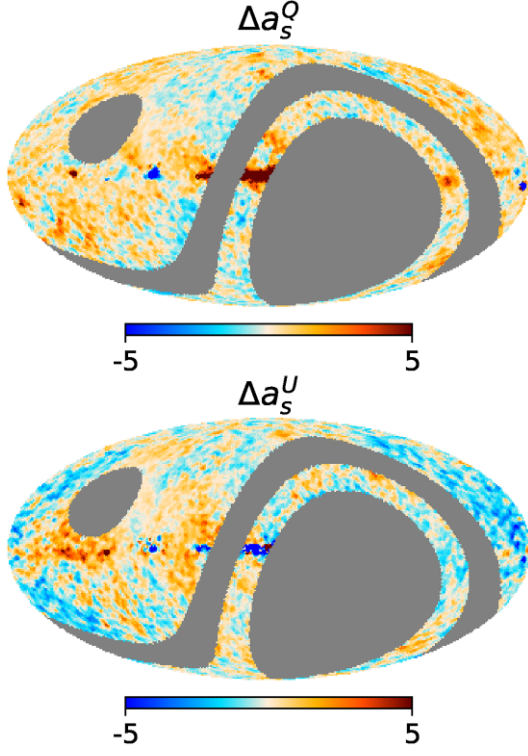


Figure 16. Difference between the synchrotron amplitude a_s^Q (a_s^U) obtained with the MFI+K/Ka+PR4 and the Commander estimate, top row (bottom row). Maps are in antenna temperature (μ K).

significantly along the Galactic plane (see Fig. 18). This difference originates since our recovered T_d map does not resemble the used T_d template, as shown in Fig. 19. We remark that although in the first case T_d is estimated from the polarization analysis, the T_d recovered values lie close to the expected value of the prior (22 K) except along the Galactic plane where the fit is not good. Moreover, it is

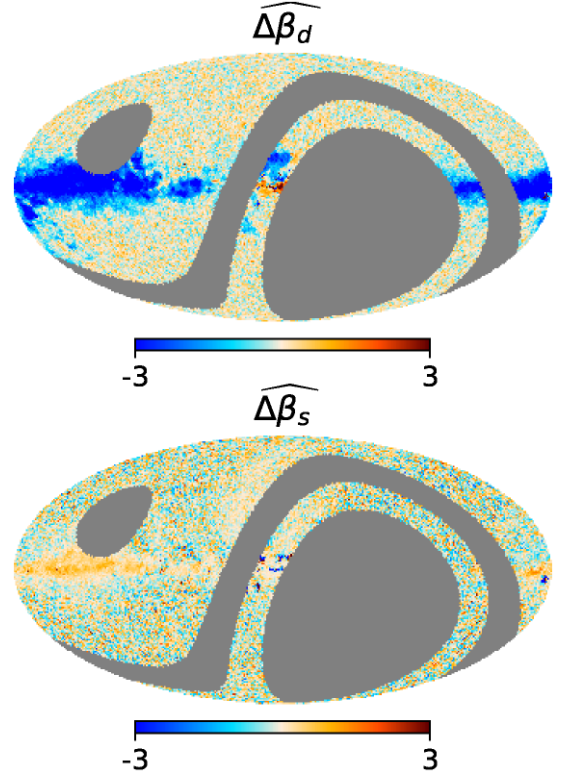


Figure 18. β_d (top row) and β_s (bottom row) relative difference map between the maps obtained when we include T_d as a model parameter and when we fix it.

very difficult to fit T_d from polarization data only, as the highest frequency is 353 GHz, and thus we are not able to trace the thermal dust peak.

In Fig. 18, we show the relative difference between spectral index map of the thermal dust and synchrotron obtained when T_d is included

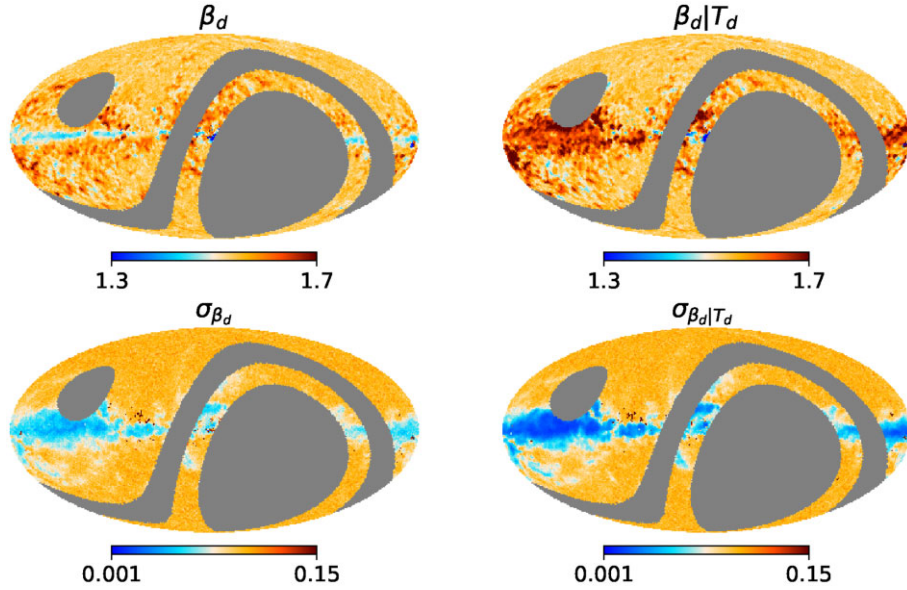


Figure 17. Left column: Estimate (top) and uncertainty (bottom) of thermal dust spectral index obtained when T_d is included as a model parameter. Right column: Estimate (top) and uncertainty (bottom) of thermal dust spectral index obtained when the T_d template obtained by Commander in the intensity analysis is used to fix T_d in the component separation process.

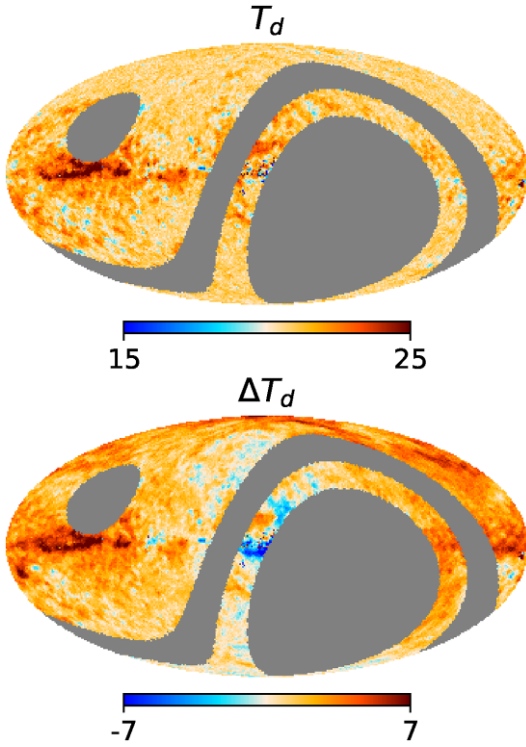


Figure 19. Top row: Thermal dust temperature map recovered in the default case. Bottom row: Difference map between the top row map and the T_d template used in the analysis. Maps are in Kelvin.

as a model parameter and when it is fixed. The relative difference is calculated as follows:

$$\widehat{\Delta\beta}_{p,1,2} = \frac{\beta_{p,1} - \beta_{p,2}}{\sqrt{\sigma_{p,\beta_1}^2 + \sigma_{p,\beta_2}^2 - 2\sigma_{p,\beta_1,\beta_2}}}, \quad (12)$$

where $\sigma_{\beta_1}^2$ ($\sigma_{\beta_2}^2$) is the variance of the β_1 (β_2) map, and σ_{β_1,β_2} is the covariance between the β_1 and β_2 maps that are being compared. As expected from Fig. 17 the differences close to the Galactic plane are significantly large in the case of β_d . On the other hand, we find that, the β_s maps recovered in both cases are compatible and the differences resemble Gaussian noise except along the Galactic plane where the model fails.

We also studied the relative difference between the β_d map obtained with the MFI+K/Ka+PR4 and K/Ka+PR4 data sets in Fig. 20. The top panel shows the relative difference when T_d is included as a model parameter and the bottom panel when T_d is fixed. We observed that both maps are compatible except in regions where the fit is not good. Moreover, when we compare the uncertainty maps we find that there is not a significant improvement when we include QUIJOTE-MFI channels. Thus, we conclude that the improvement in the characterization of low-frequency foregrounds does not help necessarily with the estimation of thermal dust spectral parameters.

5.5 Goodness of fit

In this section, we study in depth the quality of the results obtained using the default data set. In Section 5.5.1, we analyse the χ^2 distribution of the results as well as the Q and U residuals of each channel. Section 5.5.2 investigates the robustness of our results regarding the estimation of the synchrotron spectral index with respect to the prior applied to this parameter.

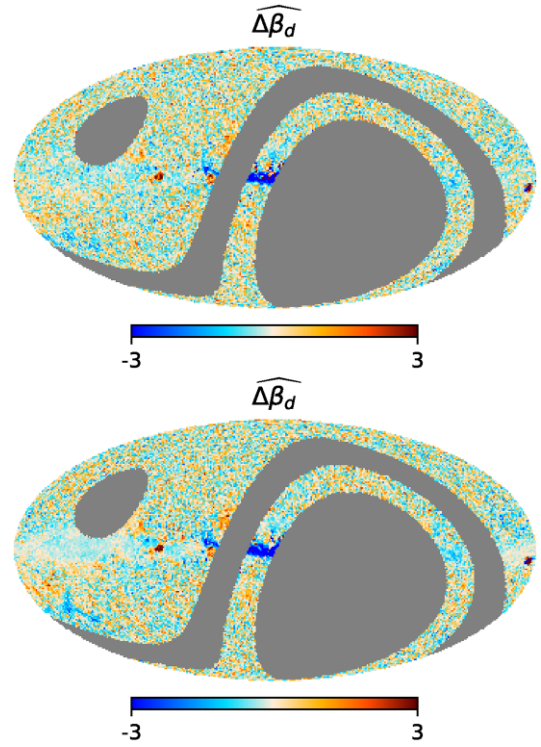


Figure 20. β_d relative difference map between the map obtained using the MFI+K/Ka+PR4 and the one obtained with K/Ka+PR4 data sets when we include T_d as a model parameter (top row) and when we fix it (bottom row).

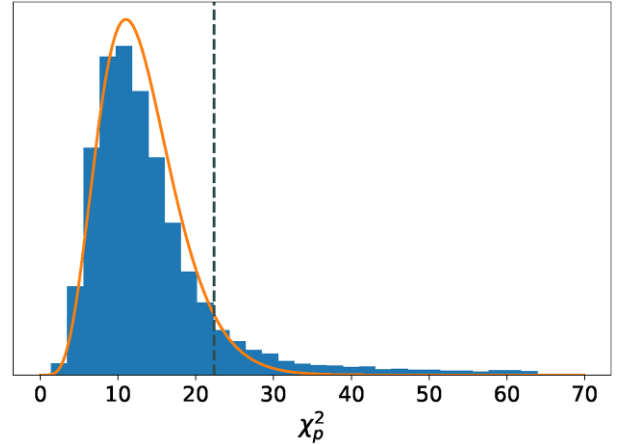


Figure 21. χ_p^2 distribution obtained using the default data set. The orange curve shows the theoretical χ^2 probability density function with $N_{\text{dof}} = 13$. The area to the left of the grey dashed line shows values within the 95 per cent confidence region.

5.5.1 χ^2 distribution and residuals

We have studied the pixel χ^2 distribution obtained from the fit using MFI+K/Ka+PR4 (see Fig. 21):

$$\chi_p^2 = N_{\text{dof}} \cdot \chi_{\text{red}}^2. \quad (13)$$

Moreover, we have also calculated the residuals per channel involved in the analysis:

$$r_{p,v} = \frac{(d_{p,v} - S_{pv})}{\sigma_{p,v}}. \quad (14)$$

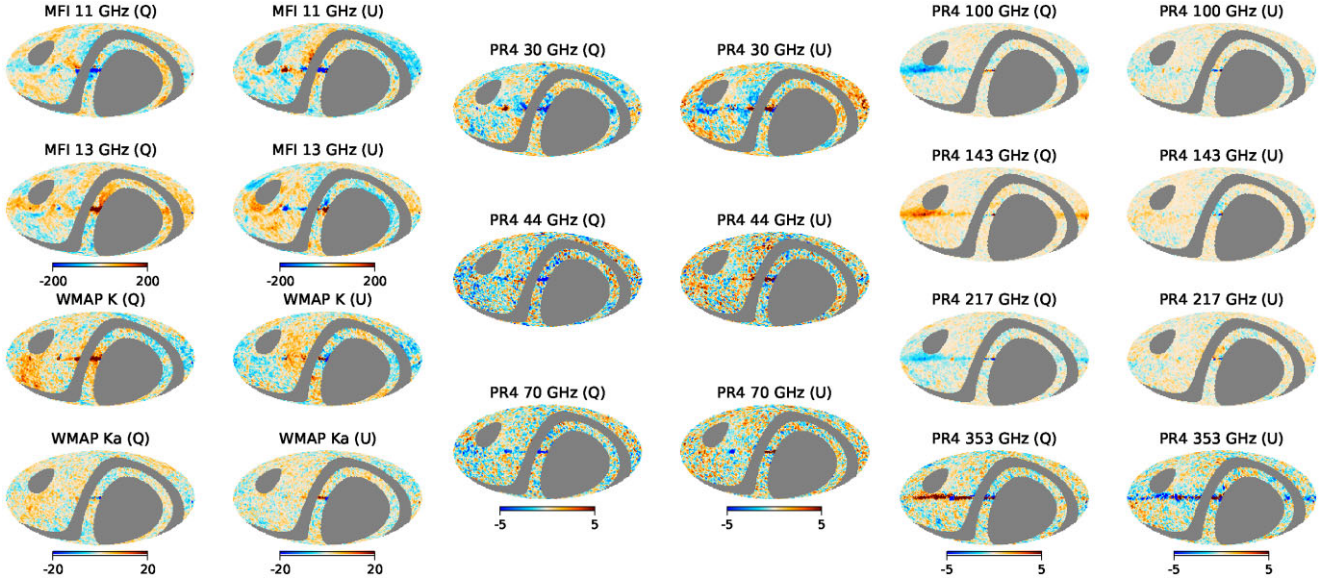


Figure 22. Q and U residual maps for each frequency channel at $N_{\text{side}} = 64$. Maps are displayed in thermodynamic temperature (μK).

In the perfect scenario, residuals maps are consistent with instrumental noise alone. Therefore, they are a valuable tool to look for either systematic effects or mismatches in the foreground modelling.

First of all, we recall that the number of dof for this analysis is 13 [11 channels \times 2 (Q and U) minus 9 free parameters]. We find $\langle\chi_p^2\rangle = 14.3$ and $\sigma = 8.9$ slightly larger than what is expected for the theoretical number of dof. Fig. 21 shows that the χ_p^2 values follow a χ^2 -like distribution, whose peak lies close to $N_{\text{dof}} = 13$. However, there is an excess of pixels at large values of χ^2 with respect to the $\chi_{N_{\text{dof}}}^2$ distribution. That excess appears since there are pixels where the model is not able to track the true sky emission, mainly in the Galactic plane. Thus, those pixels are highly inconsistent with this χ^2 distribution.

Fig. 22 shows the Q and U residuals maps of every frequency channel from the MFI+K/Ka+PR4 data set. We find that *Planck* and WMAP residuals maps are reasonably consistent with the expected noise except along the Galactic plane. The residuals in this region are a consequence of an incorrect modelling of the sky as we saw in the χ_{red}^2 maps. For the MFI channels we observe that the largest residuals are located in compact regions along the Galactic plane. We observe in the 11 GHz U channel a redder region in the NPS's closest part to the Galactic centre. This region overlaps with the area where we obtain a better goodness of fit if Faraday rotation effects are taken into account (see Fig. B2 in Appendix B). Furthermore, artefacts that resemble the FDEC morphology are present in MFI 13 GHz.

In light of these tests, we are confident of the results obtained in those pixels that are properly modelled by our assumed parametric model. The pixels outside the confidence region are located mainly in the Galactic plane, probably because our model fails to account for the complexity of this region. It would be convenient to study these regions in more detail with more complex models. However, the aim of this work is to study the diffuse components and the study of specific regions has been conducted in other works (Watson et al. in preparation; Ruiz-Granados et al. in preparation; Guidi et al. 2022).

5.5.2 Robustness with respect to the prior

As previously stated, the use of prior information is essential in Bayesian analysis, helping with convergence and computational time reduction. Besides, when the data do not have enough sensitivity, i.e. there is not enough information to obtain a reliable estimation of the spectral index, the prior tends to provide a value close to the mean value of the distribution. In other words, a conservative value is assigned to the spectral index in those pixels. Thus, in order to detect which pixels are prior dependent, we have also performed component separation using two additional Gaussian priors on β_s , $\mathcal{N}(-3.1, 0.6)$ and $\mathcal{N}(-3.0, 0.3)$. The β_s estimation and uncertainty maps with these new priors are shown in Fig. 23 together with those obtained with the prior used in the default analysis (left columns).

Comparing the results using the default prior, i.e. $\mathcal{N}(-3.1, 0.3)$, versus a less restrictive prior, i.e. $\mathcal{N}(-3.1, 0.6)$, we observe that the uncertainty on the recovered β_s increases at the prior-dominated pixels. On the other hand, in those regions where the synchrotron emission is very intense the uncertainty remains the same. Likewise, the estimated β_s in the latter pixels are very similar whereas the other pixels are visually different. The β_s distribution of the pixels outside the low-uncertainty regions are compatible with the prior distribution. This is the reason why the estimated values are different and the spread is larger when the prior is relaxed.

When we use a prior with a different expected value, i.e. $\mathcal{N}(-3.0, 0.3)$, but equal standard deviation we obtain a similar uncertainty map. The estimated β_s is almost the same in the low-uncertainty regions, i.e. the high-intensity synchrotron regions. However, a flatter spectrum (closer to -3.0 instead of -3.1) is recovered outside those areas. This is more evident from the bottom panel of Fig. 24 where the difference between the β_s map estimated with the default prior and the $\mathcal{N}(-3.0, 0.3)$ prior is shown. Outside the regions where the synchrotron emission is the largest, the difference is close to -0.1 which is the difference between the expected value of the priors. In other words, when there is not enough information from the data the recovered β_s is close to the expected value of the prior. This is an advantage of using prior information, since it assigns a

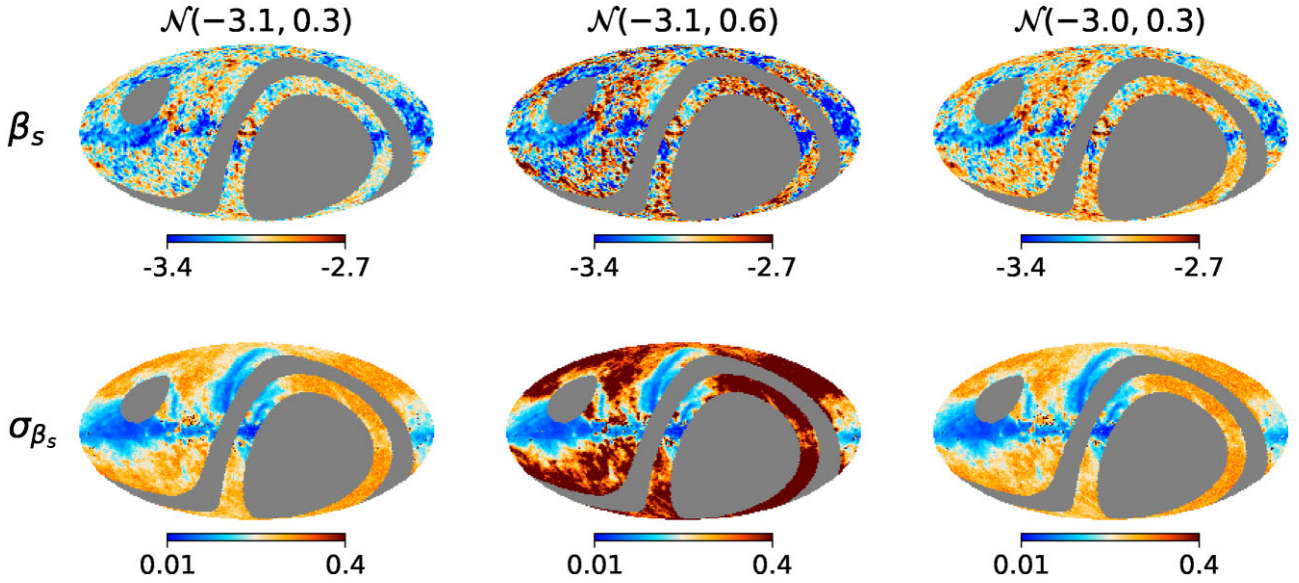


Figure 23. Synchrotron spectral index estimate (top row) and uncertainty (bottom row) obtained using different Gaussian prior distributions and the default data set (MFI+K/Ka+PR4). The synchrotron emission is modelled as a power law.

conservative value to the spectral index instead of unphysical values or simply failing to perform the fit.

6 CONCLUSIONS

In this work, we have presented the component separation products in polarization obtained from combining the QUIJOTE-MFI data at 11 and 13 GHz, with the WMAP *K* and *Ka* bands and all *Planck* polarized channels. We have seen that the inclusion of the QUIJOTE-MFI data is crucial to improve the parameter estimation of the low-frequency foregrounds, in particular for the estimation of the synchrotron spectral index.

We have obtained the first detailed β_s map of the Northern Celestial hemisphere at a scale of 2° , assuming the synchrotron emission is modelled as a power law. This model represents well the data except in the Galactic plane where the physics might be more complex. We find, using the pixels whose χ^2_{red} lies within the 95 percent confidence region, an average value of -3.08 and a dispersion of 0.13 . The latter is broader than the dispersion of commonly used β_s templates. Moreover, we have found that the spectral index is not compatible with a uniform value, i.e. there are statistical significant differences of β_s across the observable sky.

We have also modelled the synchrotron emission as a power law with curvature. The pixel-based analysis of the curvature shows that c_s is only detected in some regions in the Galactic plane where the fit is bad. When we assume a model with uniform curvature in RC1 (the region that includes all pixels whose χ^2_{red} is within the 95 percent confidence region for the power law with curvature model) we found a $c_s = -0.0797 \pm 0.0012$. We found that both models, i.e. power law and power law with uniform curvature, provide a good fit given the available data. However, there is not enough statistical significance to distinguish which model is better. A more thorough study is left for future work.

We found that our recovered synchrotron and thermal dust maps are highly correlated with the maps presented by the *Planck* collaboration using *Commander*, even though we found some large-scale difference between the synchrotron emission maps that arise from better estimation of the SED due to the addition of more frequency

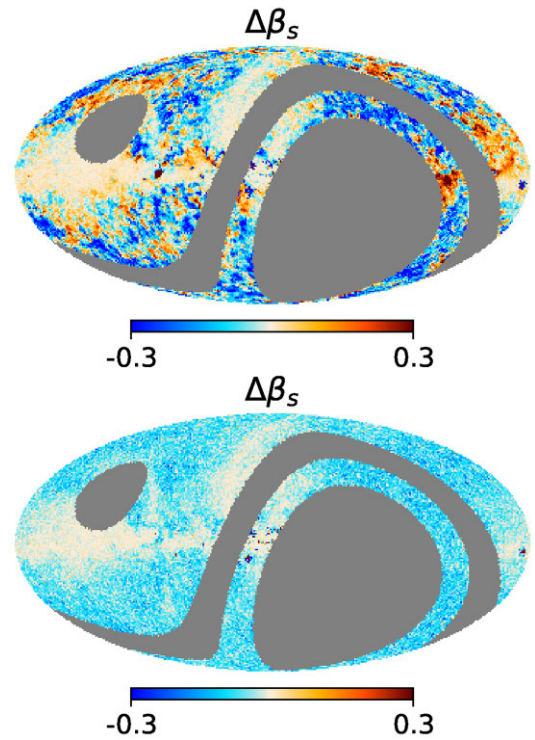


Figure 24. Difference map between the estimated β_s using the default prior, i.e. $\mathcal{N}(-3.1, 0.3)$, and the one obtained using an alternative prior, see Fig. 23. Top: $\mathcal{N}(-3.1, 0.6)$. Bottom: $\mathcal{N}(-3.0, 0.3)$.

channels. On the other hand, we recovered a CMB with less power when we use the filtered *K*, *Ka*, and PR4 with FDEC. Since our analysis focuses on the characterization of foregrounds, we keep the results obtained with the filtered maps. However, as commented in Section 5.3.1 an unbiased CMB map can be recovered following other approaches.

We have also performed different analyses to test the validity of our results. First, we found that our results are compatible with a χ^2 distribution in those pixels where the power-law model fits well the data. Furthermore, we have calculated the normalized residuals of the pixels with an acceptable goodness of fit of all frequency channels and they are all consistent within the 3σ level. Finally, we have evaluated the robustness of the estimated β_s varying the prior imposed in this parameter. We found that the estimations in the high signal-to-noise synchrotron areas are prior independent, while outside these regions the prior governs the β_s estimation.

ACKNOWLEDGEMENTS

We thank the staff of the Teide Observatory for invaluable assistance in the commissioning and operation of QUIJOTE. The QUIJOTE experiment is being developed by the Instituto de Astrofísica de Canarias (IAC), the Instituto de Física de Cantabria (IFCA), and the Universities of Cantabria, Manchester, and Cambridge. Partial financial support was provided by the Spanish Ministry of Science and Innovation under the projects AYA2007-68058-C03-01, AYA2007-68058-C03-02, AYA2010-21766-C03-01, AYA2010-21766-C03-02, AYA2014-60438-P, ESP2015-70646-C2-1-R, AYA2017-84185-P, ESP2017-83921-C2-1-R, AYA2017-90675-REDC (co-funded with EU FEDER funds), PGC2018-101814-B-I00, PID2019-110610RB-C21, PID2020-120514GB-I00, IACA13-3E-2336, IACA15-BE-3707, EQC2018-004918-P, the Severo Ochoa Programs SEV-2015-0548 and CEX2019-000920-S, the Maria de Maeztu Program MDM-2017-0765, and by the Consolider-Ingenio project CSD2010-00064 (EPI: Exploring the Physics of Inflation). We acknowledge support from the ACISI, Consejería de Economía, Conocimiento y Empleo del Gobierno de Canarias, and the European Regional Development Fund (ERDF) under grant with reference ProID2020010108. This project has received funding from the European Union's Horizon 2020 research and innovation programme under grant agreement number 687312 (RADIOFOREGROUNDS). EdIH acknowledges financial support from the *Concepción Arenal Programme* of the Universidad de Cantabria. DT acknowledges the support from the Chinese Academy of Sciences (CAS) President's International Fellowship Initiative (PIFI) with grant no. 2020PM0042. FP acknowledges support from the Spanish State Research Agency (AEI) under grant number PID2019-105552RB-C43. The authors acknowledge the computer resources, technical expertise, and assistance provided by the Spanish Supercomputing Network (RES) node at Universidad de Cantabria. Some of the presented results are based on observations obtained with *Planck* (<http://www.esa.int/Planck>), an ESA science mission with instruments and contributions directly funded by ESA Member States, NASA, and Canada. We acknowledge the use of the Legacy Archive for Microwave Background Data Analysis (LAMBDA) and the Planck Legacy Archive (PLA). Support for LAMBDA is provided by the NASA Office of Space Science. Some of the results in this paper have been derived using the HEALPIX package (Górski et al. 2005), and the HEALPY (Zonca et al. 2019), NUMPY (Harris et al. 2020), EMCEE (Foreman-Mackey et al. 2013), and MATPLOTLIB (Hunter 2007) PYTHON packages.

DATA AVAILABILITY

The parameter maps obtained from the component separation analysis in the default case, i.e. with the MFI+K/K α +PR4 data set using a power law to model the synchrotron emission, are included in

the released data products associated with the QUIJOTE-MFI wide survey.

These data products as well as the maps can be freely downloaded from the QUIJOTE web page,¹⁸ as well as from the RADIOFOREGROUNDS platform.¹⁹ They include also an Explanatory Supplement describing the data formats. Any other derived data products described in this paper are available upon request to the QUIJOTE collaboration.

REFERENCES

- Abazajian K. N. et al., 2016, preprint ([arXiv:1610.02743](https://arxiv.org/abs/1610.02743))
Ade P. et al., 2019, *J. Cosmology Astropart. Phys.*, 2019, 056
Ali-Haïmoud Y., 2013, *Adv. Astron.*, 2013, 462697
Ashdown M. et al., 2012, Astrophysics Source Code Library, record ascl:1208.005
Bennett C. L. et al., 2013, *ApJS*, 208, 20
BICEP/Keck Collaboration, 2021, *Phys. Rev. D*, 103, 022004
Carretti E. et al., 2019, *MNRAS*, 489, 2330
Carron J., Lewis A., Challinor A., 2017, *J. Cosmol. Astropart. Phys.*, 2017, 035
de la Hoz E., Vielva P., Barreiro R. B., Martínez-González E., 2020, *J. Cosmol. Astropart. Phys.*, 2020, 006
de la Hoz E., Diego-Palazuelos P., Martínez-González E., Vielva P., Barreiro R. B., Bilbao-Ahedo J. D., 2022, *J. Cosmol. Astropart. Phys.*, 2022, 032
Dickinson C. et al., 2018, *New Astron. Rev.*, 80, 1
Diego-Palazuelos P., Vielva P., Martínez-González E., Barreiro R. B., 2020, *J. Cosmol. Astropart. Phys.*, 2020, 058
Draine B. T., Lazarian A., 1999, *ApJ*, 512, 740
Eriksen H. K., Jewell J. B., Dickinson C., Banday A. J., Górski K. M., Lawrence C. R., 2008, *ApJ*, 676, 10
Errard J., Stompor R., 2019, *Phys. Rev. D*, 99, 043529
Fixsen D. J., 2009, *ApJ*, 707, 916
Foreman-Mackey D., Hogg D. W., Lang D., Goodman J., 2013, *PASP*, 125, 306
Fuskeland U., Wehus I. K., Eriksen H. K., Naess S. K., 2014, *ApJ*, 790, 104
Fuskeland U. et al., 2021, *A&A*, 646, A69
Génova-Santos R. et al., 2017, *MNRAS*, 464, 4107
Goodman J., Weare J., 2010, *Commun. Appl. Math. Comput. Sci.*, 5, 65
Górski K. M., Hivon E., Banday A. J., Wandelt B. D., Hansen F. K., Reinecke M., Bartelmann M., 2005, *ApJ*, 622, 759
Greaves J. S., Scaife A. M. M., Frayer D. T., Green D. A., Mason B. S., Smith A. M. S., 2018, *Nature Astron.*, 2, 662
Grumitt R. D. P., Jew L. R. P., Dickinson C., 2020, *MNRAS*, 496, 4383
Guidi F. et al., 2022, *MNRAS*, submitted
Hanany S. et al., 2019, *BAAS*, 51, 194
Harris C. R. et al., 2020, *Nature*, 585, 357
Herranz D. et al., 2022, *MNRAS*, in press
Hinshaw G. et al., 2003, *ApJS*, 148, 63
Hui H. et al., 2018, in Zmuidzinas J., Gao J.-R., eds, SPIE Conf. Ser. Vol. 10708, Millimeter, Submillimeter, and Far-Infrared Detectors and Instrumentation for Astronomy IX. SPIE, Bellingham, p. 1070807
Hunter J. D., 2007, *Comput. Sci. Eng.*, 9, 90
Hutschenreuter S. et al., 2022, *A&A*, 657, A43
Jones M. E. et al., 2018, *MNRAS*, 480, 3224
Krachmalnicoff N. et al., 2018, *A&A*, 618, A166
Lamagna L. et al., 2020, *J. Low Temp. Phys.*, 200, 374
Lee K. et al., 2020, *J. Low Temp. Phys.*, 200, 384
Lewis A., Challinor A., 2011, Astrophysics Source Code Library, record ascl:1102.026
LiteBIRD Collaboration, 2022, preprint ([arXiv:2202.02773](https://arxiv.org/abs/2202.02773))
Martire F. A., Barreiro R. B., Martínez-González E., 2022, *J. Cosmol. Astropart. Phys.*, 2022, 003

¹⁸<http://research.iac.es/proyecto/cmb/quijote>.

¹⁹<http://www.radioforegrounds.eu/>.

McBride L., Bull P., Hensley B. S., 2022, preprint ([arXiv:2207.14213](https://arxiv.org/abs/2207.14213))
Millea M., Anderes E., Wandelt B. D., 2019, *Phys. Rev. D*, 100, 023509
Miville-Deschênes M. A., Ysard N., Lavabre A., Ponthieu N., Macías-Pérez J. F., Aumont J., Bernard J. P., 2008, *A&A*, 490, 1093
Namikawa T. et al., 2022, *Phys. Rev. D*, 105, 023511
Planck Collaboration X, 2016a, *A&A*, 594, A10
Planck Collaboration XV, 2016b, *A&A*, 594, A15
Planck Collaboration I, 2020a, *A&A*, 641, A1
Planck Collaboration II, 2020b, *A&A*, 641, A2
Planck Collaboration III, 2020c, *A&A*, 641, A3
Planck Collaboration IV, 2020d, *A&A*, 641, A4
Planck Collaboration VI, 2020e, *A&A*, 641, A6
Planck Collaboration LVII, 2020f, *A&A*, 643, A42
Puglisi G., Mihaylov G., Panopoulou G. V., Poletti D., Errard J., Puglisi P. A., Vianello G., 2022, *MNRAS*, 511, 2052
Ritacco A., Boulanger F., Guillet V., Delouis J.-M., Puget J.-L., Aumont J., Vacher L., 2022, preprint ([arXiv:2206.07671](https://arxiv.org/abs/2206.07671))
Rubio-Martín J. A. et al., 2010, in *Highlights of Spanish Astrophysics V*. Springer, Berlin/Heidelberg, p. 127
Rubio-Martín J. A. et al., 2022, *MNRAS*, submitted
Rybicki G. B., Lightman A. P., 1985, *Radiative Processes in Astrophysics*. John Wiley & Sons, New York, NY
Sunyaev R. A., Zeldovich Y. B., 1972, *Comm. Astrophys. Space Phys.*, 4, 173
Thorne B., Dunkley J., Alonso D., Naess S., 2017, *MNRAS*, 469, 2821
Tristram M. et al., 2022, *Phys. Rev. D*, 105, 083524
Vidal M., Dickinson C., Davies R. D., Leahy J. P., 2015, *MNRAS*, 452, 656
Weiland J. L., Addison G. E., Bennett C. L., Halpern M., Hinshaw G., 2022, *ApJ*, 936, 24
Wolleben M., Landecker T. L., Reich W., Wielebinski R., 2006, *A&A*, 448, 411

Zonca A., Singer L., Lenz D., Reinecke M., Rosset C., Hivon E., Gorski K., 2019, *J. Open Source Softw.*, 4, 1298

APPENDIX A: INDEPENDENT Q AND U SYNCHROTRON SPECTRAL INDEX

In order to test the assumption of having the same β_s in both Q and U , we fit Q and U signals independently. Fig. A1 shows the spectral index, the uncertainty of the spectral index as well as the reduced χ^2 maps obtained from the three independent fits using the MFI+K/Ka+PR4 data set. We infer from the χ^2_{red} maps that the fit outside the Galactic plane is better when Q and U are fitted together. When we fit just U we observe that the goodness of fit improves significantly in the Galactic plane. However, this effect is due to the low signal-to-noise ratio in that area, not due to a better modelling of the signal.

The β_s^Q and β_s^U maps are distinctly different. The β_s^{QU} map resembles more the β_s^Q map. This is expected, since Q has more signal than U in Galactic coordinates. That is also the reason why the uncertainty on the recovered β_s is smaller when we fit just Q compared to U . However, in those regions where $\sigma_{\beta_s^U}$ is smaller than $\sigma_{\beta_s^Q}$, i.e. regions where U has more signal than Q , the β_s^{QU} values obtained are closer to those of β_s^U . This is clearly seen in Fig. A2 where the relative difference between β_s^{QU} with respect to β_s^Q (top row) and β_s^U (bottom row) is shown. The largest differences shown in the top (bottom) panel are located in regions where the signal-to-noise ratio is larger in U (Q). On the other hand, the relative difference decreases significantly in the regions where the uncertainty on β_s^Q (top) or β_s^U (bottom) is smaller.

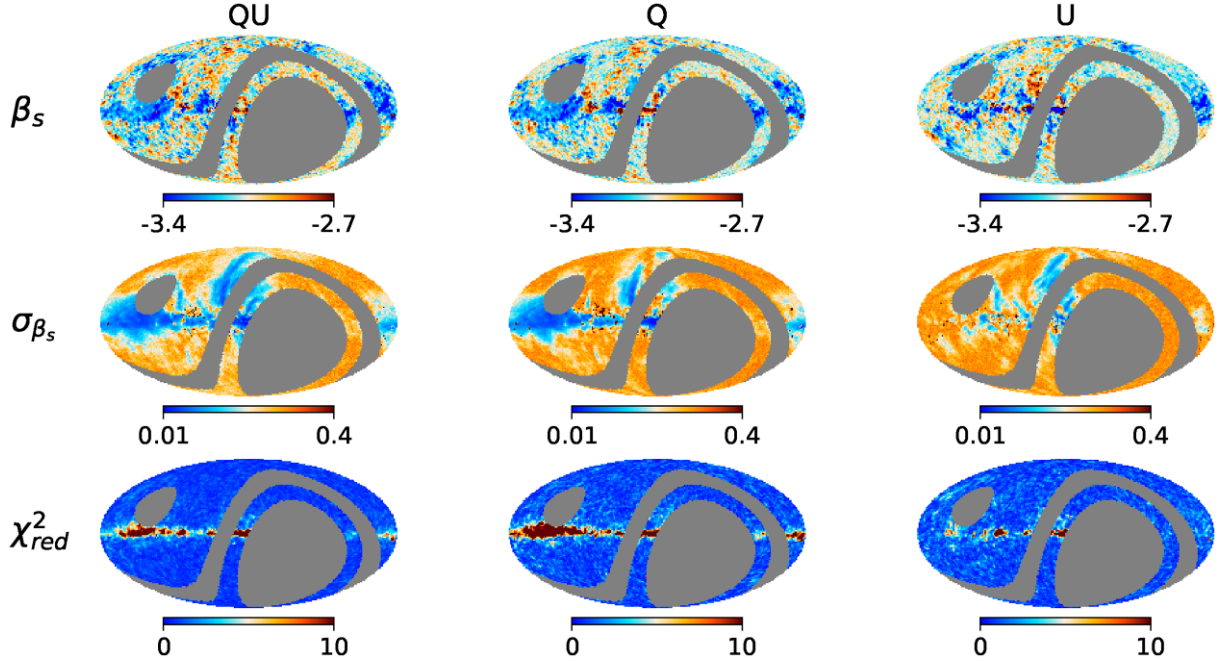


Figure A1. Synchrotron spectral index estimate (top row) and uncertainty maps (second row) obtained after component separation using the MFI+K/Ka+PR4 data set. The left column shows the β_s recovered when we assume that Q and U share the same spectral index, while the centre and right columns depict the Q and U β_s when they are assumed to be independent. Bottom row: Reduced χ^2 map for each case study considered. The synchrotron emission is modelled as a power law.

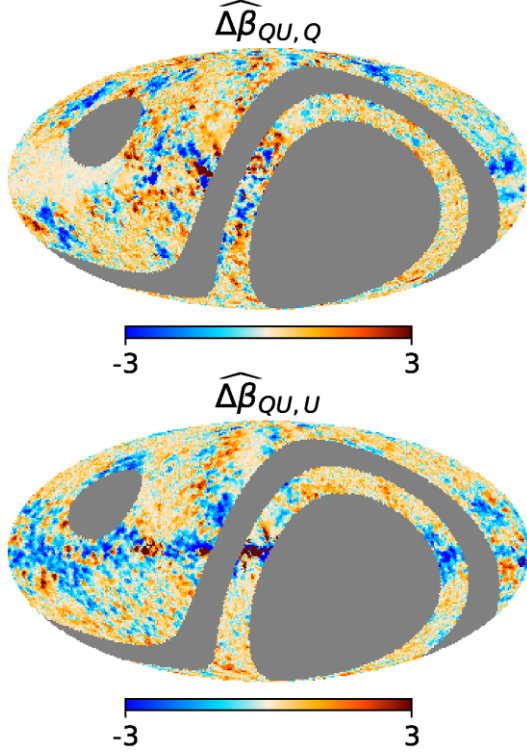


Figure A2. Relative difference map between the β_s map obtained when we assume the same β_s in both Q and U , and β_s recovered from the fit with just Q (top) and just U (bottom). The synchrotron emission is modelled as a power law.

APPENDIX B: FARADAY ROTATION

We have also studied the significance of the difference between the β_s^Q and β_s^U maps, see the top row of Fig. B1. The discrepancies larger than 3σ are concentrated in the Galactic plane, close to the Galactic centre. This could be a tracer of Faraday rotation. If Faraday rotation is non-negligible at QUIJOTE frequencies, there will be a difference between the polarization angles at QUIJOTE frequencies and those at WMAP/Planck frequencies. This yields a β_s^Q map different from β_s^U due to the bias introduced by the change in angle. That bias is reasonably cancelled out when combining both Q and U to obtain a single index.

We have studied the possibility of correcting the Faraday rotation effect in the QUIJOTE MFI maps using the model from Hutschenreuter et al. (2022). The rotation of the polarization plane experienced due to the Faraday Rotation effect can be described by

$$\Delta\phi = \text{RM}\lambda^2, \quad (\text{B1})$$

where λ is the wavelength and RM is the rotation measure. We use the RM map estimated by Hutschenreuter et al. (2022) to calculate the rotation angle maps at 11 and 13 GHz QUIJOTE frequencies. Then, QUIJOTE Q and U maps at a given frequency ν are de-rotated as follows:

$$\begin{pmatrix} Q_{\text{FR}} \\ U_{\text{FR}} \end{pmatrix}_\nu = \begin{pmatrix} \cos(2\Delta\phi_\nu) & -\sin(2\Delta\phi_\nu) \\ \sin(2\Delta\phi_\nu) & \cos(2\Delta\phi_\nu) \end{pmatrix}_\nu \begin{pmatrix} Q \\ U \end{pmatrix}_\nu, \quad (\text{B2})$$

The variance of the de-rotated Q_{FR} and U_{FR} is

$$\begin{aligned} \sigma_{Q_{\text{FR}}}^2 &= \cos^2(2\Delta\phi_\nu)\sigma_Q^2 + \sin^2(2\Delta\phi_\nu)\sigma_U^2 \\ &+ 4[\sin(2\Delta\phi_\nu)Q + \cos(2\Delta\phi_\nu)U]^2 \sigma_{\Delta\phi}^2, \end{aligned} \quad (\text{B3})$$

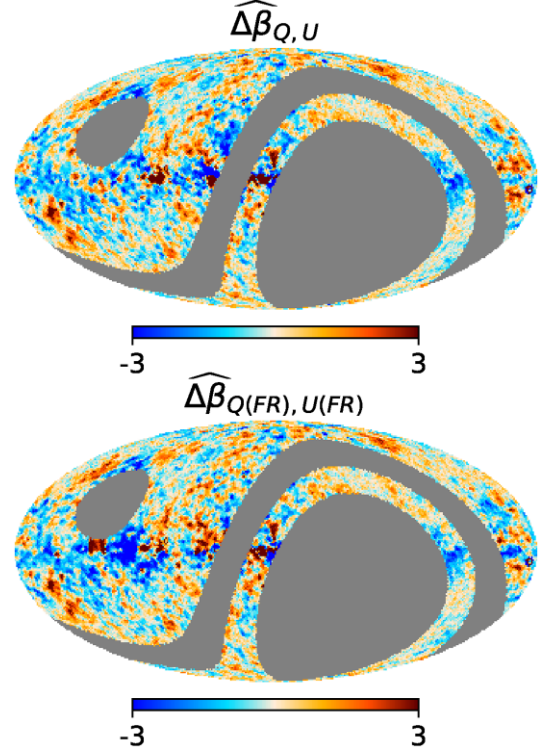


Figure B1. Relative difference map between the β_s map from the independent Q and U fit using the MFI+K/Ka+PR4 data set (top), and using the MFI(FR)+K/Ka+PR4 data set (bottom). The synchrotron emission is modelled as a power law.

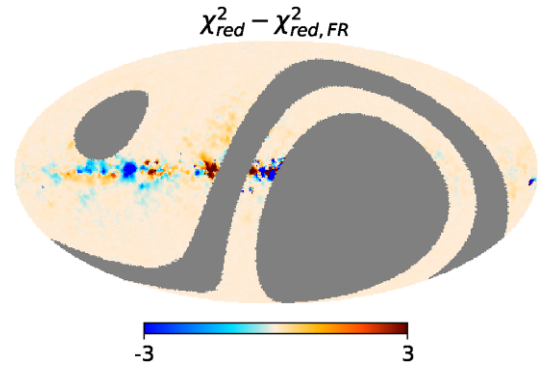


Figure B2. Difference map between the χ^2_{red} obtained with the MFI+K/Ka+PR4 data set with respect to the $\chi^2_{\text{red,FR}}$ obtained with MFI(FR)+K/Ka+PR4 data set. In both fits, we have assumed that Q and U share the same spectral indices. The synchrotron emission is modelled as a power law.

$$\begin{aligned} \sigma_{U_{\text{FR}}}^2 &= \sin^2(2\Delta\phi_\nu)\sigma_Q^2 + \cos^2(2\Delta\phi_\nu)\sigma_U^2 \\ &+ 4[\cos(2\Delta\phi_\nu)Q - \sin(2\Delta\phi_\nu)U]^2 \sigma_{\Delta\phi}^2. \end{aligned} \quad (\text{B4})$$

Therefore, we have repeated the same analysis but using the MFI(FR)+K/Ka+PR4 data set, where MFI(FR) indicates that the QUIJOTE 11 and 13 GHz maps have been de-rotated using the angle obtained from the Hutschenreuter et al. (2022) model, to correct any possible mismatch due to the Faraday Rotation effect (see the bottom row of Fig. B1).

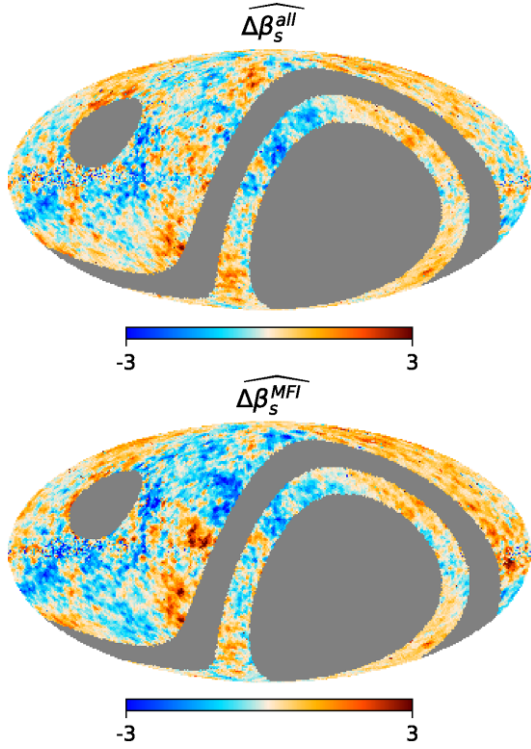


Figure C1. Relative difference map between the β_s template used in the simulation and the β_s map from the fit using the simulated data with an FDEC filter applied to all maps (top), and an FDEC filter applied only to QUIJOTE-MFI frequencies (bottom).

We compare these maps (Fig. B1) with the different map between the reduced χ^2 map (χ_{red}^2) obtained with the MFI+K/Ka+PR4 data set with respect to the reduced χ^2 ($\chi_{\text{red,FR}}^2$) obtained with MFI(FR)+K/Ka+PR4 data set shown in Fig. B2. The sky regions where the absolute value of the relative difference $\Delta\beta_{Q(\text{FR}),U(\text{FR})}$ is smaller than $\Delta\beta_{Q,U}$ are correlated to those regions where the $\chi_{\text{red,FR}}^2$ is smaller than χ_{red}^2 (reddish regions) and vice versa (bluish regions). This result suggests that Faraday rotation might be playing a role in some of the significant differences areas observed between β_s^Q and β_s^U .

APPENDIX C: FUNCTION-OF-DECLINATION CORRECTION SIMULATIONS

We studied using simulations if the application of a function-of-declination (FDEC) filter to QUIJOTE-MFI maps biases the β_s map obtained from component separation. We generated sky simulation maps with the following components at the QUIJOTE-MFI 11 and 13 GHz, K and Ka, and PR4 frequencies:

(i) CMB: Generated as Gaussian random samples using the power spectra obtained from CAMB (Lewis & Challinor 2011) with the latest *Planck* cosmological parameters (Planck Collaboration 2020e).

(ii) Synchrotron: Generated using the s1 model of the Python Sky Model (PYSM; Thorne et al. 2017).

(iii) Thermal dust: Generated using the d1 model of the PySM.

(iv) Realistic noise simulations: For each experiment, we use the ones described in Section 4.

All components are either generated or downgraded to $N_{\text{side}} = 512$. Then the components maps are added and we apply the corresponding FDEC filter to each signal map. Finally, all maps are downgraded to $N_{\text{side}} = 64$ and smoothed with a Gaussian beam of FWHM = 2 deg following the procedure described in Section 4.

We perform the component separation analysis in two scenarios: (i) when only the QUIJOTE-MFI frequency signal maps are filtered, and (ii) when all maps are filtered. Fig. C1 shows the relative difference (equation 12) between the β_s map recovered from the component separation analysis and the β_s template (equation 12 taking into account that the uncertainty of the template map is set to zero, $\sigma_{\beta_s} = 0$). We find that when only QUIJOTE-MFI channels are filtered (bottom panel) the relative differences are larger in regions such as the North Polar Spur or the R3 region than when all maps are filtered. Moreover, in those regions the β_s relative differences are larger than 3σ with respect to the template. In the case when all maps are filtered (top panel), these biases are reduced significantly.

¹Instituto de Física de Cantabria (IFCA), CSIC-Univ. de Cantabria, Avda. los Castros s/n, E-39005 Santander, Spain

²Dpto. de Física Moderna, Universidad de Cantabria, Avda. de los Castros s/n, E-39005 Santander, Spain

³Instituto de Astrofísica de Canarias, E-38205 La Laguna, Tenerife, Spain

⁴Departamento de Astrofísica, Universidad de La Laguna, E-38206 La Laguna, Tenerife, Spain

⁵Institut d'Astrophysique de Paris, UMR 7095, CNRS & Sorbonne Université, 98 bis boulevard Arago, F-75014 Paris, France

⁶Astrophysics Group, Cavendish Laboratory, University of Cambridge, JJ Thomson Avenue, Cambridge CB3 0HE, UK

⁷Kavli Institute for Cosmology, University of Cambridge, Madingley Road, Cambridge CB3 0HA, UK

⁸Dpto. de Ingeniería de Comunicaciones (DICOM), Edif. Ingeniería de Telecomunicación, Pl. de la Ciencia s/n, E-39005 Santander, Spain

⁹Dpto. de Matemáticas, estadística y computación, Univ. de Cantabria, Avda. de los Castros s/n, E-39005 Santander, Spain

¹⁰Aurora Technology for the European Space Agency (ESA), European Space Astronomy Centre (ESAC), Camino Bajo del Castillo s/n, E-28692 Villanueva de la Cañada, Madrid, Spain

¹¹Universidad Europea de Madrid, E-28670, Madrid, Spain

¹²Jodrell Bank Centre for Astrophysics, Alan Turing Building, Department of Physics and Astronomy, School of Natural Sciences, University of Manchester, Oxford Road, Manchester M13 9PL, UK

¹³Consejo Superior de Investigaciones Científicas, E-28006 Madrid, Spain

¹⁴Dpto. de Física, Facultad de Ciencias, Univ. de Córdoba, Campus de Rabanales, Edif. C2. Planta Baja, E-14071 Córdoba, Spain

¹⁵Purple Mountain Observatory, CAS, No.10 Yuanhua Road, Qixia District, Nanjing 210034, China

¹⁶NAOC-UKZN Computational Astrophysics Center (NUCAC), University of Kwazulu-Natal, Durban 4000, South Africa

This paper has been typeset from a \LaTeX file prepared by the author.

"Every new beginning comes from some other beginning's end"

Seneca

The CMB is a fundamental tool for unraveling the secrets of our Universe. Now that temperature anisotropies have been measured to the cosmic variance limit, the focus is on polarization anisotropies. This polarized signal contains unique information on the origins of the Universe. In particular, since its primordial B-modes can only be generated from tensor perturbations, their detection would constitute compelling evidence of an inflationary phase. Moreover, these polarization anisotropies can help to break the degeneracy between model parameters, test the *fluke hypothesis* on the origin of anomalies, etc.

This primordial signal is faint ($r < 0.032$ at 95% CL, (Tristram et al., 2022)) compared to other B-mode sources. Planned and future CMB experiments aim to achieve sensitivities on the order of $\sigma \lesssim 10^{-3}$, which require excellent removal of these contaminant sources, or they might prevent the detection of PGWs.

In this thesis, I present a new component separation method called B-SeCRET. B-SeCRET is a versatile method that has been applied in several contexts within different collaborations and initiatives. I proved that it is capable of obtaining compelling results when applied to both:

- ⇒ simulations in the framework of forecast studies for the future CMB satellite mission LiteBIRD, as well as initiatives of ground-based experiments such as ELFS, and
- ⇒ to data from QUIJOTE-MFI instrument, WMAP, and *Planck* to significantly improve the characterization of low-frequency foregrounds.

The papers that compose this compilation thesis present three applications of CS. Here, I review the main results of the papers included.

P.I: We showed the viability of the detection of PGWs with a ground-based telescope operating in the microwave low-frequency regime (from 10 to 120 GHz) in a handful of

different scenarios. We found this experiment can detect tensor-to-scalar ratios similar to those predicted by Starobinsky-like models (Starobinsky, 1980) in non-optimal cases. For example, when not including delensing, or not taking into account a polarized AME contribution. Furthermore, we proved that this experiment is a powerful complement to other on-ground or satellite missions, such as LiteBIRD, since it can help significantly with low-frequency foreground characterization.

- P. II: We presented an iterative analytic method to calculate the polarization angles from the multi-frequency signal. This method grounds on nulling the C_ℓ^{EB} power spectrum. To obtain analytic solutions, we apply the small angle approximation ($\lesssim 6$ deg) and find the maximum likelihood solution iteratively so that the covariance matrix does not depend on the angles. This methodology is computationally very fast and can determine the rotation angle for each frequency with sufficiently good accuracy. We also developed a method to extract the rotation angles from CS. We include the rotation angles as model parameters and use the estimation from the previous methodology as prior information. We showed that both approaches reduce this systematic error in r by a factor of 10^{-2} .
- P. III: We presented the in-flight polarization angle calibration for LiteBIRD and assessed its impact on r after correcting this systematic using simulated data. The calibration analysis was blindly conducted by two independent groups. The final calibrations angles were recovered with uncertainties on the order of a few arc minutes. We employed two CS algorithms (B-SeCRET and NILC) on the corrected and uncorrected multi-frequency maps. We discovered that angle miscalibration has only a minor effect on blind methods, but strongly biased the parametric method results. After correcting the miscalibration angles, both component separation algorithms produce an unbiased estimation of the r parameter.
- P. IV: We obtained linearly polarized astrophysical component maps of the Northern Sky using the QUIJOTE-MFI data at 11 and 13 GHz, WMAP's K and Ka bands (23 and 33 GHz), and all *Planck* polarized channels (30–353 GHz). We presented the first detailed β_s map of the Northern Celestial Hemisphere at a smoothing scale of 2° . The map has an average value of -3.08 ± 0.13 and shows significant spatial variability across the sky. Moreover, the β_s map presents higher spatial variations than commonly used templates in simulation code, (Thorne et al., 2017). Furthermore, we detected a uniform curvature in several sky regions.

Beyond this thesis

This methodology has been applied to other studies that are not yet published. Here, I outline these ongoing works.

- ⇒ Currently, I am forecasting the performance of the incorporation of a C-BASS-like 6-12 GHz receiver or the QUIJOTE-MFI2 instrument in a well-established experiment in the Southern Hemisphere, the Simons Array, and its successor, the Simons Observatory. This combination will improve the detection of PGWs and the characterization of low-frequency foregrounds in the Southern Hemisphere. On the other hand, I am also studying the possibility of incorporating measurements in the W band (75-110 GHz) in the QUIJOTE experiment and its complementarity with the LSPE-Strip experiment (Addamo et al., 2021).
- ⇒ The methodologies described in P. II have been generalized to obtain the polarization angles calibration and an isotropic *birefringence* angle simultaneously. I am applying the latter methodology to LiteBIRD simulations to determine the significance of a potential β detection. This work is part of a collaborative effort within a LiteBIRD working group.
- ⇒ I am conducting an analogous analysis to the one presented in P. IV but with intensity data. Although the MFI's temperature sensitivity is lower than that of the polarization, the MFI's frequencies can help break the degeneracies between low-frequency foregrounds, i.e., synchrotron, free-free, and AME emissions.

To sum up, the polarized CMB signal provides a unique signature of the inflationary epoch, and effective cleaning algorithms are mandatory for the unbiased detection of PGWs with future and planned CMB experiments.

"Un buen final solo es el principio de algo nuevo."

Chemi

El CMB es una herramienta fundamental para desentrañar los secretos de nuestro Universo. Ahora que las anisotropías de temperatura se han medido hasta el límite de la varianza cósmica, el foco está puesto en las anisotropías de polarización. Esta señal polarizada contiene información única de los orígenes del Universo. En particular, como sus modos B primordiales sólo pueden proceder de perturbaciones tensoriales, su detección constituiría una prueba irrefutable de la existencia de una fase inflacionaria. Además, estas anisotropías de polarización pueden ayudar a romper la degeneración entre parámetros del modelo, testar la *fluke hypothesis* sobre el origen de las anomalías detectadas con datos de temperatura, etc.

Esta señal primordial es muy débil ($r < 0,032$ a 95% CL, (Tristram et al., 2022)) en comparación con otras fuentes de modos B. Los experimentos de CMB previstos y futuros pretenden alcanzar sensibilidades del orden de $\sigma \lesssim 10^{-3}$, luego requieren una eliminación eficiente de estos contaminantes, ya que podrían impedir la detección de las PGWs.

En esta tesis, presento un nuevo método de separación de componentes llamado B-SeCRET. B-SeCRET es un método versátil que se ha aplicado en varios contextos dentro de diferentes colaboraciones e iniciativas y he demostrado que es capaz de obtener resultados convincentes cuando se aplica tanto

- ⇒ a simulaciones en el contexto de estudios predictivos para la futura misión del satélite LiteBIRD e iniciativas de experimentos en tierra como ELFS,
- ⇒ como a los datos del instrumento QUIJOTE-MFI, WMAP y *Planck* para mejorar significativamente la caracterización de los *foregrounds* de baja frecuencia.

Los trabajos que componen esta tesis por compendio de artículos presentan tres aplicaciones de separación componentes. A continuación, repaso los principales resultados de

los trabajos incluidos.

- P.I: Se demostró la viabilidad de la detección de PGWs con un telescopio terrestre que opere en el régimen de microondas de baja frecuencia (de 10 a 120 GHz) en distintos escenarios. Se encontró que este experimento puede detectar el parámetro r para modelos de inflación similares al propuesto por Starobinsky (Starobinsky, 1980) en casos no óptimos. Por ejemplo, cuando no se aplica *delensing*, o no se tiene en cuenta una contribución de AME polarizada. Además, se probó que este experimento es un gran complemento para otros experimentos, como LiteBIRD, ya que puede ayudar significativamente en la caracterización de los *foregrounds* de baja frecuencia.
- P.II: Se presentó un método analítico iterativo para calibrar los ángulos de polarización a partir de la señal multifrecuencia. Este método se basa en la anulación del espectro de potencia de C_ℓ^{EB} . Para obtener una solución analítica, se aplicó la aproximación de ángulos pequeños ($\lesssim 6$ deg) y se obtuvo la solución de máxima verosimilitud de forma iterativa, haciendo que en cada iteración la matriz de covarianza no dependa de los ángulos. Esta metodología es muy rápida desde el punto de vista computacional y puede determinar el ángulo de polarización para cada frecuencia con una precisión suficientemente buena. También se desarrolló un método para calibrar los ángulos de polarización a partir de métodos de separación de componentes. Para ello, se incluyeron los ángulos de polarización instrumentales como parámetros del modelo y se utilizó la estimación de la metodología anterior como información previa. Se demostró que ambos enfoques reducen este error sistemático en r en un factor de 10^{-2} .
- P.III: Se presentó la calibración del ángulo de polarización en órbita para LiteBIRD y se evaluó su impacto en r después de corregir esta sistemática. El análisis de la calibración fue realizado a ciegas por dos grupos independientes. Los ángulos de calibración finales que se recuperaron tenían incertidumbres del orden de unos pocos minutos de arco. Se aplicaron dos algoritmos de separación de componentes (B-SeCRET y NILC) a los mapas de multifrecuencia corregidos y no corregidos. Se probó que este sistemático tiene un efecto pequeño cuando se usan métodos ciegos como NILC, pero sesga significativamente los resultados de los métodos paramétricos. Después de corregir los mapas con las estimaciones de los ángulos de rotación, ambos algoritmos de separación de componentes recuperan una estimación insesgada de r .
- P.IV: Se obtuvieron mapas de las distintas componentes astrofísicas en polarización para el cielo del hemisferio norte utilizando los datos de QUIJOTE-MFI a 11 y 13 GHz, las bandas K y Ka de WMAP (23 y 33 GHz), y todos los canales polarizados de *Planck* (30-353 GHz). Se presentó el primer mapa detallado de β_s del hemisferio norte a una escala suavizada de 2° . El mapa obtenido tiene un valor medio de -3.08 ± 0.13 y muestra una importante variabilidad espacial a lo largo de todo el cielo. Además, el mapa

β_s presenta variaciones espaciales más grandes que los mapas de β_s que se utilizan habitualmente en los códigos de simulación de *foregrounds*, (Thorne et al., 2017). Por último, también se detectó un valor no nulo de curvatura uniforme en varias regiones del cielo.

Más allá de esta tesis

Esta metodología se ha aplicado a otros estudios que aún no se han publicado. Aquí se resumen estos trabajos que están en curso.

- ⇒ Actualmente, estoy evaluando la mejora del rendimiento al incorporar un receptor como el del experimento C-BASS (6-12 GHz), o del instrumento QUIJOTE-MFI2 (10-20 GHz), en el Simons Array, y el Simons Observatory. Esta combinación mejorará la detección de PGWs y la caracterización de los *foregrounds* de baja frecuencia en el hemisferio sur. Por otro lado, también estoy estudiando la posibilidad de incorporar medidas en la banda W (75-110 GHz) para el experimento QUIJOTE y su complementariedad con el experimento LSPE-Strip (Addamo et al., 2021).
- ⇒ Se han generalizado las metodologías descritas en el P. II para obtener los ángulos de polarización y un ángulo de *birefringencia* isótropo a la vez. En este momento, estoy aplicando esta última metodología a simulaciones de LiteBIRD para determinar la significancia de una potencial detección de β . Este trabajo forma parte de un esfuerzo de colaboración dentro de un grupo de trabajo de LiteBIRD.
- ⇒ Por otro lado, estoy llevando a cabo un análisis análogo al presentado en P. IV pero con datos de intensidad. La sensibilidad de los datos de temperatura del MFI es menor que la de la polarización, pero las frecuencias del MFI pueden ayudar a romper las degeneraciones entre los *foregrounds* de baja frecuencia, es decir, las emisiones de sincrotrón, radiación de frenado (*bremsstrahlung*) y el AME.

Como conclusión final, se ha visto que la señal polarizada del CMB proporciona una forma única de testar el Universo primigenio. Para poder detectar esta señal con los futuros experimentos del fondo cósmico de microondas, serán imprescindibles algoritmos de separación de componentes eficientes.

Bibliography

- Abazajian K., et al., 2019, arXiv e-prints, p. arXiv:1907.04473
- Abbott B. P., et al., 2021, *ApJ*, 909, 218
- Addamo G., et al., 2021, *J. Cosmology Astropart. Phys.*, 2021, 008
- Ade P., et al., 2019, *J. Cosmology Astropart. Phys.*, 2019, 056
- Ade P. A. R., et al., 2022, *ApJ*, 927, 77
- Ahmad Q. R., et al., 2002, *Phys. Rev. Lett.*, 89, 011301
- Albrecht A., Steinhardt P. J., 1982, *Phys. Rev. Lett.*, 48, 1220
- Ali-Haïmoud Y., 2013, *Advances in Astronomy*, 2013, 462697
- Allison R., Dunkley J., 2014, *MNRAS*, 437, 3918
- Aloni D., Berlin A., Joseph M., Schmaltz M., Weiner N., 2022, *Phys. Rev. D*, 105, 123516
- Alonso D., Dunkley J., Thorne B., Næss S., 2017, *Phys. Rev. D*, 95, 043504
- Alpher R. A., Herman R., 1948, *Nature*, 162, 774
- Alpher R. A., Bethe H., Gamow G., 1948, *Physical Review*, 73, 803
- Arbey A., Mahmoudi F., 2021, *Progress in Particle and Nuclear Physics*, 119, 103865
- Aumont J., Macías-Pérez J. F., 2007, *MNRAS*, 376, 739
- Aumont J., Macías-Pérez J. F., Ritacco A., Ponthieu N., Mangilli A., 2020, *A&A*, 634, A100
- Aver E., Olive K. A., Skillman E. D., 2015, *J. Cosmology Astropart. Phys.*, 2015, 011
- Azzoni S., Alonso D., Abitbol M. H., Errard J., Krachmalnicoff N., 2022, arXiv e-prints, p. arXiv:2210.14838

- BICEP2 Collaboration et al., 2014, *Phys. Rev. Lett.*, 112, 241101
- BICEP2 and Keck Array Collaborations et al., 2015, *ApJ*, 811, 126
- BICEP2/Keck Collaboration et al., 2015, *Phys. Rev. Lett.*, 114, 101301
- BICEP/Keck Collaboration et al., 2021, *Phys. Rev. D*, 103, 022004
- Baccigalupi C., et al., 2000, *MNRAS*, 318, 769
- Barreiro R. B., Hobson M. P., Banday A. J., Lasenby A. N., Stolyarov V., Vielva P., Górski K. M., 2004, *MNRAS*, 351, 515
- Baumann D., 2009, arXiv e-prints, p. arXiv:0907.5424
- Baumann D., 2022, *Cosmology*. Cambridge University Press
- Bedini L., Herranz D., Salerno E., Baccigalupi C., Kuruoglu E. E., Tonazzini A., 2005, *EURASIP Journal on Applied Signal Processing*, 2005, 2400
- Bennett C. L., et al., 2003, *ApJS*, 148, 1
- Bernardeau F., Colombi S., Gaztañaga E., Scoccimarro R., 2002, *Phys. Rep.*, 367, 1
- Bertulani C. A., 2019, in *Journal of Physics Conference Series*. p. 012002, doi:10.1088/1742-6596/1291/1/012002
- Bertulani C. A., Hall F. W., Santoyo B. I., 2022, arXiv e-prints, p. arXiv:2210.04071
- Blas D., Lesgourgues J., Tram T., 2011, *J. Cosmology Astropart. Phys.*, 2011, 034
- Bobin J., Starck J.-L., Fadili J., Moudden Y., 2007, *IEEE Transactions on Image Processing*, 16, 2662
- Bobin J., Moudden Y., Starck J. L., Fadili J., Aghanim N., 2008, *Statistical Methodology*, 5, 307
- Bobin J., Starck J. L., Sureau F., Basak S., 2013, *A&A*, 550, A73
- Bonaldi A., Bedini L., Salerno E., Baccigalupi C., de Zotti G., 2006, *MNRAS*, 373, 271
- Bottino M., Banday A. J., Maino D., 2010, *MNRAS*, 402, 207
- Bouchet F. R., Gispert R., 1999, *New A*, 4, 443
- Burles S., Tytler D., 1998, *ApJ*, 499, 699
- Campeti P., Komatsu E., Poletti D., Baccigalupi C., 2021, *J. Cosmology Astropart. Phys.*, 2021, 012

-
- Cardoso J.-F., Le Jeune M., Delabrouille J., Betoule M., Patanchon G., 2008, *IEEE Journal of Selected Topics in Signal Processing*, 2, 735
- Carretti E., et al., 2019, *MNRAS*, 489, 2330
- Carron J., Lewis A., Challinor A., 2017, *J. Cosmology Astropart. Phys.*, 2017, 035
- Casas F. J., Martínez-González E., Bermejo-Ballesteros J., García S., Cubas J., Vielva P., Barreiro R. B., Sanz A., 2021, *Sensors*, 21, 3361
- Casas J. M., et al., 2022, *A&A*, 666, A89
- Catalano A., et al., 2014, *A&A*, 569, A88
- Chevalier R. A., 1998, *ApJ*, 499, 810
- Chevallier M., Polarski D., 2001, *International Journal of Modern Physics D*, 10, 213
- Chiang H. C., et al., 2010, *ApJ*, 711, 1123
- Chluba J., Hill J. C., Abitbol M. H., 2017, *MNRAS*, 472, 1195
- Clark S. E., Kim C.-G., Hill J. C., Hensley B. S., 2021, *ApJ*, 919, 53
- Colless M., 1999, *Philosophical Transactions of the Royal Society of London Series A*, 357, 105
- Cooke R. J., Pettini M., Steidel C. C., 2018, *ApJ*, 855, 102
- de Oliveira-Costa A., Tegmark M., Gaensler B. M., Jonas J., Landecker T. L., Reich P., 2008, *MNRAS*, 388, 247
- de la Hoz E., Vielva P., Barreiro R. B., Martínez-González E., 2020, *J. Cosmology Astropart. Phys.*, 2020, 006
- de la Hoz E., Diego-Palazuelos P., Martínez-González E., Vielva P., Barreiro R. B., Bilbao-Ahedo J. D., 2022a, *J. Cosmology Astropart. Phys.*, 2022, 032
- de la Hoz E., et al., 2022b, *MNRAS*, In press.
- Delabrouille J., Cardoso J. F., 2007, *arXiv e-prints*, pp astro-ph/0702198
- Delabrouille J., Cardoso J. F., Patanchon G., 2003, *MNRAS*, 346, 1089
- Delabrouille J., Cardoso J. F., Le Jeune M., Betoule M., Fay G., Guilloux F., 2009, *A&A*, 493, 835
- Dicke R. H., Peebles P. J. E., Roll P. G., Wilkinson D. T., 1965, *ApJ*, 142, 414
- Dickinson C., et al., 2018, *New A Rev.*, 80, 1

- Diego-Palazuelos P., Vielva P., Martínez-González E., Barreiro R. B., 2020, *J. Cosmology Astropart. Phys.*, 2020, 058
- Diego-Palazuelos P., et al., 2022a, arXiv e-prints, p. arXiv:2210.07655
- Diego-Palazuelos P., et al., 2022b, *Phys. Rev. Lett.*, 128, 091302
- Dodelson S., Schmidt F., 2020, *Modern cosmology*. Academic Press
- Draine B. T., 2011, *Physics of the Interstellar and Intergalactic Medium*
- Draine B. T., Lazarian A., 1998, *ApJ*, 494, L19
- Draine B. T., Lazarian A., 1999, *ApJ*, 512, 740
- Einstein A., 1916, *Annalen der Physik*, 354, 769
- Eisenstein D. J., et al., 2005, *ApJ*, 633, 560
- Eriksen H. K., Jewell J. B., Dickinson C., Banday A. J., Górski K. M., Lawrence C. R., 2008, *ApJ*, 676, 10
- Errard J., Stompor R., 2019, *Phys. Rev. D*, 99, 043529
- Errard J., Stivoli F., Stompor R., 2011, *Phys. Rev. D*, 84, 069907
- Eskilt J. R., Komatsu E., 2022, *Phys. Rev. D*, 106, 063503
- Fernández-Cobos R., Vielva P., Barreiro R. B., Martínez-González E., 2012, *MNRAS*, 420, 2162
- Fernández-Cobos R., Marcos-Caballero A., Vielva P., Martínez-González E., Barreiro R. B., 2016, *MNRAS*, 459, 441
- Finkbeiner D. P., Davis M., Schlegel D. J., 1999, *ApJ*, 524, 867
- Foreman-Mackey D., Hogg D. W., Lang D., Goodman J., 2013, *PASP*, 125, 306
- Fukuda Y., et al., 1998, *Phys. Rev. Lett.*, 81, 1562
- Gallardo P. A., et al., 2018, in Zmuidzinas J., Gao J.-R., eds, *Society of Photo-Optical Instrumentation Engineers (SPIE) Conference Series Vol. 10708, Millimeter, Submillimeter, and Far-Infrared Detectors and Instrumentation for Astronomy IX*. p. 107083Y (arXiv:1808.05152), doi:10.1117/12.2312971
- Galloway M., et al., 2022, arXiv e-prints, p. arXiv:2201.03509
- Gamow G., 1956, *Scientific American*, 195, 136
- Génova-Santos R., et al., 2017, *MNRAS*, 464, 4107

- Goodman J., Weare J., 2010, *Communications in Applied Mathematics and Computational Science*, 5, 65
- Gordon C., 2001, PhD thesis, University of Portsmouth, UK
- Górski K. M., Hivon E., Banday A. J., Wandelt B. D., Hansen F. K., Reinecke M., Bartelmann M., 2005, *ApJ*, 622, 759
- Greaves J. S., Scaife A. M. M., Frayer D. T., Green D. A., Mason B. S., Smith A. M. S., 2018, *Nature Astronomy*, 2, 662
- Grumitt R. D. P., Jew L. R. P., Dickinson C., 2020, *MNRAS*, 496, 4383
- Gubitosi G., Paci F., 2013, *J. Cosmology Astropart. Phys.*, 2013, 020
- Guth A. H., Tye S. H. H., 1980, *Phys. Rev. Lett.*, 44, 631
- Guzmán A. E., May J., Alvarez H., Maeda K., 2011, *A&A*, 525, A138
- Hanany S., et al., 2019, in *Bulletin of the American Astronomical Society*. p. 194 (arXiv:1908.07495)
- Hansen F. K., Banday A. J., Eriksen H. K., Górski K. M., Lilje P. B., 2006, *ApJ*, 648, 784
- Hanson D., Challinor A., Lewis A., 2010, *General Relativity and Gravitation*, 42, 2197
- Harper S. E., et al., 2022, *MNRAS*, 513, 5900
- Heavens A., Jimenez R., Verde L., 2014, *Phys. Rev. Lett.*, 113, 241302
- Hensley B. S., Bull P., 2018, *ApJ*, 853, 127
- Hervías-Caimapo C., Bonaldi A., Brown M. L., Huffenberger K. M., 2022, *ApJ*, 924, 11
- Hinshaw G., et al., 2007, *ApJS*, 170, 288
- Hinshaw G., et al., 2013, *ApJS*, 208, 19
- Hobson M. P., Lasenby A. N., 1998, *MNRAS*, 298, 905
- Hu W., 2000, *Phys. Rev. D*, 62, 043007
- Hu W., Dodelson S., 2002, *ARA&A*, 40, 171
- Hu W., White M., 1997, *New A*, 2, 323
- Hubble E. P., 1926, *ApJ*, 64, 321
- Hubble E., 1929, *Proceedings of the National Academy of Science*, 15, 168
- Hurier G., Macías-Pérez J. F., Hildebrandt S., 2013, *A&A*, 558, A118

- Hutschenreuter S., et al., 2022, *A&A*, 657, A43
- Hyvarinen A., 1999, in 1999 IEEE international symposium on circuits and systems (ISCAS). pp 57–61
- Ichiki K., Kaji R., Yamamoto H., Takeuchi T. T., Fukui Y., 2014, *ApJ*, 780, 13
- Ichiki K., Kanai H., Katayama N., Komatsu E., 2019, *Progress of Theoretical and Experimental Physics*, 2019, 033E01
- Jeffrey N., Boulanger F., Wandelt B. D., Regaldo-Saint Blancard B., Allys E., Levrier F., 2022, *MNRAS*, 510, L1
- Jones M. E., et al., 2018, *MNRAS*, 480, 3224
- Joyce A., Lombriser L., Schmidt F., 2016, *Annual Review of Nuclear and Particle Science*, 66, 95
- Kogut A., Chluba J., Fixsen D. J., Meyer S., Spergel D., 2016, in MacEwen H. A., Fazio G. G., Lystrup M., Batalha N., Siegler N., Tong E. C., eds, *Society of Photo-Optical Instrumentation Engineers (SPIE) Conference Series Vol. 9904, Space Telescopes and Instrumentation 2016: Optical, Infrared, and Millimeter Wave*. p. 99040W, doi:10.1117/12.2231090
- Komatsu E., 2022, *Nature Reviews Physics*, 4, 452
- Krachmalnicoff N., et al., 2018, *A&A*, 618, A166
- Krachmalnicoff N., et al., 2022, *J. Cosmology Astropart. Phys.*, 2022, 039
- Leach S. M., et al., 2008, *A&A*, 491, 597
- Leavitt H. S., Pickering E. C., 1912, *Harvard College Observatory Circular*, 173, 1
- Lemaître G., 1927, *Annales de la Société Scientifique de Bruxelles*, 47, 49
- Lewis A., Challinor A., 2006, *Phys. Rep.*, 429, 1
- Lewis A., Challinor A., Lasenby A., 2000, *ApJ*, 538, 473
- Linde A. D., 1982, *Physics Letters B*, 108, 389
- LiteBIRD Collaboration et al., 2022, *arXiv e-prints*, p. arXiv:2202.02773
- Liu T., Cao S., Li X., Zheng H., Liu Y., Guo W., Zheng C., 2022, *arXiv e-prints*, p. arXiv:2210.02765
- Maino D., et al., 2002, *MNRAS*, 334, 53
- Maino D., Donzelli S., Banday A. J., Stivoli F., Baccigalupi C., 2007, *MNRAS*, 374, 1207

-
- Marsh D. J. E., 2016, *Phys. Rep.*, 643, 1
- Martin J., Ringeval C., Vennin V., 2014, *Physics of the Dark Universe*, 5, 75
- Mather J. C., et al., 1994, *ApJ*, 420, 439
- McBride L., Bull P., Hensley B. S., 2022, arXiv e-prints, p. arXiv:2207.14213
- Meisner A. M., Finkbeiner D. P., 2015, *ApJ*, 798, 88
- Miville-Deschênes M. A., Ysard N., Lavabre A., Ponthieu N., Macías-Pérez J. F., Aumont J., Bernard J. P., 2008, *A&A*, 490, 1093
- Namikawa T., et al., 2022, *Phys. Rev. D*, 105, 023511
- National Academies of Sciences E., Medicine et al., 2021, *Pathways to Discovery in Astronomy and Astrophysics for the 2020s*
- Nørgaard-Nielsen H. U., Jørgensen H. E., 2008, *Ap&SS*, 318, 195
- Orlando E., Strong A., 2013, *MNRAS*, 436, 2127
- Ostriker J. P., Vishniac E. T., 1986, *ApJ*, 306, L51
- Patanchon G., Cardoso J. F., Delabrouille J., Vielva P., 2005, *MNRAS*, 364, 1185
- Pelgrims V., Clark S. E., Hensley B. S., Panopoulou G. V., Pavlidou V., Tassis K., Eriksen H. K., Wehus I. K., 2021, *A&A*, 647, A16
- Penzias A. A., Wilson R. W., 1965, *ApJ*, 142, 419
- Percival W. J., Samushia L., Ross A. J., Shapiro C., Raccanelli A., 2011, *Philosophical Transactions of the Royal Society of London Series A*, 369, 5058
- Perivolaropoulos L., Skara F., 2022, *New A Rev.*, 95, 101659
- Perlmutter S., et al., 1999, *ApJ*, 517, 565
- Perraudin N., Defferrard M., Kacprzak T., Sgier R., 2019, *Astronomy and Computing*, 27, 130
- Petroff M. A., Addison G. E., Bennett C. L., Weiland J. L., 2020, *ApJ*, 903, 104
- Planck Collaboration 2016, *A&A*, 594, A10
- Planck Collaboration et al., 2016a, *A&A*, 594, A9
- Planck Collaboration et al., 2016b, *A&A*, 594, A15
- Planck Collaboration et al., 2016c, *A&A*, 594, A17

- Planck Collaboration et al., 2016d, *A&A*, 594, A17
- Planck Collaboration et al., 2016e, *A&A*, 594, A25
- Planck Collaboration et al., 2020a, *A&A*, 641, A1
- Planck Collaboration et al., 2020b, *A&A*, 641, A4
- Planck Collaboration et al., 2020c, *A&A*, 641, A7
- Planck Collaboration et al., 2020d, *A&A*, 641, A9
- Planck Collaboration et al., 2020e, *A&A*, 643, A42
- Polarbear Collaboration et al., 2020, *ApJ*, 897, 55
- Pospelov M., Pradler J., 2010, *Annual Review of Nuclear and Particle Science*, 60, 539
- Puglisi G., et al., 2018, *ApJ*, 858, 85
- Puglisi G., Mihaylov G., Panopoulou G. V., Poletti D., Errard J., Puglisi P. A., Vianello G., 2022, *MNRAS*, 511, 2052
- Qi J.-Z., Zhao J.-W., Cao S., Biesiada M., Liu Y., 2021, *MNRAS*, 503, 2179
- Qu F. J., Challinor A., Sherwin B. D., 2022, *arXiv e-prints*, p. arXiv:2208.14988
- Rees M. J., Sciama D. W., 1968, *Nature*, 217, 511
- Refregier A., 2003, *ARA&A*, 41, 645
- Remazeilles M., Delabrouille J., Cardoso J.-F., 2011a, *MNRAS*, 410, 2481
- Remazeilles M., Delabrouille J., Cardoso J.-F., 2011b, *MNRAS*, 418, 467
- Remazeilles M., Dickinson C., Eriksen H. K. K., Wehus I. K., 2016, *MNRAS*, 458, 2032
- Remazeilles M., Rotti A., Chluba J., 2021, *MNRAS*, 503, 2478
- Ricciardi S., et al., 2010, *MNRAS*, 406, 1644
- Riess A. G., et al., 1998, *AJ*, 116, 1009
- Ritacco A., Boulanger F., Guillet V., Delouis J.-M., Puget J.-L., Aumont J., Vacher L., 2022, *arXiv e-prints*, p. arXiv:2206.07671
- Rogers K. K., Peiris H. V., Leistedt B., McEwen J. D., Pontzen A., 2016a, *MNRAS*, 460, 3014
- Rogers K. K., Peiris H. V., Leistedt B., McEwen J. D., Pontzen A., 2016b, *MNRAS*, 463, 2310
- Ronneberger O., Fischer P., Brox T., 2015, *arXiv e-prints*, p. arXiv:1505.04597

-
- Rubiño-Martín J. A., et al., 2010, in *Highlights of Spanish Astrophysics V.* p. 127 (arXiv:0810.3141), doi:10.1007/978-3-642-11250-8_12
- Rubiño-Martín J. A., et al., 2022, *MNRAS*, In press.
- Rubin V. C., Ford W. Kent J., 1970, *ApJ*, 159, 379
- Rybicki G. B., Lightman A. P., 1979, *Radiative processes in astrophysics*
- Sachs R. K., Wolfe A. M., 1967, *ApJ*, 147, 73
- Salatino M., et al., 2018, in Zmuidzinas J., Gao J.-R., eds, *Society of Photo-Optical Instrumentation Engineers (SPIE) Conference Series Vol. 10708, Millimeter, Submillimeter, and Far-Infrared Detectors and Instrumentation for Astronomy IX.* p. 1070848 (arXiv:1808.07442), doi:10.1117/12.2312993
- Samtleben D., Staggs S., Winstein B., 2007, *Annual Review of Nuclear and Particle Science*, 57, 245
- Sato K., 1981, *MNRAS*, 195, 467
- Sayre J. T., et al., 2020, *Phys. Rev. D*, 101, 122003
- Scolnic D. M., et al., 2018, *ApJ*, 859, 101
- Scott D., Smoot G., 2006, arXiv e-prints, pp astro-ph/0601307
- Seljak U., Zaldarriaga M., 1997, *Phys. Rev. Lett.*, 78, 2054
- Shen S., Mo H. J., White S. D. M., Blanton M. R., Kauffmann G., Voges W., Brinkmann J., Csabai I., 2003, *MNRAS*, 343, 978
- Siah M. J., Wiita P. J., 1990, *ApJ*, 363, 411
- Sponseller D., Kogut A., 2022, *ApJ*, 936, 8
- Starobinsky A. A., 1980, *Physics Letters B*, 91, 99
- Stolyarov V., Hobson M. P., Ashdown M. A. J., Lasenby A. N., 2002, *MNRAS*, 336, 97
- Stolyarov V., Hobson M. P., Lasenby A. N., Barreiro R. B., 2005, *MNRAS*, 357, 145
- Stompor R., Leach S., Stivoli F., Baccigalupi C., 2009, *MNRAS*, 392, 216
- Stompor R., Errard J., Poletti D., 2016, *Phys. Rev. D*, 94, 083526
- Sugiyama N., Silk J., Vittorio N., 1993, *ApJ*, 419, L1
- Sunyaev R. A., Zeldovich Y. B., 1970, *Ap&SS*, 7, 3
- Sunyaev R. A., Zeldovich Y. B., 1972, *Comments on Astrophysics and Space Physics*, 4, 173

- Tassis K., Pavlidou V., 2015, *MNRAS*, 451, L90
- Tegmark M., Efstathiou G., 1996, *MNRAS*, 281, 1297
- Tegmark M., de Oliveira-Costa A., Hamilton A. J., 2003, *Phys. Rev. D*, 68, 123523
- Thorne B., Dunkley J., Alonso D., Næss S., 2017, *MNRAS*, 469, 2821
- Tristram M., et al., 2022, *Phys. Rev. D*, 105, 083524
- Trombetti T., Burigana C., De Zotti G., Galluzzi V., Massardi M., 2018, *A&A*, 618, A29
- Tsujikawa S., 2003, arXiv e-prints, pp hep-ph/0304257
- Tucci M., Toffolatti L., 2012, *Advances in Astronomy*, 2012, 624987
- Vansyngel F., Wandelt B. D., Cardoso J.-F., Benabed K., 2016, *A&A*, 588, A113
- Vazquez J. A., Padilla L. E., Matos T., 2018, arXiv e-prints, p. arXiv:1810.09934
- Viel M., Becker G. D., Bolton J. S., Haehnelt M. G., 2013, *Phys. Rev. D*, 88, 043502
- Vielva P., et al., 2022, *J. Cosmology Astropart. Phys.*, 2022, 029
- Wagner-Carena S., Hopkins M., Diaz Rivero A., Dvorkin C., 2020, *MNRAS*, 494, 1507
- Wang G.-J., Shi H.-L., Yan Y.-P., Xia J.-Q., Zhao Y.-Y., Li S.-Y., Li J.-F., 2022, *ApJS*, 260, 13
- Wolz L., et al., 2015, in *Advancing Astrophysics with the Square Kilometre Array (AASKA14)*. p. 35 (arXiv:1501.03823)
- Yu Q., Spergel D. N., Ostriker J. P., 2001, *ApJ*, 558, 23
- Zaldarriaga M., Seljak U., 1997, *Phys. Rev. D*, 55, 1830
- Zwicky F., 1933, *Helvetica Physica Acta*, 6, 110